Universidade de Aveiro Departamento de Física
2019

Jennifer Cláudia Passos Teixeira

Estudo optoelectrónico de células solares baseadas em filmes finos de Calcogenetos

Optoelectronic study of Thin Film Solar Cells Based on Chalcogenide

Universidade de Aveiro Departamento de Física
2019

Jennifer Cláudia Passos Teixeira

Estudo optoelectrónico de células solares baseadas em filmes finos de Calcogenetos

Optoelectronic study of Thin Film Solar Cells Based on Chalcogenide

Tese apresentada à Universidade de Aveiro para cumprimento dos requisitos necessários à obtenção do grau de Doutor em Física, realizada sob a orientação científica do Doutor Joaquim Fernando Monteiro de Carvalho Pratas Leitão, Professor Auxiliar do Departamento de Física da Universidade de Aveiro e coorientação do Doutor Pedro Manuel Parracho Salomé, Professor Auxiliar Convidado, do Departamento de Física da Universidade de Aveiro.

Cofinanciado por:

PORTUGAL 2020

UNIÃO EUROPEIA
Fundo Europeu
de Desenvolvimento Regional

COMPETE 2020

FCT
Fundação para a Ciência e a Tecnologia

The author acknowledge the financial support of the project UID/CTM/50025/2019, and IF/00133/2015/CP1325/CT0001 from the FCT.

Para a minha Bi.

o júri

presidente

Prof. Doutor Rui Luís Andrade Aguiar
Professor Catedrático da Universidade de Aveiro

vogais

Prof. Doutor José António de Carvalho Paixão
Professor Catedrático da Universidade de Coimbra

Prof. Doutora Teresa Maria Fernandes Rodrigues Cabral Monteiro
Professora Associada com Agregação da Universidade de Aveiro

Prof. Doutor Hugo Manuel Brito Águas
Professor Associado da Universidade Nova de Lisboa

Prof. Doutor João Pedro Dos Santos Hall Agorreta de Alpuim
Professor Auxiliar da Universidade do Minho

Prof. Doutor Joaquim Fernando Monteiro de Carvalho Pratas Leitão
Professor Auxiliar da Universidade de Aveiro

agradecimentos

Primeiramente gostaria de agradecer ao Laboratório Associado i3N pelo apoio financeiro e condições técnicas que permitiram a realização deste trabalho.

Sendo esta tese fruto de diferentes colaborações envolvendo um grande número de pessoas e instituições, gostaria de agradecer todas as pessoas e entidades envolvidas no trabalho apresentado.

Agradeço ao Prof. Doutor Joaquim Leitão e ao Prof. Doutor Pedro Salomé pela orientação ao longo deste trabalho. Duas maneiras muito diferentes de olhar para os problemas às quais devo grande parte do meu conhecimento. Para além do conhecimento científico, agradeço os valores transmitidos, essencialmente a postura honesta sobre a prática científica que ambos me incutiram e fazem deste um trabalho melhor. Agradeço ao Prof. Doutor. Joaquim Leitão a postura perante todos os problemas que eu lhe apresentei ao longo destes anos, pois hoje são a força deste trabalho.

Agradeço ao Prof. Doutor António Cunha a disponibilidade e apoio.

Agradeço ao Prof. Doutor José Castanheira a disponibilidade e entusiamos nas discussões partilhadas.

Agradeço ao Prof. Doutor Jorge Soares e Sr. Januário todas as vezes que me prestaram auxílio no laboratório.

Agradeço ao Prof. Doutor Bonifácio o apoio em atividades extra este trabalho.

Agradeço ao Bruno Falcão, Marta Sousa, Maria Batista e ao Doutor Ricardo Vieira pela ajuda na realização deste trabalho.

Aproveito também para agradecer aos meus amigos, que de algum modo me apoiaram através da partilha de conhecimento ou simplesmente através da sua boa companhia: Isabel Silva, Rosa Soares, José Carreira, Catarina Moreira, Filipe Rosário, Edgar Wright, Cláudio Nico e André Martins. Um agradecimento especial à Rita Frias, João Ramalho e Maria Relvas pela amizade e apoio na preparação destas provas, e ao Eduardo Oliveira por estar sempre por perto independentemente da distância física.

Por último, um agradecimento muito especial ao meu pai, que tanto me apoia sem pedir nada em troca. Ao Xavier, por ter chegado a meio deste percurso e ter trazido tanta alegria à nossa pequena família Cristiana, Hugo e Tia Lena.

palavras-chave

$Cu(In,Ga)Se_2$, Cu_2ZnSnS_4, defeitos, fotoluminescência, flutuações de potencial, células solares.

resumo

Nesta tese, foi estudado o papel dos defeitos nas propriedades optoelectrónicas de dois materiais com grande potencial para aplicações fotovoltaicas, Cu_2ZnSnS_4 (CZTS) e $Cu(In, Ga)Se_2$ (CIGS). Ambos os materiais são fortemente dopados e compensados, sendo que as suas propriedades optoelectrónicas são governadas pelas suas estruturas de níveis eletrónicos complexas. No sentido de melhor compreender o impacto da estrutura eletrónica no desempenho das células solares, diferentes estudos foram realizados utilizando principalmente a técnica de fotoluminescência, complementada com análise morfológica, estrutural e elétrica. Para as células solares baseadas em CZTS, foram estudadas três séries de amostras para as quais o impacto i) do tempo da temperatura máxima de sulfurização, ii) do método de sulfurização, iii) do tratamento térmico após a deposição, foi avaliado nas propriedades optoelectrónicas da camada CZTS. Para o CIGS, três tópicos principais foram abordados, i) células solares com arquitetura convencional, ii) células solares para as quais se exploram novas arquiteturas, iii) influência dos defeitos no desempenho das células solares a partir da comparação de modelos teóricos com resultados experimentais. A influência das flutuações de potencial foi evidenciada, sendo que a luminescência obtida, tanto envolvendo o CZTS como o CIGS, foi completamente explicada a partir de modelos de recombinação que envolvem a presença destas flutuações. Os estudos óticos desenvolvidos no âmbito das células solares de CZTS revelaram um grande impacto de mecanismos não radiativos e de recombinação envolvendo defeitos profundos que se relacionam com um fraco desempenho dos dispositivos estudados. Para diferentes séries de amostras de células solares baseadas em CIGS foi obtida uma correlação entre a influência das flutuações de potencial e desempenho dos dispositivos estudados. Os resultados óticos obtidos para CIGS revelaram dois mecanismos principais de desexcitação dos canais radiativos envolvendo aglomerados de dadores pouco profundos e o defeito aceitador V_{Cu}. A partir das análises teórica e experimental de células solares de CIGS, obteve-se uma maior correlação entre a influência das flutuações de potencial electroestáticas com as perdas de tensão de circuito aberto, do que aquela observada para as flutuações de hiato. Finalmente, foi demonstrada a influência das flutuações de potencial na tecnologia CIGS à temperatura ambiente. Nesta tese, foi mostrado que as propriedades optoelectrónicas do CZTS e CIGS são consistentes com a existência de flutuações de potencial, sendo que o seu impacto no desempenho das células solares é significativamente diferente em cada uma das tecnologias. Enquanto no CZTS os mecanismos de recombinação aparecem como um problema com um impacto no desempenho das células solares mais significativo que as flutuações de potencial, no CIGS uma correlação entre a influência das flutuações de potencial e o desempenho das células solares é notória.

keywords

$Cu(In,Ga)Se_2$, Cu_2ZnSnS_4, defects, photoluminescence, fluctuating potentials, solar cells.

abstract

In this thesis, we studied the role of the defects on the optoelectronic properties of two semiconductors with high potential for photovoltaic application, Cu_2ZnSnS_4 (CZTS) and $Cu(In, Ga)Se_2$ (CIGS). Both materials are highly doped and strongly compensated, and their optoelectronic properties are governed by a highly complex electronic energy levels structure. In order to further understand the impact of these complex structures on the performance of the devices, several studies were carried out using mainly the photoluminescence technique, and complemented with other optical, morphological, structural, and electrical analyses. For CZTS based solar cells, three series of samples that include studies on the impact of: i) the time of maximum temperature of the sulphurization; ii) the sulphurization method; and iii) the post-deposition annealing on the optoelectronic properties of the CZTS layer, were studied. For CIGS based solar cells, three major topics were addressed: i) solar cells with conventional architecture, ii) solar cells that explore new architectures; and iii) theoretical and experimental study of the influence of defects on the devices performance. The influence of fluctuating potential was shown, and fully explain CZTS and CIGS characteristic luminescence. The optical studies carried in CZTS based solar cells, reveal several issues related to non-radiative recombination or recombination involving deep defects that were closely linked to a poor performance of the studied devices. For different series of CIGS based solar cells, an overall correlation of the influence of the fluctuating potentials with the performance of the devices were obtained. The CIGS related optical results revealed two main recombination de-excitation channels compatible with a shallow donors cluster and the V_{Cu} acceptor defect. From theoretical and experimental analyses of CIGS based solar cells, we obtained a higher degree of correlation of electrostatic fluctuating potentials with the open circuit voltage losses of the devices, in comparison with bandgap fluctuations. Finally, we demonstrate the influence of fluctuating potentials in CIGS technology at room temperature. In this thesis, we showed that the optoelectronic properties of CZTS and CIGS are consistent with the existence of the fluctuating potentials, being its impact as a limitative factor on the studied solar cells performance significantly different in the two studied technologies. CZTS based solar cells present serious recombination issues that are significantly more critical for the performance of the device, then the existence of fluctuating potentials. For CIGS based solar cells, the influence of the fluctuating potentials and the performance of the devices are remarkably correlated.

Contents

List of Figures

List of Tables

List of main acronyms

ALD	Atomic layer deposition
CBD	Chemical bath deposition
CIGS	$Cu(In,Ga)Se_2$
CZTS	Cu_2ZnSnS_4
CZTSe	$Cu_2ZnSnSe_4$
CZTSSe	$Cu_2ZnSn(S,Se)_4$
DAP	Donor-acceptor pairs
EQE	External quantum efficiency
GGI	[Ga]/([Ga]+[In])
J-V	Current density-voltage
PDA	Post-deposition annealing
PDT	Post-deposition treatment
PL	Photoluminescence
PV	Photovoltaics
QNR	Quasi-neutral region
RT	Room temperature
SCR	Space charge region
SEM	Scanning electron microscope
SLG	Soda-lime-glass
SQ	Shockley-Queiser
SRH	Shockley-Read-Hall
XRD	X-ray diffraction

Chapter 1

Motivation

A widely and simple context of the importance of the work presented in this thesis is shown. Chalcogenide solar cells based on CIGS and CZTS are presented as promising thin film technologies to meet the future energy demand. The scope and organization of this thesis is presented at the end of the Chapter.

On 12 December 2015, 195 countries signed the Paris Agreement at the twenty-first session of the Conference of the Parties to the United Nations Framework Convention on Climate Change held in Paris, under which they agreed according to Article 2 to [1]:

(a) *Holding the increase in the global average temperature to well below 2° C above pre-industrial levels and pursuing efforts to limit the temperature increase to 1.5° C above pre-industrial levels, (...) and low greenhouse gas emissions development, in a manner that does not threaten food production;.*

In order to meet the commitment under the Paris Agreement, there is a need for urgent incentives and regulation to promote the phasing out of support for the production and consumption of fossil fuels. The International Energy Agency (IEA) recently presented the statistic data concerning the growth in the global energy demand for the year of 2017, and by comparing with earlier years (see Fig. 1.1), it is clear that the current effort to combat climate change is far from enough as the growth rate of renewable energy needs to cover rise in consumption, but also replace existing fossil fuels. Boosted by a strong worldwide economic growth, the global energy demand increased by 2.1% in 2017, which was more than twice the growth rate of 2016 (0.9%). The main problem is that over 70% of the global energy demand growth was met by fossil fuels, and if we consider the global energy consumption this value goes up to 81%. Thus, it is not surprising that when we look at CO_2 emissions data, we see a growth of 1.4% [2]. This scenario results mainly from the aforementioned economic growth, in addition to a decrease in the fossil fuels price, and a weak effort to achieve an efficient

energy use. However, the increase in CO_2 emissions was not global, important economies like the United States, United Kingdom, Mexico, and Japan presented a decline. The United States presented the biggest drop in greenhouse gas emissions, driven by a higher renewable based power generation and decline in the power sector demand. Thus, renewable energy offers an efficient and sustainable solution to the challenge of meeting the increasing worldwide energy demand [2, 3, 4].

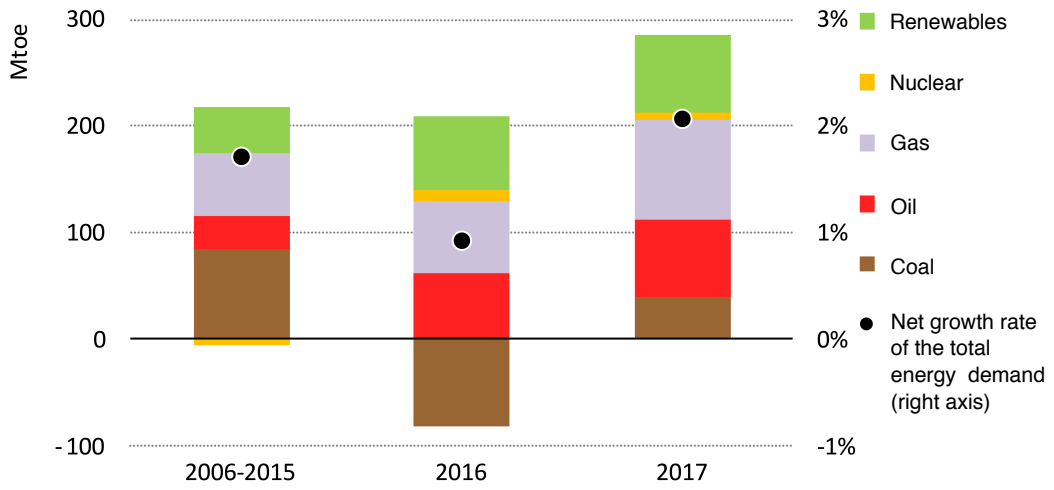

Figure 1.1: Average annual growth in energy demand by million tonnes of oil equivalent (Mtoe) from 2006 to 2015, 2016, and 2017. Adapted from [2].

Renewables saw the highest growth rate of any energy source in 2017, driven by an increase in investment, falling costs, and advances in enabling technologies. Although it looks like an impressive result, given the scenario discussed above, the renewables rate of growth falls short of that needed to meet the global climate goals. In this way, the IEA charted a path toward meeting the Paris Agreement goals. They stated a mandatory sharp decline of global greenhouse gas emissions by 2020, and due to the 2017 scenario the decline now, must be even greater. In that way, the share of low-carbon energy sources must increase by at least 1.1% every year, which is more than five times the growth of 2017. Regarding, the power sector, renewables based generated electricity must increase by an average of 700 TWh annually, which is an 80% increase compared to the 380 TWh increase in 2017 [2, 3].

Let us consider one of the energy core sectors, the power one. The worldwide electricity demand increased by 3.1% in 2017, which is significantly higher than the overall increase in energy demand (2.1%). However, renewables are becoming even more competitive to meet the electricity generation needs, as we will show below. Fig. 1.2 shows that the global renewable power capacity more than doubled in the last decade, and the capacity of non-hydropower renewables increased more than six times. The overall renewable energy accounted for an estimated 70% new installed power capacity in 2017, up from 63% in 2016. By the end of 2017, the total renewable power capacity was responsible for roughly 2195 GW [2, 3].

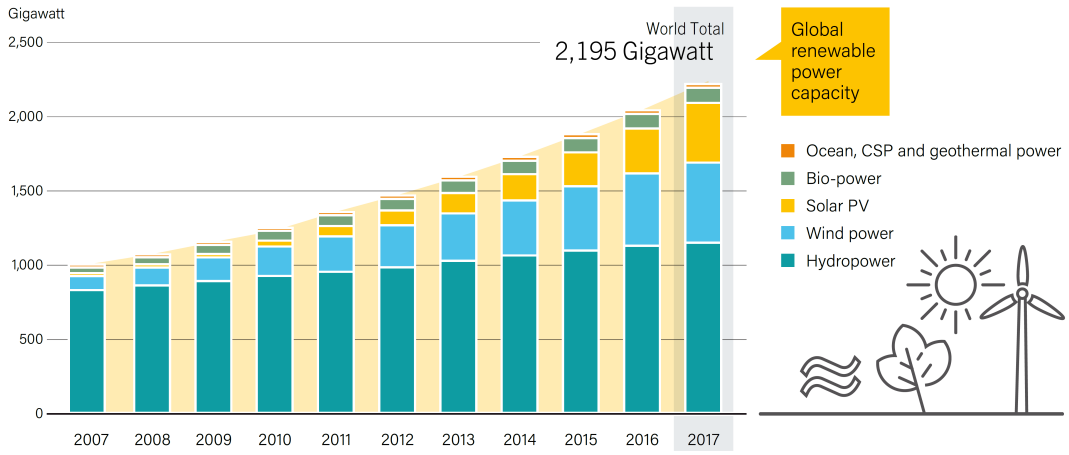

Figure 1.2: Global renewable power capacity, 2007-2017. Adapted from [3].

As Fig. 1.3 shows, in 2017 the renewable energy accounts for 26.5% of global electricity generation, this value raised by 9% (relative) over 2016[1]. PV energy is responsible for a mere 1.9% of the worldwide electricity. However, it accounts for 55% of newly installed renewable power capacity. The transition to a renewable based electricity is under way, but needs to be accelerated with a continued improvement in the cost/competitiveness, namely of PV and wind power technologies [2, 3].

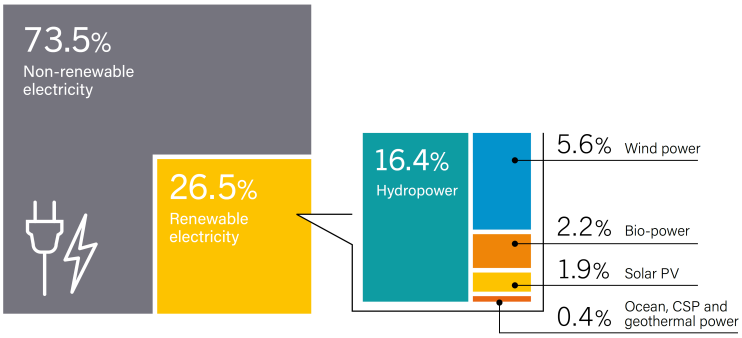

Figure 1.3: Estimated renewable energy share of total electricity production in 2017. Adapted from [3].

The impressive increase in the PV energy global capacity in the last decade is shown in Fig. 1.4 a). In 2017, at least 98 GW of PV capacity was installed, increasing the global capacity by nearly one-third in comparison to 2016, which gives a cumulative value of 402 GW. There are no doubts that the year 2017 was a landmark one for PV, the world added more capacity from PV, than from any other type of power generating technology. More PV was installed than the net capacity additions of fossil fuels and nuclear power combined. The significant PV market increase in 2017 was due to the Chinese market, where new installations accounted for more than 50% of the total, adding more PV

[1] According to another source, IEA data, renewables based electricity generation increased 6.3% in 2017, accounting now for 25% of global electricity generation [2].

capacity (nearly 53.1 GW), than was added worldwide in 2015 (51 GW). Taking into account the top five PV markets, China, United States, India, Japan, and Turkey, these countries were responsible for nearly 84% of newly installed PV capacity. However, countries on all habitable continents have begun to contribute to a global PV energy growth [2, 3].

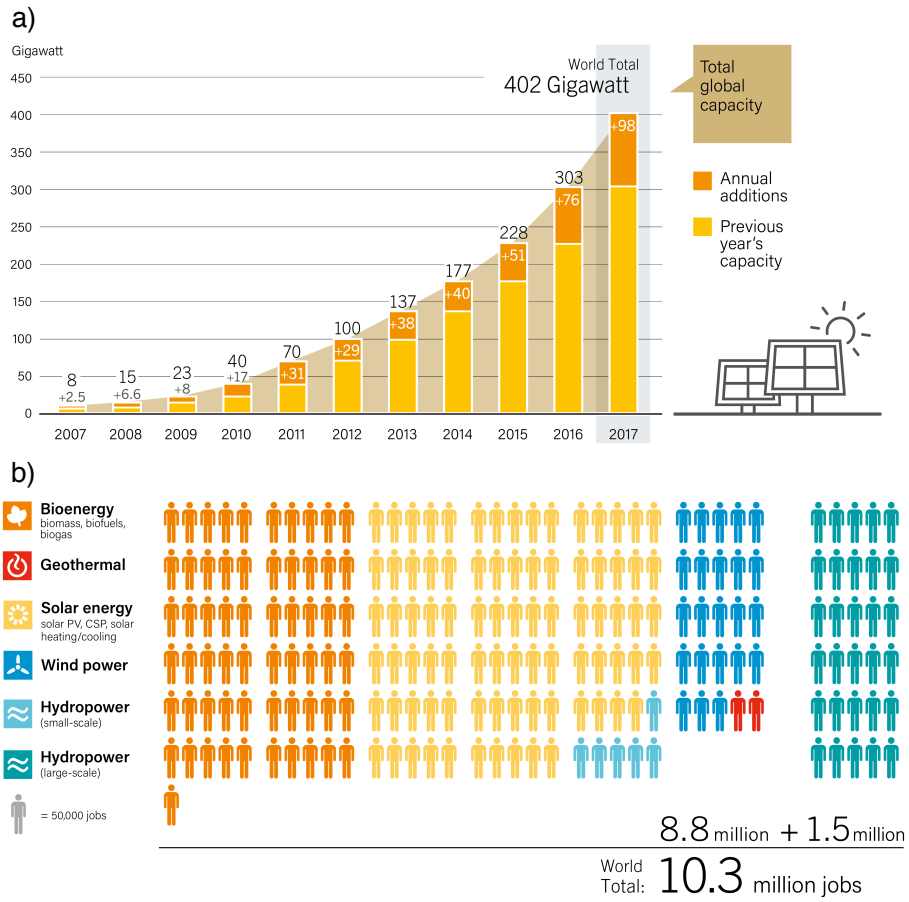

Figure 1.4: a) Photovoltaic energy global capacity and annual additions, 2007-2017. b) Total number of jobs in renewable sector given by different renewable markets. Adapted from [3].

From a local economic point of view, the renewable energy sector employed, directly and indirectly, approximately 10.3 million people in 2017. As shown in Fig. 1.4 b), the PV industry was the largest employer of the renewable sector. Global employment in solar PV was estimated at 3.4 million jobs in 2017, 9% higher than in 2016. As the leading PV manufacturer and market, China accounted for 2.2 millions. The United States, by contrast, registered the first decline ever in PV employment, driven by a decrease in new PV installations, policy uncertainties and of course, due to the self-imposed import tariffs impositions. PV employment also declined in Japan and in the European Union [3].

The PV global market expansion was promoted by an increase on the competitiveness of the PV market combined with a higher demand for electricity, as well as an increase in the awareness of PV potential to solve the issue of the global climate change. Throughout 2017, modules prices continued to fall, but at a slower rate than in 2016. Installed costs also declined globally over the course of 2017.

Since the cost of PV systems is nowadays only partly determined by the cost of the solar cells being the rest of the costs dedicated to the balance of systems, BoS, (wirings inverter, batteries, installation, etc), an increase of the efficiency per module reduce the cost of solar energy, as for the same modules with more power, the cost of BoS is the same as modules with a lower efficiency. In fact, new records of light to power efficiencies for solar cells and modules were achieved in 2017, whereas at the same time there are several new material systems being studied to achieve high efficiency at lower costs [5, 6]. Thus, several challenges remain to be addressed before solar PV may become a mature and major source of the worldwide electricity. Although, there are several countries including, Germany, Greece, Honduras and Italy, that already have a significant PV based electricity generation [2, 3].

1.1 Thin film technology

The commercially available PV market is shared by two technologies: wafer based silicon (Si) (1st generation of solar cells) and thin films (2nd generation). Fig 1.5 shows that over the decades the PV market has been dominated by silicon wafer based technology, crystalline (c-Si) and multi-crystalline (mc-Si) Si. Although it has always been dominated the market, there have been some periods when its domain has lost some strength. However, it was always capable to return to its strong leadership. Such dominance from the Si wafer based technology is explained by the high availability of the raw material, the compatibility with the microelectronics technology, the high efficiency of the modules, and more recently a reduction of costs driven by reducing the wafer thickness and by the implementation of the passivated emitter rear cell (PERC) architecture. The commercially available thin film based technologies[2] includes cadmium-telluride (CdTe), amorphous silicon (a-Si) and copper indium gallium diselenide ($Cu(In,Ga)Se_2$, CIGS). In 2017, Si wafer based PV technology accounted for about 95% of the global PV production. The share of mc-Si technology is now about 62% and all thin film technology accounted for about 5% (down from 6% in 2016 and 8% in 2015) of the total annual PV production [3, 5].

The enhancement of the PV market requires further strategies to reduce the costs of production and increase the efficiencies, and this may finally be the breakthrough opportunity for thin film technology in PV market, mainly for CIGS and alternative alloys labelled as composed of abundant and non-toxic elements. CIGS and CdTe thin film based technologies present a huge advantage over Si based solar cells, which is the high absorption coefficient of these two materials, that outcome from their direct bandgap nature. This enables a scale down on the thickness of the absorber layer leading to a reduction of the modules fabrication cost. On the other hand, Si based technology is limited by the low absorption coefficient due to the indirect bandgap energy, which restricts further reduction in cost production. Flexible substrates are believed to be the next step to take in thin film technology, since will enable for a roll-to-roll fabrication, which lowers the costs even further. At this point, the question that remains is what is driving away the thin film technology to a prominent position in the

[2]These technologies are named according to the semiconductor used as absorber layer.

PV market. There are two main reasons that include the low efficiencies of the modules comparing to Si ones, and the scarcity and toxicity of some elements present in the alloys in thin film technology. A non technological reason is related with the lack of confidence from investors in thin film technology [4].

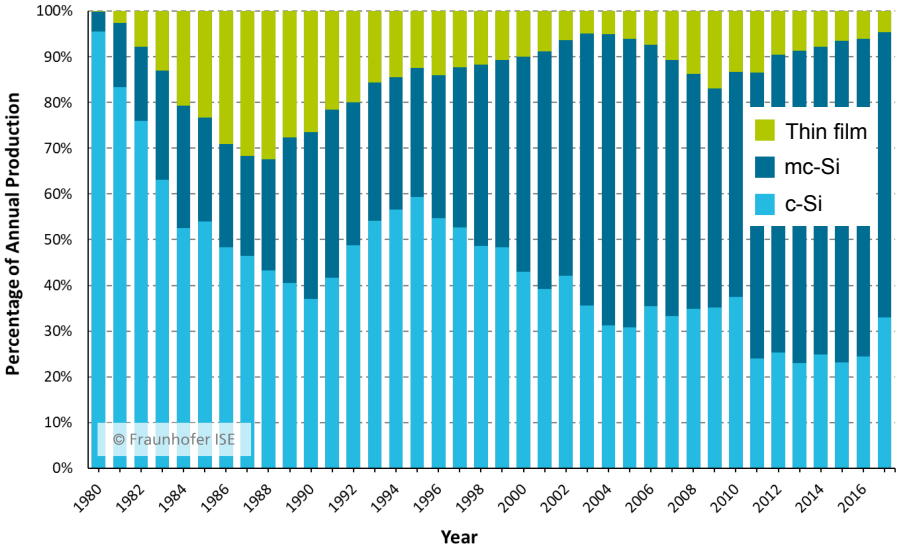

Figure 1.5: Percentage of global annual production by technology: silicon wafer based, crystalline (c-Si) and multi-crystalline (mc-Si), and thin film, from 1980 until 2017. Adapted from [5].

A striking difference between record light to power efficiency of laboratory solar cells and the record efficiency of commercial modules is obtained in the thin film technology. Due to the already very low production costs of silicon modules, only photovoltaic technologies that allow for very high light to power performance are now viable. The highest laboratory light to power efficiency in thin film technology is 23.35% for CIGS, being this value higher than the obtained for mc-Si 22.3% [6, 7]. The efficiencies obtained by thin film modules (record for CdTe of 18.6%, and CIGS of 19.2%) are lower than the ones for Si wafer based modules (record for c-Si of 24.4%, and mc-Si 19.9%) [6]. Although, the lower efficiencies of the thin film modules comparing to the Si wafer based ones, these values are promising and there are room for improvements, as the recent improvements 23.35% for CIGS laboratory solar cells suggests.

The scarcity of indium (In), gallium (Ga), selenium (Se), and tellurium (Te) pose a challenge due to their limited availability. So, the costs of these raw materials are high and tend to fluctuate. Moreover, cadmium (Cd) is classified as a toxic and carcinogenic element, forbidden in high concentrations in several important markets. Thus, CdTe does not fit into the vision of the PV as a sustainable solution to meet the increase of the energy demand. New strategies toward reducing the consumption of the aforementioned elements have been taken through: i) reduce even further the thickness of the absorber layer, and ii) new material systems composed of abundant and non-toxic elements. CIGS based technology already charted the strategy to increase its competitiveness in the PV market. Ultrathin devices are believed to be the path forward in this technology, as it enables for the reduction of material

consumption. On the other hand, kesterite semiconductors such as Cu_2ZnSnS_4 (CZTS), $Cu_2ZnSnSe_4$ (CZTSe), and $Cu_2ZnSn(S,Se)_4$ (CZTSSe)[3] have been identified as a potential technology for thin films PV applications, mainly due to the earth abundance of copper (Cu), zinc (Zn), and tin (Sn) [8, 9, 10]. Additionally, CZTSSe presents optical and electronic properties similar to CIGS, which makes this technology even more appealing. Hence, kesterites are considered a potential alternative at medium to long term to CdTe and CIGS technologies. However, from the aforementioned kesterite alloys, only the pure sulfide, CZTS, may be truly labelled as composed only by abundant and non-toxic elements, then a real low-cost and sustainable PV technology. Thus, CIGS as a established technology that holds significant potential for further improvements and CZTS as a promising emergent technology will be the studied technologies in this thesis.

1.2 From Shockley-Queiser model to thin film solar cells based on Chalcogenides

The Shockley-Queisser (SQ) model establishes the upper efficiency limit of single-junction solar cells [11]. The SQ detailed balance formulation is based on the following assumptions: i) all photons with energy higher than the bandgap energy ($h\nu > E_g$) are absorbed, while there is no absorption of photons with energy $h\nu < E_g$; ii) each absorbed photon generates one single electron-hole pair and both charge carriers will reach their respective contacts; iii) radiative recombination is the only loss mechanism. This model assumes a step function for the absorptance $a(h\nu)$ of the absorber layer, i.e., $a(h\nu) = 1$ for $h\nu \geq E_g$ and $a(h\nu) = 0$ below this energy value. Under the SQ detailed balance formulation, the saturation current density (J_0) and short circuit current density (J_{SC}) become,

$$J_0^{SQ} = e \int_0^\infty a(h\nu)\phi_{bb}(h\nu, T)\mathrm{d}h\nu = e \int_{E_g}^\infty \phi_{bb}(h\nu, T)\mathrm{d}h\nu, \tag{1.1}$$

$$J_{SC}^{SQ} = e \int_0^\infty a(h\nu)\phi_{Sun}(h\nu)\mathrm{d}h\nu = e \int_{E_g}^\infty \phi_{Sun}(h\nu)\mathrm{d}h\nu, \tag{1.2}$$

where e is the elementary charge, $\phi_{bb}(h\nu, T)$ the black body spectrum at the temperature T (300 K) of the solar cell, and $\phi_{Sun}(h\nu)$ is the solar spectrum ($cm^{-2}s^{-1}eV^{-1}$) [12]. Then, the open circuit voltage (V_{OC})[4] may be obtained as follows:

$$V_{OC} = \frac{K_B T}{e}\, ln\left(\frac{J_{SC}^{SQ}}{J_0^{SQ}} + 1\right), \tag{1.3}$$

being K_B the Boltzmann constant. Due to the step function for the absorptance $a(h\nu)$, Eqs. 1.1-1.2 depend essentially on one input parameter related to the absorber layer (i.e., E_g). Thus, the SQ detailed balance formulation states the maximum efficiency for a given absorber bandgap energy.

[3] Throughout this thesis, kesterite technology may be also address as CZTSSe, when we want to mention the three alloys, CZTS, CZTSe, and CZTSSe.

[4] J_0, J_{SC}, and V_{OC} are figures of merit characteristic of solar cells, that will be addressed later in this thesis (Section 5.3.6).

Fig 1.6 a)-d) show the calculated dependencies of J_0^{SQ}, J_{SC}^{SQ}, V_{OC}^{SQ} and the respective light to power conversion efficiency (η^{SQ}[5]) on the bandgap energy of the absorber layer, considering the AM1.5 solar spectrum (data provided by the National Renewable Energy Laboratory, NREL [13]). The SQ model establishes an optimum bandgap energy range of ∼0.9-1.9 eV to obtain a minimum of efficiency of 30% from the device. The bandgap energy of the two studied materials CIGS (1.2 eV)[6] and CZTS (1.5 eV [14]) fits well in the aforementioned range of energies.

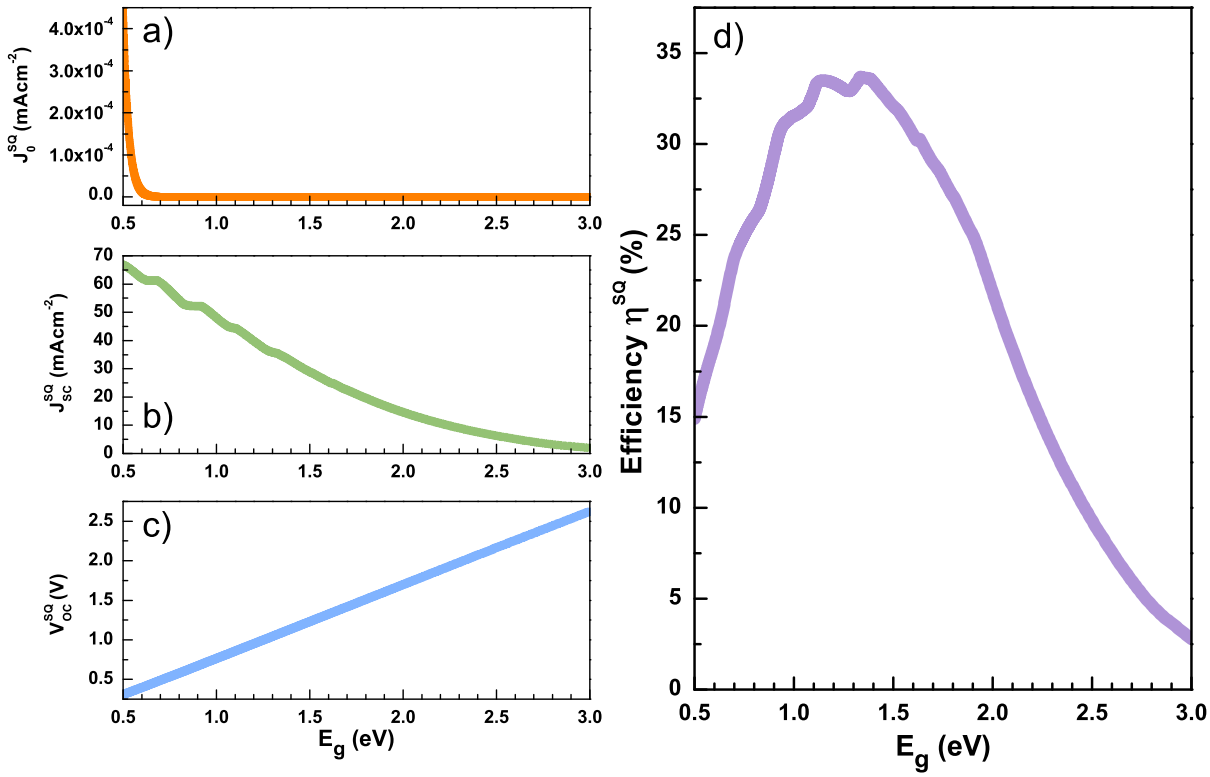

Figure 1.6: Calculated dependence on the bandgap energy of the a) J_0^{SQ}, b) J_{SC}^{SQ}, c) V_{OC}^{SQ}, and d) the respective η^{SQ} from the AM1.5 solar spectrum.

Table 1.1 shows the values for the electrical parameters J_{SC}, V_{OC}, and η reported in the literature for champions CIGS, CZTS[7], CZTSe, and CZTSSe solar cells. From the analysis of the electrical parameters values, it is clear a quite large gap between the champion efficiencies obtained by the CIGS based solar cell (22.9%) and any of the kesterites devices (10.04%, 11.6%, and 12.6% for CZTS, CZTSe, and CZTSSe, respectively). From the reported bandgap energy for each solar cell we also show the previously mentioned electrical parameters obtained from the SQ detailed balance. The performance of the analysed chalcogenides based solar cells falls below their estimated SQ limit, as expected. Nonetheless, the performance of the CIGS solar cell is substantially closer to the SQ limit, than that

[5] Obtained from Eq. 5.25.

[6] Obtained from Eq. 3.1 for a [Ga]/([Ga]+[In]) ∼ 0.3.

[7] A value of 11.01% for a CZTS solar cell with an area of 0.2339 cm^2 was also reported together with the value of 10.04% for a solar cell with an area of 1.113 cm^2, presented in Table 1.1 [8].

obtained by the three kesterite based solar cells. Calculated V_{OC} losses, defined as E_g/e-V_{OC}, are also presented for both experimentally reported and SQ calculated V_{OC}. This parameter is always lower than the bandgap of the material, even considering the SQ limit, as can be seen by the obtained V_{OC} losses for the V_{OC}^{SQ}, which is consequence of the radiative recombination considered by the SQ model. The V_{OC} losses are smaller in the CIGS device, than in the kesterite based solar cells. The systematic high values obtained for the V_{OC} losses is many times reported in the literature as the most relevant limiting factor for the improvement of the efficiency in CZTSSe technology [8, 9, 10]. Moreover, and in order to compare the performance of the solar cells with their respective SQ limit, we present the fraction of the SQ limit for the J_{SC} (J_{SC}/J_{SC}^{SQ}), and V_{OC} (V_{OC}/V_{OC}^{SQ}) achieved by the champions solar cells. Indeed the CIGS solar cell reached values of J_{SC} and V_{OC} equivalent to 89% and 84% of their SQ limit values, respectively. On the other hand, when we look to CZTS, CZTSe, and CZTSSe based solar cells, the values of J_{SC} and V_{OC} compared with their obtained SQ limit, falls down to values close to 80% for the J_{SC} and 60% for the V_{OC}. Regardless of the technology, the four discussed champions cells presented higher losses regarding the V_{OC} in comparison to J_{SC}, considering their SQ limit. A solar cells that show a J_{SC} lower than the SQ limit suffer from incomplete light absorption (light management) or incomplete collection of generated charge carriers (carriers management), whereas a reduced V_{OC} reflects unwanted charge carriers recombination (carriers management) [4]. The results presented in Table 1.1 reflect the trend obtained in the literature for a better performance of the J_{SC} in comparison to the V_{OC}, which may shows that light management may be more optimized than charge carriers management in both studied technologies.

Table 1.1: The electrical parameters J_{SC}, V_{OC}, and η values calculated from SQ model according to the bandgap energy of the considered state-of-art solar cells based on CIGS, CZTS, CZTSe, and CZTSSe, for which the J_{SC}, V_{OC}, and η are also presented. Calculated $E_g/e - V_{OC}$ for the SQ and champions solar cells, and the fractions of the SQ limit for J_{SC}/J_{SC}^{SQ}, and V_{OC}/V_{OC}^{SQ}.

	E_g (eV)	J_{SC} (mA.cm^{-2})	V_{OC} (mV)	η (%)	$E_g/e - V_{OC}$ (mV)	J_{SC}/J_{SC}^{SQ} (%)	V_{OC}/V_{OC}^{SQ} (%)	Ref.
SQ	1.0	48.2	765	32	235	-	-	-
CZTSe	1.0	40.6	423	11.6	577	84	55	[9]
SQ	1.13	43.4	886	33	244	-	-	-
CIGS	1.13	38.5	746	22.9	384	89	84	[15]
CZTSSe	1.13	35.2	513.4	12.6	617	81	58	[10]
SQ	1.5	28.9	1023	31	477	-	-	-
CZTS	1.5	21.77	708.3	10.04	792	75	69	[8]

1.3 Scope of this work and thesis organization

The main goal of the studies carried out in this thesis was to contribute positively to the discussion on the role of the defects, in the optoelectronic properties of the CIGS and CZTS semiconductors used as absorber layers in thin film based solar cells. Both materials are quaternary alloys with close crystalline structure and they present similar electronic properties. Additionally, CIGS and CZTS are highly doped and strongly compensated semiconductors, which makes the interaction between defects (namely, charged ones) critical, since may lead to a highly complex electronic energy levels structure, that is not yet fully understood. This complex structure will necessarily influence the charge carriers transport that at a great extent will dictates the performance of the solar cells. Although being many times pointed as analogous technologies, there are several fundamental and technological issues that lag the performance of the CZTS based solar cells far from the CIGS ones which anticipates significant differences in the recombination mechanisms between the two materials.

Photoluminescence is one of the most suited techniques to study the electronic energy levels structure of a semiconductor. Thus, in this thesis we explore its potential, complemented with other optical, morphological, structural, and electrical analyses, to study the influence of defects on the optoelectronic properties of the chalcogenide thin film based solar cells. The combination of these results alongside with a detailed theoretical description provides an overview of the role played by defects on the limiting factors in both technologies.

This thesis allows for a further understanding of thin film solar cells by addressing the basic steps in the implementation of the architecture and the main issues that limit the performance of the final device in the CIGS and CZTS technologies. However, it is the present stage of development of the two technologies that have dictated the path and uniqueness of the carried out studies for each one of the absorber materials. Indeed, each technology has its own issues, which led to studies carried necessarily in different directions. Moreover, the results presented in this thesis are part of more comprehensive studies, achieved through different collaborations. In fact, most of the studies do not share a detailed topic, but are part of a bigger plan that aim to contribute for a further knowledge of CIGS and CZTS fundamental properties, and more importantly for a comprehensive overview of the chalcogenide technology.

From a technological point of view, “CIGS know-how” have been directly implemented in the CZTS technology, so in the theoretical fundamentals we will address primarily the CIGS based solar cells and then the CZTS ones. On the other hand, for the experimental results we present first the CZTS studies then the CIGS ones, since for the former, more fundamental studies were carried out that served as background to the studies performed for CIGS based solar cells. Hereupon, the present thesis is organized in 8 Chapters. The following three present the theoretical fundamentals that will be used as background for a discussion that is intended to be rigorous enough of the obtained results. In Chapter 5 the experimental details for the solar cells fabrication and for the fundamental characterization are presented. The experimental results and discussion of the carried studies in CZTS

and CIGS based solar cells are presented in Chapters 6 and 7, respectively. At last, an overview of the main conclusions, as well as of future work, are presented in Chapter 8. As follows, a global view of each Chapter is presented:

2: Solar cell basic principles of operation and loss mechanisms are discussed from the point of view of the CIGS and CZTS technologies.

3: The conventional architecture of a chalcogenides thin film based solar cell is presented and briefly discussed. CIGS and CZTS fundamental physical properties are presented in the framework of the studies carried out in this thesis.

4: A review of several models of fluctuating potentials based on different sources of disorder is presented. Experimental evidences for different types of fluctuating potentials and estimation of tails states amplitude from absorption coefficient and photoluminescence measurements are discussed in chalcogenides solar cells.

5: The solar cells fabrication process is generically presented for CZTS and CIGS. The characterization techniques used are briefly discussed according to the requirements of the carried out studies.

6: A fundamental characterization of the defects present in the CZTS thin films and their influence on the electronic energy levels structure is presented throughout different studies.

7: An experimental and theoretical investigation of the influence of the fluctuating potentials on the CIGS based solar cell is presented throughout studies that address current topics in the technology.

8: An overview of the studies carried out in this thesis and final conclusions, followed with new ideas for further work.

Chapter 2

Physics of solar cells based on pn-heterojuction

A classic overview of solar cell basic principles of operation and loss mechanisms is presented. Furthermore, some physical properties of the studied chalcogenides are discussed in order to understand particular loss mechanisms assigned to these materials, that may be limitative to the studied solar cells performance.

A solar cell is an optoelectronic device that transforms light into electrical energy. The studied solar cells in this thesis are based on pn-heterojunctions. When photons reach the solar cell with sufficient energy, they are absorbed by the p-type semiconductor, and an electron-hole pair is generated in this layer. If the absorption occurs in the space charge region of the pn-heterojunction, the charge carriers are separated by the electric field and either recombine or are collected at their respective electrical contact, generating an electric photocurrent. The physics of a heterojunction solar cell is generically explained in classic semiconductor textbooks [16, 17] and, in more detail, in solar cells specialized ones [12, 18, 19, 20]. Thus, the next sections give a simple description of solar cell basic principles of operation following the context of this work: thin film solar cells based on chalcogenides.

2.1 Solar spectrum

Conventionally, solar cells are characterized and certified at 25°C using the AM1.5 spectrum with an intensity of $100\,\mathrm{mW\,cm^{-2}}$. This set of conditions is referred to as the standard test conditions (STC). The AM1.5 is a typical solar spectrum measured on the surface of earth, with an input power of $100.037\,\mathrm{mW\,cm^{-2}}$ [13, 21].

To convert sunlight into electrical energy, photons generate electron-hole pairs. Hence, the knowledge of the incoming photon flux is the onset to discuss and evaluate solar cell performance. Spectral

photon flux is shown in Fig. 2.1. A total of 4.3×10^{17} photons s^{-1} cm^{-2} may be obtained from the integration of the spectral photon flux over the energy, from ~0.3 to 4.4 eV, which means that up to 4.3×10^{17} electron-hole pairs per second for every cm^2 could be generated, when the solar cell is illuminated with the AM1.5 spectrum.

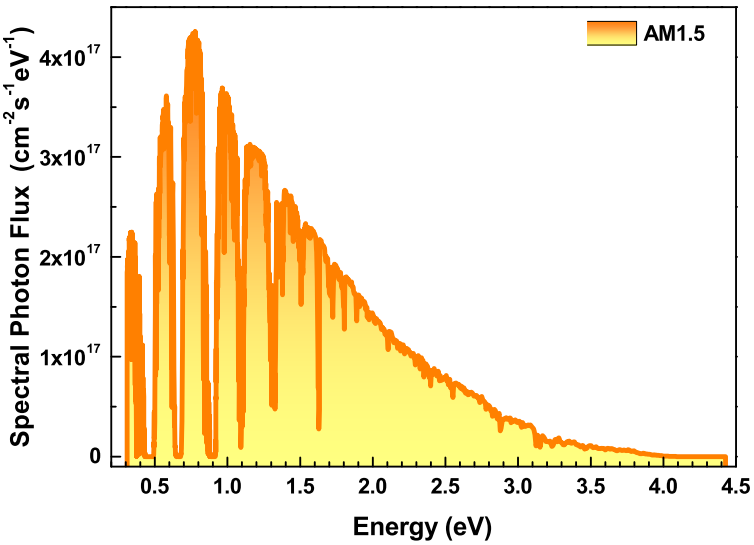

Figure 2.1: Spectral photon flux of the AM1.5 solar spectrum. Data from [13].

2.2 Generation: interaction of photons and semiconductor

From a macroscopic point of view, light interaction with a particular material layer may be classified by the follow optical phenomena [22]:

i) reflection at the interface between the two media with different refractive index values (n);

ii) absorption, if the energy of the photon is higher or equal than the bandgap energy of the semiconductor ($h\nu \geq E_g$);

iii) transmission, if the energy of the photon is lower than the bandgap energy of the semiconductor ($h\nu < E_g$).

The fraction of the incident photons with an energy $h\nu$ that are reflected, absorbed, or transmitted on/in a material with a finite thickness W can be quantified by their optical properties: reflectance (r), absorptance (a), and transmittance (t). These parameters are related to each other by [22]:

$$r(h\nu) + a(h\nu) + t(h\nu) = 1. \tag{2.1}$$

The overall sunlight/solar cell layers interaction, illustrated in Fig. 2.2, determines to a great extent the device performance. In general, the sunlight photons in the relevant spectral range, which means energies higher or equal to the bandgap energy of the absorber layer, should be transmitted through

the top of the solar cell until they hit the absorber layer (front layers, $t(h\nu) = 1$). At this point the absorption should be as efficient as possible (absorber layer, $a(h\nu) = 1$). Then, if any photon that fulfill ii) reaches the back contact (previous condition is not satisfied, absorber layer with $a(h\nu) < 1$), the photons should be reflected (back contact, $r(h\nu) = 1$) so that those photons are reflected back to the absorber layer. Thus, the different layers of the solar cell should be optimized in order to accomplish their requirements for an efficient solar cell. This topic is matter of discussion in Chapter 3.

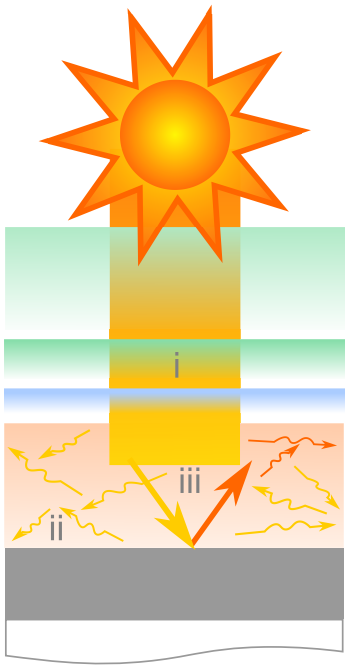

Figure 2.2: Illustration of the interaction among sunlight and an ideal solar cell. The optical phenomena i) transmission, ii) absorption, and iii) reflection are schematically illustrated.

2.2.1 Absorption coefficient

A fundamental issue to convert the sunlight into electrical energy requires an efficient absorption of photons in the absorber layer. For the purpose of evaluate the performance of the studied materials as absorber layers, let us consider the absorptance $a(h\nu)$ obtained for a planar absorber layer with zero front reflectance and total reflection on the back contact given by [23, 24, 25]:

$$a(h\nu) = 1 - \exp[-2\alpha(h\nu)W], \tag{2.2}$$

where $\alpha(h\nu)$ is the absorption coefficient. To obtain the desirable $a(h\nu) \sim 1$ in the absorber layer, $\alpha(h\nu)W$ must be as high as possible. However, it is easy to understand that this requirement may be in conflict with the aim of a thin absorber layer, unless the material has a high absorption coefficient. In fact, the success of thin film technology is strongly dependent on a high absorption coefficient of the absorber layer.

Fig. 2.3 a) shows the optical absorption spectrum for CIGS with varied [Ga]/([Ga]+[In])(GGI)= 0.00, 0.31, 0.45, 0.66, and 1, CZTS, and CZTSe. The CIGS $\alpha(h\nu)$ values were calculated according to

$$\alpha(\lambda) = \frac{4\pi k}{\lambda}, \tag{2.3}$$

being λ the wavelength and k the extinction coefficient, which corresponds to the imaginary part of the complex refractive index ($n(\lambda) = n + ik$). The data of Paulson *et al.* [26] for the extinction coefficient was used. CZTS and CZTSe optical absorption spectra are experimentally obtained and presented in [27] and [28], respectively. All the presented absorption coefficients have values up to $\sim 10^4\,\mathrm{cm}^{-1}$ and in the case of CIGS, they even reach values up to $\sim 10^5\,\mathrm{cm}^{-1}$, in the relevant range of the solar spectrum.

In the context of the carried experimental studies (Chapters 6 and 7) the following discussion will be focused on CIGS with GGI = 0.31 and on pure sulfide CZTS. In order to establish the relevant spectral range for these two materials, bandgap energies of 1.17 ± 0.01 and $1.49 \pm 0.05\,\mathrm{eV}$ were obtained for CIGS and CZTS, respectively, from the fit to the absorption coefficient $\alpha(h\nu)$ data with the semi-empirical expression that describes $\alpha(h\nu)$ for $h\nu > E_g$ [20],

$$\alpha(h\nu) = \alpha_0 \sqrt{\frac{h\nu - E_g}{K_B T}} + \alpha_1 \exp\left(\frac{h\nu - E_1}{B_1}\right), \tag{2.4}$$

being α_1, E_1, and B_1 fitting parameters. The first term is the fundamental equation for a direct bandgap semiconductor and describes the absorption coefficient for energies close to E_g, whereas the second term describe the high energy region [20]. The AM1.5 spectral region that is absorbed in the solar cell is the one with photon energy above 1.17 eV for CIGS and 1.49 eV for CZTS. Due to the lower CIGS bandgap energy, the absorbed photon flux is higher for this material than for CZTS, 2.7 and $1.8 \times 10^{17}\,\mathrm{photons\,s^{-1}\,cm^{-2}}$, respectively. The absorption coefficients just above the bandgap energy were found to be $\sim 10^4\,\mathrm{cm}^{-1}$, whereas for CIGS exceeds $10^5\,\mathrm{cm}^{-1}$ at energy values above 2.0 eV. An absorption coefficient α_0 of 1.24×10^4 and $5.41 \times 10^3\,\mathrm{cm}^{-1}$ were obtained for CIGS and CZTS, respectively. The obtained α_0 value for CZTS is significantly lower than the values over $10^4\,\mathrm{cm}^{-1}$ reported in the literature [29].

According to the optical phenomena aforementioned, no absorption will be expected at energies lower than the bandgap energy of the material. However, both CIGS and CZTS are self doped materials, with high density of defects, which means that photons with $h\nu < E_g$, may also be absorbed. Hence, the observed extension of the absorption spectrum to lower energies than the bandgap energy of these materials in Fig. 2.3 a). The physical meaning of this sub-bandgap absorption will be theoretically and experimentally addressed later in this thesis.

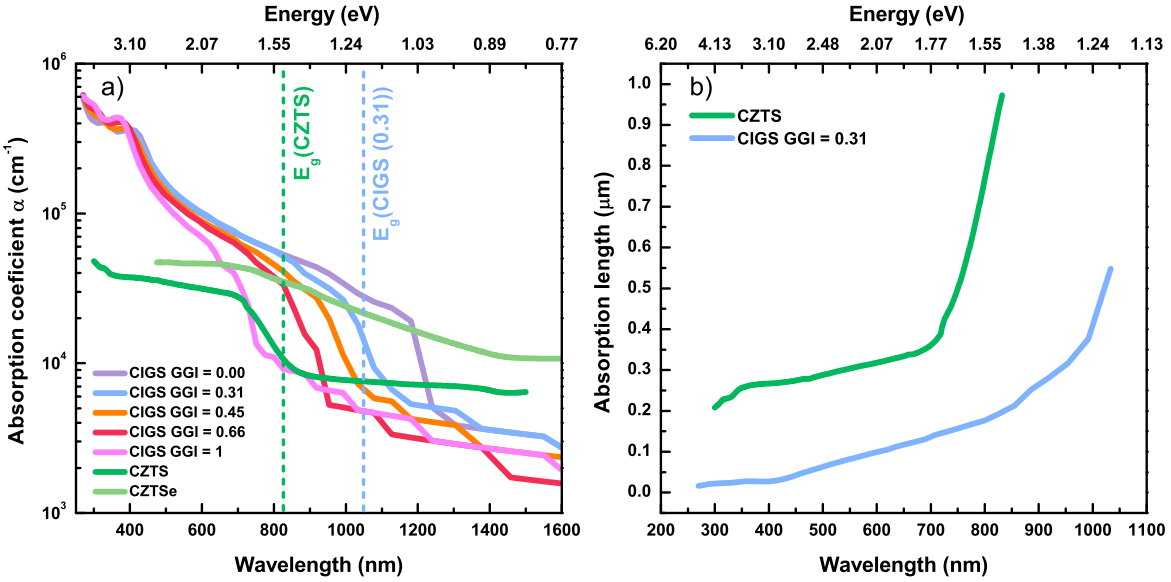

Figure 2.3: a) Calculated absorption coefficient with Eq. 2.3 for CIGS with varied GGI ratio using the extinction coefficient data from [26]. CZTS and CZTSe absorption coefficient spectra reproduced from [27] and [28], respectively. The bandgap energy obtained from Eq. 2.4 for CIGS with GGI= 0.31 and CZTS is pointed out in order to illustrate the relevant spectral range for these two materials. b) Calculated absorption length ($1/\alpha$) for CIGS, with a GGI= 0.31, and CZTS.

Now that we looked over the absorption coefficient, the required absorber thickness to absorb the incoming sunlight can be stated. This thickness is largely determined by the absorption length of the material defined as $1/\alpha$, which is the distance from the surface where light intensity drops by a factor of $1/e \simeq 1/3$ [22]. Fig 2.3 b) shows the absorption length for CIGS (GGI= 0.31) and CZTS. Since both materials have high absorption coefficients, they are able to absorb nearly all the incident sunlight photons with energy down to their bandgap in hundreds of nanometers, ∼600 nm are needed in CIGS and ∼1000 nm in CZTS. The optical properties discussed until this point, make both chalcogenides suitable materials for application as absorbed layers in thin film solar cells and likely options to explore for ultrathin solar cells.

2.3 Charge carriers separation

Fig. 2.4 a) presents a p- and n-type semiconductor with no contact between each other. The two semiconductors have different bandgap energies and doping densities, being the doping level higher in the n-type semiconductor than the p-type one. The Fermi level has a different position in the two semiconductors. When the two different semiconductors are brought into contact by an interface, also called metallurgic junction, a pn-heterojunction is formed as shown in Fig. 2.4 b), then, a sequence of processes takes place. Electrons and holes diffuse from regions of high concentration to low concentration regions. Diffusion leaves fixed ionised donors in the n-region and fixed ionised

acceptors in the p-region. The fixed charges induce an built-in electric field, $\vec{E}$, that opposes the diffusion of the charge carriers. As a result, a physical region on both sides of the interface becomes almost totally depleted of free charge carriers and it is known as a depletion region or space charge region (SCR). In the common representation, at thermal equilibrium, the Fermi level is the same in the entire junction, which leads to the representation of bending of the energy bands throughout the pn-heterojunction. Due to the band bending, electrons in the conduction band of the n-region will see a potential barrier when they move into the p-region, the built-in potential barrier, V_{bi} [16]. As shown in 2.4 b), beyond the SCR in the absorber layer lies a quasi-neutral region (QNR) where carriers behave as if there is no junction. The strong built-in electric field in the part of the SCR inside the p-type material will superimpose on the random movement of carriers accelerating holes in the same direction of the field to the QNR and electron to the pn interface.

In practice, when the solar cell is illuminated with the AM1.5 spectrum, the system is no longer in thermal equilibrium and the Fermi level splits in both sides of the heterojunction, which means that the free charge carriers are described by quasi-Fermi levels, rather than by a single equilibrium Fermi level.

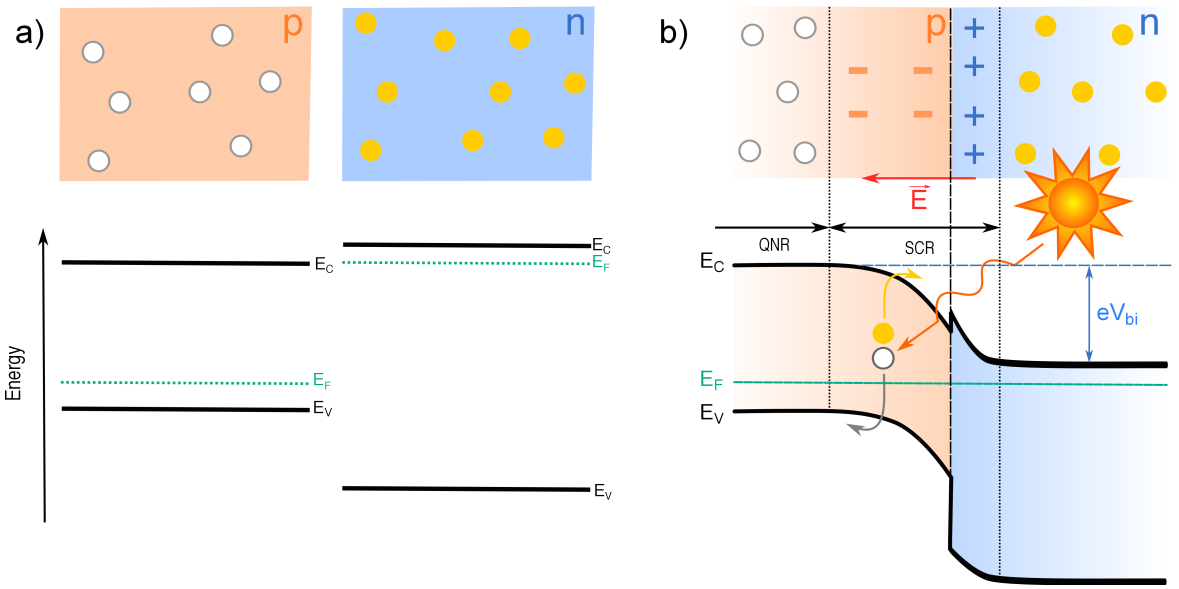

Figure 2.4: Conceptual illustration of a random distribution of holes and electrons in an p- and n-type semiconductor, respectively: a) before and b) after forming a pn-heterojunction. Additionally, band diagram at thermal equilibrium for a) p and n-type semiconductors and b) for pn-heterojunction, are shown. The p and n symbols refer to the doping type of the material. All band diagrams have their Fermi level (E_F) represented. In b) it is represented the generation of an electron-hole pair, the quasi-neutral region (QNR), the space charge region (SCR), the built-in electrical field ($\vec{E}$), and the built-in potential barrier V_{bi}.

2.3.1 Space charge region

Ideally, the SCR of a solar cell should be almost as wide as the absorber layer itself so that the generated charge carriers will promptly move to the respective contact. For this purpose, and knowing that the width of the SCR in each region is inversely proportional to the square root of the doping density in the region, the buffer layer is projected to be more highly doped than the absorber layer. Thus, the doping changes abruptly from the p to the n-region (p-n$^+$), which allows to determine the width that the SCR extends into the p-region for the case of zero applied voltage as follows [17],

$$W_D = \sqrt{\frac{2\epsilon_0\epsilon_r V_{bi}}{eN_a}} \tag{2.5}$$

where N_a represents the concentration of acceptors, ϵ_0 and ϵ_r are the absolute vacuum electric permittivity and relative dielectric constant of the p-type material, respectively. CIGS relative dielectric constant varies from 13.6 to 11 for a GGI ratio from 0 to 1, respectively [30]. On the other hand, CZTSSe has a lower dielectric constant, which varies from 8.6 to 6.7 from pure selenide to pure sulfide, respectively [14]. Thus, the SCR in the kesterite are smaller than in CIGS for the same doping levels.

Considering the pn-heterojunction chalcogenide/CdS, the SCR is located largely within the chalcogenide layer, due to the lower net doping in this layer compared to CdS. Commonly, solar cells based on chalcogenides, both chalcopyrites and kesterites, have reported W_D values $\geq 0.3\,\mu$m. However, as shown in Table 2.1, state-of-art solar cells do not have necessarily large SCR width. Take for instance, two solar cells based on CZTSSe with efficiencies of 12.3 and 12.6% and W_D of 0.187 and 0.15 μm, respectively. The obtained values for these W_D are far from the value of 0.39 μm also reported for a W_D in a CZTSSe solar cell. Following these evidences, high efficient solar cells do not have necessarily the larger W_D. Consequently, these solar cells have a higher free holes density (p)[1], in comparison with less efficient solar cells. Similar results were stated by NREL for solar cells based on CIGS. It was shown that the most efficient solar cells were not the ones presenting larger W_D and lower free holes density in the whole set of studied samples [31]. This apparent contradictory fact may be explained in some cases by a higher minority carrier diffusion length value that compensate the low value of SCR width, but also due to the non-radiative recombination that occurs in this region.

[1] Also called in the literature as net doping or just doping.

Table 2.1: Absorber layer thickness W, space charge region W_D, free holes density p, minority carrier lifetime τ, minority carrier diffusion length L_D, and solar cell efficiency η values for solar cells based on CIGS and CZTSSe. This list of parameters is not exhaustive and just highlights the differences between solar cells based on chalcopyrite and kesterites.

	Technique	W (μm)	W_D (μm)	p (cm^{-3})	τ (ns)	L_D (μm)	η (%)	Ref.
CIGS	Co-evaporation	2.5	0.39	1.9×10^{16}	255	11.7	15.2	[32]
	Co-evaporation + TD	2.5	0.25	0.7×10^{16}	388	9.8	18.7	[32]
	Co-evaporation	2	-	-	-	4.5	17.4	[33]
	Co-evaporation	2.3	-	-	250	-	-	[34]
CZTS	Thermal-evaporation	0.6	0.180	-	-	0.35	8.4	[35]
	Co-sputtering	1.25	0.316	1×10^{16}	-	-	-	[36]
	Sol-Gel + PDT	-	-	-	10-28	-	5.94-7.62	[37]
CZTSe	Thermal Co-evaporation	1.5	0.3	1×10^{16}	2	0.5	9.42	[38]
	Co-evaporation	2.2	0.23	1×10^{16}	2.0-2.5	2.1	11.6	[9]
	Hydrazine-based	2	-	-	15-1.5	1.2-1.0	6.9-10.2	[39]
	Hydrazine-based	2	-	-	-	1.2	6.9	[39]
	Hydrazine-based	2	0.15	$<7\times10^{15}$	-	0.75	12.6	[10]
	Hydrazine-based	2	-	-	6.7	-	11.1	[40]
CZTSSe	Co-sputtering	1.25	0.390	6×10^{15}	-	-	-	[36]
	Sputtering	2.2	0.238	5×10^{15}	1.47	-	10.2	[41]
	Sputtering	1.8	0.187	-	-	-	12.3	[42]
	Sputtering	1.8	0.222	-	-	-	10.6	[42]
	Sputtering	1.8	0.149	-	-	-	8.3	[42]

2.4 Collection of photogenerated carriers

The collection function is the probability for a generated charge carrier to be collected at their contact, being the collection width L_C roughly approximated to $L_C = W_D + L_D$, where L_D is the minority carrier diffusion length [20]. The minority carrier diffusion length is defined as the $1/e$ distance that generated carriers diffuse before recombination and depends on minority carriers lifetime τ as follows,

$$L_D = \sqrt{D\tau} \tag{2.6}$$

where D stands for diffusion coefficient. The longer is the carriers lifetime the higher will be the diffusion length, which will increases their chance of collection at their respective contact.

The probability of collection, depends on the location inside of the absorber layer of the electron-

hole pair generation [20]:

i) **SCR:** ideally, the collection function in the SCR will be close to unity. However, for highly doped materials this is not a valid assumption and recombination in the SCR cannot be neglected.

ii) **QNR:** charge carriers generated within the QNR either diffuse randomly to the edge of the SCR or recombine. The collection function diminish for carriers generated in the QNR and depends strongly on carriers diffusion length, more strongly on the minority charge carriers.

An efficient transport of minority charge carriers is more important for a solar cell, due to their lower density, as compared to majority carriers. In fact, it is their collection that determines the performance of the device. Table 2.1 shows chalcogenides minority carrier lifetime and diffusion length values reported in the literature. It is clear that CIGS[2] has a higher diffusion length than kesterites, which is also systematically longer than the thickness of the conventional CIGS layer. Regarding the minority charge carriers lifetime in CIGS the values are usually two orders of magnitude higher than the ones obtained in CZTSSe. Moreover, Hages *et al.* estimated for CZTSe and CZTSSe minority carrier lifetimes (300 K) in the order of hundreds of picoseconds, rather than the few nanoseconds reported by other authors after photoluminescence time resolved measurements. The authors conclude that the obtained sub-nanosecond minority carrier lifetime is the main limitation in the performance of the devices based on kesterites [43].

The collection width in solar cells based on chalcopyrites is commonly larger than the thickness of the CIGS layer. On the other hand, the expected scenario in kesterite technology is different. Let us take for instance two CZTSe solar cells presented in Table 2.1 with 11.6% and 9.42% power conversion efficiency. If in the first case the $L_C = 2.33\,\mu$m is larger than the thickness of the absorber layer ($W = 2.2\,\mu$m), in the second case a collection width of $0.8\,\mu$m was obtained, meaning that the active layer is just 53% of the total thickness of the CZTSe ($1.5\,\mu$m). Moreover, for CZTSSe state-of-art solar cell with an efficiency of 12.6% the obtained active layer was only 45%. These results, show that there is a large room to improve the quality of CZTSSe, which is far behind the one achieved in CIGS.

2.5 Loss mechanisms in solar cell

A real solar cell is significantly less efficient than the ideal limits stated in Chapter 1. Hence, we will briefly address the main loss mechanisms that degrade the performance of chalcogenides devices.

2.5.1 Optical losses

Processes that limit the absorption of light by the absorber layer are defined as optical losses. The main sources that contribute to the optical losses are:

[2]Some of the minority carrier lifetime and diffusion length values presented in Table 2.1 were obtained by simulations.

i) shading effect of the grids, which reduce the active solar cell area.

ii) reflection at the optical window/air interface especially due to different refractive indexes. Reflection losses can be reduced through a better matched refractive index between the mediums. A magnesium fluoride (MgF_2) anti-reflection coating (ARC) is often used, however it is not fully effective. An ARC further improves the device efficiency by about 1-2% [20].

iii) parasitic absorption, mainly at high energies due to the light absorption in the buffer/optical window front layers. CdS and ZnO have bandgap energies of 2.4 and 3.3 eV, respectively, which means that they can absorb photons with energy down to these values. These losses may be limited by a minimum thickness in both layers and by a buffer layer with higher bandgap energy [20].

iv) transmission of all photons with an energy lower than the bandgap energy of the absorber layer, which do not have enough energy to generate an electron-hole pair.

v) lack of absorption due to the optical path being lower than the effective absorption length, allowing the photons to be transmitted by the absorber layer. A solution goes through improving the internal reflection at the back contact/absorber interface [44].

2.5.2 Optoelectronic losses

Ideally, we will expect that all the generated charge carriers may be collected by their respective contacts, before their loss by recombination. Alongside with the continuous generation of charge carriers, recombination processes takes place, reducing the generated charge carrier collection. In thin film solar cells, different recombination mechanism exist. Some of the most important ones are schematically shown in Fig. 2.5, and can be classified considering the particles, which results from the recombination process:

i) radiative recombination, the energy is dissipated by the emission of photons;

ii) non radiative defect mediated recombination, the energy is dissipated by the emission of phonons;

iii) non radiative Auger recombination, the energy is dissipated by the excitation of a third charge carrier, which thermalizes to the edge of the band.

Radiative recombination

Radiative recombination of an electron-hole pair under creation of a photon is the main reason for a theoretical efficiency limit of a pn-heterojunction, described in the SQ model, discussed in Chapter 1. Radiative band-to-band recombination in a direct semiconductor, is unavoidable, but is not detrimental as non radiative recombination and it is not considered as a loss [11].

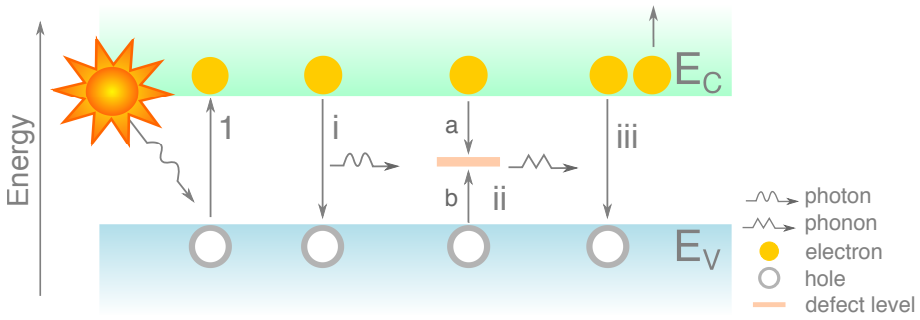

Figure 2.5: Illustration of 1) electron-hole pair generation and i) radiative, ii) Shockley-Read-Hall, and iii) Auger recombination mechanisms. In ii), a) capture of an electron by a neutral defect b) capture of a hole at a negatively charged defect. E_C stands for conduction band edge, and E_V for valence band edge. The Auger recombination is shown as two electron process, but may also take place as two hole process.

Non-radiative recombination involving defects

As discussed in Chapter 1, the V_{OC} of any solar cell is considerably lower than it is stated by the radiative limit, meaning that non radiative recombination should be dominant in real devices. As Auger recombination is negligible in chalcogenides [20], only recombination mediated by defects will be discussed in the following.

Non-radiative recombination involving defects is a limitative mechanism for solar cell efficiency, since it contributes for a reducing in the minority carrier lifetime, then in the collection of the generated carriers. In the literature, the non-radiative recombination process involving defects is assumed to occur through a localized state in the bandgap described by the classic Shockley-Read-Hall (SRH) statistics [45, 46]. As shown in Fig. 2.5 this process requires a capture of an electron by a neutral defect a), followed by the capture of a hole at the negatively charged defect b). So, the overall recombination rate scales with the slower of the two processes, and increases roughly exponentially with the increase of the transition energy [47]. Hence, the most efficient recombination states are localized in the middle of the bandgap (traps), which enhances the capture of both carriers. Moreover, to the dependence on the energy of the recombination state, the magnitude of the capture cross sections, the distribution of both charge carries and localized states also contribute for establishing the recombination mechanism, which may be beyond the classical SRH. In highly doped and compensated semiconductors recombination through an impurity band rather than localized states and/or recombination involving tail states, should be also taken into account [48]. Furthermore, tunneling-enhanced recombination in the interface and SCR or multi-step processes involving shallow localized states are also recombination mechanisms expected to occur in highly doped materials, like those studied in this thesis [21, 47, 49].

An accurate distinction and identification of the localization of the main recombination mechanism would be a major help in order to improve absorber layer quality and or device architecture. The recombination location in absorber layer is governed by [50]:

i) **at the front interface:** the recombination mechanism will depend on, the conduction band offset, the nature and density of the defects, and the Fermi level pinning. This region is highly recombinative as its nature is based on a heterointerface.

ii) **in the SCR:** it is expect that the main SRH recombination mechanism to be located in this region of the absorber, because there is a narrow region somewhere in the SCR where a crossover in the electron and hole population occurs [15]. In this region, recombination is enhanced by tunneling of free carriers into the recombination centers.

iii) **in the QNR:** the recombination is dominant when the generation of charge carriers in this region occurs at a distance from the SCR higher than its diffusion lengths. Thus, recombination occurs before collection.

iv) **at the back interface:** recombination at the back interface may become dominant, when there is generation near or diffusion to the back contact, that is, when i) the absorber thickness is comparable to or smaller than the absorption length; or ii) when the minority charge carriers diffusion length is larger than the thickness of the absorber layer, respectively. Therefore, considering the conventional thickness of the chalcogenide layer ($2\,\mu m$) as well as diffusion length expected for kesterites and chalcopyrites (Table 2.1), back recombination should not be dominant in solar cells based on CZTSSe, but has to be considered for CIGS ones [20]. Some strategies have been applied in CIGS technology to avoid recombination in this region, throughout a Ga-profile (higher GGI at the back contact than at the front contact) and more recently, passivation of this interface [44, 51].

In real devices based in a pn-heterostructure, all recombination mechanisms presented are active at the same time. However, one recombination mechanism at a particular region of the solar cell will be dominant over the others [20]. In a first stage, the current density-voltage and the dependence of the V_{OC} on the temperature are helpful tools to obtain some insight into SRH recombination, from which it is possible to extract the diode ideality factor (A) and the activation energy for the main recombination mechanism, E_A [21, 51, 52, 53]. However, these analyses are not straightforward. In the limit of the SRH recombination, A is weakly dependent on temperature and it is limited by $1 \leq A \leq 2$. For $A = 1$, if the dominant recombination mechanism occurs in the QNR and $A = 2$ if the dominant recombination is in the SCR. Then, if $E_A < E_g$, interface recombination is dominant, while recombination in the SCR dominates if $E_A = E_g$. However, some literature reveal chalcogenide devices exhibiting ideality factor with significant temperature dependence and values of $A > 2$. Thus, these parameters cannot be explained by the classic SRH statistic [21, 54, 55]. However, several studies in chalcogenides solar cells follow this discussion. Bulk non-radiative recombination mechanism (SCR or QNR) dominates state-of-art solar cells based on CIGS [32, 51, 56, 57]. On the other hand, in kesterite solar cells the dominant recombination mechanism appears to be related with [S]/[Se] ratio. CZTS and CZTSSe/CdS devices are limited by interface recombination [56, 58-61]. While for pure

selenide, CZTSe, bulk recombination is often observed [53, 56, 62, 63].

Thermalization losses

When photons with higher energies than the bandgap energy of the absorber layer are absorbed, charge carriers will generated charge carriers into higher energy states in the respective band. The generated carriers tend to reach a thermal equilibrium with the lattice and, consequently, relax to the edge of the bands. The excess of kinetic energy is lost by the creation of phonons that heat up the device.

Thermalization and transmission present an optimization trade-off problem. Thus, while the bandgap should be as high as possible, to reduce thermalization, a low bandgap would be desirable to collect as many photons as possible without loosing them by transmission [20, 64]. As these losses are intrinsic to device operation, they are usually not considered as losses that can be solved.

2.6 In Summary

The solar cell basic principles of operation may be described in three steps processes: i) absorption of light and generation of electron-hole pairs; ii) splitting of the electron-hole pair; and iii) collection of the electron and hole in the corresponding electrical contacts. The overview presented in this Chapter allowed us to discuss the light absorption in the studied chalcogenides and the processes that limit the charge carriers generation and recombination mechanisms, most importantly minority carrier diffusion length and consequently lifetime. At this point, we can state that the main difference between chalcopyrites and kesterites stands mainly on the minority carrier lifetime, which may be two orders of magnitude lower for CZTSSe in comparison to CIGS. Kesterite compounds have also a smaller dielectric constant, intrinsically leading to a smaller SCR than in CIGS. These parameters will negatively affect the collection length in CZTSSe devices. Thus, CZTSSe carriers generated away from the SCR region will have a high probability of recombining before reaching their contacts. This is a strong indication for a higher recombination rate in solar cells based on kesterites compatible with the significant lowers V_{OC} values obtained in this technology compared with the ones obtained in solar cells based in CIGS.

The next Chapter will address how solar cells based on chalcogenides are designed to achieve the best performance considering the several issues discussed in the present Chapter, which are limiting the efficiency of both chalcopyrites an kesterites based solar cells.

Chapter 3

Thin film solar cells based on Chalcogenides

The conventional architecture of the chalcogenides thin film based solar cells is presented and critically discussed. Then, an overview on the fundamental physical properties for CIGS and CZTS are addressed being the focus in the properties that may be important in the discussion of the obtained results.

The conventional CIGS/CZTSSe solar cell architecture is based on a pn-heterojunction and it is typically made up of a substrate and five layers, as illustrated in Fig. 3.1 a). On top of the soda-lime-glass substrate (SLG), it consists of the following layers: a metallic molybdenum (Mo) back contact layer, a p-type CIGS or CZTSSe absorber layer, a n-type CdS buffer layer, an intrinsic ZnO (i-ZnO) layer, and an optical window consisting a transparent conductive oxide, usually a doped ZnO:Al (or SnO_x:In) layer. Laboratory cells also have a metallic grid on top to ease carrier extraction made by Ni/Al/Ni [65].

The most experimental suitable equilibrium band alignment for thin film solar cells based on chalcogenides is schematically shown in Fig. 3.1 b) and depicts a spike in the conduction band at the absorber/CdS heterojunction. The electrons coming from the absorber must pass this spike, while entering the buffer layer and must pass a conduction band cliff while entering the window layer [65]. Although, intuitively this spike-like conduction band offset could be considered non beneficial, since it could act as a potential barrier for electrons, in practice a positive conduction band offset up to 0.4 eV hinders interface recombination, which improves directly the V_{OC} and the performance of the device [66-69].

In the following Sections all the common layers from CIGS and CZTS based solar cells are first presented and discussed in parallel in order to enable a better identification of the strengths, as well as the barriers that both technologies must be able to overcome. Then, the physical properties that

are matter of interest for the discussion of the obtained results in this thesis will be addressed for both, CIGS and CZTS.

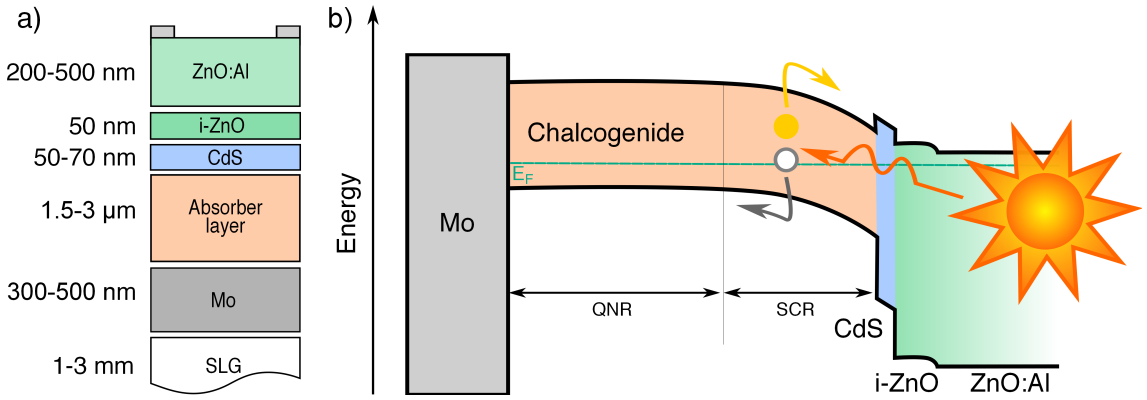

Figure 3.1: a) Schematic view of the layers in conventional chalcogenide solar cell and b) spike-like band diagram of a typical complete chalcogenide solar cell at equilibrium [70]. In b) it is represented the quasi-neutral region (QNR), the space charge region (SCR) and the Fermi level (E_F). In both a) and b) the thickness of the different layers are not at scale.

3.1 Substrate

Glass is used in both, laboratories and in the CIGS photovoltaic industry, as a substrate in thin film solar cells and modules, because it is cheap, available in a large volume, rather stable over time, can have several shapes and sizes, resistant, and easy to handle. The commonly used glass is SLG, the normal window glass [71]. Its coefficient of thermal expansion is $90\times10^7\,K^{-1}$, the strain point is around 514 °C, the annealing point is around 550 °C, the glass transition temperature is around 570 °C and a softening Littleton Point is at 720 °C [71]. During the growth of CIGS or CZTSSe, at temperatures between 450-600 °C, the glass goes through some of these transitions, the mobility of the ions is greatly increased, and sodium (Na) ions diffuse from the glass substrate into the absorber layer. It should be noted that for temperatures lower than 500 °C the amount of Na released is very low. Whereas for temperatures higher than 600 °C, SLG is not rigid enough to be flat and thus, the deposition of the chalcogenide layer is not possible [71].

The incorporation of Na in CIGS and CZTSSe has been systematically reported as beneficial for the electrical performance of the resulting solar cells [71-74]. Nevertheless, it has been demonstrated that is more convenient to control its diffusion and final amount in the absorber layer via an extrinsic source of Na [71]. The most studied strategies to introduce Na in the CIGS layer has been through alkali post-deposition treatment (PDT), deposition of a NaF precursor layer on top of the Mo, or the use of a Na doped Mo layer instead of a pure Mo layer [44, 75, 76, 77]. As aforementioned, a large number of companies use SLG, but for instance Solar Frontier [78], sometimes report the use of SLG with a diffusion barrier to block or control the amount of Na that diffuses into CIGS. Thus, glass

coated with a diffusion barrier (SiN_x, SiO_x, Al_2O_3, TiN), have also been used as strategy to control the supply of Na in CIGS technology [78, 79].

Most of the CIGS based solar cells world records of the past were established using SLG substrates, being the only exception the 20.4% record in 2013 on flexible polyamide by Swiss Federal Laboratories for Materials Science and Technology, EMPA [80]. In addition to polyamides [80, 81], stainless steel flexible substrates [82, 83, 84] have been also used in CIGS solar cells with a promising performance, 17.7% was achieved on Mo/Ti-coated stainless steel foils without any other additional metal-oxide or metal-nitride impurity diffusion barrier layer [83].

All champion CZTSSe based solar cells were obtained using SLG substrates. Nevertheless, flexible solar cells based on kesterites have been reported to be successfully produced: a 4.9% CZTS device reported on polyamide [85], a 6.1% CZTSe device on stainless steel foil [86], and for CZTSSe a remarkable 11.5% was achieved by a hydrazine-based deposition using ultrathin yttria-stabilized zirconia as a substrate, at IBM T. J. Watson Research Center [87].

So far, flexible chalcogenides solar cells have been reported to be successfully produced on a variety of suitable substrates. However, SLG is still preferred, due to the advantages presented above, in addition to the disadvantages of the two most used flexible substrates, the low-temperature required on polyimide processing and the impurity diffusion in steel based substrates, which may be seriously detrimental for the performance of the devices.

3.2 Back contact

The main requirement for the back contact is to provide a low series resistance and an ohmic contact to the absorber layer. In chalcogenides based solar cells, a Mo bilayer deposited by sputtering, is usually used as back contact [71, 88, 89, 90]. The Mo film is simultaneously characterised by high conductivity and strong adhesion [90]. The bottom layer (sputtered with high pressure) is designed to have good adhesive properties, while the top layer (sputtered with low pressure) is designed to be low ohmic and conduct the current, providing an electrode with good adhesion and good electrical conductivity [90]. Apart from adhesion and conductivity, other properties are important as well. Since, the presence of Na have been important in the improvement of CIGS based solar cells, the Mo/Na interaction is a matter of importance. If a SLG is used for the Na supply, the Na diffusion through the Mo layer must be uniform and sufficient [90]. Another advantage to use Mo in CIGS based solar cells is its ability to form an ohmic contact with the absorber layer, by forming an interfacial layer of $MoSe_2$ [91, 92, 93]. Alternatives to Mo have been studied [94], but until now Mo is empirically the best choice.

Following the success of the Mo as back contact in CIGS technology, the same approach was adopted for solar cells based on CZTSSe. However, there are serious doubts regarding the Mo suitability as back contact layer into CZTSSe solar cells. Thermodynamic studies suggests that Mo/CZTSSe interface may not be as chemically stable as Mo/CIGS interface [95]. In parallel the formation of a

thick $MoS(Se)_2$ layer during the sulphurization (selenization) may, favour the formation of secondary phases such as Cu, Zn, and Sn sulfides (selenides) ($Cu_2S(Se)$, ZnS(Se), and SnS(Se)), which are harmful for charge carriers transport at the back contact [95]. Two strategies have been adopted to overcome this issue: i) an alternative metal to the Mo back contact, preferentially a less reactive material [96], and ii) an intermediate layer between the Mo and CZTSSe [97, 98, 99]. Nevertheless, most of CZTSSe state-of-art devices have been produced in the conventional architecture Mo/CZTSSe, which suggest that in the end, Mo is for now the best choice [10].

3.2.1 Back contact/CIGS interface

According to the obtained minority carriers diffusion length and the conventional thickness of the CIGS layer, it is likely that back contact recombination affects the devices efficiency. In the early 2000s, several studies showed that the electrical performance of CIGS solar cells were mainly limited by bulk recombination [66, 100, 101] and that the interfaces were not problematic. However, after years of improvement of the absorber layer recent studies showed that the improvement of CIGS interfaces may lead to a substantial enhancement in the solar cell performance [44, 102].

For many years, the main strategy to oppose the back contact recombination was addressed by an intentional Ga-profile, i.e. a variation of GGI in depth from the buffer layer to the back contact. The Ga-profile will induce the formation of a quasi-electric field that will superimpose on the random movement of the carriers, then the electrons will be drifted to the pn interface, pushing the electrons away from the highly recombinative back interface. Two different Ga-profiles have been often implemented: i) normal profile, a linear gradient with a high concentration of Ga at the back and a low concentration at the surface of the CIGS [102], and ii) notch profile, a high concentration of Ga at the back and a decrease of Ga concentration towards the surface, being the minimum concentration located at a few hundreds nm from surface [102, 103, 104]. Many CIGS based solar cells with Ga-profiles have been fabricated and studied, but the actual effect of such an in-depth variation of the bandgap is still not clear. However, it is clear that does not fully minimizes the rear recombination due to the very high minority carriers diffusion length in CIGS [33].

Ultrathin devices have recently been studied in detail and successfully implemented [43, 105-109]. However, this architecture makes the back interface recombination more likely. Thus, new strategies combining back contact passivation with improvement of the back contact optical reflectivity to avoid rear recombination have been developed in parallel with CIGS ultrathin technology [44, 105, 106].

3.3 Buffer Layer

A n-type buffer layer should be able to transmit most of the incoming light to the absorber layer and form a high quality pn-heterojunction, in order to reach low interface recombination. To achieve these characteristics, the ideal buffer layer needs to have [110, 111]:

i) a wide bandgap ($\gtrsim$3 eV);

ii) a suitable conduction band line-up to the absorber and to the front contact;

iii) a complete coverage of the surface, using a layer thinner than the current thickness of 70 nm of the CdS layer to further increase transparency;

iv) a deposition methods that causes no surface damage to the absorber layer;

v) a good lattice match with absorber layer;

vi) a surface type inversion to shift the position of the Fermi level close to the conduction band of the absorber layer.

Traditionally, the most used buffer layer in chalcogenides based solar cells is CdS, deposited by chemical bath deposition (CBD). The above requirements are more or less fulfilled by the CdS buffer layer. However, both material and deposition technique, have some drawbacks, namely: CdS has a relative low bandgap, 2.4-2.5 eV [112] and the CBD process is the only non-vacuum step in the processing line of CIGS based solar cells. Furthermore, Cd is classified as a toxic and carcinogenic element, forbidden in high concentrations in several important markets (European Union, Japan). Thus, finding an alternative material for application as buffer layer, has become a hot topic within the chalcogenides investigation.

In regard to CIGS based solar cells, different wide bandgap materials, such as Zn(O,S) [113], $Zn_{1-x}Sn_xO_y$ [114], $Zn_{1-x}Mg_xO$ [115], and In_2S_3 [116, 117], as well as alternative deposition methods, have been intensively studied (see Fig. 3.2). In comparison to CdS, all the above buffer layers have in common, the increase of the J_{SC}, and in most cases a decrease of V_{OC} and fill factor (FF) of the solar cells [110, 111]. These results have been discussed in the literature and several suggestions have been proposed to justify why the CdS layer provides solar cells with a better junction namely, a good lattice matching between CIGS and CdS, a buried homojunction (result from a Cd n-doping of the top surface of the CIGS) and the remove of natural oxides that are formed directly during non-vacuum transfers. No agreement exists about this topic, but it is probably a combination of all these properties, that dictates the success of the CdS deposited by CBD in the performance of solar cells.

Several approaches to substitute the toxic CdS layer in kesterite solar cells have also been attempted. Table 3.1 shows the electrical parameters obtained from different studies for kesterite/CdS in comparison to kesterite/Cd-free based solar cells. A clear difference between Cd-containing and Cd-free is observed in CZTS based devices in comparison to CZTSe and CZTSSe ones. For Cd-free CZTS based solar cells the overall V_{OC} increases followed by an improvement in the efficiencies in comparison to those with a CdS layer. On the other hand, the V_{OC}, FF, and η decreased on Cd-free CZTSe and CZTSSe based solar cells in comparison with the reference devices with a CdS buffer layer.

As far as J_{SC} is concerned, no trend is clearly observed for solar cells based on kesterite, which do not follow the observed improvement of this electrical parameter in the CIGS Cd-free technology.

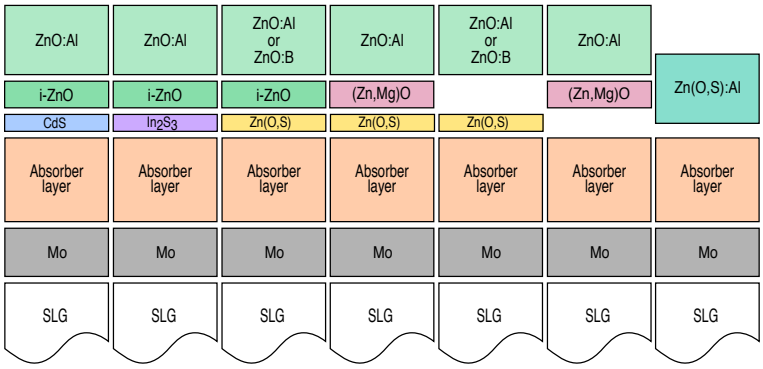

Figure 3.2: Illustration of different CIGS based solar cells grown on SLG/Mo substrates with alternative buffer layer systems in comparison to the commonly used CdS/i-ZnO. Adapted from [110].

Table 3.1: Electrical parameters J_{SC}, V_{OC}, FF, and η for solar cells based on kesterite/CdS in comparison to kesterite/Cd-free ones.

	Buffer layer	J_{SC} (mA.cm^{-2})	V_{OC} (mV)	FF (%)	η (%)	Ref.
CZTS	CdS	15.9	641	53.7	5.4	[118]
	In_2S_3/CdS	17.6	714	52.7	6.6	[118]
	CdS/In_2S_3	13.7	651	46.6	4.1	[118]
	In_2S_3	12.1	716	30.2	2.6	[118]
	CdS	20.4	665	57.4	7.8	[119]
	$Zn_{1-x}Cd_xS$	19.5	747	63.2	9.2	[119]
	CdS	20.5	608	58.0	7.2	[120]
	ZnSnO	21.6	679	61.4	9.0	[120]
CZTSe	CdS	35.9	388	57.9	8.0	[121]
	Zn(O,S)	33.5	358	60.0	7.2	[121]
CZTSSe	CdS	27.1	465	62	7.7	[122]
	In_2S_3	29.2	435	55	7.1	[122]
	In_2S_3 (ARC)	32.3	424	55	7.5	[122]
	CdS	24.0	362	60	5.2	[123]
	ZnSn	23.5	309	54	3.8	[123]
	CdS	34.2	361	58.5	7.2	[124]
	(Zn,Mg)O	15.9	332	44.4	2.3	[124]

3.3.1 CIGS/buffer layer interface

The nature of the CIGS/buffer interface is crucial for the solar cell performance. This interface has been the topic of many studies, in general focused into electronic, structural and chemical properties [66, 125, 126, 127]. In any heterojunction solar cell, reducing the recombination at the absorber/buffer layer interface is a major challenge. The surface type inversion in the CIGS surface, and the bandgap widening on Cu-poor CIGS surface layer are the main "intrinsic mechanisms" that reduce interface recombination [101]. "Extrinsic mechanisms" based on a surface reconstruction due to a post deposition alkali treatment are now being developed that also lower surface recombination.

For the case of a pn-heterojunction semiconductor-semiconductor with different work functions, a band bending close to the heterojunction will take place. For high values of efficiency in CIGS based solar cells, it is mandatory for the Fermi level to be located close to the CIGS conduction band minimum at the CIGS/buffer interface, to reduce interface defects [125]. This is called surface type inversion, i.e., the Fermi level at near the interface moves closer to the minimum of the conduction band, whereas, in the bulk of the CIGS, the Fermi level is much closer to the top of the valence band [101, 125]. The surface type inversion at the CIGS is a result of Fermi level pinning by interfacial states close to the conduction band (donors) [128].

It has been shown that a major role in the suppression of interface recombination is played by the Cu-poor surface layer that forms in Cu-poor chalcopyrites and leads to surface bandgap widening [101]. A study of the dependence of the density current-voltage measurements on temperature for CIGS based solar cells, showed that Cu-rich devices are dominated by recombination at the CIGS/buffer layer interface, with activation energies smaller than the bandgap energy of the CIGS ($E_A < E_g$). On the other hand, in Cu-poor devices, electronic losses are dominated by bulk recombination [100]. The formation of a Cu depleted layer at the surface of Cu-poor films plays a critical role in the heterojunction formation. This has been explained by a low interface recombination velocity, due to a lattice matching by the buffer layer and/or a buried interface [125].

A suitable conduction band line-up between CIGS and the buffer layer, also has a major role in the performance of the solar cell. Taking into account the energy band alignment between CIGS and the buffer layer, a small positive conduction band offset (0.08-0.4 eV) between the two semiconductors, which commonly is referred to as a spike, is considered optimal for device performance. A larger spike can create a barrier for minority carriers. A lower or negative conduction band offset is undesirable, since it reduces the surface type inversion close to the interface and leads to increased recombination via interface states [66, 129, 130].

Additionally, a common concern for thin film solar cells, is the diffusion of elements between the absorber and the buffer layer. This is important for both cases of CIGS and CZTSSe, since both contain mobile atoms like Cu. For example, as mentioned CIGS based solar cells have systematically a Cu-poor interface between the absorber and buffer layers, and may form mixed phases via the incorporation of buffer layer constituents, e.g. Cd for the case of CdS buffer layer. Moreover, recent

results indicate that there is a diffusion process that replaces Cu with Cd in the CIGS layer and Cd with Cu in the CdS [131]. Many studies showed that this absorber/buffer interface is in general intermixed [131-134].

CdS

CdS is a II-VI semiconductor compound, which exhibits a direct optical bandgap of 2.4-2.5 eV [112]. As was already discussed, CdS deposited by CBD is traditionally used as buffer layer in CIGS based solar cells. Many factors are pointed for the success of this combination, material/deposition technique [126].

The conduction band offset between a CIGS absorber (commonly with a bandgap energy of 1.15 eV) and CdS, is ∼0.3 eV, which is a suitable conduction band line-up. The lattice matching between CdS and CIGS is another advantage of this semiconductor [126, 135]. However, with the addition of Ga, the bandgap of the absorber increases mainly due to the shift of the conduction band and the lattice parameter decreases. Thus, the CIGS absorbers with very high Ga content create an unfavourable band alignment with CdS, as well as a poor matching between the layers at the interface [136].

The diffusion of Cd into the CIGS, appears to be beneficial, after a natural process of oxygenation that neutralises the positively charged surface of the CIGS (see Section 3.5.6). Cd will diffuse into the Cu-poor surface layer of the CIGS and possibly create Cd_{Cu} antisite donors, making it possible to restore the positive charges on the surface, which give rise to a surface type inversion at the CIGS surface (see Fig. 3.3). The importance of the Cd in the performance of the CIGS based solar cell was well showed by Ramanathan *et al.*, that found out that a Cd-electrolyte bath in CIGS buffer-free solar cells provide a better electrical performance in these devices than in the ones without treatment [137]. The authors argued that the beneficial effect of the Cd treatment is related to the diffusion of this element into the CIGS.

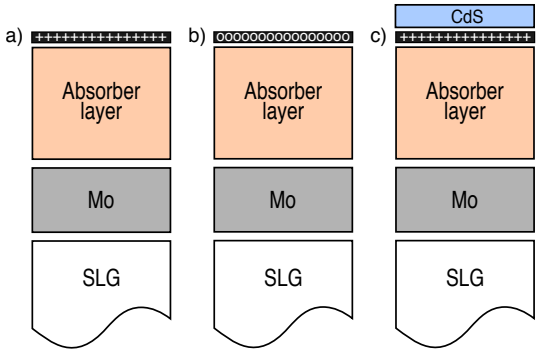

Figure 3.3: Schematic view of interface charges during the fabrication of a CIGS/CdS interface. a) On as-prepared films, the thin film surface is positively charged because of the presence of the dangling bonds; b) air exposure neutralises these charges; and c) the oxide passivation of the surface is removed by the CBD process. The re-established positive charges give rise to a surface type inversion at the CIGS surface. Adapted from [65].

Regarding the role of the CBD, is well known that it removes the natural oxide from the film surface. It is plausible that at least a part of the surface In-O bonds are removed by the chemical bath, due to its reductive nature [137].

All the evidences discussed above, would explain part of the reported importance of the CdS chemical bath deposition step to the attainment of a CIGS based solar cell with a high performance [138].

ZnSnO

$Zn_{1-x}Sn_xO_y$ (ZnSnO) is non-toxic, abundant, and has a tunable bandgap energy between 3.2-3.7 eV [139]. This ternary metal-oxide material has the intrinsic properties required, for an ideal buffer layer and has been successfully grown by vacuum compatible techniques, as atomic layer deposition (ALD) [139, 140]. In previous works, it was shown that by changing the Sn fraction and the deposition temperature, it is possible to change the bandgap energy, mainly through the position of the conduction band edge [70, 114, 139, 141]. In this way, the ability to change the conduction band energy level of ZnSnO can be used to achieve a suitable conduction band alignment with CIGS, even with a high Ga content, and i-ZnO [139].

Recently, ZnSnO has shown potential as a Cd-free buffer layer for CIGS based solar cells, exhibiting performance comparable to devices with CdS buffer layers. Lindahl *et al.*, achieved a power conversion efficiency of 18.6% for CdS-based devices and 18.2% for ZnSnO ones [140].

Regarding the role of the ALD, it is a chemical vapour deposition technique based on an alternation of self-limiting gas to solid reactions, which enables the growth of thin films with excellent conformity and thickness control down to atomic levels. The main drawback of this deposition method is that the film growth rate is low, compared to other deposition techniques [142]. Un-annealed ALD ZnSnO films deposited in a temperature range of 120-150 °C have in general been found to be amorphous for compositions of [Sn]/([Sn]+[Zn]) above 0.1, which reduces the amount of recombination centers at the grain boundaries in the buffer layer and at the CIGS/ZnSnO interface [141, 143, 144]. Moreover, ZnSnO grows uniformly and conformably on CIGS and the interface between CIGS and ZnSnO is sharp with little or no diffusion between the layers [70, 145].

3.3.2 CZTSSe/buffer layer interface

No doubts exists that the nature of the pn-heterojunction interface is crucial for the solar cell performance. In fact, the nature of the kesterite/CdS band alignment is presently an open question in the scientific community [53, 61, 146, 147, 148]. The analysis of the recombination path in kesterites reveals significant differences between solar cells based on sulfide kesterite (CZTS, CZTSSe) and its selenide equivalent, CZTSe. If on the one hand CZTSe solar cells are limited by bulk recombination, on the other hand CZTS and CZTSSe main recombination path appears to be located at the interface [58, 60, 61, 63]. Thus, a spike-like band alignment at the CZTSe/CdS interface, and a cliff-like band alignment for S-containing kesterites have been ascribed in order to explain the different paths of

recombination in the solar cells based on kesterite. Note that, a cliff-like conduction band offset is undesirable, since leads to increased recombination via interface states and reduces V_{OC}. For any heterojunction solar cell, reducing the recombination at the absorber/buffer layers interface is a major challenge. In this way, several authors in the literature concluded that CdS is a suitable buffer for CZTSe, but not the ideal choice for CZTS or CZTSSe based solar cells [61, 146]. However, as shown in Fig. 3.4, several conduction band offset measurements obtained a cliff-like conduction band offset in CZTS/CdS for devices with efficiency below 5%, but when the efficiency improves up to 7% the same measurements reveal a spike-like or nearly flat conduction band offset [147]. Thus, the cliff-like type of conduction band alignment will give rise to devices with poor performances, not being expected to exist in the state-of-art CZTS based solar cells.

By an ab-initio theoretical study, Crovetto *et al.* presented evidences that bandgap narrowing at the heterojunction, caused by surface states that extend the CZTS valence band into the bandgap, may be the main explanation of the large V_{OC} deficit on CZTS/CdS solar cells. Those surface states were consistently found in CZTS, but not in CZTSe. This observation may explain why interface recombination is dominant in CZTS solar cells, but not in CZTSe ones [147]. The authors also suggested that Zn-containing buffer layers are advantageous, due to the ability of Zn to passivate the identified surface defects, which is compatible with a reported improvement of the V_{OC} using a ZnSnO buffer layer in comparison with the conventional CdS [149].

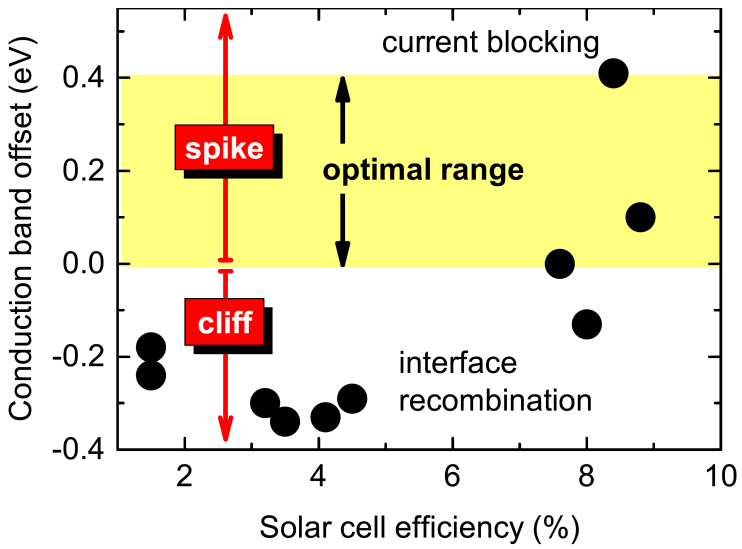

Figure 3.4: Dependence of the conduction band offsets at the CZTS/CdS interface on solar cell efficiency. Adapted from [147].

3.4 Window layer

The window layer must be highly transparent, in order to minimize photons absorption, create a favourable band alignment at the buffer/window interface, with low recombination losses, and form a high resistant element to screen shunts. In order to achieve these properties, it is fundamental a bilayer structure of a high and thin resistance layer over the buffer layer, followed by a low resistance one [65]. For this propose, typically in the best CIGS and CZTS based solar cells and in CIGS industrial systems, a bilayer of i-ZnO and ZnO:Al are used [145, 150].

The role of the i-ZnO layer is to eliminate possible conducting paths from the back contact, through the CIGS and buffer layer to the ZnO:Al front contact. The sum of these conducting paths is referred to as shunt conductance and is harmful for the device, allowing current to pass through alternative paths to the junction. The ZnO:Al is conductive and therefore capable of collecting the free electrons. In the literature, some works show that with increased substrate temperature during ZnO:Al deposition, the conductivity increases [151]. Because the window layer is deposited after the formation of the pn-heterojunction, the substrate temperatures during deposition is limited to about $\sim$100 °C in order to avoid detrimental diffusion. Indium tin oxide, SnO_x:In (ITO), is also often used in solar cells based on CZTSSe as the conductive window layer instead of ZnO:Al [152].

3.5 Absorber layer: CIGS

3.5.1 Structural properties

The alloys system I-III-VI_2 (e.g. Cu(In,Ga)Se_2) may crystallize in two tetragonal crystal structures: chalcopyrite (space group $I\bar{4}2d$, corresponding to a tetragonal structure) as their ground-state phase and CuAu-like (space group $P\bar{4}m2$) as metastable phase [153, 154]. The latter phase has a formation energy which is only 8.2 meV/4-atom higher than the equilibrium chalcopyrite phase for $CuInSe_2$ (CIS). However, this value increases to 36.2 meV/4-atom in $CuGaSe_2$ (CGS) [155]. Thus, Wei *et al.* predicted that CuAu-like phase can coexist in nominally chalcopyrite CIS, while such coexistence is less likely in CGS [155].

The chalcopyrite and CuAu-like structures may be taken as derived from zincblende (ZB) binary II-VI, Fig. 3.5 a), by isoelectronic substitution of the group II elements with an equal amount of elements from group I and group III (see Fig. 3.5) and a duplication of the unitary cell where $c \approx 2a$. Nevertheless, it is more complex than a simple substitution of elements, due to their different chemical nature. The chalcopyrite and CuAu-like structures are shown in Fig. 3.5 as b) and c), respectively. All compounds with structures derived from the more simple diamond structure are said to be "adamantin" [156].

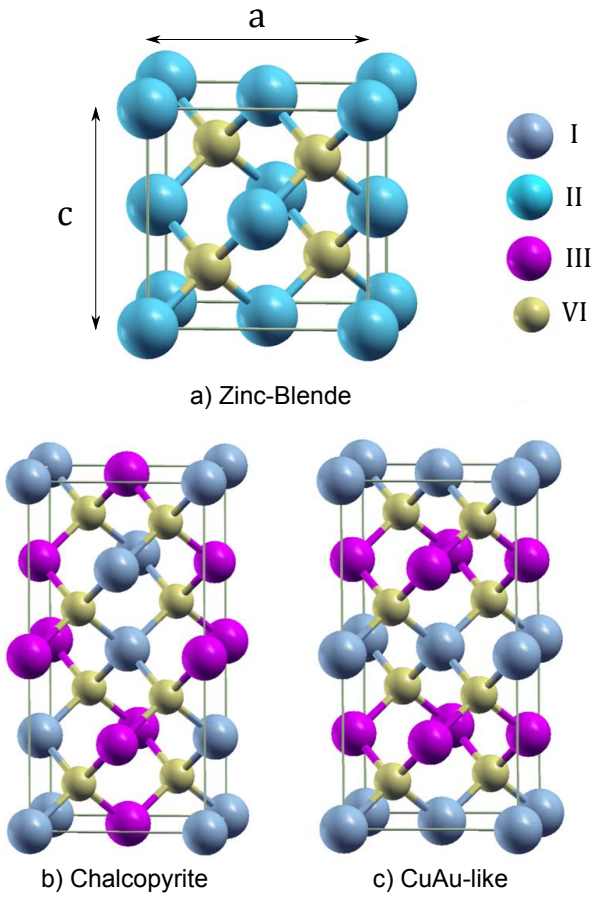

Figure 3.5: Crystal structure of a) zincblend, b) chalcopyrite and c) CuAu−like lattice. In a) the lattice parameters a and c are presented. Adapted from [157].

In chalcopyrite and CuAu-like structures, the VI anion (Se) is always surrounded by two I and two III cations. So, there are three significant structural differences in comparison to the ZB structure: i) the strengths of the I-VI and III-VI bonds are in general different ($R_{I-VI} \neq R_{III-VI}$); ii) the unit cell is tetragonally distorted with a distortion parameter of $\eta = c/2a \neq 1$, where a and c are lattice parameters; iii) the anions are displaced from the ideal tetrahedral site, 0.25, by an amount $u = 0.25 + [(R^2_{I-VI} - R^2_{III-VI})/2]$. Any of these three factors can lead to a crystal-field, which will influence the electronic structure discussed in Section 3.5.2 [158].

Taking into account the structural parameters presented in Table 3.2, the lattice parameter a of the chalcopyrite structure is larger than that of CuAu-like structure. So, in the CuAu-like structure, the Cu→ Se→ Ga orientation is along the c-axis, while in the chalcopyrite structure, it is along the a-axis, and considering that, i.e. the values for the strengths of the I−VI and III−VI bonds in CIS are R_{I-VI} =2.39- 2.424 Å and $R_{III-VI} = 2.61$ Å [159, 160]. Then, the CuAu-like structure along the c-axis is longer than along the a-axis [157].

When In is substituted by the smaller atom Ga, the lattice compression should result in changes in bond properties of CIGS, as well as in the anion displacement. For CIS, the c parameter is slightly

dilated, being lower for CGS. The distortion parameter η, for the case of the chalcopyrite structure, is smaller than unity for CGS ($\eta < 1$), while larger than unity for CIS ($\eta > 1$). In CGS the anion has an almost ideal position, due to almost equal ionic radii for Cu^{+} and Ga^{3+}, in contrast with the displaced anion position in CIS, which deviates strongly from the ideal value (see Table 3.2). Following the context of this thesis a main attention will be given to the CIGS alloy at chalcopyrite ground-state phase in the next discussion.

Table 3.2: Lattice parameters a and c, tetragonal distortion parameter η and anion displacement u for CIS and CGS.

	Chalcopyrite				CuAu-like				
	a (Å)	c (Å)	η	u	a (Å)	c (Å)	η	u	Ref.
CIS	-	-	-	-	4.088	5.810	1.421	0.2245	[161]
	5.880	11.833	1.006	0.2177	4.181	5.850	-	0.2181	[162]
	5.78	11.55	-	-	-	-	-	-	[163]
	5.784	11.616	-	0.224	-	-	-	-	[164]
CGS	5.670	-	0.993	-	5.616	-	1.009	-	[157]
	5.561	11.00	-	-	-	-	-	-	[163]
	5.614	11.03	-	0.250	-	-	-	-	[164]

3.5.2 Electronic properties

Chalcopyrites have a direct bandgap due to the alignment of the minimum of the conduction band with the maximum of the valence band at the center of the Brillounin zone (Γ point). The bandgap of CIGS is tunable by varying the Ga fraction, ranging from around 1.01 to 1.68 eV at room temperature, for CIS and CGS, respectively [163]. The bandgap of the CIGS, can be calculated by the empirical expression,

$$E_g = 1.010 + 0.626x - 0.167x\,(x-1) \tag{3.1}$$

where x is the GGI ratio [165]. The possibility of engineering the bandgap energy of the compound by adjusting the elemental substitution of In by Ga, is a very important feature for the fabrication of CIGS based solar cells.

The change of the bandgap in CIGS compounds is caused by two important factors: i) repulsive p-d states, forming the valence band, which are associated with the Cu d-orbitals; ii) the anion displacement, caused by $R_{I-VI} \neq R_{III-VI}$ [166]. Once CIS and CGS have an equal d-character of the Cu-Se bond, the different values of the bandgap are related with the anion position parameter of CGS and CIS, which is different for each alloy (see Table 3.2), due to the different value of R_{III-VI}. For CIS

and CGS, $R_{In-Se} = 2.61$ Å and $R_{Ga-Se} = 2.44$ Å, respectively [159]. According to Jaffe and Zunger, an higher tetragonal distortion parameter η (remember that for CIS, η>1, and for CGS, η<1) leads in compounds with a similar d-character of Cu-Se bond, to smaller values of the bandgap [158]. It is also known, that increasing GGI, the valence band maximum decreases slightly while the conduction band minimum increases. Consequently, the bandgap also increases. The valence band offset between CIS and CGS was found to be ΔE_V = -0.04 eV and the conduction band offset ΔE_C = 0.60 eV [167].

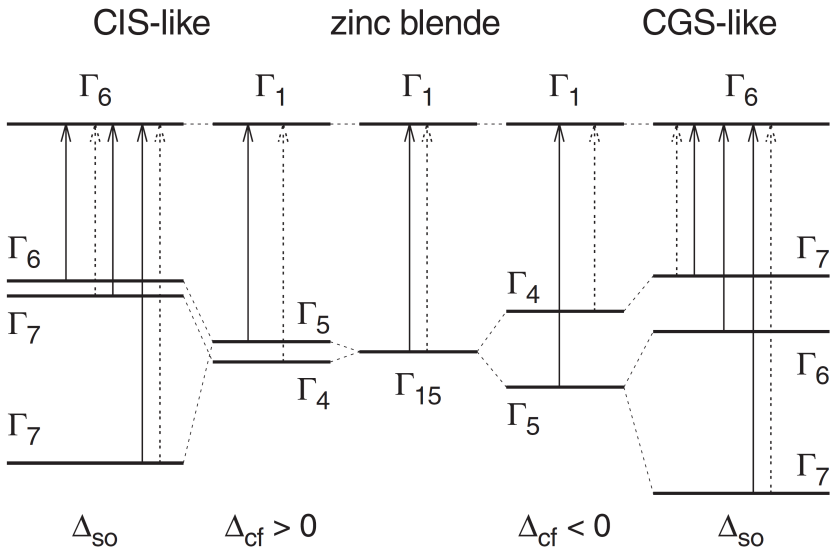

Figure 3.6: Schematic derivation of energy bandgap states of CIS (left) and CGS (right) from a hypothetical. The starting point structure is a hypothetical ZB one, without spin-orbit splitting. For CIS and CGS-like structures, the crystalline field and spin-orbit are included. Adapted from [165].

Fig 3.6 schematically shows the energy states at the bandgap of CIS and CGS derived from a ZB structure without spin-orbit coupling, i.e. due to the mutual interaction of both spin and orbital magnetic moments for the electron, which causes a split of the valence band at the Γ point [165]. The introduction of the tetragonal distortion, will cause in valence band maximum a crystal-field splitting (Δ_{CF}), which is the energy level difference between the two states resulting from the Γ_{15} state, Γ_5 and Γ_4 states [165]. This splitting is positive for CIS and negative for CGS, due to the different tetragonal distortions, as seen in the CIGS structural properties (Section 3.5.1). The introduction of spin-orbit interaction finally leads to three topmost valence bands at the Γ point, as shown in Fig 3.7.

The heavily- and lightly-hole valence bands are degenerated at the Γ point. At this point, the holes effective mass parallel and perpendicular to the *c*-axis are given in Table 3.3, where it is observed, $m^{\perp}_{v1}(m_0) < m^{\perp}_{v2}(m_0)$ and $m^{||}_{v1}(m_0) > m^{||}_{v2}(m_0)$ for CIS, and the opposite for the case of CIGS and CGS $m^{\perp}_{v1}(m_0) > m^{\perp}_{v2}(m_0)$ and $m^{||}_{v1}(m_0) < m^{||}_{v2}(m_0)$ [159].

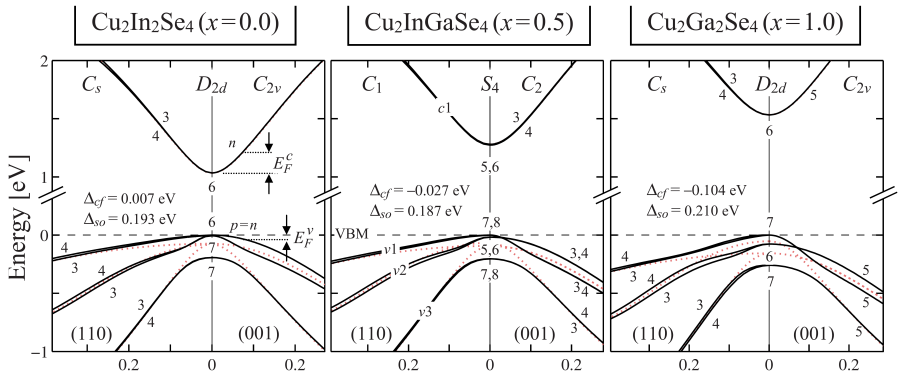

Figure 3.7: Electronic structure of CIGS near the Γ-point when spin-orbit interaction is included (solid lines) and excluded (dotted red lines). Adapted from [159].

The properties of the band structure influence the effective mass, for both electrons and holes. For chalcopyrite CIS, CIGS, and CGS they are presented in Table 3.3. The electrons effective masses are lower than the hole effective masses. Additionally, they are approximately isotropic for electrons, which is not observed for holes. The difference in the value of the effective masses of electrons and holes will influence the allowed radiative transitions in these materials (Subsection 4.2.4).

Table 3.3: The Γ-point effective masses of electrons ($m_{c_1}^{\perp}$, $m_{c_1}^{\parallel}$) and holes ($m_{v_i}^{\perp}$, $m_{v_i}^{\parallel}$ $i = 1, 2, 3$), where v_1 and v_3 are the topmost and lowmost valence bands, for CIS, CIGS and CGS, for directions parallel and perpendicular to the c-axis [159].

	$m_{c1}^{\parallel}(m_0)$	$m_{c1}^{\perp}(m_0)$	$m_{v1}^{\parallel}(m_0)$	$m_{v1}^{\perp}(m_0)$	$m_{v2}^{\parallel}(m_0)$	$m_{v2}^{\perp}(m_0)$	$m_{v3}^{\parallel}(m_0)$	$m_{v3}^{\perp}(m_0)$
CIS	0.09	0.08	0.66	0.14	0.12	0.25	0.28	0.27
CIGS	0.11	0.10	0.14	0.40	0.61	0.17	0.40	0.29
CGS	0.13	0.13	0.15	0.47	0.61	0.20	0.49	0.29

3.5.3 Phase Diagram

The complete phase diagram for CIGS is relatively complex, since we are dealing with a quaternary compound and a big number of two- and three-elements secondary phases may appear. However, it can be reduced to a simpler pseudo-binary phase diagram along the section between Cu_2Se-In_2Se_3 and Cu_2Se-Ga_2Se_3, for CIS and CGS, respectively.

The pseudo-binary phase diagram for Cu-In-Se in Fig. 3.8 a) shows four different relevant phases: the α-phase tetragonal (CIS), the β-phase ($CuIn_3Se_5$), the δ-phase (the high-temperature sphalerite phase) and $Cu_{2-y}Se$. Fig. 3.8 b) shows the pseudo-binary phase for Cu-Ga-Se system along the Cu_2Se-Ga_2Se_3 pseudo-binary section. The phase labelled α is the CGS and the β region contains $CuGa_5Se_8$ phase [168].

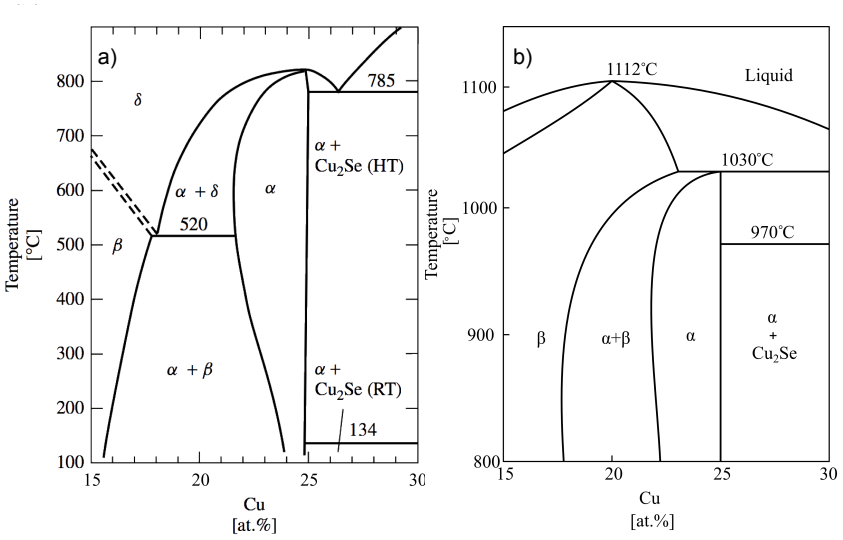

Figure 3.8: a) Pseudo-binary phase diagram of the Cu-In-Se system along the section between Cu_2Se-In_2Se_3. b) Pseudo-binary phase diagram Cu-Ga-Se system along the Cu_2Se-Ga_2Se_3 section. From [168, 169].

The single-phase region of the α-phase at 100 °C is small (24 at.%< Cu < 24.9 at.%) and not includes the stoichiometric composition of CIGS. The Cu content in CIGS absorber layer typically varies between 22 and 24 at.% Cu. At the growth temperature (∼520 °C) and with this content of Cu, the obtained material lies within the single phase stable region of the α-phase. The introduction of Ga will allow to widen the range of single-phase region of the α-phase. It is also important to take into account that, the diffusion of Na in the absorber layer will also increase the allowed range to growth CIGS α-phase [65]. Considering the reasons presented above and the fact that to ∼25 at.% Cu the secondary phase $Cu_{2-y}Se$ starts to appear, typically the CIGS based solar cells have a Cu-poor absorber layer composition in a single chalcopyrite phase [145].

3.5.4 Defects

The crystal defects determine the optoelectronic properties of semiconductors. A better knowledge of the diversity of these defects helps to improve the solar cell performance. In general, crystal defects can be grouped in four classes, according to their dimensional nature [170, 171, 172]:

i) **three-dimensional defects:** precipitates, inclusions, voids, etc;

ii) **two-dimensional defects (planar defects):** stacking faults, grain boundaries, surface, etc;

iii) **one-dimensional defects:** dislocations or line defects;

iv) **point defects:** several types of defects can appear, namely:

iv. i) impurities;

iv. ii) vacancies (e.g. a missing lattice atom A, V_A);

iv. iii) interstitial (e.g. an additional host atom A within the lattice, A_i);

iv. iv) antisite defects (e.g. in an AB compound, an A atom occupies a B site, A_B).

3.5.5 Native point defects

In the ternary chalcopyrite semiconductors CIS, CGS, and even more in the quaternary CIGS, a large diversity of native point defects exist, due to the presence of 3 or 4 distinct atomic species. As a consequence, these materials are typically highly doped and compensated, and their optoelectronic properties are governed by native point defects. The doping of CIGS is controlled by such a large density of defects that depends on the formation energy, that vary considerably with both Fermi energy and with the chemical potential of the atomic elements (i.e., by the elemental composition of the material) [173]. Moreover, the off-stoichiometry composition, the diffusion of atomic elements (namely, Na, K, O) from the commonly used SLG substrate, Cd and Cu interdiffusion in CIGS/CdS interface, and the non-intentional incorporation of impurities during the growth, will promote the formation of even more native point defects [131, 174, 175].

Using first-principles self-consistent electronic structure theory, Zhang *et al.* calculated several defect formation energies and defect energy level's in CIS and CGS [173, 174]. The authors showed that it is much easier to form a Cu vacancy (V_{Cu}) in CIS than to form cation vacancies in II-VI's. For the V_{Cu} defect in Cu-poor or in stoichiometric material, the calculated formation energy actually becomes negative. A low (but positive) formation energy is also found for In-Cu antisite (In_{Cu}). These two defects originates the complex $[2V_{Cu}^{-}+In_{Cu}^{2+}]$, which have a remarkably low formation energy [173] and is electrically neutral, not having an energy level inside the bandgap. Similar results were found for CGS, except that it requires a higher formation energy to form $[2V_{Cu}^{-}+Ga_{Cu}^{2+}]$ in CGS than to form $[2V_{Cu}^{-}+In_{Cu}^{2+}]$ in CIS, and the Ga_{Cu} donor level is much deeper than In_{Cu} donor level [174].

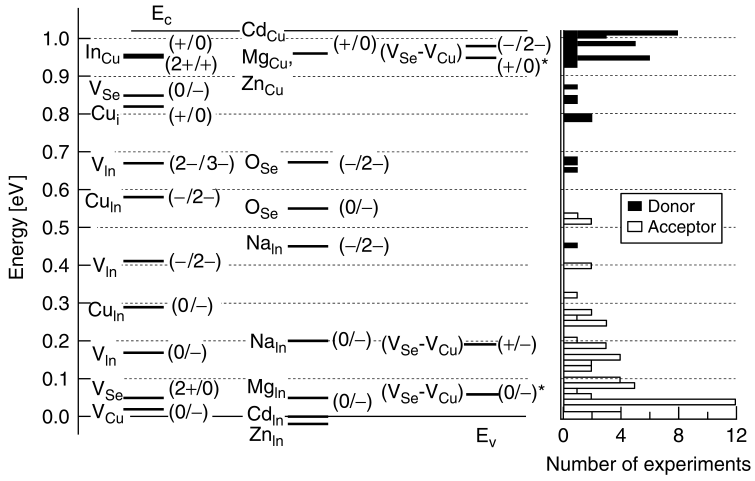

Figure 3.9: Theoretical values of electronic defect transition levels in CIS. $*$ mark transitions which only occur in a metastable state. Adapted from [20].

In contrast with the study presented by Zhang *et al.* [173], Pohl *et al.* [176] in a more recent work, found that In_{Cu} is a very shallow donor, which is a better explanation to the good tolerance of CIS to the off-stoichiometry, rather than the formation of the complex $[2V^{-}_{Cu}+In^{2+}_{Cu}]$ as Zhang *et al.* presented in their study [176].

The p-type self-doping capability of Cu-poor CIGS is ascribed to the low formation energy of the V_{Cu} defect, which is ∼30 meV above the valence band (Fig. 3.9), and the dominant compensating donor, the V_{Se} defect. This feature means that the doping type of CIGS can be controlled without external dopants [65].

Metastable effect induced by light and reverse bias have been observed in CIGS, mainly in electric characterization [177, 178]. The metastable effect in CIGS have been associated to changes of the charge state of the defect accompanied by large lattice relaxations [177-181]. Due to the amphoteric nature of the V_{Se} defect, the Se-Cu divacancy complex [V_{Cu}-V_{Se}] has been identified as a possible responsible of this effect, as well as the In_{Cu} antisite defect [179, 180].

Although, it is widely accepted that the beneficial effect of Na in CIGS technology results partially from the enhanced p-type conductivity inside the chalcogenide absorber layer, which yields to a higher V_{OC}, how the Na incorporation enhances the p-type conductivity is not well understood, as the following discussion will expose [71, 72, 182, 183]. According to Wei *et al.* the main effect of Na incorporation in CIS is to reduce intrinsic donor defects. For low Na concentrations, Na will first reduce the density of the In_{Cu} antisite defect, then automatically increase the effective holes density [184]. Note that In_{Cu} defect is associated with the high tolerance of CIS to the off-stoichiometry, directly associated by the In_{Cu} defect or by the neutral complex $[2V^{-}_{Cu}+In^{2+}_{Cu}]$ that involves In_{Cu}. However, this is not compatible with the fact that the diffusion of Na in the absorber layer will also increase the allowed range to growth CIGS α-phase, discussed in the former Subsection. Another, model is based on the fact that Na is only electrically active at the grain boundaries and acts on the V_{Se} defect along with oxygen (O) (the effect of O on V_{Se} is discussed in the following Subsection) [185].

Experimentally, there are an huge amount of data related to defects from various methods, such as, photoluminescence [186-189], cathodoluminescence [190], admittance spectroscopy [191, 192, 193]. However, since CIGS is self-doped, may have different compositions, and may be grown by different methods, the optoelectronic properties may do change significantly. Thus, these studies are not always in agreement with each other. However, many of these optical and electrical characterization techniques point to the existence of one very shallow intrinsic donor and at least two intrinsic acceptors in CIS, CGS, and CIGS [176]

3.5.6 The free CIGS surface: defects and structural properties

The understanding of the properties of the free surface of CIGS thin films is especially important for further improvements of the solar cell performance. The free surface of Cu-poor CIGS films exhibit two important features, firstly observed by Schmid *et al.* [194]: i) a Cu-poor surface compared with

the bulk, and ii) a wider surface bandgap than the bulk.

To explain both observations the presence of an ordered vacancy compound (OVC) layer, in between the CIGS and CdS layers, was proposed [194, 195]. Following the phase diagram this layer was assigned to the n-type β-phase $CuIn_3Se_5$. This model claims that the device functions as a buried CIGS/OVC homo-junction. According to Zhang *et al.* [173], the defect complex $[2V_{Cu}^{-}+In_{Cu}^{2+}]$ leads to a so-called ordered defect compound (ODC). It is important to note, a OVC or ODC surface layer with different structure will have different optoelectronic properties, which will affect the active heterojunction of the solar cell (CIGS/buffer layer).

The origin of surface Cu depletion on Cu-poor chalcopyrite thin films, and its consequences for the solar cells, has been discussed for the past 20 years. In 2002, a direct measurement of the surface bandgap of polycrystalline CIS films by Morkel *et al.* proved that at the surface the bandgap is about 1.4 eV, i.e., 0.3 eV larger than the bandgap in the bulk [129]. Romero *et al.* [196] also found that the bandgap of the surface layer in a CIGS film can be wider than that in the bulk material. In other work, a convergent-beam electron diffraction and energy dispersive X-ray spectrometry study specifically looked at the top 2 μm of Cu-poor CIGS films. The authors found that the surface layer is structurally similar to the bulk. Nevertheless, a slight Cu-depletion near the surface was detected, indicating that different native point defects may exists [197]. Thus, the CIGS surface is a topic of debate and it is still not fully understood.

So far, a direct structural proof of the ODC surface layer is still missing, and a surface n-type $CuIn_3Se_5$ is not sufficient to achieve the surface type inversion required in CIGS based solar cells (discussed in Section 3.3.1) [65]. Moreover, Rau *et al.* showed that the surface type inversion in CIGS as-grown films, is eliminated after exposure of several minutes to air [198]. Given these evidences, other two models were presented in the literature to discuss the surface of CIGS thin films and of a homojunction formation, see Fig 3.10: i) the surface-state model [198], and ii) the defect layer model [199].

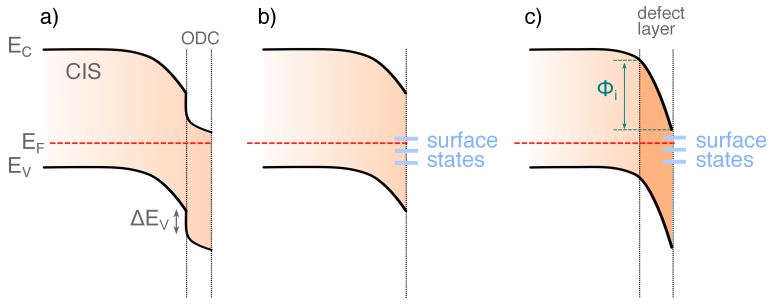

Figure 3.10: Models for the CIS surface: a) OVC or ODC layers; b) band bending due to surface charges; c) band bending induced by Cu depletion at the surface, creating a surface defect layer [65]. E_C is the conduction band edge energy, E_V the valence band edge energy, ΔE_V an internal valence band offset, E_F the Fermi level, and ϕ_i an internal barrier to the electrons transport, caused by the defect layer. Adapted from [65]

The two models argued that the surface type inversion results from the presence of shallow surface states, i.e. Fermi level pinning by shallow surface donors. In the first model, positively charged surface (donors) is theoretically expected on CIGS, due to dangling bonds related with V_{Se} defects [200, 201]. The elimination of the surface type inversion after exposure at air is explained by the oxygenation's model of Kronik *et al.* [202]. The oxygenation on CIGS surface, has the effect of passivation of the V_{Se} donors by O atoms, which will cause a decrease in the positive charge at the CIGS surface and creates acceptors recombination centers (O_{Se}) [202].

The second model, the defect layer one represents a compromise between the ODC and the surface-state models, as it takes into account a modification of the band structure due to the Cu depletion on the surface of the CIGS, as well as the presence of positively charged surface states [65, 194, 198, 199].

3.5.7 CIGS Growth

A wide variety of thin film growth methods have been used to fabricate CIGS, which may be classified in three main categories [20, 65, 203, 204]: i) co-evaporation, ii) selenization of vacuum-deposited metallic precursors, and iii) non-vacuum techniques.

Among the different deposition methods developed for the production of CIGS based solar cells, co-evaporation and selenization of vacuum-deposited multi-stacked precursors are so far the elected candidates for large-scale photovoltaics industry, due to the right compromise between production cost, feasibility, and performance [205]. On the other hand, non-vacuum methods have been considered as an emerging technology for CIGS, and are mainly based on solution approaches which includes electrodeposition [206], nanoparticles solution technique [207], and spray pyrolysis [208]. However, these methods have so far presented low efficiency values [205-208].

Despite the significant differences between co-evaporation and selenization grown methods, both lead to CIGS with similar properties as long as the following requirements are fulfilled:

i) the substrate temperature should reach $\sim$500 °C;

ii) the overall composition of the CIGS should be Cu-poor;

iii) an oversupply of Se during the CIGS growth;

iv) a 0.2-0.3 GGI ratio.

These are some of the growth conditions/parameters essentials for CIGS to have a good performance as absorber layer. Thus, the way in which CIGS is grown, greatly influences the performance of the device. Changes on the Cu content strongly affects the thin film growth and the final properties of the device. CIGS grown with a Cu-rich composition, i.e. [Cu]/([In]+[Ga])(CGI)>1, has very good crystal properties, but it lacks good optoelectronic properties [210, 211, 212], resulting in a poor performance of the solar cells. On the other hand, CIGS grown with a Cu-poor composition, i.e. CGI <1, lack good crystal quality, but has superior optoelectronic properties [210, 211, 212]. In order to address

the limitation of preparing CIGS with both good structural and good optoelectronic properties, the absorber layer is usually prepared in several stages [213]. An oversupply of Se during the CIGS growth is mandatory. This element has a reduced sticking coefficient and a much higher vapour pressure than the used for the other elements [214]. The relative amount of Ga, GGI, determines the bandgap energy of the CIGS. Bandgap energy values of 1.1-1.2 eV, corresponding to a GGI$\sim$0.3, are used in high-efficient devices [65]. More specific considerations regarding co-evaporation will be discussed next, since the CIGS studied samples were grown by this method.

Co-evaporation

The co-evaporation is the most common method used to grow CIGS, and involves evaporation of the constituent elements (Cu, In, Ga, Se), from their pure element sources, in single or sequential processes with an oversupply of Se during the whole CIGS fabrication [203, 215]. Thus, different co-evaporation growth schemes have been developed in order to fulfill the requirements presented above, different evaporation stages, distinguished by different evaporation rates and substrate temperatures [65, 204, 216]. To obtain the large grains of the Cu-rich stage with the good optoelectronic properties of the Cu-poor composition, advanced process schemes always include a Cu-rich stage during the growth process and end up with an Cu-poor overall composition. Depending upon the number of stages, the co-evaporation method may be classified as: three-stage, two-stage or Boeing , and one-stage or in-line processes (see Fig. 3.11).

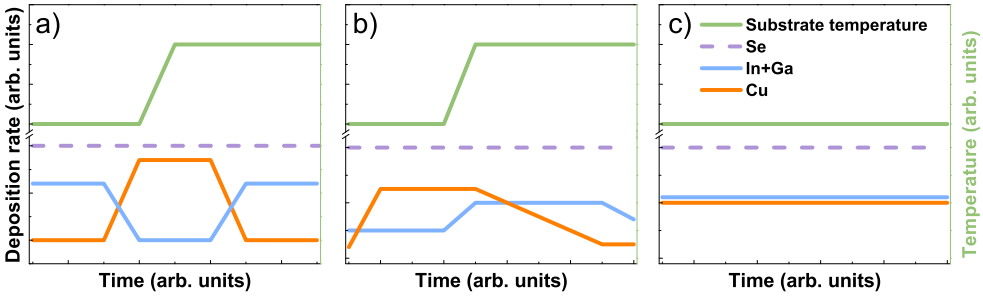

Figure 3.11: Schematic illustration of the deposition rate for Cu, Ga+In, and Se and substrate temperature profiles for co-evaporation processes: a) three-stage, b) two-stage, and c) in-line processes. Adapted from [65].

i) **Three-stages co-evaporation process:** in the first stage, In and Ga, are evaporated to form a first layer ($(In,Ga)_2Se_3$). During the second stage, the temperature is ramped up and Cu is added until the film becomes slightly Cu-rich. Finally, in the third stage, In and Ga are evaporated again, and the deposition is finished when the desired Cu-poor composition and thickness are reached. This process is difficult to implement in the large-scale photovoltaics industry, because of its complexity to control the evaporation rates and the abrupt change of temperature from the first to the second stage. [20, 51, 78, 203]. The success of this method has commonly been attributed to two properties: i) the growth of CIGS with large grains and

smoother surface, and ii) the self-formation of a notch Ga-profile (an example of a Ga-profile is given in Fig. 7.5).

ii) **Two-stages or Boeing process:** Cu, In, are Ga, are evaporated to form a film slightly Cu-rich in the end of the first stage. In the following stage the Cu deposition rate is decreased, while Ga and In rates are increased. The substrate temperature is ramped up in the beginning of the second stage. The final CIGS thin film has a Cu-poor composition and presents good structural properties [217].

iii) **One-stage or In-line:** this process emerged from the need of a simple deposition method, due to the technical complexity of the three-stage process. Cu, In, Ga and Se are deposited at constant rates, and frequently at a constant substrate temperature during the deposition process [51].

3.6 Absorber layer: CZTS

3.6.1 Structural properties

CZTS and CZTSe are quaternary compounds that belong to the alloy system I_2-II-IV-VI_2 which, according to the octet rule[1], may crystallize in three tetragonal crystal structures: kesterite (space group $I\bar{4}$, stannite (space group $I\bar{4}2m$) and primitive mixed CuAu-like (PMCA) (space group $P\bar{4}2m$). These three crystal structures are presented in Fig 3.12 [154].

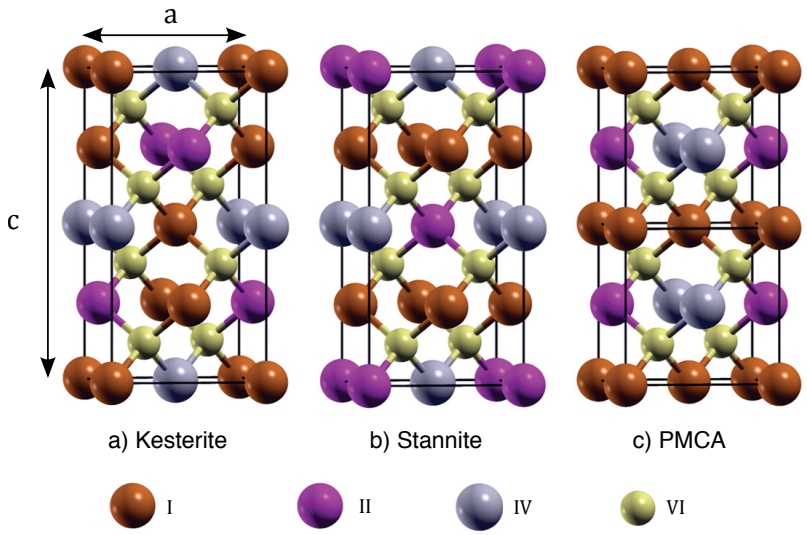

Figure 3.12: Crystal structure of a) kesterite, b) stannite and c) primitive mixed CuAu-like lattice (PMCA). In a) the lattice parameters a and c are presented. Adapted from [218].

[1]The octet rule ensures eight electrons around each anion atom, the S anions should be coordinated by the Cu (in +1 valence state), Zn (in +2 valence state) and Sn (in +4 valence states) cations in a way that makes all S anions in eight-electron full-shell state, so the local charge neutrality is satisfied around all S anions.

In order to understand the origin of the three presented crystal structures, we will start from the ternary compounds with an alloy system I-III-VI_2, which crystallize in chalcopyrite or CuAu-like structures. The latter two crystal structures were discussed in Section 3.5 for CIGS, and as discussed may be derived from the ZB structure. Kesterite structure results from a reduction of symmetry in the chalcopyrite structure, arising from the replacement of the cations of group III by two elements of groups II and IV. Both, stannite and PMCA structures are derived from the CuAu-like structure [154]. Different explanations may be find in the literature in order to explain the origin of the kesterite and stannite structures. According to Schorr *et al.*, the structure that results from chalcopyrite is the stannite and then, a change in the cations position in this structure will give origin to the kesterite one [219].

Kesterite and stannite structures are body-centered tetragonal with $c \approx 2a$, and may be seen as two S face centered cubic (FCC) lattices stacked on top of each other with Cu, Zn, and Sn occupying half the tetrahedral voids within the FCC lattice (see Fig. 3.12). The PMCA structure is primitive tetragonal with $c \approx a$. As seen in Fig. 3.12, kesterite and stannite structures differ in the arrangement of the Cu and Zn cations. The crystalline structure of the kesterite is characterized by alternating planes containing cations: Cu and Zn, or Cu and Sn. In the case of stannite and PMCA there is alternation of a plane containing Cu with other containing Zn and Sn. In the stannite structure the atoms Zn and Sn change their positions from layer to layer, which does not happen in the PMCA one, allowing the distinction between these two structures [218]. It is widely accepted that kesterite is the most stable phase of the CZTS or CSTSe, presenting a lower formation energy compared to the stannite and PMCA phases. This is compatible with the knowledge regarding the ternary alloy I-III-VI_2, for which the formation energy is lower for chalcopyrite phase in comparison to the CuAu-like (see Section 3.5.1). As the substitution of the cations in the transition from chalcopyrite to kesterite is done between neighbour (III→II and IV), the size of the atoms does not differ much. Hence, the formation energies of these two phases are close and smaller than the CuAu-like and its derivatives, stannite and PMCA. However, the formation energies difference among kesterite and stannite is small, between 3-5 meV/atom, which indicates that these two phases may coexist [154, 156, 218]. These differences increase for the pure selenide compound [154].

Neutron diffraction measurements performed by Schorr *et al.* showed the existence of a partially disordered kesterite phase [219-223]. The planes containing Cu and Zn present disorder in the position of the atoms, while in the ones containing Cu and Sn, the atoms remain in the original site. Note that this randomly arrangement between Cu and Zn in the kesterite structure has a higher energy than the other phases presented here, since it does not respect the octet rule [154]. However, as Cu and Zn are adjacent elements in the periodic table, they have similar mass and atomic radius. Thus, they may swap position with low enthalpic cost (9.1 meV/atom) in comparison to the 77.8 meV required for Cu and Sn change sites [154]. The lattice sites in the Cu/Zn planes have an equal probability of being occupied by Cu or Zn, which means that the partially disordered kesterite structure has the

same space group as the stannite structure, $I\bar{4}2m$.

Table 3.4 shows CZTS and CZTSe lattice parameters a and c, and tetragonal distortion parameter η calculated theoretically and obtained experimentally for kesterite and stannite structures. The calculated parameters for both kesterite and stannite structures are in good agreement with experimental values. Note that the lattice parameters calculated for the PMCA structure do not respect the $c \approx a$ discussed earlier in this section. The lattice parameters a and c are slightly smallers on pure sulfide CZTS than in CZTSe, regardless the crystal structure. Nevertheless, for kesterite crystal structure of both CZTS and CZTSe, the tetragonal distortion parameter is slightly smaller than for the other two structures. As discussed for CIGS case, $\eta \neq 1$ has influence in the electronic structure, leading to a split of the crystalline field and, consequently, to a non-degenerate maximum at the top of the valence band. The signal of the crystalline field is important for the symmetry of the top of the valence band, which is reflected in the effective holes masses [14].

Table 3.4: Lattice parameters a and c, and tetragonal distortion parameter η for CZTS and CZTSe. T and E stands for theoretical and experimental studies, respectively.

	Kesterite			Stannite			PMCA			
	a (Å)	c (Å)	η	a (Å)	c (Å)	η	a (Å)	c (Å)	η	Ref.
CZTS	5.467	-	0.999	5.458	-	1.004	5.459	-	1.005	T [154]
	5.466	10.929	1.000	5.460	10.976	1.005	5.478	10.942	0.999	T [224]
	5.424	10.861	1.001	-	-	-	-	-	-	E [225]
CZTSe	5.763	-	0.998	5.762	-	1.000	5.753	-	1.004	T [154]
	5.68	11.36	1.001	-	-	-	-	-	-	E [226]
	-	-	-	5.776	11.677	1.011	-	-	-	E [227]

3.6.2 Electronic properties

The CZTSSe electronic band structure calculations reveal a direct bandgap type structure [14]. Through the analysis of Table 3.5 it is possible to verify that Density Functional Theory (DFT), Local Density Approximation (LDA), Generalized Gradient Approximation (GGA), and Perdew-Burke-Ernzerhof (PBE) theoretical approaches were inefficient to estimate the bandgap energy of CZTSSe, presenting values much lower than those obtained experimentally [228, 229]. However, methods such as Heyd-Scuseria-Ernzerhof Hybrid Functional (HSE) and others that derive from this, point to a bandgap energy values close to 1.5 eV for CZTS and 1.0 eV for CZTSe, which are in agreement with experimental results [14, 230-233].

The E_g of CZTSSe, can be calculated by the empirical expression [234, 235, 236],

$$E_g = xE_g(\text{CZTS}) + (x-1)E_g(\text{CZTSe}) - bx(1-x) \tag{3.2}$$

where x is the [S]/([S]+[Se]) ratio, E_g(CZTS)= 1.5 eV is the bandgap of pure sulfide CZTS, E_g(CZTSe)= 0.96 eV the one of pure selenide CZTSe, and b is the bowing factor, which has been reported to be from -0.19 to 0.1 eV. The possibility of engineering the bandgap energy of the compound by adjusting the chalcogens concentration, is an important feature for the fabrication of solar cells based on kesterites. It is worth to note, that the best performance in thin film solar cell based on kesterite have been obtained for CZTSSe. Moreover, and following CIGS technology, bandgap grading may bring further enhancement to kesterite devices, as already shown by Yang *et al.* that obtained a bandgap-graded CZTSSe solar cell with 12.3% of efficiency [42].

Table 3.5: CZTS and CZTSe bandgap energy (E_g) obtained from theoretical calculations and experimental measurements.

		Kesterite	Stannite	PMCA	
	Method	E_g(eV)	E_g(eV)	E_g(eV)	Study
CZTS	HSE06 (GGA)	1.50 (0.09)	1.38 (-0.3)	1.35 (-0.06)	[154]
	HSE (PBE)	1.487 (0.096)	1.295 (-0.03)	-	[224]
	HSE (LDA)	1.52 (0.09)	1.27 (-0.11)	-	[228]
	(GGA+U) (scGW)	(0.86) (1.64)	(0.63) (1.33)	-	[228]
	HSE (PBE) (GW)	1.39 (0.28) (1.57)	1.26 (0.17) (1.40)	-	[237]
	Experimental	1.45-1.6	-	-	[14, 230, 231]
	Experimental	-	1.46-1.51	-	[232, 233]
CZTSe	HSE06 (GGA)	0.96 (-0.3)	0.82 (-0.44)	0.79 (-0.47)	[154]
	HSE	0.94	0.75	-	[228]
	Experimental	1.0-1.08	0.75	-	[28, 238]

The magnitude of the CZTSSe bandgap can be understood according to the chemical nature of the states of the conduction and valence bands. The predominant orbital character of each band is indicated in Fig. 3.13 a). From Fig. 3.13 a) it can be observed that the conduction band minimum results from the hybridization of the s states of the Sn cation and p sates of the anion S(Se), which is due to the lower s orbital energy of Sn than that of the other cations. Regarding the valence band, see Fig. 3.13 b), it splits at the Γ point, as a result of the crystalline field and the spin-orbit interaction [14, 154]. The top of the valence band results essentially from the contribution of the d and p orbitals of Cu and S(Se), respectively, similarly to CIS and CGS. Theoretical calculations show that

the influence of Zn on the edge of the two bands is small [14, 154, 224]. Although small variations in the lattice parameters a and c have negligible effects on the bandgap, there is a large variation of the bandgap with the variation of the anion position, as shown in Fig 3.13 c). This variation is similar for both, top and the bottom of the valence and conduction bands, respectively [228, 229]. The dependence between the position of the anions and the bandgap energy is essentially related to the fact that the displacement of the anions is directly dependent on the bond between Cu and S which, as already mentioned, influence the electronic properties of the top of the valence band, while the anion S also has influence on the minimum of the conduction band [229, 239].

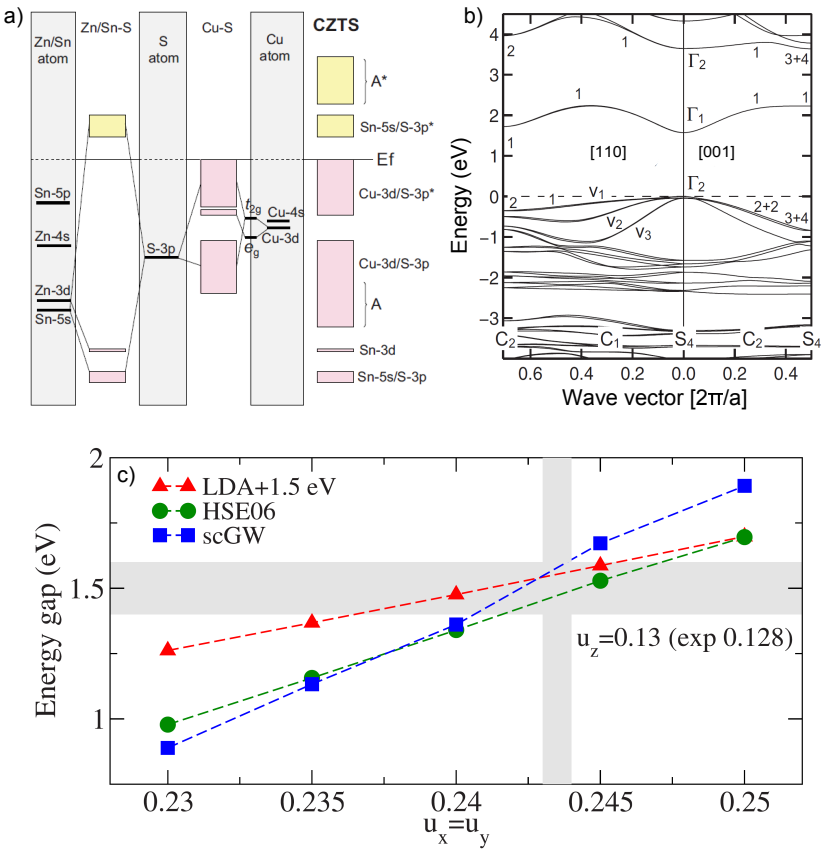

Figure 3.13: a) Molecular interaction diagram illustrating the energy levels of an electron (gray zone on the left side) and CZTS structure (right side) [224]. b) Electronic band structure of kesterite structures of CZTS along the two symmetry directions [110] and [001]. Adapted from [14]. c) Dependence of the bandgap energy on the anion displacement $u_x = u_y$ for kesterite CZTS, calculated by DFT-LDA (△), HSE06 (○), and scGW (□). DFT-LDA values are upshifted by 1.5 eV. Adapted from [228].

The effective masses, for kesterite and stannite structures, are found in the Table 3.6. It is possible to verify that the effective electrons masses for the lowest conduction band is approximately isotropic, whereas the effective holes masses for the topmost valence band presents a significant anisotropy [14].

The effective masses of electrons are lower than the ones for holes, which is determinant in the allowed radiative transitions observed for these materials (Section 4.2.4).

At this point an overview of structural and electronic properties of CZTSSe were presented. Following the context of the presented work in this thesis, from now on a main attention will be given to the pure sulfide CZTS.

Table 3.6: The Γ-point effective masses for electrons($m_{c_1}^{\perp}$, $m_{c_1}^{\parallel}$) and for holes ($m_{v_i}^{\perp}$, $m_{v_i}^{\parallel}$ $i = 1, 2, 3$), where v_1 is the topmost valence band, for CZTS and CZTSe with kesterite and stannite structures, for directions parallel and perpendicular to the c-axis [14].

	$m_{c1}^{\parallel}(m_0)$	$m_{c1}^{\perp}(m_0)$	$m_{v1}^{\parallel}(m_0)$	$m_{v1}^{\perp}(m_0)$	$m_{v2}^{\parallel}(m_0)$	$m_{v2}^{\perp}(m_0)$	$m_{v3}^{\parallel}(m_0)$	$m_{v3}^{\perp}(m_0)$
CZTS Kesterite	0.20	0.18	0.22	0.71	0.52	0.35	0.76	0.26
CZTS Stannite	0.18	0.17	0.84	0.33	0.88	0.27	0.17	0.73
CZTSe Kesterite	0.08	0.08	0.09	0.33	0.50	0.09	0.28	0.24
CZTSe Stannite	0.06	0.06	0.66	0.09	0.09	0.15	0.15	0.29

3.6.3 Phase Diagram

CZTS is a quaternary compound, then the growth of a single phase is unlikely, since there are several secondary phases, involving the different atomic elements, that frequently appear. Additionally, the CZTS chemically stable region is much narrower than the CIGS one discussed previously. For typical growth temperatures, a deviation of only 1-2% is allowed for CZTS single phase, whereas for CIGS the value rises up to 4% [240-244].

From the isothermal section of the Cu_2S-SnS_2-ZnS system at 670 K shown in Fig. 3.14, it is possible to note that a small deviation from the chemically stable region (region label as 1) is enough to form other phases beyond the CZT one, such as Cu_2S, ZnS, SnS_2, Cu_4SnS_4, and Cu_2SnS_3 (CTS). The ZnS and CTS phases are nearly always present in CZTS stoichiometric based samples, due to the only small amount of 0.1 eV required to separate the stoichiometric CZTS into these secondary phases [235, 245]. As shown in Table 3.7 these two latter mentioned secondary phases in addition to the Cu_2S one, have similar lattice parameters to the ones of the CZTS (see Tab. 3.4), which makes difficult an accurate identification of these phases by X-ray diffraction. Secondary phases with lower bandgap than CZTS (Cu_2S, SnS, Cu_4SnS_4, and CTS) may be detrimental for the V_{OC} of the device, while secondary phases with higher bandgap (ZnS, SnS_2) may contribute to current losses.

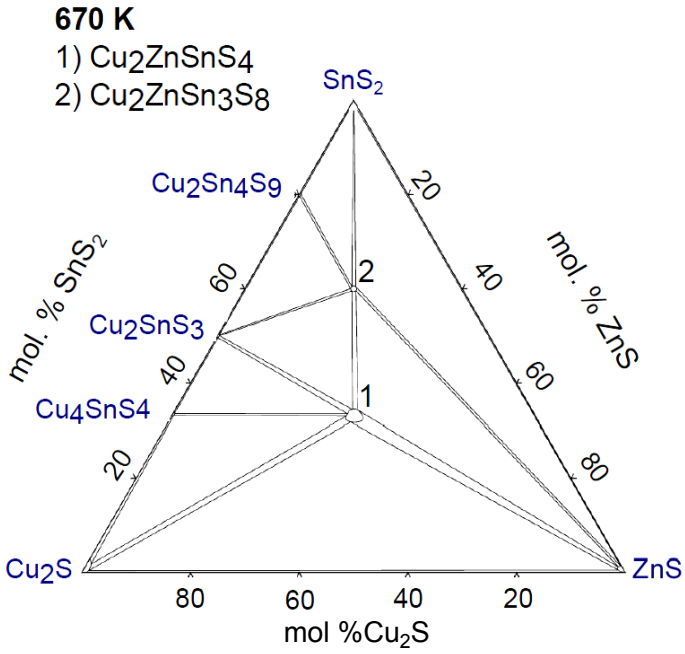

Figure 3.14: Isothermal section of the $Cu_2S - SnS_2 - ZnS$ system at 670 K [246].

In order to enhance CZTS based solar cell performance, Chen *et al.* proposed to grow the CZTS layer under Cu-poor and Zn-rich [243]. In fact, the CZTS absorber layer from state-of-art solar cells is always grown far from the stoichiometric region: $[Cu]/([Zn]+[Sn]) \sim 0.7\text{-}0.9$ and $[Zn]/[Sn] \sim 1.0\text{-}1.3$ [247]. The size of this range is surprising large, considering the narrow range to obtain CZTS single phase. Therefore, ZnS is often detected even in CZTS based state-of-art devices, due to Zn-rich required composition. However, single phase off-stoichiometric CZTS for Cu-rich/Zn-poor composition have been successfully obtained [248].

Table 3.7: Bandgap energy values E_g and lattice parameters a and c for CuS, Cu_2S, SnS, SnS_2, ZnS, Cu_4SnS_4, and CTS.

Secondary phase	Structure	E_g (eV)	a (Å)	c (Å)	Ref.
Cu_2S	Tetragonal	1.04(2)	4.0022(3)	11.276(1)	[249]
SnS	Tetragonal	1.07	3.98	11.18	[250]
SnS_2	Tetragonal	2.22-2.88	3.6297	5.9402	[251, 252, 253]
ZnS	Cubic	3.7	5.403	-	[163]
Cu_4SnS_4	Orthorhombic	1.2	6.416(2)	13.566(2)	[254, 255]
CTS	Tetragonal	0.96-1.35	5.413	10.824	[256, 257, 258]
CTS	Cubic	1.15	5.43	-	[258, 259]

3.6.4 Native point defects

Native point defects and even defect clusters are extremely important in solar cells, they determine at great extent the device performance. As discussed in Subsection 3.5.4, being CZTS a quaternary alloy there are many possible of native point defects, such as vacancies, atoms in exchanged positions and atoms in interstitial positions.

Table 3.8 shows the formation energies for CZTS intrinsic defects, obtained by theoretical calculations for a region of stable Cu-poor CZTS. The defects formation energy will depend on the composition of the CZTS, and also on the Fermi energy level. For charged acceptors, the formation energy decreases when the Fermi level shift from the valence band to the conduction one, whereas the same energy for charged donors decreases with the shift of the Fermi level from the conduction band to the valence band [242]. The donor defects have a higher formation energy than the acceptors, which is consistent with the experimental results in that the CZTS samples exhibit intrinsic p-type conductivity [260].

Table 3.8: Formation energies of intrinsic point defects in CZTS. The values presented are the lowest within the region of stable Cu-poor CZTS. Data from [242].

	Vacancies				Interstitials			Antisites					
	V_{Cu}	V_{Zn}	V_{Sn}	V_S	Cu_i	Zn_i	Sn_i	Cu_{Zn}	Cu_{Sn}	Zn_{Cu}	Zn_{Sn}	Sn_{Cu}	Sn_{Zn}
	A	A	A	-	D	D	D	A	A	D	A	D	D
Energy (eV)	0.21	0.39	1.77	1.09	3.23	6.02	8.22	-0.16	0.85	2.43	0.36	6.54	4.11

According to the theoretical studies carried out so far, the defect with the lowest formation energy in CZTS corresponds to the occupation of the Zn position by Cu (Cu_{Zn}) [242, 243, 261, 262]. Due to the lower formation energy of the Cu_{Zn}, the p-type conductivity presented by CZTS is attributed to this defect. However, this defect is located at 150 meV of the valence band (see Fig. 3.15), which makes it an acceptor not as shallow as desirable. In fact, this situation may be detrimental to applications in solar cells, as it will reduce the mobility of the charge carriers. Note that the Cu vacancy (V_{Cu}) located at 30 meV from the top of the valence band, which is the defect that determines the conductivity in CIGS, is easily formed in Cu-poor and Zn-rich compositions [262]. Following the discussion of the former Section the ideal elemental ratios of: [Cu]/([Zn]+[Sn]) $\sim$ 0.7-0.9 and [Zn]/[Sn] $\sim$ 1.0-1.3 favours the formation of V_{Cu} and suppresses the Cu_{Zn} and the very harmful antisite acceptor Cu_{Sn} [242, 243, 261, 263].

From the point of view of deep defects under Cu-poor and Zn-rich conditions, the most likely candidates could be the acceptors Zn_{Sn} and V_{Sn}, and the donors V_S, Zn_i, and Sn_{Cu}.

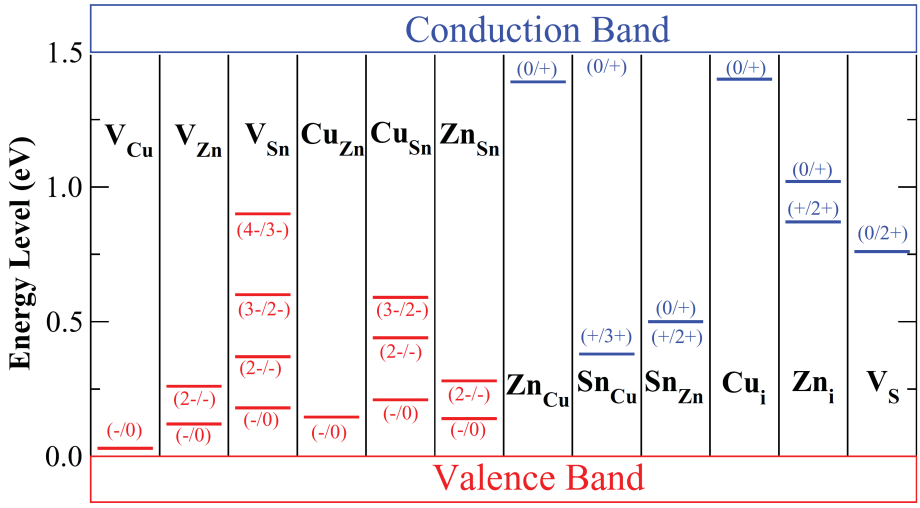

Figure 3.15: Ionization levels of CZTS intrinsic defects in the bandgap. The red bars show the acceptor levels and the blue ones the donor levels, with the initial and final charge states labelled in parentheses. From [263].

The role of electrically neutral complex defects is important, since they have extremely low formation energies and electronically passivate the deep levels in the bandgap energy. For example, the formation of the $[V_{Cu}^{-} + Zn_{Cu}^{+}]$ pair in Cu-poor and Zn-rich conditions should be beneficial for the the solar cells performance [242, 243].

3.6.5 X-ray diffraction in CZTS

CZTS contains atomic elements that are electronically similar, Cu and Zn. They are neighbour in the periodic table, both Cu^{+} and Zn^{2+} cations have 28 electrons each, resulting in an identical scattering factor, which is proportional to the measured intensity of the X-ray diffractogram. This makes it difficult to identify crystalline phases involving these elements by X-ray diffraction (XRD) [156, 221]. As presented in Section 3.6.1, kesterite, stannite, PMCA, and the partially disorder kesterite structures differ exactly and only in the Cu and Zn order. From Fig. 3.16 a) it is possible to see that it is not straightforward the identification of the different CZTS structures using only an XRD diffractogram. However, there are two diffraction peaks at $2\theta \simeq 69.07^{o}$ and $2\theta \simeq 69.26^{o}$ (identified by arrows) that allow the identification of the kesterite and the stannite phases, since the relative intensities of these diffraction peaks appear reversed from a phase in comparison to the other. The polycrystalline nature of the CZTS samples hinders the identification of these two diffraction peaks.

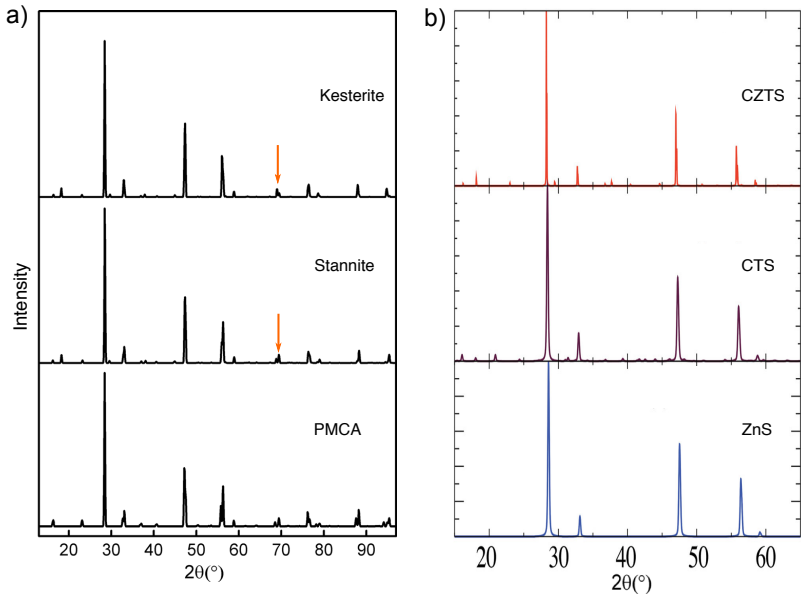

Figure 3.16: Simulated X-ray diffractograms a) CZTS kesterite, stannite, and PMCA and b) kesterite CZTS, CTS, and ZnS. a) and b) adapted from [218] and [235], respectively.

As discussed previously in Subsection 3.6.3, CZTS, ZnS, CTS, and Cu_2S have very similar structures and lattice parameters (see Table 3.7). Thus, most of CZTS reflections occur in the same angular position as the reflections of the above mentioned phases. This issue is a clear difficulty for CZTS structural characterization and it is shown by Fig. 3.16 b). However, there are XRD peaks that would at least show unambiguously the presence of CZTS, even though the existence of ZnS, CTS, and Cu_2S would be ruled out [264]. There are other secondary phases like, SnS, SnS and Cu_4SnS_4, that may be formed during the growth of CZTS, but since they have quite different structures and lattice parameters their reflections are resolved from the CZTS ones.

Neutron diffraction allows to distinguish the different crystalline phases of CZTS and secondary phases. However, it is an expensive and not easily available characterization technique. In the following Section, Raman spectroscopy will be introduced as complementary technique to XRD for an accurate identification of CZTS and secondary phases present in the samples.

3.6.6 Raman in CZTS

It has been already shown that Raman spectroscopy is a sensitive technique in the identification and distinction of secondary phases that potentially arise during the growth of CZTS thin films [27, 245, 260, 265]. For this reason, Raman spectroscopy is used to complement the structural analysis made by XRD.

Raman scattering probes mainly the optical phonon modes at the Γ point of the first Brillouin zone. Thus, the analysis of the vibrational modes observed in Raman, it must be take into account that CZTS has eight atoms per unit cell, so group theory predicts twenty four modes. Three of these

modes are acoustic and zero at the center of the Brillouin zone, and the remaining ones are optical. It is possible from the literature to obtain the irreducible representation of the optical vibrational modes of the three CZTS structures, obtained from the crystal symmetry and group theory [218, 266, 267]:

$$\text{Kesterite}: \quad \Gamma = 3A + 6B + 6E_1 + 6E_2 \tag{3.3}$$

where 15 of the 21 modes are Raman active, and 12 of modes B, E_1, and E_2 are also infrared (IR) active;

$$\text{Stannite}: \quad \Gamma = 2A_1 + A_2 + 2B_1 + 4B_2 + 6E \tag{3.4}$$

where 14 of the modes A_1, B_1, B_2, and E are Raman active and 10 of B_2 and E are simultaneously IR active;

$$\text{PMCA}: \quad \Gamma = 2A_1 + 2A_2 + B_1 + 4B_2 + 6E \tag{3.5}$$

where 13 of the modes A_1, B_1, B_2, and E are Raman active and 10 of the B_2 and E modes are also IR active.

The first-order spectrum of the CZTS presented in Fig. 3.17 shows the characteristic vibrational modes associated with optical phonons: 251-252 cm^{-1}, 287-289 cm^{-1}, 336-33 cm^{-1}, 349-354 cm^{-1}, and 368-374 cm^{-1}, the last two vibrational modes occur only under certain conditions that are not yet clear [27, 218, 245, 260, 266, 267, 268]. According to the study presented in [218], phonons in the frequency range 50-160 cm^{-1} correspond mainly to the vibration of the three metal cations (Cu, Zn, Sn) with a small contribution of the S anion. In the range of 250-300 cm^{-1}, the phonons involve in the vibration of Zn and S with a contribution of the Cu cation. For frequencies between 310-340 cm^{-1}, the phonons come essentially from the vibration of the S anions. Finally, in the frequency range between 340-370 cm^{-1}, the vibrations of Sn and S are observed. As it can be seen from Fig. 3.17 the two most intense vibrational modes observed experimentally in CZTS Raman spectrum are located at 338 cm^{-1} and 287 cm^{-1} [269, 260]. The frequencies of the Raman vibrational modes observed in CZTS, are summarized in Table 3.9.

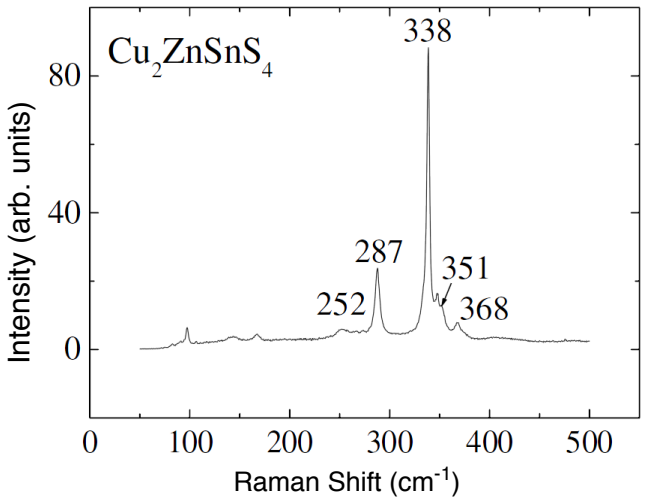

Figure 3.17: Raman Spectrum of CZTS at room temperature using the 532 nm line of a solid state laser [260].

Next, the Raman vibrational modes for the most common secondary phases that may be formed during CZTS growth are presented. ZnS can be identified by a vibrational mode at 352 cm^{-1} and another less intense mode at 275 cm^{-1}. The tetragonal CTS has a shoulder between 280 and 290 cm^{-1}, which appears associated with the vibrational mode at 297 cm^{-1}. This phase presents also two more vibrational modes at 336-337 cm^{-1} and 351-352 cm^{-1} [27, 257]. The cubic phase of the CTS has three vibrational modes easily identifiable at 267 cm^{-1}, 303 cm^{-1}, and 355-356 cm^{-1} [27, 257]. SnS has three associated vibrational modes, at 160-163 cm^{-1}, 189-190 cm^{-1}, and 219-220 cm^{-1}, while SnS_2 has an intense vibrational mode at 312-315 cm^{-1} and another with low intensity, being only detectable in samples of high quality, at 215 cm^{-1} [27, 245]. $Cu_{2-x}S$ compounds have a very intense vibrational mode at 475 cm^{-1} and a less intense at 264 cm^{-1} [27, 257].

Table 3.9: Experimental and calculated Raman frequencies for CZTS kesterite and (stannite) structure.

Symmetry	Experimental (cm^{-1})				Theoretical (cm^{-1})
	[27]	[260]	[270]	[271]	[218]
E/B			97	98	98.82; 98.83 (95.85; 95.86)
E/B			143	142	
E/B			166	168	166.65; 168.21 (161.68; 162.63)
E/B		252	252	252	250.26; 257.85
$A(A_1)$	287	287	287	288	284.30 (277.12)
$A(A_1)$	338	338	337	338.6	340.04 (334.08)
E/B		351	347	347	351.55; 366.35 (346.01; 364.87)
E/B	367			365	(360.12; 370.63)
E/B	375	368			355.80; 374.05 (360.12; 370.63)

3.6.7 CZTS Growth

CZTS has been fabricated by several methods, under both vacuum and non-vacuum conditions. Non-vacuum includes electrodeposition [272], nanocrystal dispersion [273], hydrazine-based deposition [10], among others. The current champion kesterite solar cell was fabricated using the hydrazine-based solution method [10]. However, hydrazine is both highly toxic and reactive, which limits the application of this growth method in a large-scale photovoltaics industry [274]. Regarding vacuum approaches to growth CZTS include: direct current (DC) and (radio frequency) RF magnetron sputtering [152], thermal evaporation [59], pulsed laser deposition [275], among others. Regardless, the used method, a Cu-poor and Zn-rich composition is required for a CZTS based solar cell with good performance. However, the complex phase diagram, and the Sn volatility upon heating, makes compositional control a challenge that must be overcome [60, 243, 276]. Contrary to the CIGS case,

where only two families of growth methods dominate the used techniques, CZTS clearly suffers from a dominant method. This hinders the progress of the growth knowledge as each group focus on a very specific technique.

From the aforementioned methods, the sputtering approach is a very promising method for CZTS fabrication, due to the electrical performances achieved so far (10.04% [8]), and the fast heating rates and short sulphurization times achieved with the replacement of the traditional furnaces by a rapid thermal processing (RTP) furnace. Next, we will focus on this growth method, since the studied CZTS based samples were fabricated following the two steps process, sulphurization of evaporated/sputtered multi-stacked precursors [60, 274].

Sulphurization of multi-stacked metallic precursors

Sulphurization of multi-stacked metallic precursors involves two steps: the sputtering of precursors, in which Cu, Zn, and Sn are deposited as multi-stacked metallic precursors on a Mo-coated SLG substrate, followed by a sulphurisation annealing (∼500-600 °C), in which S is added and the CZTS is formed from the metallic precursors [274]. There are two common approaches to perform the sulphurization step and the difference between them stands on the S source: i) by a elemental vapour or a hybrid gases (e.g. sulphurization in S flux), and ii) by a solid piece (e.g. graphite box) [277]. For the case of annealing/reactive annealing, the S is provided as elemental S vapour and/or hybrid gases, namely hydrogen sulphide (H_2S) might be used [225, 277-280]. The hybrid gases are toxic, which in addition to the use of the CdS buffer layers make the CZTS based technology label as "non-toxic", questionable. However, H_2S is widely used, because it is highly reactive and easy to control precisely. The main alternative is to anneal the metallic precursor with solid S, either by depositing a solid layer of S or by placing solid S in the reaction chamber, or even both approaches using the RTP process.

The composition, order, and thickness of the multi-stacked metallic precursors and the sulphurization time, temperature, pressure, and source of S, have a significant impact on properties on the CZTS film. The optimisation of both steps should lead to a CZTS thin film with higher quality [277, 281, 282, 283].

3.7 In Summary

In this Chapter we overviewed the conventional architecture of the studied devices and the fundamental properties of the two studied materials, we are able to additionally look to the barriers that each technology still has to overcome to reach or settle on the photovoltaic industry. The architecture, SLG/Mo/(CIGS or CZTSSe)/CdS/i-ZnO/ZnO:Al is conventionally used in CIGS and CZTS state-of-art solar cells. Although some inherent issues and the effort to adopt a Cd-free buffer layer, this one remains the main choice in both technologies. However, there are serious doubts about the suitableness of the inherited Mo and CdS layers from CIGS to the CZTS based technology.

From a fundamental point of view, CIGS and CZTS both have direct bandgap and a related structure that may be derived from the ZB. However, several fundamental differences may be the reason of the CZTS lag to the CIGS technology: i) CZTS contains always some degree of structural disorder that do not exist in CIGS, ii) contrary to CIGS that is a pseudo-ternary compound, CZTS is a quaternary compound with a narrower phase stability region than the CIGS one, which favours the appearance of secondary phases and greatly increase the density of defects in the CZTS in comparison to CIGS, iii) the p-type conductivity in CIGS and CZTS, is mainly ascribed to the low formation energy of the acceptors V_{Cu} and Cu_{Zn}, respectively. The V_{Cu} is a shallower acceptor than the Cu_{Zn}, being less detrimental to the solar cell performance. Furthermore, the above enumerated properties may contribute to the appearance of tails states in the bandgap of both materials, which may influence the dynamic of the charge carriers that at great extent dictates the principle of operation of the solar cell. The impact of the presence of the tails states in the electronic energy levels structure will be matter of discussion in the next Chapter.

Chapter 4

Influence of fluctuating potentials on chalcogenides

A review of several fluctuating potentials models based on different sources of disorder is provided. Experimental evidences for different types of fluctuating potentials, and estimation of the average potential wells/tails states amplitude from absorption coefficient and photoluminescence measurements in chalcogenides solar cells, are discussed.

As shown in several works and discussed in Chapter 3, the efficiency of CIGS or CZTSSe based solar cells is higher for Cu-poor thin films [35, 51, 243, 284-288]. Additionally, for the above semiconductors, due to the presence of 4 or 5 distinct atomic elements, a large diversity of native point defects exists, as well as fluctuations in the composition [101, 173, 175]. As a consequence, these materials are typically highly doped and compensated, and it is expect that their optoelectronic properties may be influenced by the presence of fluctuating potentials, namely electrostatic and bandgap ones, resulting from electronic and structural inhomogeneities, respectively.

Further improvements of solar cells performance depend on understanding its limiting factors and the fundamental physical properties of the absorber layers, namely, the electronic energy levels structure and dynamics of the charge carriers [20, 65, 101]. The investigation of fluctuating potentials is presently an open issue in the scientific community, which justifies its study from theoretical and experimental point of views [223, 289, 290, 291].

4.1 Fluctuating Potentials

In electronic band theory, a well defined conduction and valence band edges requires a periodic potential, which results from a perfect spatial order, i.e. a regularly spaced atoms in the lattice. When this periodicity is perturbed, the previous electronic description changes. A continuous deviation from

the ideal periodic potential may promote the appearance of localized states in the bandgap. At high densities, of a particular defect that creates sufficiently deep states, the interaction between them results in the formation of a band, a so called impurity band. In addition, other effects may cause the perturbation of the bands by the formation of tails states, which smear the conduction and valence bands edges into the bandgap. This results in an obvious bandgap shrinkage [16, 292, 293]. The impact of the deviation from the periodic potential in electronic energy levels structure is well illustrated in Fig. 4.1, through the increase of an acceptor density in an initially periodic lattice. However, the perturbation of the periodic potential may have different origins. Next we will present, the ones which have a higher influence in the CIGS and CZTSSe electronic energy levels structure [223, 289, 290, 291].

Considering a perfect single crystal with regularly spaced atoms in the lattice, the thermal energy will induce the atoms to vibrate randomly over their equilibrium positions. This vibration will cause a random fluctuation in the distance between these atoms, which slightly disrupt the periodicity of the lattice. This atomic vibration is present in all semiconductors and is named thermal disorder. For undoped crystalline materials, the only disorder that is present at room temperature is the thermal one. The tails states with origin in thermal disorder results from a purely random effect [292, 294].

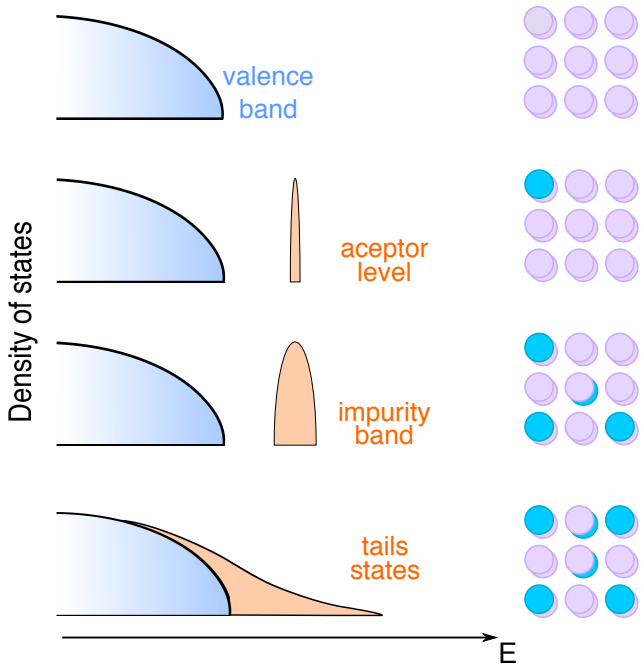

Figure 4.1: Conceptual illustration of a periodic lattice disrupted by the introduction of an acceptor defect, that create an energy level within the bandgap close to the top of the valence band. A progressive increase of the acceptor density causes a broadening of the discrete energy level to an impurity band that progressively merges with the top of the valence band. Adapted from [295].

In semiconductors, a deviation from stoichiometry generates point defects. In this case, not only is the periodic order of the atoms disrupted, but also the ideal chemical bonding between atoms is broken, both will change the optoelectronic properties of the material. Considering, a high density of randomly

charged defects, i.e. a strong perturbation on the potential, an ionized donor will exert an attractive force on the conduction electrons and a repulsive force on the valence holes. Since the charged defects are randomly distributed in the lattice, the local interaction will depend on the local density of charged defects. Fig. 4.2 a) shows the perturbation of the band edges by Coulomb interaction with randomly distributed charged defects, i.e. electrostatic fluctuating potentials. The bandgap energy remains constant along the semiconductor and the conduction and valence bands follow the same electrostatic potential caused by the charged defects. At high enough concentration of a particular type of defects that induce sufficient deep localized states in the bandgap, these states form an impurity band which follows the electrostatic fluctuating potentials (dashed line in Fig. 4.2 a)) [296, 297].

Spatial fluctuation in the composition of the material will cause local changes in the bandgap, the so called bandgap fluctuating potentials. Fig. 4.2 b) illustrates the case of bandgap fluctuations, where the tails states are inversely correlated for the conduction and valence bands. This is an important difference between electrostatic and bandgap fluctuating potentials [175, 298]. Note that both electrostatic and bandgap fluctuating potentials may coexist, which is the expected scenario in the materials studied in this thesis.

Finally, structural disorder[1] as a source of perturbation of the periodic potential, may also be observed. Let us take in consideration CZTSSe, which is the studied material that presents this type of disorder. As discussed previously, for kesterite structure the planes at $z = \frac{1}{4}$ and $\frac{3}{4}$ contains only Cu and Zn atoms. Cu/Zn disorder arises, because of the low enthalpic cost of atomic exchange between Cu and Zn within these planes, while the rest of the lattice is undisturbed [222, 299, 300].

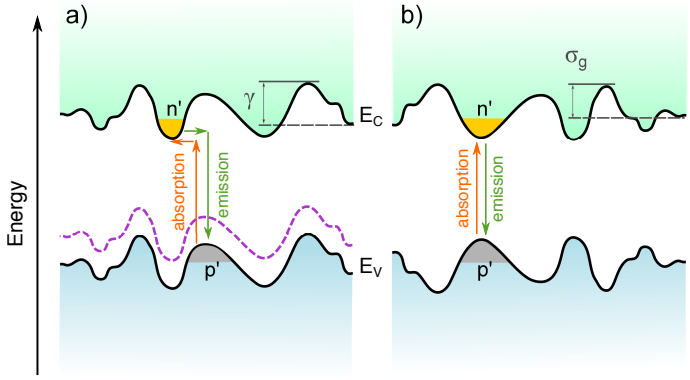

Figure 4.2: Illustration of a) electrostatic and b) bandgap fluctuating potentials. In a) the dashed line illustrates an acceptor impurity band. γ represents the root-mean-square amplitude of the characteristic potential well and σ_g the standard deviation from the mean value of $E_{g,mean}$. n' and p' stands for minority and majority charge carriers, respectively. Adapted from [298].

[1]Structural disorder, is a particular case of a high density of a native point defects, that is well known to occur in the studied kesterite materials. However, it is widely treated in the literature as a different problem from native point defects. Thus, we present the structural disorder as an additional perturbation to the period potential.

4.1.1 Electrostatic Fluctuating Potentials

It has been demonstrated that Cu-poor chalcopyrites and kesterites are highly doped and strongly compensated, resulting from a high density of charged defects and a low free carrier concentration [298, 301-306]. Next section is focused on the relation between charged defects and fluctuating potentials in highly doped and strongly compensated semiconductors, in order to better understand the electronic energy levels structure of these materials.

Highly doped and compensated semiconductors

Let us start by addressing the highly doped condition as well as the degree of compensation. The material is called highly doped if there is an overlap between electronic states belonging to different defects. In the case of acceptors, the highly doped condition is $N_{\mathrm{a}}a_h^3 >> 1$, being N_{a} the concentration of acceptors and a_h the Bohr radius of the acceptor state. Due to the considerably lower effective mass of electrons compared to that of holes (see Tables 3.3 and 3.6, for CIS and CZTS, respectively), in the case of CIS, the heavy doping condition for acceptors is obtained for a concentration that could be more than one order of magnitude higher than for donors. This difference is lower in the case of CZTS [48, 307, 308].

The degree of compensation, which depends on the relative density of donors and acceptors, in a p-type semiconductor is defined as $\mathrm{K} = \mathrm{N_d}/\mathrm{N_a}$, being $\mathrm{N_d}$ the concentration of donors. A strongly compensated semiconductor ($\mathrm{K} \approx 1$) has properties that are significantly different from a weakly compensated one. At sufficiently low temperatures, all N_d are positively charged ($\mathrm{N_d^+}$), because they lose electrons to acceptors ($\mathrm{N_d^+} = \mathrm{N_a^-}$), which become negatively charged after accepting electrons. This results in a high concentration of charged defects N in the semiconductor, $\mathrm{N} = \mathrm{N_d^+} + \mathrm{N_a^-}$. The remaining concentration of acceptors $\mathrm{N_a^{'}}$ ($\mathrm{N_a^{'}} = \mathrm{N_a}$ - $\mathrm{N_d}$) have a neutral charge, which will become charged with the increase of temperature [48, 297, 307].

The random distribution of charged defects leads to a random electrostatic fluctuating potential that will strongly affect the electronic states with energy $|E_i - h\nu| < \gamma$ for $i = C, V$ being

$$\gamma(r_0) = 2\sqrt{\pi}\frac{e^2}{4\pi\epsilon_0\epsilon_r\, r_0}\sqrt{N\, r_0^3}, \tag{4.1}$$

the root-mean-square amplitude of the characteristic potential well [309], and r_0 the screening length [48, 297, 307], given by

$$r_0 = \frac{1}{2}a_0\left(\frac{\pi}{3}\right)^{\frac{1}{6}}(pa_0^3)^{-\frac{1}{6}}. \tag{4.2}$$

It is clear that the compensation reduces the density of the free holes p in a p-type highly doped material. In fact, according to Eq. 4.2, the increase on the compensation will induce an increase in the magnitude of r_0, and consequently, of γ.

Let us assume a potential well of charged defects randomly distributed according to Poisson statistics, with a characteristic spatial dimension of R. The mean number of charged defects in this volume

will be $N\,R^3$ and the standard deviation $\sqrt{NR^3}$. The potential well amplitude is obtained by considering the mean-square fluctuations in the number of defects, $\sqrt{NR^3}$, and is given by

$$\gamma(R) = 2\sqrt{\pi}\frac{e^2}{4\pi\epsilon_0\epsilon_r\,R}\sqrt{N\,R^3}. \tag{4.3}$$

Thus, with the increase of R, the amplitude of the tails raises. However, the redistribution of the free carriers, may be able to cancel completely the defects charge of the larger fluctuations. A fluctuation will be totally screened when in a p-type semiconductor the number of free holes p in the volume R^3 equals the standard deviation of charged defects in the same volume, which leads to $p\,R^3{=}\sqrt{N\,R^3}$. If $p \gg \frac{\sqrt{N\,R^3}}{R^3}$, the free holes become slightly distributed over the crystal and will neutralize the charge of the fluctuations and smooth out their influence completely. If $p \ll \frac{\sqrt{N\,R^3}}{R^3}$, the fluctuations are unscreened. From the above discussion, it is clear that the fluctuations are screened when $R{>}\,r_0$, while those with $R{<}\,r_0$ remain. Thus, the characteristic size of deepest tail states will always be described by $R{\simeq}\,r_0$. For the highly doped and strong compensation conditions, the screening length r_0 is particularly large and, for a p-type semiconductor with ($\mathrm{N_a} > \mathrm{N_d}$), its order of magnitude is

$$r_0 \propto \frac{N^{\frac{1}{3}}}{p^{\frac{2}{3}}} \propto \frac{2^{\frac{2}{3}}N^{-\frac{1}{3}}}{(1-K)^{\frac{2}{3}}}, \tag{4.4}$$

Then, $\gamma(r_0)$ can be rewritten as

$$\gamma(r_0) \propto 2\sqrt{\pi}\frac{e^2}{4\pi\epsilon_0\epsilon_r}\frac{N^{\frac{2}{3}}}{p^{\frac{1}{3}}}. \tag{4.5}$$

Following Fig. 4.3, the tails states with size $R{\simeq}\,r_0$ are responsible for the Gaussian form of the density of states [48, 297, 307]. For shallower tails states with characteristic size of $\mathrm{R} < r_0$, the density of states of the tails states will be described by different power functions as follows, from deeper tails to the continuum, and after the Gaussian form the dependence of the density of states on the energy of the tail states will be described by a 5/4 power law (missing in Fig. 4.3), an exponential (Urbach), or a 1/2 power law (Halperin-Lax). Note that as the value of r_0 decreases (screening effect), R will follows this decrease down to continuum being this progressive decrease of the tails states described by the different density of states functions described above.

The absorption of light for $h\nu < E_g$ occurs only as a result of diagonal transitions, as shown in Fig. 4.2. The probability of this process decreases exponentially with the increase in the spatial dimension of the tails R, and therefore fluctuations governing the shape of the optical absorption spectrum, $\alpha(h\nu)$, have a characteristic size R clearly smaller than r_0. The luminescence intensity $I(h\nu)$ is governed, by the free carrier populations in the ground and excited states. Since these populations decrease on increase in the probability of radiative recombination, fluctuations between R and r_0 will participate in this process, depending on the used excitation power [48, 307]. Thus, it is expected to scrutinize deeper tails with PL than with absorption measurements.

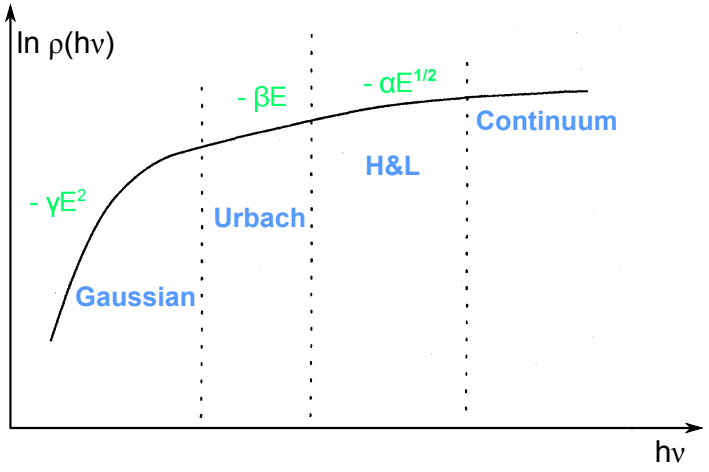

Figure 4.3: Schematic dependence of the density of states ρ on the energy hν, showing four different regions. The continuum and the Gaussian regions are contracted and the Halperin-Lax region expanded relative to the Urbach region [294].

4.2 Detection of fluctuating potentials

In order to discuss the amplitude of the fluctuating potentials several approaches have been proposed in the literature. This Section aims to describe these approaches that may be applied to estimate the amplitude of the fluctuating potentials from absorption coefficient and luminescence measurements.

4.2.1 Sub-bandgap optical spectra

The most direct and perhaps the simplest method to a basic study of the band structure of a semiconductor is to measure the optical absorption spectrum, $\alpha(h\nu)$ [28, 238, 310]. For a perfect crystal at very low temperatures it is expected no absorption below the bandgap energy and, therefore, a steep decay absorption edge should be observed. However, according to Tauc, a characteristic optical absorption spectrum of a real semiconductor may present three distinct absorption regions [311]. Taking into account the optical absorption spectrum, from lower to higher energies, it is observed [311]: i) a weak absorption tail, which originates from defects and impurities; ii) an "exponential" optical absorption edge, which is strongly related with an extension of the density of states into the bandgap; and iii) a high absorption region, which determines the optical bandgap energy. In some approaches this latter region may be seen as two different regions, as discussed in Eq. 2.4, one close to the bandgap energy value and another far above this value.

Now, we will focus on understanding of the origin of the "exponential" region from the absorption spectrum. There has been no consensus or clear physical explanation of a general way to treat

the nearly universal exponential absorption edge (insulators and crystalline or amorphous semiconductors). Different models based on different sources of disorder have been discussed since the first observations of this "exponential" absorption edge [312-316]. The used models in the literature regarding this particular region in CIGS and CZTSSe absorption spectra, will briefly discussed.

The "exponential" absorption edge has been given the name of Urbach tails after the first observation in 1953 by Franz Urbach, in the transmission spectra of different materials like AgBr, AgCl, Ge, TiO_2 and CdS. These "exponential" absorption edge may be empirically described by the Urbach model as follows [317]:

$$\alpha(h\nu) \sim exp\left(\frac{h\nu - E}{E_U}\right), \tag{4.6}$$

where E is a characteristic energy of transition with a value close to the bandgap energy of the material, and E_U is an energy parameter related with the amplitude of the band tails (Urbach energy). According to the literature, it is commonly assumed two contributions for E_U, $E_U = E_T + E_{STD}$, a part arising from the thermal excitation of phonons (E_T) and another from static disorder (E_{STD}). For undoped crystalline semiconductors, $E_{STD} = 0$, and there is a general agreement that the observed exponential absorption edge is a direct measure of temperature induced disorder and reflects the thermal occupancy of phonon states in the crystal. In the case of non-crystalline semiconductors (polycrystalline, amorphous) there is the non-thermal (i.e. static) contribution to the disorder [318].

The Urbach model is unequivocally the most used theory to study the "exponential" absorption edge or proportional physical properties. As discussed earlier, the shape of the sub-bandgap region of the optical absorption is less probable to be governed by the deepest fluctuations. Indeed, it was shown that the "exponential" behaviour is not universal [319], and in the case of the heavily doped semiconductors, the opinions diverge. Actually, John and Cohen stated that the exponential tail may not be observed in highly doped semiconductors, but only on systems with a rapidly decaying short range correlations, as in a-Si [318]. However, it seems that the short range correlation is not a necessary condition for exponential band tails. Lewis *et al.* and Kemp *et al.*, postulating the existence of a dilute concentration of charged defects, claim that the Coulomb interaction leads effectively to an exponential band tail [320, 321]. Nevertheless, other shapes of tails states have been observed and theoretically described. These models assume that the absorption coefficient is proportional to the density of states. Thus, the tails in that density translates into an extension in the absorption spectra up to the bandgap energy.

A general treatment using a semiclassical or the Thomas-Fermi type approximation to determine the density of states of highly doped semiconductors was simultaneously proposed by different authors [312, 315, 316]. Taking advantage of the long range nature of the charged defects potential, it was shown that for a Gaussian distribution of fluctuating potentials, the deep tail states are given by a Gaussian dependence [312]:

$$\alpha(h\nu) \propto exp\left(\frac{h\nu - E}{\sqrt{2}\gamma}\right)^2. \tag{4.7}$$

It should be noted that, at energies very deep in the tail, the approximation of a Gaussian statistic fails [314, 322].

Efros showed that the semiclassical (Eq. 4.7) approximation has a limited region of applicability. In his optimal-fluctuation theory for electrostatic fluctuating potentials with a spatial dimension less than the screening length, $R < r_0$, the absorption coefficient does not exhibit a Gaussian behaviour, but rather a 5/4 power dependence on energy of the argument of the exponential[2] [297, 298, 301],

$$\alpha(h\nu) \propto exp\left(\frac{2}{5\sqrt{\pi}}\left(\frac{h\nu - E_g}{\gamma/2}\right)^{\frac{5}{4}}\right). \tag{4.8}$$

Other intermediate models to the Urbach and Gaussian ones have been proposed. The Franz-Keldysh effect from ionized defects has also been used to explain band tails, which lead to a 3/2 power dependence on energy [316]. In addition, Halperin-Lax used numerical methods to demonstrate that the power dependence on energy of the density of tails states could range between 0.5 and 2, depending on the amplitude of the fluctuating potentials. Sa-yakanit later applied the path-integral approach to derive an analytic expression for the Halperin-Lax model [312-316].

In a more recent work, Katahara and Hillhouse presented a generalized absorption coefficient model. The sub-bandgap absorption includes semiclassical, Franz-Keldysh, optimal-fluctuation, and Urbach models and is given by [315, 316, 323]:

$$\alpha(h\nu) \propto N_c\, exp\left(-\left|\frac{h\nu - E_g}{\gamma}\right|^{\phi}\right), \tag{4.9}$$

where N_c is a normalization constant. The decay of the tail states depends on the exponent ϕ and energy parameter γ. Here, ϕ may vary between 0.5 and 2, reflecting the Halperin-Lax and Sa-yakanit models. Discrete values of ϕ may reduce to the following analytic models: Urbach ($\phi = 1$; $\gamma \equiv E_U$), optimal-fluctuation ($\phi = 5/4$; γ proportional to the 2/5 root of the total charged defects concentration), Franz-Keldysh ($\phi = 3/2$; γ proportional to internal electric field), and semiclassical approach ($\phi = 2$; γ proportional to the root mean square amplitude of the fluctuating potential) [315, 316, 323]. Fig. 4.4 compares the sub-bandgap region described by Eq. 4.9 for the above discussed ϕ values, and for that purpose, the authors calculated the absorptance instead of the optical absorption spectrum.

The particular case of bandgap fluctuations was addressed by Mattheis *et al.*, which assumed a Gaussian distribution of the local bandgaps (E_g^{Loc}) around a mean value, $E_{g,mean}$, with a standard deviation σ_g [175, 298]. The proposed model for the absorption coefficient,

$$\alpha(h\nu) \propto \int_0^{\infty} \frac{1}{\sigma_g\sqrt{2\pi}} exp\left[-\frac{1}{2}\left(\frac{E_g^{Loc} - E_{g,mean}}{\sigma_g}\right)^2\right]\left(\frac{\sqrt{h\nu - E_g^{Loc}}}{h\nu}\right) dE_g^{Loc}, \tag{4.10}$$

demand that the bandgap fluctuations occur over a small length scale in comparison to the minority carrier diffusion length.

[2] For simplicity we refer this model as a 5/4 power law

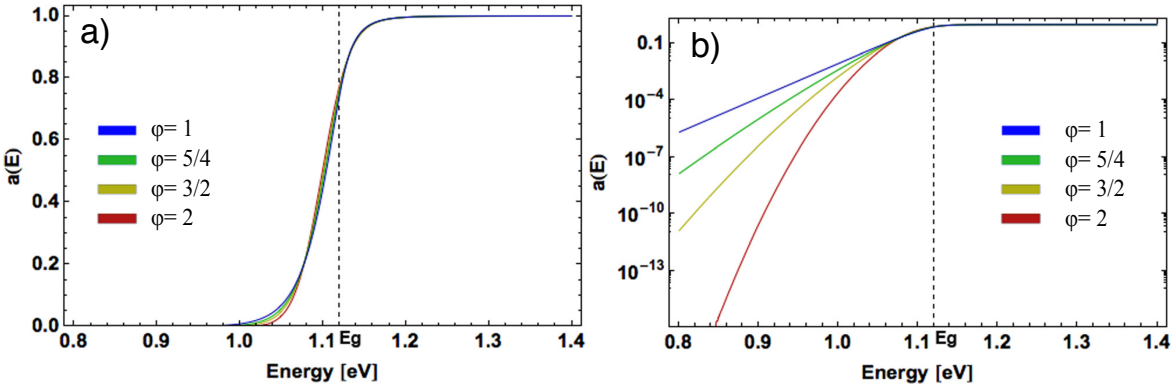

Figure 4.4: a) Absorptance curves calculated from $a(h\nu) = 1 - exp(\alpha(h\nu)W)$ replacing $\alpha(h\nu)$ by Eq. 4.9 for ϕ=1, 5/4, 3/2, and 2 with equivalent fraction of sub-bandgap absorption. b) Same curves as a), but plotted on a logarithmic scale. Adapted from [315].

4.2.2 Estimation of fluctuating potentials by investigation of sub-bandgap optical spectra on chalcogenides

In this Section we will discuss the extraction of the influence of fluctuating potentials in CIGS and CZTSSe using different theoretical models discussed above, through the analysis of several published studies. The influence of fluctuating potentials have been extracted from experimental results obtained using several methods that produce qualitatively equivalent spectra to the sub-bandgap absorption one: i) transient photocapacitance (TPC); ii) photothermal deflection spectroscopy (PDS); iii) internal quantum efficiency (IQE); iv) external quantum efficiency (EQE); and v) photoluminescence excitation (PLE). However, the comparison of results obtained from the different techniques is not straightforward. This difficulty is clearly shown in the study of Malerba *et al.* in which, the authors estimated for CZTS significantly different Urbach energies, E_U, from the absorption spectrum and the exponential region in the EQE curve at low energies, 77 and 45 meV, respectively [324]. This work shows that E_U values obtained from different experimental approaches, even being equivalents, should not be compared straightforward. Thus, this conclusion should be extrapolated to the discussion of the parameters that describe the amplitude of the fluctuating potentials, i.e E_U, γ, and σ_g.

The empirical Urbach model is the most used one to study the sub-bandgap region in chalcogenides [36, 291, 324-332]. Table 4.1 presents experimental values of E_U obtained for the studied chalcogenides in this work. Despite the different experimental approaches used to obtain E_U, it is clear that the values obtained for CIGS are systematically lower than the ones obtained for CZTSSe and related compounds. This trend was directly observed by Islam *et al.* from the fit of the Urbach model to the exponential region of the TPC spectra [36]. It was obtained an E_U value of 28 meV for CIGS and significantly higher values of 69 and 54 meV for CZTS and CZTSSe, respectively. The increase of the E_U value for CZTSSe in comparison to the ones obtained for CIGS is ascribed to an increase of the band tails due to an increase of the structural disorder [36]. In fact, Cu and Zn

atoms present in the kesterite structure of CZTSSe can swap with low enthalpic cost, as already discussed [222, 299]. Note that this issue does not exist in CIGS due to the larger chemical mismatch between Cu and In/Ga. Additionally, higher experimental values of E_U for CZTS, in comparison with CZTSe, are regularly obtained. This trend may be observed in the results of Phuong *et al.* that using the optimal-fluctuation model to fit the low energy side of the PLE spectra, verified that band tails tend to be less severe with the increase of Se content and the consistently better performances obtained for Se-rich CZTSSe based solar cells [333]. Regarding the obtained E_U values for CIGS (17-28 meV) they are sufficiently close to K_BT at room temperature, which suggests that the disorder is due to thermal vibration of the atoms. Moreover, tails with amplitude less than K_BT should have a minor effect, since these can be overcome with the thermal energy. However, as seen before in this Section, the effective value of E_U should be carefully analysed due to its qualitative nature.

Table 4.1: E_U values (in meV) obtained from optical absorption (OA), transient photocapacitance (TPC), photothermal deflection spectroscopy (PDS), external quantum efficiency (EQE) and internal quantum efficiency (IQE) curves for CIGS and CZTSSe.

Method	CIGS	CZTS	CZTSe	CZTSSe	Ref.
PDS	25-27	-	-	-	[325]
TPC	18-26	-	-	-	[326]
TPC	17-23	-	-	-	[327]
IQE	27-28	-	-	-	[328]
TPC	28	69	54	-	[36]
EQE	-	-	25	-	[332]
EQE	-	-	50	-	[334]
OA	-	-	26-29	28-32	[291]
TPC	-	-	-	13-31	[329]
OA	-	791±20	-	-	[330]
OA	-	70-80	-	-	[331]
OA	-	64-77	-	-	[324]
EQE	-	45	-	-	[324]

The studies discussed until this point present E_U values obtained at room temperature. Nevertheless, in Section 4.2.1 it was mentioned that E_U is linked to thermal disorder. In this regard, it is expected a dependence on the temperature of E_U. Shioda *et al.* and Wasim *et al.* for CIS (see Fig. 4.5), and Troviano for Cu-poor CIGS, studied the dependence of the E_U on the range of 90-300 and 150-300 K for CIS and CIGS, respectively [328, 335, 336]. Whereas for CIS a weak increase of E_U was obtained with the increase of the temperature (Cu-poor: $\Delta E_U \sim 3$ meV; Cu-rich: $\Delta E_U \sim 4$ meV [335]), for CIGS E_U remained almost constant in all range of the studied temperatures.

This behaviour does not follow the temperature dependence expected theoretically. In addition to the thermal disorder, it is therefore expected that the stoichiometric deviations strongly affects E_U values in chalcogenides based materials. In this respect, Shioda *et al.* studied CIS single crystals samples with different Cu contents [335]. The E_U values were almost constant for near-stoichiometric Cu-rich samples, while it increased with the decrease of Cu content.

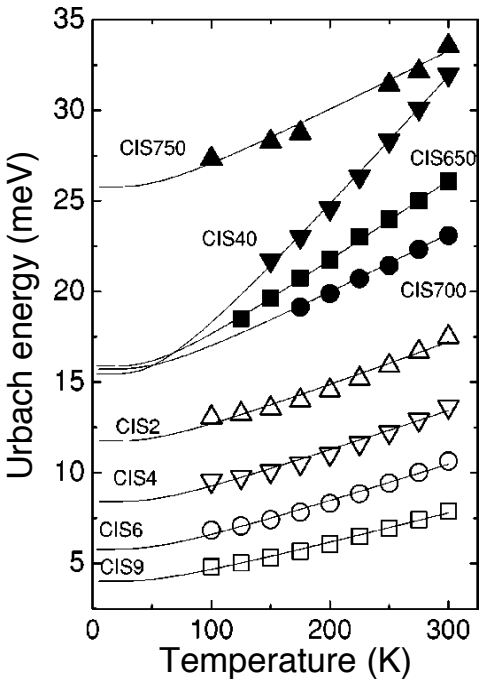

Figure 4.5: Dependence on the temperature of E_U values for different Cu-poor CIS samples [335, 336, 337] (CIS650, CIS700, CIS2, CIS4, and CIS9) and Cu-rich (CIS750, CIS40, and CIS6) [336]. Adapted from [336].

There are studies in the literature, where the sub-bandgap edge were not described by a single exponential behaviour as proposed by Urbach. Mendis *et al.* verified that the Gaussian model, Eq. 4.7, was the one that better describes their experimental CZTS EQE spectrum, obtaining a significant γ value of 100.6 ± 0.4 meV [334]. The optimal-fluctuation model have been also used to estimate the influence of the electrostatic fluctuating potentials in chalcogenide samples [298, 301]. Dirnstorfer *et al.* reported an increase in the electrostatic fluctuating potentials as the CIGS samples became more Cu-poor, obtaining values of γ of 10 and 20 meV. This study is compatible with the one of Shioda *et al.*, which used the Urbach model [335]. Gokmen *et al.* used optimal-fluctuation model to compare CIGSSe and CZTSSe samples, obtaining higher γ values for CZTSSe, which is also consistent with the studies performed with the Urbach model approach. In this same work, the authors complemented their study using the Mattheis model for bandgap fluctuations. The obtained σ_g values follow the γ ones being also higher for CZTSSe than CIGSSe (CZTSSe: σ_g= 75-85 meV and γ= 55-65 meV;

CIGSSe: σ_g= 42-48 meV and γ=32-38 meV) [298]. The study of the bandgap fluctuations was also addressed by Hages *et al.* for CZTSSe, for which a σ_g of 55 meV was obtained [338]. Additionally, the sub-bandgap edge was also fitted by the Urbach model extracting an E_U value of 34 meV. As shown in Fig. 4.6, both approaches, Gaussian and exponential, describe quite well the obtained data. Rey *et al.* also studied the sub-bandgap region of the absorption spectra for CZTSe and CZTSSe. Following the aforementioned results, the authors obtained σ_g values higher than the ones obtained for E_U (CZTSe: σ_g= 49-59 meV; E_U= 26-29 meV and CZTSSe: σ_g= 74-87 meV; E_U= 28-32 meV) [291]. Note that the estimated values for bandgap fluctuating potentials are systematically higher than the ones obtained from the Urbach model or optimal fluctuating potentials model.

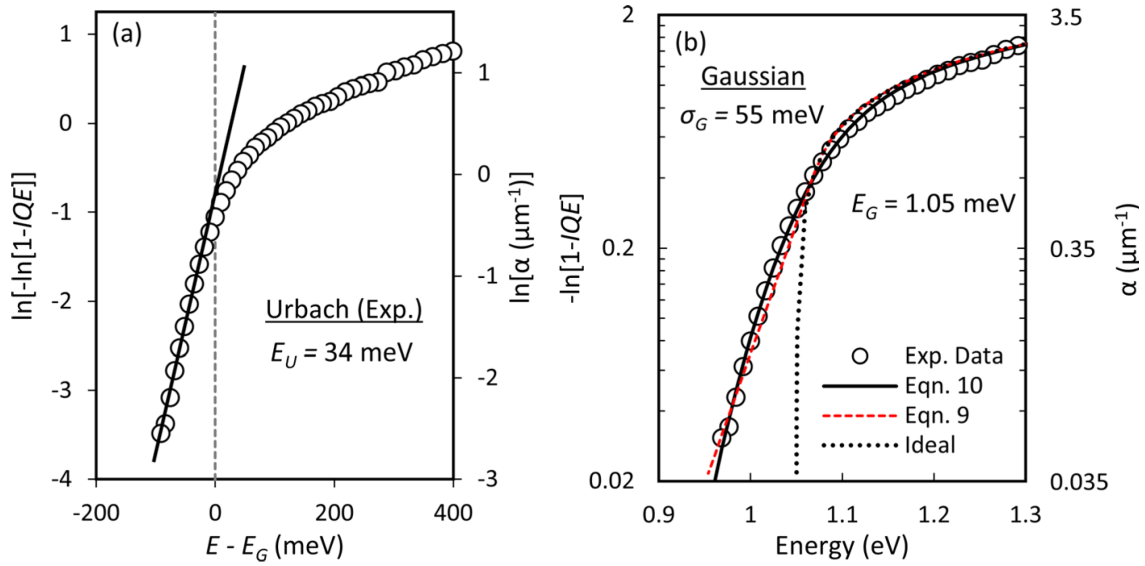

Figure 4.6: a) ln[-ln[1-IQE]] and ln[α] vs. energy shift from the bandgap. The solid line represents the fit to the experimental points by Eq. 4.6. b) ln[1-IQE] vs. energy. The solid line represents the fit to the experimental points by Eq. 4.10 and the red-dashed line represents the fit to the experimental points by Eq. 4.6. The black fine-dotted line represents an ideal absorption model for a direct bandgap semiconductor without band tails for comparison. Adapted from [338].

After discussing the fundamental studies in the chalcogenides absorber layers, now we look into devices. Miller *et al.* identified a correlation between E_U and the voltage deficit/V_{OC} losses in CZTSSe devices [329]. Fig. 4.7 shows the dependence on E_U of both V_{OC} and V_{OC} losses (obtained from EQE curves and TPC spectra). The V_{OC} losses estimated from the two different experimental techniques have both a quasi-linear relation with E_U. The authors conclude that the increased V_{OC} losses and the corresponding poorer device performance are, at least in part, a result of the increase of the tails amplitude related to an increased degree of static disorder [329].

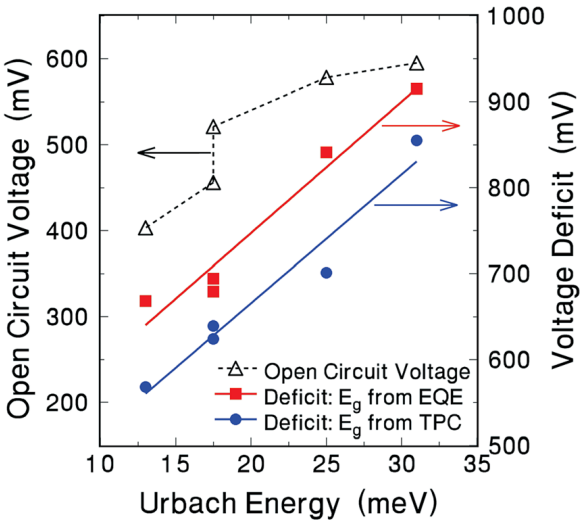

Figure 4.7: Dependence on E_U of both V_{OC} (the triangles and left hand scale) and voltage deficit/V_{OC} losses (right-hand scale). The V_{OC} losses (E_g/e-V_{OC}) was obtained two ways: I) by estimating E_g from EQE data (■) and, ii) by estimating E_g from the TPC spectra (•). Adapted from [329].

4.2.3 Estimation of the fluctuating potentials influence by photoluminescence

Photoluminescence (PL) is a well suited non-destructive technique to study the electronic energy levels structure of a semiconductor. Additionally, PL provides important insights concerning the radiative and non-radiative de-excitation channels in the material, which is very relevant for optoelectronic applications, like photovoltaics. The radiative and non-radiative mechanisms depend strongly on the doping and compensation levels. The radiative transitions observed in a highly doped and strongly compensated semiconductor are quite different from the ones typically found in a lightly doped semiconductor, for which flat bands are assumed (see Fig. 4.8 a)) [48]. As follows, we will start by addressing the simplest case of lightly doped semiconductors then we will look to the fairly more complex analysis of the highly doped semiconductor.

Radiative transitions observed in lightly doped semiconductors, include (see Fig. 4.8 a)): recombination of free and bounded excitons (Fx, and D^0x, A^0x, respectively), donor-acceptor pairs (DAP), free-to-bound (hD^0 and eA^0), and band-to-band (BB) transitions. Over the time, a few different radiative models have been considered in the assignment of chalcogenides related luminescence with relevance to DAP transitions. Thus, from all transitions mentioned for the lightly doped semiconductors, we will focus on that particular type of radiative transition, which will be helpful for the discussion of the results presented in Section 6.1. Considering a lightly or even moderately doped semiconductor, both donors and acceptors will be present in significant concentrations providing radiative recombination channels throughout the corresponding localized states within the bandgap [48, 296, 339]. Tran-

sitions involving DAP recombination have been assigned to both Cu-poor and Cu-rich chalcogenide luminescence, as shown in a recent study [340].

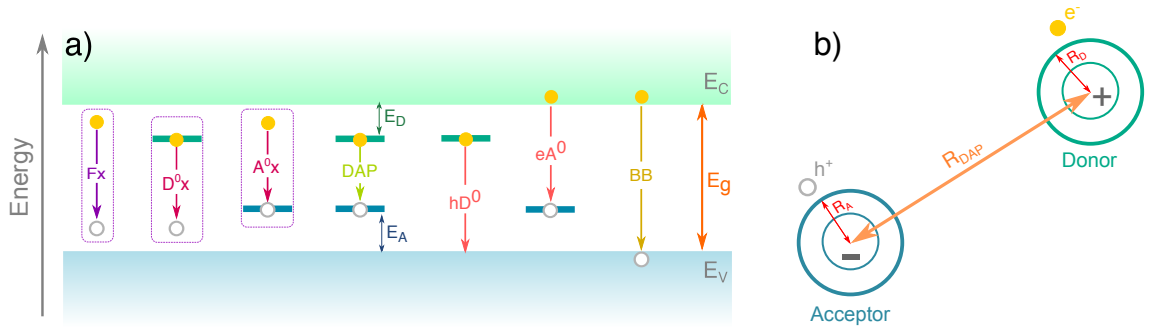

Figure 4.8: Energy band diagram for a) lightly doped semiconductor. Radiative transitions are illustrate: free and bounded excitonic (Fx and D^0x, A^0x, respectively), donor-acceptor pairs (DAP), free-to-bound (hD^0 and eA^0), and band-to-band (BB) transitions. b) DAP separated by a R_{DAP} from which depends the energy of the emitted photon in a DAP transition according to Eq. 4.11. a) and b) adapted from [341] and [339], respectively.

A DAP transition requires as initial state (or radiative state) a neutral donor and a neutral acceptor (D^0 and A^0), which means an electron (e^-) bounded to an charged donor and a hole (h^+) bounded to an charged acceptor. After a certain time, electron and hole recombine leading to a final state with charged donor and acceptor (D^+ and A^-):

$$D^0 + A^0 \rightarrow D^+ + A^+ + h\nu.$$

The energy of the emitted photon in a DAP transition is given by [64]:

$$h\nu = E_g - (E_D + E_A) + \frac{1}{4\pi\epsilon_0\epsilon_r}\frac{e^2}{R_{DAP}} \tag{4.11}$$

where E_D and E_A are the ionization energies of the donor and acceptor, respectively, and R_{DAP} the separation between the ionized donor and acceptor. The last term in Eq. 4.11 accounts for the Coulomb interaction of the charged DAP after the emission.

Since the defects are located at discrete positions in the lattice, substitutional or interstitial, R_{DAP} is then a discrete variable (see Fig. 4.8 b)), leading to a spectrum composed of individual lines, each of which lines corresponds to an allowed value of R_{DAP}. Nonetheless, as the separation R_{DAP} increases, the difference between energies $h\nu(R_{DAP})$ for consecutive distances decreases, and the zero-phonon lines start to merge into a broad and asymmetric band. A radiative DAP transition is easily identifiable when the sharp lines in the emission spectrum are observed [339]. In the absence of these lines it is necessary to perform different studies, in order to allow its identification, for instance, the dependence of the shape of the emission and peak energy on the temperature and excitation power. Increasing the temperature, the thermal energy in the sample will approach the shallower defect energy, the recombination will preferably occur via eA^0 or hD^0 rather than via DAP transitions. If

the temperature is increased even further, also the deeper defect may be ionized and BB recombination may be observed.

According to Eq. 4.11, the luminescence observed for a DAP recombination is governed in the high energy side by the transitions between close pairs, whereas distant pairs, are responsible for the low energy side of the emission. These latter pairs, have a large capture cross section and a very low recombination rate. In this way, these pairs are easily saturated with the increase of the excitation power and pairs with a lower separation become excited. The rate of recombination of the pair increases as the separation decreases. Thus, the increase of the excitation power leads to an increase of the relative intensity of the luminescence from recombination of DAPs with minor separations. In consequence, a moderate blueshift of the DAP emission with the increase of excitation power is observed. The theoretical model proposed by Zacks and Halperin, translates this behaviour of the relation between the peak energy of the zero-phonon band ($h\nu$) and the excitation power P, as

$$P(h\nu) \propto \frac{(h\nu - h\nu_\infty)^3}{h\nu_B + h\nu_\infty - 2E} exp\left(-\frac{2(h\nu_B - h\nu_\infty)}{h\nu - h\nu_\infty}\right), \tag{4.12}$$

being $h\nu_\infty = E_g - (E_D + E_A)$ and $h\nu_B = h\nu_\infty + \frac{1}{4\pi\epsilon_0\epsilon_r}\frac{e^2}{a_B}$.

As discussed before in this Chapter any sort of perturbation of the perfect lattice contributes to the appearance of distinct energy levels in the bandgap energy. The DAP model is only valid for low donor and acceptor concentrations. A continuous increase in the doping will lead the Coulomb interaction between defects that will be responsible for the formation of tails in the bandgap. These states will affect critically the possible radiative transitions observed in the semiconductor (see Fig. 4.9) [48, 297, 342]. Let us take as an example a p-type semiconductor ($N_a > N_d$) for which the electron has a considerably lower effective mass than the hole, as is the case of the studied materials in this work. Thus, the heavy doping condition ($N_d a_e^3 >> 1$, a_e the Bohr radius of the donor state) is much more readily satisfied by donors than by acceptors. Additionally, single donors do not form bound states for electrons and the localized states in the conduction band tails appear just for sufficiently large number of donors. Regarding the acceptor levels, they follow the fluctuations of the valence band. Depending mainly on the concentrations of acceptors, but also of donors, the radiative transitions may involve the recombination of electrons near the quasi-Fermi level for electrons or trapped by sufficiently deep states in conduction band tails, with holes bound to localized acceptor states. The corresponding transitions are band-impurity (BI) and tail-impurity (TI), respectively [48]. Other radiative transitions, in particular tail-tail (TT), band-tail (BT) and band-band (BB), may also be observed depending mainly on the semiconductor temperature, excitation rate and the depth of the acceptor level.

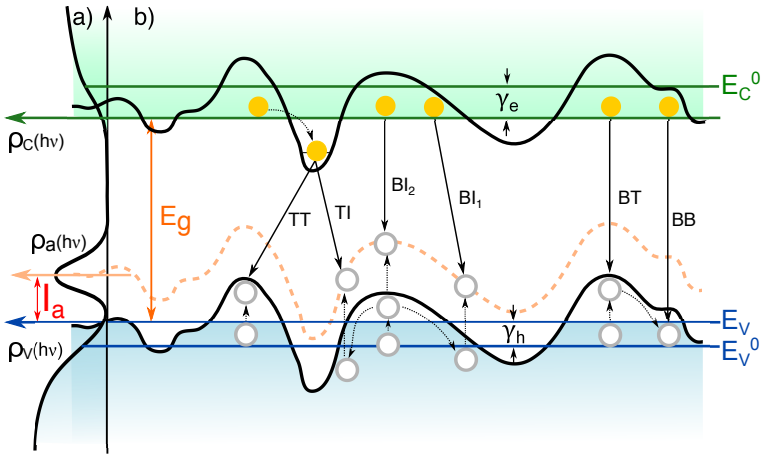

Figure 4.9: a) Density of states $\rho(h\nu)$ and b) energy band diagram for a highly doped semiconductor and strongly compensated. The dashed line represents the acceptor level with an I_a ionization energy and density of states of $\rho_a(h\nu)$. γ_e (γ_h) stands for the separation energy between the minimum of the conduction band E_c^0 (maximum of the valence band E_v^0) of the undoped material and the percolation level for electrons E_c (holes E_v). Radiative transitions of the type band-impurity (BI), tail-impurity (TI), tail-tail (TT), band-tail (BT) and band-band (BB), are illustrated. Adapted from [48].

Luminescence shape

The density of states of the band tails has a significant influence on the luminescence, contributing to its asymmetric shape. In fact, the intensity of the luminescence in the low energy side ($I_{\mathrm{LE}}(h\nu)$) follows the density of states of the band tails, whereas on the high energy side, the intensity decrease is more abrupt and follows the thermal broadening [48]. Thus, the following discussion will be focused in the low energy side of the luminescence. In spite of the occurrence of tails on both bands, it is often the case that due to the difference of the effective masses of both carriers, the tails in the valence band are able to bind holes whereas the tails in the conduction bands do not bind electrons. Thus, the density of states of the valence band tail has a higher influence on the luminescence, contributing to the asymmetric shape of the luminescence. However, in the case of transitions involving agglomerates of donors the low energy side of the luminescence may follow the density of the states of the conduction band [342].

Since the density of states of the tails states depends on the amplitude of the fluctuating potentials, two models based on the tails amplitude have been proposed in order to extract that amplitude from the low energy side of the luminescence [48, 343]. For fluctuating potentials that are deep enough, the density of states follows a Gaussian distribution. Thus, the intensity of the luminescence in the low energy side can be described as [48]:

$$I_{\mathrm{LE}}(h\nu) \propto \exp\left(\frac{h\nu - E}{\sqrt{2}\gamma_{Gauss}}\right)^2. \tag{4.13}$$

On the other hand, for shallower fluctuating potentials the density of states is better described by an

exponential [48]:

$$I_{\mathrm{LE}}(h\nu) \propto exp\left(\frac{h\nu - E_g}{\gamma_{exp}}\right). \tag{4.14}$$

Following these two generic models to describe the low energy side of the luminescence, equations for different radiative transitions type may be found in the literature (Eq. 7.1 in Section 7.1) [48].

Dependence of the luminescence on the excitation power

The dependence on the excitation power of the peak energy in highly doped semiconductors shows a strong blueshift. This behaviour is explained in the literature by two arguments: i) state filling [344, 345, 346] and/or ii) screening effect [188, 196, 347].

Regarding the state filling hypothesis, the fluctuating potentials model assumes the existence of tail states with different amplitudes in the bandgap. The deeper ones are separated by longer distances and are statistically less probable. For a low excitation power regime, populating these deeper tails is favoured. The increase of the excitation power will promote the state filling by populating more shallow tail states, which have a higher density [48, 344, 345]. This change from deeper to shallower tail states is reflected on a significant blueshift of the luminescence. An increase of the blueshift is expected as the doping level and the degree of compensation increases.

The amplitude of the fluctuating potentials may also decrease due to the screening of the electrostatic fluctuating potentials by photogenerated free carriers [348]. Due to the excitation power, free carries are photogenerated and they cause a reduction of the screening length, r_0, by a creation of free charges and/or a reduction of the charged defects (see Eq. 4.4). In the particular case of electrostatic fluctuations, the relation between γ and the charged defects density N follows the Eq. 4.5. A reduction in r_0 due to screening is then accompanied by a reduction in γ, which causes a widening of the bandgap. Thus, the large blueshift with the increase of the excitation power is also explained by a screening effect [297]. The physical mechanism responsible for the observed blueshift (a state filling effect or a screening effect) should essentially be roughly independent of the nature of the transition [346]. In the literature, the dependence of the peak energy on the excitation power (P) is often described by the following relation [344, 345, 346, 348, 349]:

$$E = \beta\ ln\left(\frac{P}{P_0}\right), \tag{4.15}$$

where β characterizes the energy shift and P_0 is a fitting parameter. Values of $\beta \gtrsim 2\,\mathrm{meV}$ are usually ascribed to highly doped semiconductors, whereas for lightly doped semiconductors the obtained values are close to 1 [344, 345, 346, 348].

The dependence of the PL integrated intensity (I) on the excitation power can be parameterized by [341]:

$$I \propto P^m, \tag{4.16}$$

where m is an adjustable parameter. Usually, values of $m > 1$ are ascribed to the recombination of free or bound excitons, whereas values of $m < 1$ are related with free-to-bound recombinations

or transitions involving defects [341]. In the context of fluctuating potentials, the interpretation of the m values is not straightforward. In highly doped materials the existence of excitons is virtually impossible and isolated defects should not necessarily bound carriers. As a consequence, values of m lower than 1 should reflect globally a localization of carriers that can occur in isolated defects or clusters of defects described by the tails [302, 344, 345, 346]. Commonly, the dependence given by Eq. 4.16 involves measurements for more than two orders of magnitude of the excitation power values. With such a a large range of values, a diminishing of the slope is expected, which is ascribed to a progressive saturation of the optical centers responsible for the luminescence [341].

Dependence of the peak energy on temperature

The dependence of the peak energy on the temperature in highly doped semiconductors is strongly influenced by the used excitation power [301, 342, 350, 351]. In the literature, the most observed behaviours show a redshift [302, 352] or a combination of a red and a blueshift [32, 102, 301, 308, 347, 349, 350, 353-357]. As the temperature is increased it is commonly observed a redshift followed by a blueshift. The magnitude of the redshift have been reported to be dependent on the excitation power. A decrease on the redshift have been shown with the increase of the excitation power by Krustok *et al.* for CGS [358], Schumacher and Botha for Cu(In,Ga)(S,Se)$_2$ [347], and Larsen *et al.* [359] for CIS and CGS. The transition from the red to the blue usually happens at temperatures $\sim$100 K [32, 102, 301, 308, 347, 350]. The explanation often given for this observed behaviour is that a transition from a TI to a BI recombination occurs [301, 347, 350]. However, based on the theoretical recombination models suggested by Osipov *et al.*, the dependence on the temperature of the BI and TI transitions, by itself, may be responsible for this behaviour [308, 342, 351].

We will now discuss in more detail TI and BI transitions. Let us consider the case where in the neighbourhood of each donor cluster exist several acceptors. This is due to the fact that the number of donor clusters is much lower than N_d in a p-type semiconductor. Due to the bending of the bands near a donor cluster, and that the acceptor states follow the edge of the valence band, as the separation r between the donor cluster and the acceptor states diminishes, the energy of the hole increases (see Fig. 4.10). So, at low temperatures, holes occupy acceptor states that are far from the cluster, reducing the probability of recombination according to [48],

$$\varsigma(r,z) = \varsigma_0 \exp\left(-\frac{2rz}{a_e}\right), \tag{4.17}$$

where ν_0 is a constant and z is the number of donors in the cluster. The energy of the radiative recombination of both carriers is

$$h\nu = E_e - E_h + \frac{e^2}{4\pi\epsilon_0\epsilon_r r}, \tag{4.18}$$

where E_e and E_h are the energy of the electron in the donor cluster and the energy of the hole in the acceptor state, at the distance r from the cluster, respectively. As the temperature is increased, the behaviour of the peak energy is usually a strong function of the excitation power of the semiconductor and may be given by [48]

$$h\nu = E_g^0 - I_a - \gamma_e - K_B T \ln\left(\frac{N_c}{n}\right) + 2\sqrt{(K_B T)^2 \ln\left(\frac{N_c}{n}\right) + K_B T \gamma_e}, \tag{4.19}$$

where E_g^0 is the bandgap for the undoped material, I_a is the ionization energy of the acceptors, γ_e is the separation energy between the minimum of the conduction band of the undoped material and the percolation level for electrons, N_c is the effective density of states of the conduction band, and n is the concentration of electrons in the conduction band. This equation shows that, when the excitation rate is raised, the emission suffers a blueshift. At very low temperatures (close to absolute zero), the dependence on the temperature is independent of the excitation power values and may be simplified to

$$h\nu = E_g^0 - I_a - \gamma_e + 2\sqrt{K_B T \gamma_e}. \tag{4.20}$$

At higher temperatures, hν is a function of the excitation power: i) for a low excitation level ($n \lesssim 10^{-2} N_c$), hν almost linearly decreases with the increase of the temperature due to the thermal escape of electrons from the shallower donor clusters, which results in the lowering of the quasi-Fermi level; ii) for a high excitation level, hν increases monotonically with T due to the filling with electrons of almost all donor clusters; in this case, the radiative transitions involve the recombination of electrons bound to the shallowest clusters with free holes, which may approach much more easily to the donor wells.

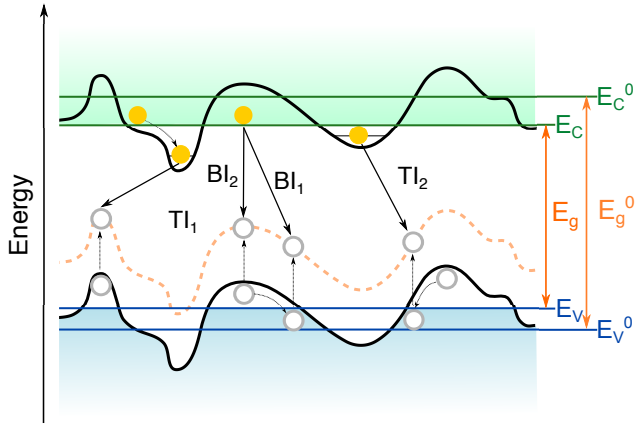

Figure 4.10: Energy band diagram for a heavily doped and strongly compensated semiconductor. TI_1 and TI_2 represents radiative transitions involving a sufficiently deep and a shallow donor cluster, respectively. The dashed line represents the acceptor level. E_g^0 and E_g are the bandgap energy of the undoped and doped semiconductor, respectively. Adapted from [342].

Increasing temperature, promotes the release of electrons from progressively deeper donor clusters and also the release of holes from the acceptor states to the valence band, both of which contribute to the diminishing of the luminescence intensity of the emission band. In parallel with this thermal quenching process, a second band (see Fig. 4.10) can be observed as a consequence of populating of shallower donor clusters [48, 342]. The concentration of these shallower clusters is higher than the

deeper ones, and they may be approached by the holes more easily. Thus, the relative importance of the shallower clusters increases, and a second emission band for higher energies may be observed. The dependence on temperature of the peak energy of that second band may be described by Eq. 4.20, which shows that $E^2_{\max}$ increases with the increase of the temperature. The energy separation between the two bands is about $kT \ln\left(\frac{N_c}{n}\right)$, which depends strongly on the excitation rate: for $T \sim 100\,\mathrm{K}$, the energy separation can change from $\sim$1 meV up to a few tens of meV, usually it is difficult to perform the deconvolution of the two bands for higher temperatures. Thus, for low enough excitation power values, the maximum of intensity of the PL starts with a redshift followed by a blueshift for the higher values of temperature.

BI transitions are observed when the doping of the semiconductor is such that the potential wells in the conduction band do not bind electrons. The experimental behaviour under the change of temperature or excitation power is similar for degenerate or non-degenerate material, i.e., does not depend on the position of the quasi-Fermi level for electrons [48, 360]. At low temperatures, the shape of the observed band is asymmetric whereas as the temperature or the excitation power increase, the band broadens and becomes symmetric. This modification of the shape is accompanied by a blueshift for both dependencies. However, for a low temperature regime, a redshift may be observed with the increase of temperature [302, 360].

Dependence of the peak energy

Quasi-donor-acceptor pair (QDAP) recombination concept have been used in several works that study highly doped and strongly compensated semiconductors [188, 196, 308, 347, 361-364]. It assumes DAP transitions in the presence of fluctuating potentials, and considers that the nonequilibrium charge carriers are localized in tails states and they recombine radiatively through donors and acceptors, with photon energy given by [309]

$$h\nu \approx E_g - (E_D + E_A) - 2\gamma. \tag{4.21}$$

Here, the Coulomb term considered in the equivalent Eq. 4.11 for DAP transitions is neglected. Different authors argued that the luminescence shifts to lower energies by an amount equal to 2γ, which follows the amplitude of the band tails [188, 196, 308, 347, 361-364]. This model is simplistic and will be discussed in more detail in Section 4.2.4, following the context of the recombination models ascribed to the chalcogenides related luminescence.

4.2.4 Photoluminescence on chalcogenides

Different models are considered in the literature for the luminescence of CIGS and CZTSSe, namely, excitonic recombination [365, 366, 367], free-to-bound transition [188, 352, 353, 366, 368, 369], DAP recombination [340, 369-373], QDAP recombination [188, 196, 308, 347, 361-364] and radiative channels involving fluctuating potentials [102, 188, 301, 302, 306, 308, 344, 345, 347, 354, 368, 374, 375].

No agreement exists concerning the nature of involved states and also on the nature of the radiative transitions, mainly due the featureless structure in these materials related luminescence.

In general, the luminescence in Cu-rich films commonly consists in bands with a full width at half maximum (FWHM) up to just a few tens of meV and is ascribed to recombination of excitons or DAP transitions. Three models are usually used for the discussion of the nature of the radiative transitions in the Cu-poor films: DAP, QDAP and fluctuating potentials. In the case of Cu-poor films, usually just one broad asymmetric band is observed with a FWHM considerably higher than in the case of Cu-rich films. This change on the PL spectra from Cu-rich to Cu-poor films is shown in Fig 4.11 [188, 368, 376].

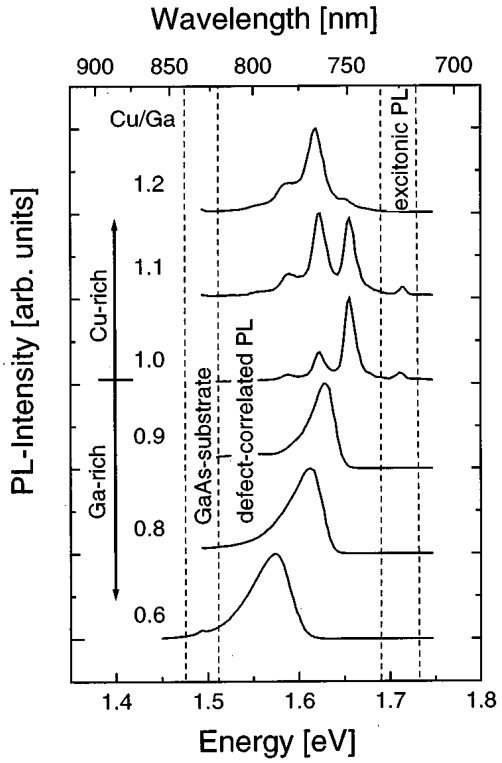

Figure 4.11: PL spectra of CGS epitaxial layers for different [Cu]/[Ga] ratio mesured at 10 K. Three energy ranges are given (dashed lines) to distinguish between excitonic luminescence, defect-correlated optical transitions, and luminescence from the GaAs(001) substrate [188].

In order to discuss these models for CIGS and CZTSSe, the dependence on excitation power and temperature of PL, is commonly addressed. Regarding the effect of the increase of excitation power on PL, the peak energy evidences a blueshift of a few meV [188, 340, 368] to several meV [188, 301, 347, 353, 354, 368]. The case of a blueshift with few meV is usually observed in Cu-rich films and the estimated values for the m parameter (see Eq. 4.16) are lower than 1, which are interpreted as a localization of charge carriers [368]. The second case, blueshift of several meV, is observed mainly in Cu-poor films.

Concerning the temperature increase, the luminescence from Cu-rich films show a redshift [352]

or a combination of a red and a blueshift [369] as the temperature is increased, whereas in Cu-poor films, it has been reported a blueshift [354], or a complex behaviour (redshift followed by a blueshift) [32, 301, 308, 347, 353-356].

Next we will focus on the QDAP and fluctuating potentials models used to discuss the luminescence of Cu-poor chalcogenides. The QDAP model was first introduced by Yu [309] to explain asymmetric "moving-emission bands" in strongly compensated GaAs crystals, which showed a significant blueshift with the increase of the excitation power. The author argued that this type of radiative transitions occurs just in strongly compensated regions where spatial fluctuations of the electrostatic potential exist. It is clear that Yu realized the difference between DAP transitions and the transitions that he was observing, and created the concept of QDAP to fit his experimental observations. The QDAP is above only a concept without a physical model behind it. However, as the doping concentration increases, it is mainly the collective interaction between impurities that determines the radiative transitions due to the decrease of their mean distances between impurities. Even for the intermediate-doping regime, Dobrego and Shlimak argued that the model of DAP transitions is not appropriate since charge carriers are captured in energy levels not related to isolated impurities, but to impurity aggregates [377]. Thus, for semiconductors with high enough doping and compensation levels, as is the case of CIGS and CZTSSe, and taking into account the differences between the effective masses of the two charge carriers, it is meaningless to assume radiative transitions that involve localized donors (E_D parameter in Eq. 4.21) as proposed by Yu [308].

In the fluctuating potentials model, it is assumed the existence in fluctuations of the concentration of charged defects along the film that create tail states, which can bind charge carriers depending on both the amplitude of the tail and the effective mass of the carrier. Assuming this model, the study of the luminescence in CIGS and CZTSSe is mainly based on two particular approaches, both proposed by Osipov and applicable to: i) "heavily doped and highly compensated semiconductors" [48, 378] and ii) "semiconductors heavily doped with shallow donors and with a fairly high concentration of deep acceptors[3], which does not satisfy the heavy-doping" [48, 342]. These cases are expected to be found in CIGS and CZTSSe, since are both highly doped and compensated materials, the donors are much shallower than the acceptors and the heavy doping condition is much more readily satisfied for donors than for acceptors, because the considerably lower effective mass of the electron in comparison to the one of the holes [173, 242, 301, 302, 308]. The luminescence assuming i) is dominated by TT or TI (for acceptor levels deeper than the tail states) transitions, at low temperatures and moderate excitation power, and BT or BI transition at high temperatures and/or high excitation power. According to ii), the TI at low temperatures and at moderate excitation power should dominate the luminescence and the BI transition at high temperatures and/or high excitation power. In both approaches depending on the excitation power and temperature, other transitions involving impurities, tail states, and band states can be observed [346, 378]. At different excitation power and temperatures, these different

[3] "deep acceptors" in this context means that the state should be at an energy deep enough to be able to form an acceptor band separated from the valence band.

radiative transitions have been ascribed to CIGS and CZTSSe: BI [102, 302, 375, 379, 380, 381], TI [308], TT [32, 354], BT [356, 379, 380] and BB transitions [32, 354, 356, 379].

Table 4.2: γ_{Gauss} and γ_{exp} values obtained for CIGS and CZTSSe.

	γ_{Gauss} (meV)	γ_{exp} (meV)	Study
CIGS	35.2, 39.6	-	[131]
	34, 67	-	[32]
	16.7	-	[382]
	17	-	[356]
CZTS	172	-	[302]
	55.3	-	[382]
	102-188	45-100	[383]
	-	11	[271]
CZTSe	88	-	[28]
	24-27	-	[384]
	24-39	-	[385]
	44-51	-	[386]
	-	24-39	[385]
CZTSSe	26	-	[387]

The analysis of the low energy side of the luminescence measured at low temperature should be more sensitive to the influence of electrostatic fluctuating potentials over the other sources of fluctuating potentials [298]. Table 4.2 shows experimental values of γ for the studied chalcogenides. Grossberg *et al.* and Phuong *et al.* showed that for CZTSSe the γ value increases with the increase of the S content, which was in accordance with consistently better performances obtained for Se-rich CZTSSe based solar cells [9, 10, 333, 388]. The Gaussian model is the one most used to analyse the low temperature luminescence, whereas, for the study of the sub-bandgap absorption, at high temperatures, the Urbach model is regularly the chosen one. The models used to study the luminescence and the sub-bandgap absorption, are in accordance with the discussion in Section 4.1 that it is expected to scrutinize deeper tails by PL than by absorption measurements. However, despite the used model, the obtained trend follows the one observed in the study of the sub-bandgap absorption (Section 4.2.2), i.e. the obtained γ values for CZTS are significantly higher than the ones obtained for CZTSe, CZTSSe, and CIGS.

4.3 In Summary

The dominant mechanisms that give rise to fluctuating potentials in CIGS and CZTSSe are presented. As long as both semiconductors present high levels of doping and compensation, we focused our attention on the impact of the electrostatic fluctuating potentials on the electronic energy levels structure and on the dynamics of the charge carriers that at great extent influences the solar cell basic principles of operation. A review of several models of fluctuating potentials based on different sources of disorder are also presented. Based on these models, experimental evidences for different types of fluctuating potentials and estimation of the tails states amplitude from absorption coefficient and PL measurements, were discussed. Despite the different theoretical models or experimental approaches used to estimate the amplitude of the fluctuating potentials, the values obtained for CIGS are systematically lower than the ones obtained for CZTSSe. These results are consistent with the fundamental properties discussed for both materials in the previous two Chapters (2-3), and the electronic performance obtained so far in both technologies (Chapter 1).

Chapter 5

Fabrication processes and characterization techniques

The solar cells fabrication process is generically presented for CZTS and CIGS. The characterization techniques used to assess the morphological, structural, optical, and electrical properties of the studied devices are briefly discussed according to the requirements of the carried studies.

5.1 Fabrication process: solar cells based on CZTS

The CZTS based solar cells were fabricated at The Thin Film and Photovoltaic Research Group (TFPR) at the i3N/Department of Physics of University of Aveiro. TFPR follows a two steps process, sulphurization of evaporated/sputtered multi-stacked precursors deposited on Mo coated SLG. Table 5.1 summarizes the fabrication process of the studied solar cells based on CZTS, deposition methods and resultant thickness values of the different layers, beyond the substrate, are presented [389, 390, 391].

Table 5.1: Deposition methods and typical thicknesses of each layer in CZTS based solar cells studied in this thesis.

Layer	Deposition method	Typical thickness (nm)
Mo-s	Direct current magnetron sputtering	500
Mo	Direct current magnetron sputtering	500+300
CZTS	Sulphurization of sputtered/evaporated Multi-stacked precursors	2000
CdS	Chemical bath deposition	50-70
i-ZnO	Radio frequency sputtering	50
ITO	Radio frequency sputtering	200-300
ZnO:Al	Radio frequency sputtering	230

Substrate

SLG substrates $3 \times 3\,\mathrm{cm}^2$, were used. Before the deposition of the Mo back contact, the substrates are cleaned with consecutive ultrasonic baths in acetone, alcohol, and hot deionized water for 10 min each, then dried using a nitrogen gas (N_2) flux [392].

Back contact

The Mo back contact was deposited following the baseline of Salomé *et al.* in a DC magnetron sputtering [392]. Argon (Ar) is the used sputtering gas. The base pressure of the chamber is 5.0×10^{-4} Pa and the sputtering power of density $0.5\,\mathrm{Wcm}^{-2}$. Two different methods of deposition were used:

i) **single layer (Mo-s):** the layer is deposited at 1.0 Pa. The obtained Mo back contact layers have a sheet resistance below $1\,\Omega/\square$ and thickness around $\sim$500 nm [391].

ii) **bilayer (Mo):** the bottom layer is deposited at 1.0 Pa with a thickness of $\sim$500 nm and the top layer deposited at 0.1 Pa with a thickness of $\sim$300 nm. The bilayers produced present good adhesion and sheet resistivity between 0.5 and $0.8\,\Omega/\square$ [392].

Absorber layer

Different sulphurization methods of sputtered/evaporated multi-stacked precursor layers were studied in order to increase the control of the stoichiometry along the thin film and the formation of secondary phases.

Deposition of multi-stacked precursors:

i) **Sputtering/Evaporation:** two different multi-stacked sequences of sputtered/evaporated precursors are studied in this work. $8 \times (Zn/SnS_2/CuS)$ $(4 \times (Zn/Sn/Cu))$ periodic stacks using a hybrid evaporation/sputtering system, were prepared. In this process, Zn is thermally evaporated while SnS_2 and CuS (Sn and Cu) are sputtered successively using a RF magnetron sputtering of the compound targets. This process is repeated in 8 periods (4 periods) to prepare multi-stacked layers of precursors. The base pressure of the deposition chamber is $\sim 10^{-3}$ Pa. The deposition is done in a $90\%\,Ar + 10\%\,H_2$ atmosphere at an operating pressure of 4.0×10^{-1} Pa [277, 281, 389, 391].

ii) **Sputtering:** $8 \times (ZnS/SnS_2/Cu)$ RF magnetron sputtered precursors were deposited. The deposition is done in a $90\%\,Ar + 10\%\,H_2$ atmosphere at a operating pressure of 4.0×10^{-1} Pa [152, 390]

Sulphurization:

i) **Sulphur flux:** the precursors were sulphurized in a tubular furnace at a constant pressure of 5.0×10^4 Pa. The precursors are directly exposed to a flux of $95\%\,N_2 + 5\%\,H_2$ and S vapour at flow rate of $40\,ml\,min^{-1}$. In this process, S is evaporated at 230 °C. The sulphurization is performed at a maximum temperature of 570 °C during 30 min, then the samples cooled down to room temperature at a natural rate [277].

ii) **Graphite box:** precursors are sulphurized in the same furnace mentioned in i), but the samples are placed inside a graphite box together with 240 mg of high purity S pieces. The pressure inside the furnace is 5.0×10^4 Pa with the gas mixture of $95\%\,N_2 + 5\%\,H_2$. The sulphurization is performed at a maximum temperature of 570 °C during 30 min, then the sample cooled down to room temperature at a natural rate [277].

iii) **RTP i:** the sulphurization was performed in the RTP furnace at atmospheric pressure consisting of partial pressures of $95\%\,N_2 + 5\%\,H_2$ and S vapour resulting from the evaporation of 20 mg of S pieces placed near the sample. This process is carried out with the samples inside a graphite susceptor. The sulphurization is performed at a maximum temperature of 550 °C during 1 (2) mins, then the samples were cooled at 5 °C/s down to 50 °C. After 6 min at 50 °C the samples are cooled down to room temperature at a natural rate [281].

iv) **RTP ii:** the sulphurization was performed in the RTP furnace at atmospheric pressure consisting of partial pressures of $95\%\,N_2 + 5\%\,H_2S$. This process is carried out with the samples inside a graphite susceptor. The sulphurization is performed at a maximum temperature of 520 °C during 30 mins, then the samples cooled down to room temperature at a natural rate [152, 390].

As-deposited CZTS are submitted to a standard potassium cyanide (KCN) treatment. The sample is dipped in a 5 wt% KCN solution in H_2O for 2 min, then rinsed in deionized water and dried with N_2 flow [389, 390, 391].

Buffer layer

The CdS buffer layers was deposited by conventional CBD. The CBD contains a solution with 7.14 M ammonia (NH_3), 0.6 M thiourea (CH_4N_2S), and 0.03 M cadmium acetate $Cd(CH_3(CO_2)_2)$. The solution is mixed in a beaker at room temperature then the samples is immersed into the beaker, which is placed inside a water bath at 65-70 °C. Deposition time is ∼15 min. After that, the sample is directly removed from the CBD beaker and immersed in clean deionized water to stop the growth process and dried using a flow of N_2. This process produces CdS films with a thickness of ∼50-70 nm [389, 390, 391].

Front contact

The window layers were deposited using a magnetron-assisted RF magnetron sputtering, using i-ZnO and ITO targets. The system is evacuated into a base pressure of $\sim 5.0 \times 10^{-5}$ Pa. First, ZnO is sputtered using a working power of 100 W and a pressure of ∼2.6 Pa, using a mixture of above 97% Ar and less than 3% O_2. Finally, ITO is deposited with a power of 120 W and a pressure of 4.6 Pa using Ar as a gas. The ZnO and ITO layers with thicknesses around 50 and 200-300 nm, are respectively obtained. i-ZnO/ZnO:Al window layer deposited following the Ångström baseline was also used in solar cells based on CZTS the deposition process is described in the next Section [140, 390].

Post-treatment deposition

A post-deposition annealing (PDA) in the CZTS based solar cell at 300 °C, was carried out on a hot plate at atmospheric pressure, in an atmosphere of N_2 for 15 mins.

CZTS studied samples

Table 5.2 presents the architecture of all studied solar cells based on CZTS. The multi-stacked precursors and sulphurization methods are presented for each sample, as well as the composition obtained by energy dispersive X-ray spectrometry. The different set of samples will be studied in individual Sections in Chapter 6, which are also identified. Note, that whenever it will be relevant details on the fabrication process will be recalled during the study of the physical properties of the samples.

Table 5.2: CZTS based solar cells fabricated at the TFPR in the i3N/Department of Physics of the University of Aveiro. The Sections in Chapter 6 regarding the study of each set of samples are mentioned.

Sample	Metallic Precursors	Sulphurization	[Cu]/([Zn]+[Sn])	[Zn]/[Sn]	Solar cell architecture	PDA	Section
	8× ($Zn/SnS_2/CuS$)	RTP i	0.81	0.99	SLG/Mo/CZTS/CdS/i-ZnO/ITO	No	6.1
A	8× ($Zn/SnS_2/CuS$)	RTP i	0.78	0.87	SLG/Mo/CZTS/CdS/i-ZnO/ITO	No	6.2
B	8× ($Zn/SnS_2/CuS$)	RTP i	0.81	0.99	SLG/Mo/CZTS/CdS/i-ZnO/ITO	No	
A	4× (Zn/Sn/Cu)	Tubular Furnace: S flux	0.97	0.91	SLG/Mo/CZTS/CdS/i-ZnO/ZnO:Al	No	6.3
B	4× (Zn/Sn/Cu)	Tubular Furnace: Graphite Box	0.84	1.27	SLG/Mo/CZTS/CdS/i-ZnO/ZnO:Al	No	
A	8× ($ZnS/SnS_2/Cu$)	RTP ii	-	1.18	SLG/Mo-s/CZTS/CdS/i-ZnO/ITO	No	6.4
B	8× ($ZnS/SnS_2/Cu$)	RTP ii	-	1.18	SLG/Mo-s/CZTS/CdS/i-ZnO/ITO	Yes	

5.2 Fabrication Process: solar cells based on CIGS

The studied CIGS based solar cells were fabricated at the Ångström Solar Center at Uppsala University according to the Ångström solar cell baseline (ÅSC) [44, 75, 90, 140, 393]. We studied solar cells based on co-evaporated CIGS with different compositions, Ga-profiles, and architectures. Table 5.3 summarizes the fabrication process of the studied CIGS based solar cells. The deposition methods and thickness values of the different layers, are presented. We must note that, each particular sample has only some of the listed layers.

Table 5.3: Deposition methods and typical thicknesses of each layer in CIGS based solar cells studied in this thesis.

Layer	Deposition method	Typical thickness (nm)
Mo	DC sputtering	350
NaF	Evaporation	15
Al_2O_3	Atomic layer deposition	18
CIGS	Co-evaporation	1700
CdS	Chemical bath deposition	50-70
ZnSnO	Atomic layer deposition	17
i-ZnO	RF sputtering	90
ZnO:Al	RF sputtering	350

Substrate

Low-iron SLG substrates of 12.5 × 12.5 cm^2, were used. Alternatively, it was used as Na-free substrate a polished ceramic Aluminium oxide (Al_2O_3). Before the deposition of the Mo back contact, the substrate is submitted to a cleaning process [75, 90, 140].

Back contact

The bilayer Mo back contact in the ÅSC baseline is deposited in a DC sputtering system in Ar atmosphere, where the substrate passes in front of the target with a speed of 7 cm/min. A power of 1500 W was used for both bottom and top layers. Ar pressures of ∼2.0 Pa for the bottom layer and ∼0.8 Pa for the top layer are used. The obtained Mo back contact layer have a sheet resistance lower than 0.5 Ω/□ and thickness of 350 nm [75, 90, 140].

NaF layer

Sodium fluoride (NaF) precursor layer of 15 nm was evaporated at a pressure of 2.0×10^{-3} Pa, as Na source for CIGS doping [75, 394].

Passivation layer

A 18 nm Al_2O_3 layer, was deposited by ALD on SLG/Mo/NaF at 200 °C, using the Trimethyl aluminium (TMA) precursor gas as aluminum source and H_2O as oxygen source, followed by a 420 nm of Polymethyl Methacrylate (PMMA) resist deposition on SLG/Mo/NaF/Al_2O_3 substrate. The nanopattern is first defined lithographically by exposing the resist to an e-beam lithography system at 100 kV, and consisted of a square array of openings/holes of ∼400 nm diameter separated by 2000 nm among them. Then, the resist is developed at room temperature by spray of pure methyl isobutyl ketone (MIBK) for 40 s, using isopropanol as a stopper. Opening of the Al_2O_3 layer is done by reactive ion etching (SPTS ICP) with a chlorine based chemistry, where Mo is etched at 60.8 nm/min, Al_2O_3 at 96.4 nm/min, and PMMA at 297.6 nm/min. Finally, the PMMA resist is removed by acetone. The created array allows for ∼97% passivated area leaving ∼3% of the area for contacting [44, 393].

Absorber layer

The CIGS thin films were growth by co-evaporation in a Se rich atmosphere, according to two different processes:

i) **one-stage process:** a base pressure of 1.0×10^{-4} Pa with a maximum substrate temperature of 540 °C is used in this process. Four evaporation sources, In, Ga, Cu and Se are present. Two Ga-profile were implemented: i) linear decreasing of GGI ratio from the back contact to the front of the film (normal Ga-profile), and ii) constant evaporation rate to obtain a constant GGI (flat Ga-profile). The active time of the deposition may be varied in between 5 and 20 minutes.

ii) **three-stages process:** the process starts with evaporation of In, Ga and Se (stage I) followed by the evaporation of Cu and Se at a higher temperature (stage II), and a Cu-poor composition of the final absorber film is achieved by once again evaporating In and Ga in a constant Se atmosphere (stage III). The total process takes about 52 min: stage I took 18 min; stage II, 17 min; stage III, 17 min. The sample holder is kept at a temperature of 480 °C during the first stage. During the second stage this temperature is ramped up to 540 °C and it is then held at that value until the end of the evaporation. Immediately after that, the heater is turned off and the sample is left to cool in vacuum. CIGS absorbers prepared by a three-stage process present a notch Ga-profile.

Buffer layer

The buffer layers were deposited as soon as possible after the samples are unloaded from the CIGS co-evaporator. This is done to minimize oxidation of the CIGS layer that occurs with exposure to air. Ensure minimum exposure time is especially important for alternative buffer layers deposited with the dry ALD, which lacks the CIGS surface etching that is a part of the CBD process due to the presence of ammonia [140].

CdS: The CdS buffer layer was deposited by CBD. The CBD contains a solution with 1.1 M NH_3, 0.100 M CH_4N_2S, and 0.003 M $Cd(CH_3(CO_2)_2)$. The solution is mixed in a beaker at room temperature, and the samples are immersed into the beaker, which is subsequently heated to 60 °C in a water bath. During the growth process, the solution is stirred for 10 s each minute. The baseline process time is 8 min and 15 s. The sample is directly removed from the CBD beaker and immersed in clean deionized water to stop the growth process. This process produces layers with a thickness of 50-70 nm.

ZnSnO: The $Zn_{1-x}Sn_xO_y$ buffer layer was grown by using a Microchemistry F-120 ALD reactor kept at a deposition temperature of 120 °C. As precursors, diethyl zinc (DEZn or $Zn(C_2H_5)_2$), tetrakis (dimethylamino) tin (TDMASn or $Sn(N(CH_3)_2)_4$), and deionized water are used together with N_2 as carrier and purge gas. The deposition involves the total of 625 ALD cycles, where the pulse lengths were 400/400:800:400:800 ms long for the Sn/Zn:N_2:H_2O:N_2 pulses, respectively.

Front contact

To deposit the intrinsic ZnO layer (i-ZnO) and, subsequently, the Al-doped ZnO (ZnO:Al) front contact of the cells in a single run a RF horizontal sputtering system is used, where the substrates are stationary during deposition. The ZnO:Al target has a 2% weight of Al_2O_3, and both, the ZnO:Al and the i-ZnO target, with 8 inches, have a purity of 3N. The RF power is 200 W for the i-ZnO layer and 300 W for the ZnO:Al layer. The Ar flow during the sputter deposition is 14 sccm, and a throttle valve is used to achieve a sputter pressure close to 0.133 Pa. There is an additional flow of O_2 of 5 sccm present under ignition and target conditioning. The diameters of both of the targets are 125 mm, which limit the maximum substrate size to $5 \times 5\,cm^2$ for reasonably uniform ZnO layers. The highly resistive i-ZnO layer in ÅSC baseline devices has a typical thickness of 90 ± 10 nm, when deposited on a glass substrate. The thickness of the ZnO:Al front contact, when deposited directly on a glass substrate, is 350 ± 20 nm, and the sheet resistance is $30 \pm 10\,\Omega/\square$ [140].

Grid deposition

Ni/Al/Ni grid was deposited in an evaporation system that contains an electron-beam heated evaporation source with multiple crucibles mounted on a turntable, where a grid pattern is defined using an aperture mask. The evaporation rate and film thickness are monitored with a quartz-crystal

microbalance. The total grid thickness is 3000 ± 500 nm. Sheet resistance measurements on none-structured grid layers deposited on a glass substrate give values between 0.01 and $0.02\,\Omega/\square$ [140].

Studied Samples

Table 5.4 presents the architecture of the studied set of solar cells based on CIGS. The co-evaporation method and Ga-profile is presented for each sample, as well as the composition obtained by X-ray fluorescence (XRF) performed in a Panalytical Epsilon 5 spectrometer. The different set of samples will be studied in individual Sections in Chapter 7, which are also identified. Note, that whenever it will be relevant details on the fabrication process will be recalled during the discussion of the physical properties of the samples.

Table 5.4: CIGS based solar cells fabricated according to ÅSC baseline, at the Ångström Solar Center at Uppsala University. The Sections in Chapter 7 regarding the study of each set of samples are mentioned

Sample	Evaporation	Ga-profile	GGI	CGI	Solar cell architecture/Deposition order	Section
A	In-line	normal	0.31	0.84	SLG/Mo/CIGS/CdS/i-ZnO/ZnO:Al	7.1
B	In-line	normal	0.3	0.77	Al_2O_3/Mo/CIGS/CdS/i-ZnO/ZnO:Al	
A	three-stages	notch	0.4	0.92	SLG/Mo/CIGS/CdS/i-ZnO/ZnO:Al	7.2
B	In-line	normal	0.4	0.92	SLG/Mo/CIGS/CdS/i-ZnO/ZnO:Al	
	In-line	normal	0.42	0.86	SLG/Mo/CIGS/CdS/i-ZnO/ZnO:Al	7.3
A	In-line	normal	0.42	0.86	SLG/Mo/CIGS/CdS/i-ZnO/ZnO:Al	7.4
B	In-line	normal	0.42	0.86	SLG/Mo/CIGS/ZnSnO/i-ZnO/ZnO:Al	
A	In-line	flat	0.295	0.7	SLG/Mo/NaF/CIGS/CdS/i-ZnO/ZnO:Al	7.5
B	In-line	flat	0.295	0.7	SLG/Mo/Al_2O_3/NaF/CIGS/CdS/i-ZnO/ZnO:Al	
Cu53	In-line	flat	0.3	0.53	SLG/Mo/CIGS/CdS/i-ZnO/ZnO:Al	7.6
Cu71	In-line	flat	0.3	0.71	SLG/Mo/CIGS/CdS/i-ZnO/ZnO:Al	
Cu84	In-line	flat	0.3	0.84	SLG/Mo/CIGS/CdS/i-ZnO/ZnO:Al	

5.3 Characterization techniques

In this section the basic theory behind the used characterization techniques will be presented, focusing on its applicability in the carried studies [21, 395, 396, 397]. The results presented in this thesis are just part of more extensive studies, most of them published in peer review scientific journals, that have been achieved through collaborations. Thus, whenever necessary published results obtained by other techniques, in addition to those presented in this section, will be added to the discussion in Chapters 6 and 7.

The studies presented in this thesis are the result of the cross interpretation of different characterization techniques in order to understand the electronic energy levels structure and then the dynamics of the charge carriers in the chalcogenides based solar cells. After the previous overview of the physical properties of two studied chalcogenides, CZTS and CIGS, and the presentation of the conventional architecture of both devices, it is obvious that each technology has its own issues, which led that the studies carried for the two chalcogenides took necessarily different directions.

i) **solar cells based on CZTS:** a fundamental characterization of the CZTS physical properties was carried out. From the structural and chemical point of view, properties like crystalline phases, chemical composition, and secondary phases were addressed. The results obtained from these characterizations were the basis for the interpretation of the PL results. The structural and optoelectronic properties were correlated with the fabrication processes and performance of the devices. The experimental techniques used comprises scanning electronic microscopy, X-ray diffraction, Raman spectroscopy, and PL.

ii) **solar cells based on CIGS:** the studied CIGS based solar cells were fabricated mainly with two different purposes: i) understand some empirical knowledge that have been inherent to this technology, and ii) understand some recent proofs-of-concept in the solar cell architecture. In order to understand the impact of the studied properties in i) and the architecture changes implemented in ii) on the fundamental properties of CIGS, a deep optical study was carried out using PL. In this technology we focused our attention in the understanding of the possible influence of fluctuating potentials on the electrical performance of the solar cells. In this way, PL, external quantum efficiency, and current density-voltage measurements were the used characterization techniques.

5.3.1 Scanning Electron Microscopy

Scanning electron microscope (SEM) is a powerful tool available for materials science characterization, providing namely, surface topography, atomic number distribution, chemical composition [395].

The working principle of this technique is based on the incidence of a high-energy and focused electron beam onto a sample surface. There are several different signals generated from the interaction

between the electron beam and the sample, that include: Auger, secondary[1], and backscattered electrons, and characteristic X-rays, among others. Figure 5.1 shows that each interaction process occurs in a specific volume within the sample, resulting from the different penetrating depth the incident electron beam request for each type of radiation to be produced and may be used to study different properties of the samples. For instance, emitted electrons allow the study of the sample surface, while the X-rays allow the study of the sample composition [395, 398].

SEM images are generated by probing the sample with a focused electron beam that is scanned across the sample surface [395]. The image resolution obtained by SEM is dependent not only on the electron beam (diameter, energy, and intensity), but also on the interaction of the latter with the sample. The sample must have superficial electrical conductivity, being usual a carbon layer deposition. For SEM imaging, the most important signals are given by secondary and backscattered electrons, because they interact close to the surface of the sample, providing the topography of the surface. The most common SEM operation mode is the observation by secondary electrons, which have low energy and consequently come from regions of the sample near the point of impact of the electron beam. The image acquired by secondary electrons has a strong topographic contrast. Information about the distribution of the local atomic number in the sample is achieved via backscattered electrons [395, 398]. Cross-section images of CZTS solar cells, obtained from secondary electrons emission, allowed an accurate analysis of the of CZTS morphology, the conformity between the solar cell layers, and their thickness.

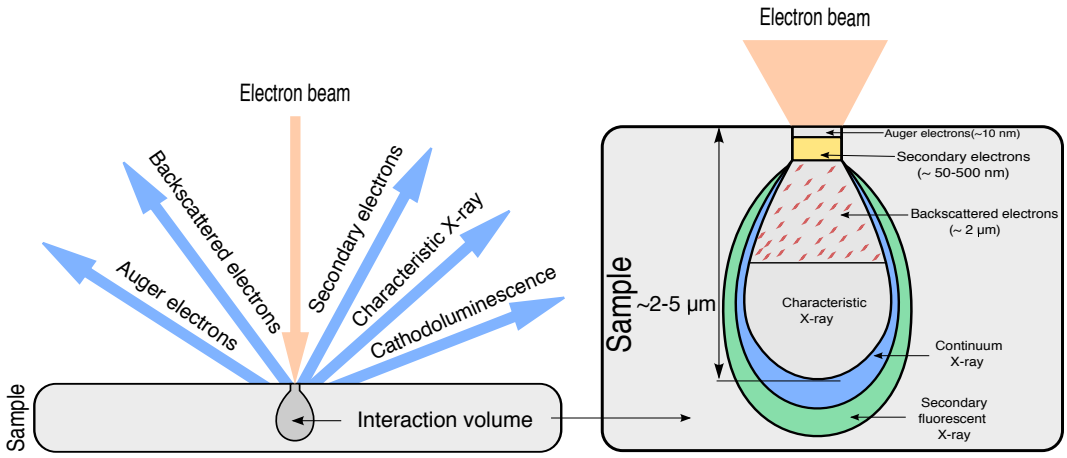

Figure 5.1: Schematic illustration of the emitted radiation resultant from the interaction volume between the electron beam and a sample. Adapted from [395].

Energy dispersive X-ray spectrometry

One of the most important features of the SEM equipment is the possibility to carry out the analysis of the emitted characteristic X-rays. As illustrated by Fig. 5.2 when a high energy electron

[1]Secondary electrons are outer-shell electrons from the atom that receive enough kinetic energy during inelastic scattering of the electrons of the beam to be ejected from the atom [398].

collides with the sample: i) it may be scattered by an inner-shell electron of a atom, transferring enough energy to that electron, allowing it to be ejected from the atom and leaving a hole in the inner-shell; ii) the hole is then reoccupied by an electron from an outer-shell. The difference in potential energy between the two electronic states in an atom is transferred to a bound electron, which may be emitted as an Auger electron or a X-ray photon [395, 398]. Thus, these characteristic X-rays have specific energies for each given atomic element in the sample. There are two methods of detecting characteristic X-rays: i) energy dispersive X-ray spectrometry (EDS), and ii) wavelength dispersive X-ray spectrometry (WDS) [395]. EDS is the most popular attachment to SEM, because it is easy to use, has a high X-ray detection efficiency, and a short measurement time. On the other hand, WDS is used for particular analysis of compounds where X-ray lines are very close or even superimpose to each other, also for the analysis of light elements, and those present at down to ~0.01 at.%. The EDS data can be acquired as either a spectrum, a line-scan, or an X-ray map.

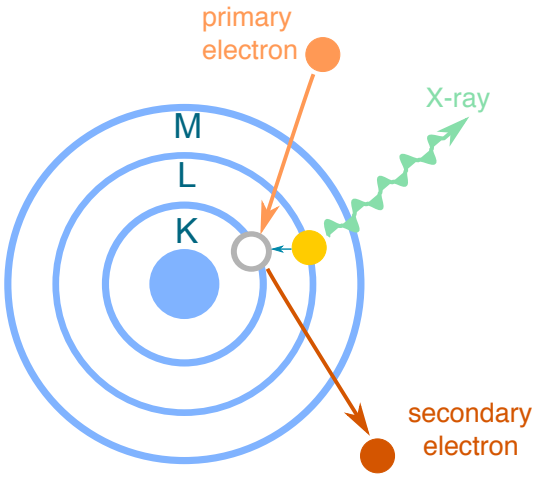

Figure 5.2: Schematic illustration of the interaction of the electron beam with the electron shells of the sample, generating secondary electrons. The mechanisms by which characteristic X-ray are created is indicated. Adapted from [395].

Experimental considerations: Cross-section morphology was studied by a FEI Quanta 650 FEG SEM microscope. The average composition was evaluated by EDS with a Rontec EDS system operated at an acceleration voltage of 25 kV. The use of 25 kV acceleration voltage allows to distinguish between Cu and Zn L_α lines in CZTS, since these emissions nearly overlap. However, the quantity of S was not measured, due to the superimposition of the S and Mo L_α lines.

5.3.2 X-Ray Diffraction

X-Ray Diffraction (XRD) explores the scattering of X-rays by the atoms in a lattice, being one of the fundamental methods used in structural characterization of thin film materials, providing information on the crystalline phases and structure [399].

The elastic scattering of X-rays may be described following the classical electromagnetic theory: an electron exposed to an electromagnetic wave will oscillate with the same frequency of the wave [396]. Thus, when a monochromatic wave collides with an atom, the electrons around that atom will begin to oscillate with the same frequency as the incident radiation, emitting electromagnetic radiation. The sum of the contributions of these waves to the scattered amplitude of all the electrons of a given atomic element of the crystal, corresponds to the atomic form factor f. The atomic form factor depends largely on the incident angle (θ): when θ=0, all the scattered waves are in phase and the atomic form amplitude corresponds to the sum of the contribution from all electrons of an atom with an atomic number Z, i.e. $Z = f$. As the angle increases, f becomes smaller than Z, because the increase of the destructive interference effect [396].

Consider a perfect single crystal with regularly spaced atoms in the lattice, as schematically shown in Fig. 5.3 [396]. For most of the directions to which the waves are scattered, destructive interference occurs, and only for a small fraction of these directions does a constructive interference occur. The amplitude of the scattered wave is dependent on the atomic form factor, f, of all the atoms in the unit cell. The phase difference between all scattered waves in the different atoms in the unit cell, must also be taken into account. The overall sum is expressed by the dimensionless quantity F_{hkl}, the geometric structure factor. For a family of lattice planes with Miller indices (h, k, l), the structure factor is given by:

$$F_{hkl} = \sum_{n=0}^{N} f_n exp[2\pi i(hx_n + ky_n + lz_n)], \tag{5.1}$$

where N is the number of symmetrically nonequivalent atomic positions in the unit cell and x_n, y_n, z_n the atomic coordinates. The intensity of the scattered X-ray waves, I_{hkl}, is proportional to the square of the structure factor $I_{hkl} \propto |F_{hkl}|^2$, being this the value measured in an XRD experiment [396].

Consider the incidence of monochromatic wave in a periodic structure whose separation between atomic planes is of the same order of magnitude of the wavelength of the incident radiation, Fig. 5.3. The condition for a constructive interference between scattered waves in two consecutive planes is given by the Bragg equation,

$$2d_{hkl} sen(\theta) = \lambda \tag{5.2}$$

where λ is the wavelength of the incident radiation, d the interplanar distance for the set of planes (h, k, l) of the crystal structure and θ the incident angle of the X-rays measured between the incident beam and the crystalline planes [396]. As discussed in Chapter 3, XRD can be used to identify the presence of CZTS, but not for the identification of all secondary phases. Thus, the structural studies will be complemented with Raman spectroscopy [27, 28].

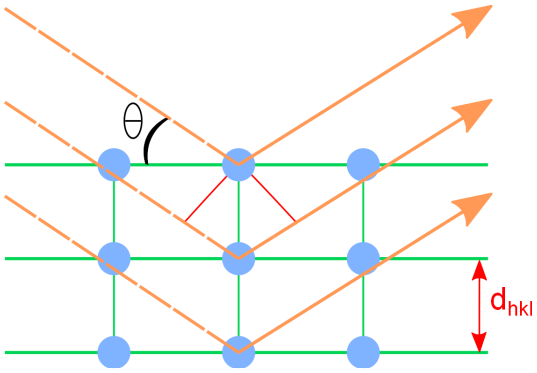

Figure 5.3: Schematic representation of the scattering of waves from lattice planes separated by a distance d_{hkl}. The dashed lines indicate incident X-ray radiation, at an incident angle θ. Adapted from [396]

Experimental considerations: XRD measurements were carried out in the Bragg-Brentano configuration (θ-2θ), with a Philips PW 3710 system equipped with a Cu-K$_\alpha$ source (λ=1.540 Å). The lattice parameters a and c, were calculated using the tetragonal relationship given by:

$$\frac{1}{\mathrm{d}_{\mathrm{hkl}}^2} = \frac{\mathrm{h}^2 + \mathrm{k}^2}{\mathrm{a}^2} + \frac{\mathrm{l}^2}{\mathrm{c}^2}. \tag{5.3}$$

5.3.3 Raman Spectroscopy

Raman spectroscopy is an optical nondestructive technique based on the analysis of the electromagnetic radiation inelastically scattered by a material. In the case of the interactions between light and semiconductor materials, light scattering is a straightforward consequence of the dielectric properties of the medium [265, 397]. The macroscopic theory of inelastic light scattering by phonons, provides a simple but consistent description of the underlying physical processes described as follows [265]: an externally applied sinusoidal plane electromagnetic field, described by

$$\vec{E}(\vec{r},t) = \vec{E}_i(\vec{k_i},\omega_i)cos(\vec{k_i}.\vec{r} - \omega_i t) \tag{5.4}$$

will induce a polarization in the medium with the same frequency, ω_i, and wavevector, $\vec{k_i}$, as those of the incident radiation. This polarization is given by

$$\vec{P}(\vec{r},t) = \vec{P}(\vec{k_i},\omega_i)cos(\vec{k_i}.\vec{r} - \omega_i t), \tag{5.5}$$

where $\vec{P}(\vec{k_i},\omega_i)$ is the amplitude of the polarization vector, which depends on the electric susceptibility χ, according to

$$\vec{P}(\vec{k_i},\omega_i) = \varepsilon_0 \chi(\vec{k_i},\omega_i)\vec{E}_i(\vec{k_i},\omega_i). \tag{5.6}$$

This description provides a picture of elastic light scattering, where the radiation scattered by the medium has the same frequency as the incident one. However, Raman scattering (inelastic interaction) requires a more accurate analysis of the polarization mechanism.

At temperatures above 0 K, the atoms of the medium do not occupy static positions, but they oscillate around their equilibrium positions with characteristic frequency. The thermal activation of the atomic vibration modes in the lattice of a material at temperature T will cause time-dependent fluctuations in χ. The atomic displacements $\vec{Q}(\vec{r},t)$ associated with a phonon with wave vector $\vec{q}$ and a frequency ω_0 can be expressed as plane waves

$$\vec{Q}(\vec{r},t) = \vec{Q}(\vec{q},\omega_0)cos(\vec{q}.\vec{r} - \omega_0 t). \tag{5.7}$$

In the adiabatic approximation, one can consider a phonon as a *quasi-static* deformation of the unit cell representing the crystal, and define for each instant a susceptibility that is a function of $\vec{Q}(\vec{r},t)$. As at room temperature the amplitudes of these vibrations are small, when compared to the lattice constant, the electric susceptibility χ can be expanded in a Taylor series

$$\chi(\vec{k_i},\omega_i,\vec{Q}) = \chi_0(\vec{k_i},\omega_i) + \left(\frac{\partial\chi}{\partial\vec{Q}}\right)_0 \vec{Q}(\vec{r},t) + ..., \tag{5.8}$$

where $\chi_0(\vec{k_i},\omega_i)$ stands for electric susceptibility of the medium in the absence of phonons. The second term represents an oscillating susceptibility induced by the crystal lattice wave $\vec{Q}(\vec{r},t)$. Truncating the expansion in the second term and replacing Eq. 5.8 in Eq. 5.6, the polarization vector of the medium due to the vibrations of the lattice, may be expressed as

$$\vec{P}(\vec{r},t,\vec{Q}) = \vec{P}_0(\vec{r},t) + \vec{P}_{ind}(\vec{r},t,\vec{Q}) \tag{5.9}$$

where

$$\vec{P}_0(\vec{r},t) = \varepsilon_0\chi_0(\vec{k_i},\omega_i)\vec{E}_i(\vec{k_i},\omega_i)cos(\vec{k_i}.\vec{r} - \omega_i t) \tag{5.10}$$

is a polarization vector that vibrates in phase with the incident radiation. $\vec{P}_{ind}(\vec{r},t,\vec{Q})$ corresponds to the polarization vector induced by phonons and is expressed by

$$\vec{P}_{ind}(\vec{r},t,\vec{Q}) = \varepsilon_0\left(\frac{\partial\chi}{\partial\vec{Q}}\right)_0 \vec{Q}(\vec{r},t)\vec{E}_i(\vec{k_i},\omega_i)cos(\vec{k_i}.\vec{r} - \omega_i t). \tag{5.11}$$

After replacing Eq. 5.7 in Eq. 5.11, it is possible to deduce an expression for the polarization vector induced by the phonons as a function of the frequencies and the associated wavevectors,

$$\begin{aligned}
\vec{P}_{ind}(\vec{r},t,\vec{Q}) &= \varepsilon_0\left(\frac{\partial\chi}{\partial\vec{Q}}\right)_0 \vec{Q}(\vec{q},\omega_0)cos(\vec{q}.\vec{r} - \omega_0 t)\vec{E}_i(\vec{k_i},\omega_i)cos(\vec{k_i}.\vec{r} - \omega_i t) \\
&= \varepsilon_0\frac{1}{2}\left(\frac{\partial\chi}{\partial\vec{Q}}\right)_0 \vec{Q}(\vec{q},\omega_0)\vec{E}_i(\vec{k_i},\omega_i) \\
&\times \{cos[(\vec{k_i}+\vec{q}).\vec{r} - (\omega_i+\omega_0)t] + cos[(\vec{k_i}-\vec{q}).\vec{r} - (\omega_i-\omega_0)t]\},
\end{aligned}$$

Note that $\vec{P}_{ind}$ is composed of two sinusoidal waves: a Stokes wave dispersion, with the wavevector $\vec{k}_S = (\vec{k_i} - \vec{q})$ and frequency $\omega_S = (\omega_i - \omega_0)$, and a ani-Stokes wave dispersion, with the wavevector $\vec{k}_S = (\vec{k_i} + \vec{q})$ and frequency $\omega_S = (\omega_i + \omega_0)$. Since the phonon frequency is equal to the difference between the frequency of the incident photon, ω_i, and the frequency of the dispersed photon, ω_s, this difference is called the Raman frequency or Raman shift.

The position and shape of the Raman bands are determined by several features of the sample, namely: the crystalline structure, chemical composition, crystal defects, impurities, and strain [397]. The analysis of the characteristic vibrational modes contributes to the identification of secondary phases.

Experimental setup and consideration: Raman spectroscopy measurements were performed in a backscattering configuration on a LabRam Horiba, HR800 UV spectrometer, using the 532 nm line of a solid state laser. Raman spectra were calibrated using a reference sample, in our case, the value of 521.0 cm^{-1} for the position of the Raman peak corresponding to the optical phonon mode in a Si bulk crystal; in the literature, the value of this phonon is not unique, which can lead to different calibrations [28]. From CZTS optical absorption spectrum presented in Chapter 2, Raman effective analysis depth may be estimated. For the backscattering configuration this depth may be roughly estimated by $d \sim 1/(2\alpha)$, where 2 comes from the fact that the measured light has to penetrate the material, scatter and return back to the surface. Thus, only ∼149 nm of the CZTS is scrutinized in the Raman analysis. In fact, the inspection of only a thin near surface region is perhaps, the biggest issue of this technique.

5.3.4 Photoluminescence

Photoluminescence is a characterization technique based on the radiative recombination of non--equilibrium carriers generated by light absorption. Through the analysis of the dependence of the luminescence on different parameters (excitation power, temperature, wavelength excitation, etc.) general information on the semiconductor electronic energy levels structure may be assessed.

In the context of the investigation of the optical properties of the solar cells, this technique has significant advantages: i) it is non-destructive; ii) it does not requires particular sample preparation; iii) it provides information mainly on minority carrier properties, that may be complementary to electrical characterization, and for a high density of generated carriers than the free carriers concentration, also majority carriers properties are assessable; iv) impurities may be detected even at low densities; and v) it gives energetically resolved information that allows the study of the electronic energy levels structure of a semiconductor. However, photoluminescence also has some disadvantages: i) it is very difficult to obtain quantitative information on concentration of defects; ii) only indirectly non-radiative recombination processes may be assessed; and iii) only a near surface thin region defined roughly by the light penetration depth and the minority carriers diffusion length can be investigated [64].

Let us consider a photoluminescence experiment in a direct bandgap semiconductor. A non-equilibrium distribution of electron-hole pairs is created by illumination via laser light. Illumination of the semiconductor with energy higher or equal than the bandgap energy ($h\nu \geq E_g$) will excite electrons from the valence band to the conduction one resulting in free electrons and free holes in the conduction and valence band, respectively. In most cases electrons and holes will thermalize by loosing

their excess of kinetic energy reaching the quasi-thermal equilibrium distributions. This results in a fast establishment of a quasi-equilibrium, where charge carriers are distributed at band edges and in defect levels at low temperature. In order to establish a uniform distribution, the charge carriers tend to diffuse. Additionally, free electrons and free holes may interact via the Coulomb force to form excitons, which may also diffuse in the material and be eventually localized in defects. The excited, electrons and holes may recombine radiatively, under the emission of photons with energy equal to the difference between the two states involved in the transition. Thus, as shown Fig. 5.4, PL process may be described in four general categories: i) excitation, ii) thermalization, iii) diffusion, and iv) radiative recombination.

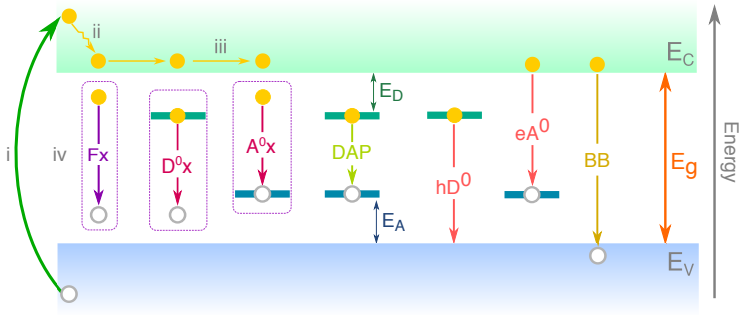

Figure 5.4: Following the schematic illustration presented in Fig. 4.8 of the energy band diagram for a lightly doped semiconductor showing the different categories of processes in a PL experiment: i) excitation, ii) thermalization, iii) diffusion, and iv) radiative recombination processes. In iv) several types of radiative transitions are illustrated, namely, the recombination of free and bound excitons (Fx and D^0x, A^0x, respectively), donor-acceptor pairs (DAP), free-to-bound (hD^0 and eA^0), and band-to-band (BB) transitions.

The investigation of the dependence of the luminescence on the excitation power and temperature are essential to the investigation of the radiative and non-radiative transitions. In Section 4.2.3 we discussed the dependence of the excitation power in highly doped semiconductors, as well as for the particular case of DAP transitions in lightly doped ones. For both cases, we also discuss the expected dependence of the peak position of the luminescence with the increase of the temperature. Thus, the dependence of the luminescence integrated intensity on the temperature was not addressed yet. This latter dependence is of great interest in order to understand the electronic levels structure involved in the de-excitation channels. The following discussion may be applied to both, light and highly doped materials.

The quenching of the PL integrated intensity with increasing temperature may be interpreted considering the thermal activation of non-radiative channels [400]. The increase of the thermal energy will contribute to the release of charge carriers from the radiative energy state to one or more discrete energy states with higher energy than the radiative one, or to a band. The discrete energy levels can describe excited states of the radiative state or be related to other defects present in the sample. The equation that describes the dependence on temperature of the PL integrated intensity is given

by [400]:

$$I(T) = I_0 \left\{ \left[1 + \sum_i c_i exp\left(-\frac{E_i}{kT} \right) + c_{bx} T^{\frac{3}{2}} exp\left(-\frac{E_{bx}}{kT} \right) \right] \left[1 + \frac{g}{1 + c_{nr} T^{\frac{3}{2}} exp(-\frac{E_{nr}}{kT})} \right] \right\}^{-1} \quad (5.12)$$

where I_0 is a parameter related to the PL intensity at 0 K given by $I(0) = I_0/(1+g)$, and g accounts for the temperature-independent ratio between the carrier capture cross section at a radiative energy state and a competing shallow one. The second term in the first square bracket parameterizes one or more non-radiative de-excitation channel(s) involving each one a discrete energy level related with the activation energy E_i. The third term parameterizes a non-radiative de-excitation channel involving a band at an energy separation of E_{bx} from the radiative energy state. The factors c_i are parameters proportional to the ratio between the degeneracies of the respective excited and radiative levels, whereas $c_{bx}\, T^{\frac{3}{2}}$ accounts for the effective density of states of the band involved and c_{bx} is a fitting parameter. The expression within the second pair of parenthesis accounts for the possible thermal supply of charge carriers (or excitons) by shallow discrete energy levels that are separated by an energy E_{nr} from the band. The term $c_{nr}\, T^{\frac{3}{2}}$ accounts for the effective density of sates of the involved band, where c_{nr} is a fitting parameter.

As shows Fig. 5.4 for the particular case of a lightly doped semiconductor, a number of different transitions may occur, depending on the measurement conditions and the material properties. In general, the different transitions may be distinguished by their dependencies on the excitation power and temperature, as summarized in Table 5.5. Free and bound excitons (D^0x, A^0x for a donor or acceptor bound exciton, respectively) appear at low temperatures (K_BT $<$ Ex, being Ex the binding energy of the exciton). Both types of radiative transitions do not present a clear shift with the increase of the excitation power, and the dependence of the luminescence intensity on the excitation power may be described by Eq. 4.16, with m values between 1 and 2. As the temperature is increased, the exciton related luminescence follows the dependence of the E_g on temperature, which for a greater number of semiconductors consists in a redshift. For high enough temperature values, the thermal energy approaches the biding energy of the exciton and the related luminescence suffers a quenching. As discussed before, DAP transitions present a slight blueshift with increase of the excitation power and temperature, and the dependence of the intensity on the excitation power follows the power function aforementioned with m values lower than 1. The obtained E_{bx} will correspond to the release of the less bounded carrier to the correspondent band. The latter phenomenon will contribute to hD^0 or eA^0 transitions. For these transitions, with the raise of the excitation power, no clear shift is observed and the estimated m values are lower than 1. With the increase of the temperature, the luminescence should follow the behaviour of the E_g, and the value of E_{bx} will correspond to the release of the bounded carrier to the correspondent band. Then, being the two carriers free in their respective bands, both charge carriers will recombine. Typically, this type of radiative recombination (band-to-band), is observed for high temperatures and for higher energies (compared to band-to-free transitions) and it follows E_g dependence on the temperature. The understanding of the recombination

mechanisms in lightly doped materials is an essential background for the analysis of the luminescence in highly doped and strongly compensated ones. The same summary of the expected behaviour for the observed transitions in highly doped and compensated material is not straightforward. With the increase of the excitation power a strong blueshift is expected and m values close to 1 are commonly reported. However, due to the strong dependence of the temperature on the excitation power used to perform this dependence, different behaviours may be obtained for the same type of radiative transition.

Table 5.5: Characteristic dependence of the luminescence for lightly and highly doped semiconductors on the excitation power and temperature. For lightly doped semiconductors, the transitions analysed involve the recombination of free excitons (Fx), bound excitons (D^0x and A^0x), donor-acceptor pairs (DAP), or are of the type free-to-bound (hD^0 and eA^0) and band-to-band (BB). For highly doped semiconductors, it is discussed the behaviour for the luminescence under the influence of the fluctuating potentials (FP). Ex corresponds to the binding energy of the exciton, E_{loc} the localization energy of a free exciton on a (donor or acceptor) defect, and E_{def} is the ionization energy of the defect (hD^0 or eA^0 transitions) or of the less bounded charge carrier (DAP recombination).

	Excitation Power		Temperature	
Transition	Peak energy	PL intensity	peak energy	PL intensity
Fx	no shift	$1 \leq m \leq 2$	follows E_g	E_{bx}=Ex
D^0x/ A^0x	no shift	$1 \leq m \leq 2$	follows E_g	E_{bx}=E_{loc}
DAP	Small blueshift	m<1	small blueshift	E_{bx}=E_{def}
hD^0/ eA^0	no shift	m<1	follows E_g	E_{bx}=E_{def}
BB	no shift	m>1	follows E_g	-
FP	strong blueshift	$m \sim 1$	?	?

Experimental considerations: PL measurements were performed in a Bruker IFS 66v Fourier Transform Infrared (FTIR) spectrometer, equipped with a Ge diode detector. A helium gas flow cryostat was used to change the temperature of the samples in the range 5-300 K. The 514.5 nm line of an Ar^+ ion laser was used as the excitation source, 457.9 and 632.9 nm were also punctually used. The excitation power was measured at the front of the cryostat window. The spectral response correction of the Ge detector was performed for all PL spectra. To avoid the oxidation of the chalcogenide surface, the presented PL measurements were always performed in samples containing the buffer layer or in fully completed solar cells.

From CZTS and CIGS (GGI= 0.3) optical absorption spectra, presented in Chapter 2, PL effective analysis depth may be estimated by $d \sim 1/(\alpha)$. Thus, for an excitation source of 514.5 nm, d values of ∼292 and ∼70 nm for CZTS and CIGS layer, respectively, were obtained. However, the scrutinized layer in PL depends also on the minority carriers diffusion length. Taking into account the values

obtained in the literature for the minority carrier diffusion length for CZTS and CIGS, presented in Table 2.1, the scrutinized layer in CZTS will mostly contain the CZTS/CdS interface and the SCR, whereas in the CIGS case, we should be inspecting all the absorber layer. The narrower region inspected by PL in CZTS is not problematic, because the luminescence in this semiconductor is dominated by interface recombination.

In order to establish a relation between the used excitation power in the PL measurements and an equivalent N-times the solar spectrum (N-Sun), we used the AM1.5 spectrum to calculate the number of absorbed photons within the CZTS and CIGS for a bandgap energy value of 1.49 and 1.17 eV, respectively. The absorbed photons in the CZTS and CIGS were obtained by the integration of the spectral photon flux over the energy down to their bandgap values. The comparison among the used excitation power and equivalent to N-Sun for CZTS and CIGS are presented in Table 5.6. Take as an illustrative example, for a excitation power of 1 mW, an equivalent of 1.8 more charge carriers are generated in the CZTS layer than when this layer is illuminated by the AM1.5 spectrum, for CIGS the equivalent value goes down to 1.22. The excitation power range of values used in this thesis goes from 0.000767 to 184 the AM1.5 spectrum.

Table 5.6: Range of studied values of excitation power (P) and incident photons per s (P'), density of incident photons (P") and equivalent values of N-times the solar spectrum (N-Sun), and equivalent N-Sun for CZTS, and CIGS, respectively.

P (mW)	P' (s^{-1})	P" ($cm^{-2}s^{-1}$)	N-Sun	N-Sun$_{CZTS}$	N-Sun$_{CIGS}$
0.001	2.6×10^{12}	3.3×10^{14}	0.000767	0.183	0.00122
0.01	2.6×10^{13}	3.3×10^{15}	0.00767	0.0183	0.0122
0.1	2.6×10^{14}	3.3×10^{16}	0.0767	0.183	0.122
1	2.6×10^{15}	3.3×10^{17}	0.767	1.83	1.22
10	2.6×10^{16}	3.3×10^{18}	7.67	18.3	12.2
100	2.6×10^{17}	3.3×10^{19}	76.7	183	122
200	5.2×10^{17}	6.6×10^{19}	153	367	244
240	6.2×10^{17}	7.9×10^{19}	184	439	292

Gaussian fitting model

The shape of an optical spectrum can be understood taking as an example, the laser line broadening. Let us consider the ideal scenario where two energy states are involved in a radiative transition, are known without any uncertainty. In this case, the shape of the transition would be a delta function. However, due to the uncertainty principle, the energy difference between the two states has an uncertainty which is reflected in a certain width in the wavelength of the radiative transition. Depending on the nature of the uncertainty two types of broadening may be found: homogeneous and inhomogeneous. If the fluctuation in the energy is due to a phenomenon that is the same for each quantum emitter, there is homogeneous broadening, while if each quantum emitter has a different

type of fluctuation, the broadening is inhomogeneous. The homogeneous broadened line will have a Lorentzian profile, while the inhomogeneously broadened emission will have a Gaussian profile. The latter scenario describes the measured luminescence by PL.

All PL spectra discussed in Chapters 6 and 7 were fitted according to a Gaussian model that describes the obtained spectra with the lower number of Gaussian components. The fitting model should be able to describe all spectra measured on the dependence of the luminescence on the excitation power and temperature. The fits were done in order to choose the parameter values that minimize the deviation from the measured spectra. In this way, two algorithms for the minimization of functions were used, Levenberg-Marquardt and Simplex.

Figure 5.5 show the dependence of the luminescence on the excitation power for a generic sample based on CIGS (SLG/Mo/CIGS/CdS). We will use this example in order to illustrate the procedure carried out to implement the Gaussian fitting model used to discuss the PL experimental results. Bear in mind that the following discussion is just illustrative, each studied sample has its own fitting model developed according to the overall obtained luminescence, dependencies on excitation power and temperature. A vast amount of work is applied to ensure that the fittings are meaningful and the optimal ones for each set of data.

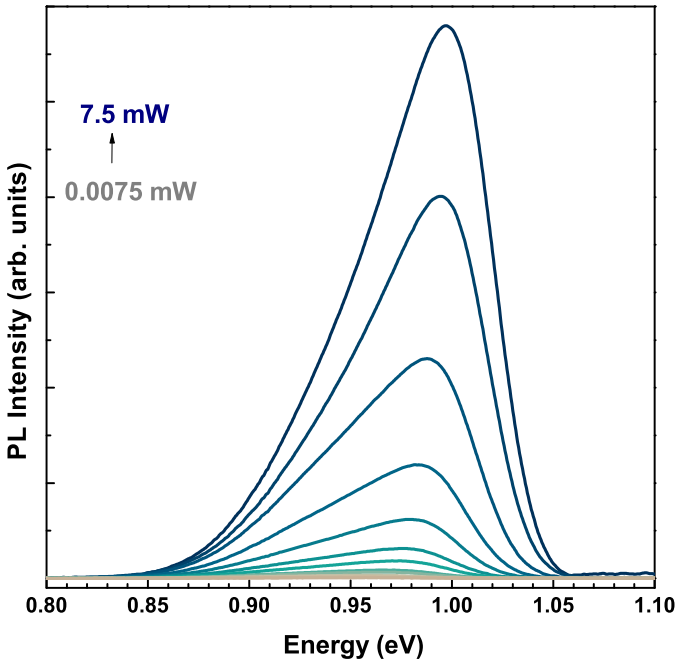

Figure 5.5: Dependence of the luminescence on the excitation power measured at 5 K for a generic sample based on CIGS.

The starting point is a Gaussian component with a FWHM of a few hundreds of meV in order to simulate the baseline of the measured spectra. This component is kept as unchanged as possible throughout the luminescence dependence on excitation power and temperature. The importance of a correct definition of a base line increases with the decrease of the signal-to-noise ratio.

Figure 5.6 illustrates the fitting model used to describe the PL spectra obtained for excitation power values of 0.0075, 1.5, and 7.5 mW. Consider these PL spectra as representative of the progressive changes on the luminescence with the increase of the excitation power, which will involve necessarily adjustments on the fitting model in order to describe changes on the shape of the spectrum. For the full range of the studied excitation power the luminescence is broad and asymmetric. Two Gaussian components were used to describe the 0.0075 mW PL spectrum (#1 and #2). The increase of the excitation power showed the need to add two more components with significantly lower area than #1 and #2. The new Gaussian components were added to the lower energies side of #1 and #2 and were named as #1' and #2', respectively. Thus, 1.5 and 7.5 mW spectra are well described by four Gaussian components, which suggests a higher asymmetry in the luminescence shape in comparison to the 0.0075 mW one. The relative intensities of the pairs of components $\#1'$, #1 and $\#2'$, #2 were kept approximately constant for all measured spectra. In addition, the peak energy of $\#1'$ and $\#2'$ follow quite well the behaviour of the peak energy of #1 and #2, respectively. These two behaviours together suggest that the studied luminescence has the contribution from two asymmetric radiative transitions, 1 and 2, each one described by a pair of Gaussian components $\#1'$, #1 and $\#2'$, #2, respectively. In fact, the asymmetric shape is characteristic of electronic transitions occurring in semiconductors with high density of charged defects, as discussed before in this thesis.

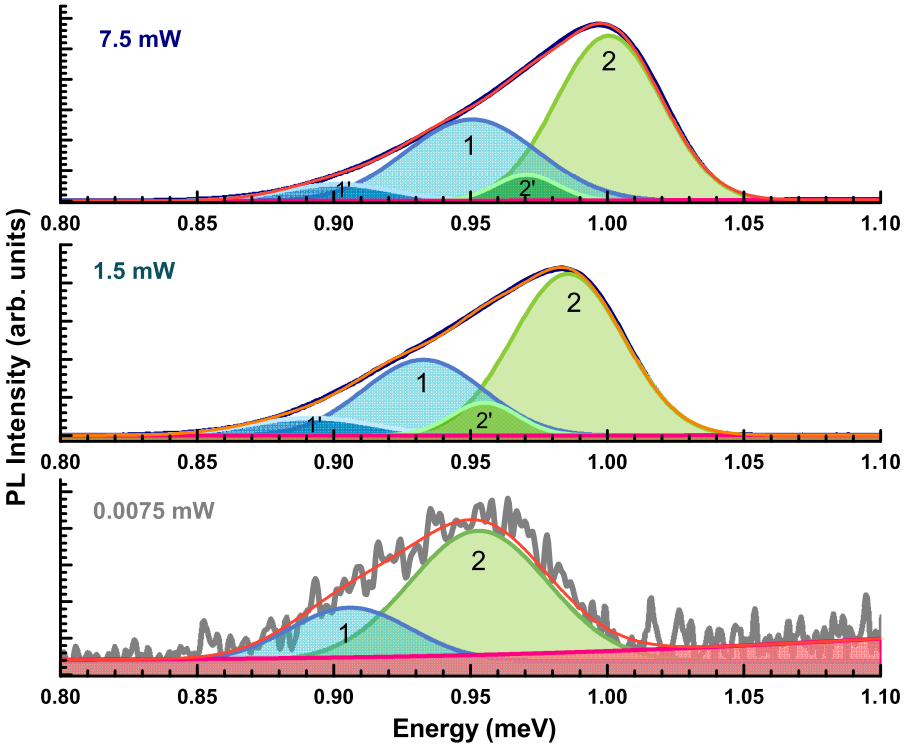

Figure 5.6: PL spectra obtained for excitation power values 0.0075, 1.5, and 7.5 mW, measured at 5 K, for a generic sample based on CIGS. The fitting model with Gaussian components are shown for each excitation power. The two radiative transitions are described by the two pairs of components $(\#1', \#1)$ and $(\#2', \#2)$. The pink component describes the baseline in each spectrum.

In order to study the dependence of the peak energy of the radiative transitions on the excitation power, we took the peak energy of #1 and #2 from transition 1 and 2, respectively, since these two components are present throughout the excitation power, and both have significantly lower error in the peak energy than the components #1' and #2', that are mainly describing the asymmetric shape of the transition. The integrated intensity of each transition was obtained through the sum of the areas of the two components that describe the transition. The same procedure was implemented to the dependence of the luminescence on the temperature.

Regarding the studied luminescence and the used fitting model, the goodness of the fit is characterized by an adjusted R-square value higher than 0.99 for the PL spectra with higher signal-to-noise ratio. However, when the signal-to-noise ratio is $\lesssim 5$ the adjusted R-square values diminish until $\sim$0.7.

5.3.5 External Quantum Efficiency

The spectral response of a solar cell may be determined by quantum efficiency (QE) measurements. There are two different types of the quantum efficiencies used for solar cell characterization: internal quantum efficiency (IQE) and external quantum efficiency (EQE). IQE compares the collected charge carriers with the photons absorbed by the solar cell, i.e. the reflectance of the solar cell is not taken into account. On the other hand, EQE compares the collected charge carriers with all the incident photons. Thus, EQE spectrum will provides losses information on either carrier generation and/or collection. Additionally, from the EQE spectrum we may assess to other significant electrical and physical properties: i) the J_{SC} can be determined by integrating the EQE spectrum over the AM1.5 photon flux; ii) the effective bandgap energies of the different layers in the solar cell; and iii) the presence of the fluctuating potentials [21]. In this thesis the EQE spectra were used to extract the bandgap energy and the influence of the fluctuating potentials at room temperature.

Several methods have been used to extract the bandgap energy value from the EQE spectrum.

i) Let us consider Grätner's model [20, 401]

$$EQE(h\nu, V) = t(h\nu)(1 - r(h\nu)) \left(1 - \frac{exp(-\alpha(h\nu)W_D(V))}{1 + \alpha(h\nu)L_D}\right). \tag{5.13}$$

Three approximations need to be taken into account, as follows: i) a perfect solar cells needs to be considered, according to the discussion in Section 2.2, total transmittance in the window and buffer layers t($h\nu$)= 1, and zero reflectance in the absorber layer $r(h\nu)$= 0; ii) for high values of energy with $\alpha(h\nu)W_D(V) \gg 1$, EQE approaches the unity and does not depend on the voltage, and iii) the thickness of the absorber layer is significantly higher than minority carriers diffusion length L_D, we may consider $\alpha(h\nu)L_D \ll 1$ [20, 338, 402]. Then Eq. 5.13 become

$$EQE(h\nu, V) = 1 - exp(-\alpha(h\nu)W_D). \tag{5.14}$$

According to Tauc's law, the dependence of the absorption coefficient $\alpha(h\nu)$ on photon energy $h\nu$ may be given by [403],

$$\alpha(h\nu) = \alpha_0 \frac{\sqrt{h\nu - E_g}}{h\nu}. \tag{5.15}$$

Replacing $\alpha(h\nu)$ by Eq. 5.15, in Eq. 5.14 we obtain

$$-h\nu\, ln(1 - EQE) = W_D \alpha_0 \sqrt{h\nu - E_g}. \tag{5.16}$$

The plot of $[h\nu\, ln(1-EQE)]^2\, vs.\, h\nu$ around the bandgap energy usually shows a linear behaviour, which may provide a rough estimation of the bandgap energy value. Indeed, the interception of the linear fit with the abscissa corresponds to the bandgap energy of the material ($h\nu = E_g$) [402, 404, 405].

ii) Following the discussion of i), but replacing $\alpha(h\nu)$ by the first term of Eq. 2.4, for a constant temperature T, which is the often used approximation for a direct bandgap semiconductor describing $\alpha(h\nu)$ for energies close to E_g,

$$\alpha(h\nu) \propto \alpha_0 \sqrt{h\nu - E_g}, \tag{5.17}$$

and replacing $\alpha(h\nu)$ by Eq. 5.17 in Eq. 5.14 we obtain,

$$ln(1 - EQE) = W_D\, \alpha_0 \sqrt{h\nu - E_g} \tag{5.18}$$

from the plot of $[ln(1 - EQE)]^2\, vs.\, h\nu$ and following the procedure in i), an estimation of the bandgap of the material may also be obtained.

iii) This approach follows also Tauc's law, replacing $\alpha(h\nu)$ by $EQE(h\nu)$ in Eq. 5.15,

$$h\nu\, EQE(h\nu) = \alpha_0 \sqrt{h\nu - E_g}, \tag{5.19}$$

from the plot of $(h\nu\, EQE)^2\, vs.\, h\nu$ and following the procedure in i), an estimation of the bandgap of the material may also be obtained [406].

iv) Replacing $\alpha(h\nu)$ by EQE in 5.17,

$$EQE(h\nu) = \alpha_0 \sqrt{h\nu - E_g} \tag{5.20}$$

from the plot of $EQE^2\, vs.\, h\nu$ and following the procedure in i), an estimation of the bandgap of the material may also be obtained [51, 407, 408].

v) 20% EQE: an alternative method is simply assign the bandgap energy value to the energy value where a 20% EQE value is observed for the low energy side of the spectrum [406].

vi) Cut-off: from EQE measurements the bandgap energy value of the material can be extracted from the cut-off energy [107].

In order to understand if there is a best method to extract the bandgap energy from the studied samples, we will briefly discuss the methods i) to iv). Due to the empirical nature of the methods described in v) and vi), they will not be addressed. We will focus our attention in the aforementioned

methods that are based on the proportionality between the occupation of the density of sates and the absorption in an energy region close to the bandgap energy, which is the same assumption used to obtain the presence of the fluctuating potentials. i) and ii) are based on Grätner's model assuming a minority carriers diffusion length significantly lower than the thickness of the absorber layer, which allows the approximation $\alpha(h\nu)L_D \ll 1$. However, as discussed in Chapter 2 the minority carries diffusion length values in CIGS technology are consistently of the order of the width of the absorber layer. To show an overview of the issue, we plot in Fig. 5.7 $\alpha(h\nu)\,L_D\,vs.\,h\nu$, considering different values of L_D= 4.5, 2.0, 1.0, and 0.5 μm. It is clear that the approximation $\alpha(h\nu)L_D \ll 1$ for energies around the bandgap energy (1.17 eV), and even considering the L_D= 0.5 μm it is not obeyed, and may not be the more accurate methods to be used in the CIGS technology. In the methods iii) and iv) we replace $\alpha(h\nu)$ by $EQE(h\nu)$, being the difference among them the absorption Eq. 5.17 used to extract the bandgap energy. Following the discussion of the absorption coefficient for the studied materials in Section 2.2, where we used Eq. 5.17 to extract the bandgap energy for the studied chalcogenides, and the acceptable values obtained using iv) in the literature [51, 407, 408], the bandgap energy in the studied samples was extracted following this method.

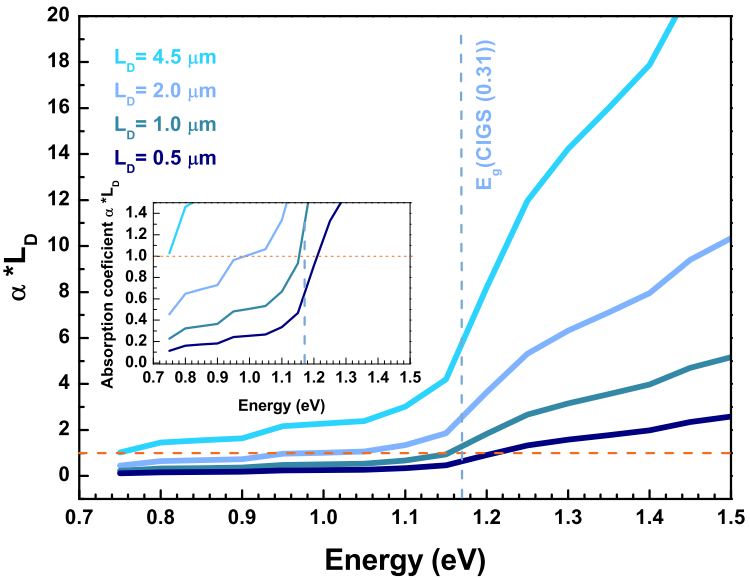

Figure 5.7: Absorption coefficient times minority carries diffusion length (L_D), as a function of energy, for values of L_D= 0.5, 2.0, 1.0, and 0.5 μm. The absorption coefficient was calculated with Eq. 2.3 for CIGS with GGI=0.31, taking k values from [26]. The inset shows the region around $\alpha(h\nu)L_D \approx 1$.

For absorber layers with a Ga-profile, which means a variation of the bandgap energy throughout the absorber thickness, it is not clear the meaning of the bandgap energy measured by the presented methods. However, in the literature it is usually referred to as the minimum bandgap in the absorber layer [405, 406]. Despite not being an absolute value of the bandgap energy, the extracted values enable the comparison between a set of samples.

Following the discussion in Subsections 4.2.1 and 4.2.2, the influence of the different types of

fluctuating potentials may be extracted by fitting the different absorption $\alpha(h\nu)$ Eq. 4.6, 4.8, and 4.10 in the sub-bandgap energy region.

Experimental consideration: The spectral EQE measurements were performed in CIGS based solar cells mainly to extract the bandgap energy, and to study the influence of the fluctuating potentials at room temperature. An in-house built system, was used for the EQE measurements in the studies presented in this thesis. EQE was determined under ambient light, using chopped monochromatic light that was scanned through a wavelength range of 360-1200 nm with 2 nm steps.

5.3.6 Current Density-Voltage

Current density-voltage (J-V) measurements under standard test conditions, are the most common tool for evaluation and characterization solar cells. The current density of an ideal solar cell under illumination may be expressed as

$$J(V) = J_{diode}(V) - J_{ph}(V), \tag{5.21}$$

where J_{ph} is the photocurrent density generated by the solar cell and J_{diode} is the diode current density or dark current density and is given by

$$J_{diode}(V) = J_0 \left[\exp\left(\frac{eV}{kT}\right) - 1\right], \tag{5.22}$$

being J_0 the saturation current density and V the applied voltage. However, a solar cell is not a perfect diode and a series resistance (R_S) and a shunt resistance (R_{SH}), have to be taken into account. The R_S and the R_{SH} are determined from the slope of the J-V curve at higher voltages than the V_{OC} and near the J_{SC} point, respectively, (see Fig. 5.8). Then, the diode current density should be rewritten as

$$J_{diode}(V) = J_0 \left[\exp\left(\frac{eV - eJR_s}{AkT}\right) - 1\right] + \frac{V - JR_s}{R_{SH}} \tag{5.23}$$

where A is the diode ideality factor, which is 1 for the ideal case (Eq. 5.22), and takes values between 1 and 2 according to the SRH recombination model (Chapter 2).

A J-V curve measured under illumination for a generic CIGS solar cell is presented in Fig. 5.8, where it is shown that it is quite simple to extract the characteristic electrical parameters of a solar cells, being the most important ones:

i) short-circuit current density (J_{SC}): the photogenerated current that flows trough the solar cell when $J_{diode} = 0\,\mathrm{mA.cm^{-2}}$ ($V = 0\,\mathrm{mV}$, $R_S = 0\,\Omega\mathrm{cm}^2$, and $R_{SH} = \infty\,\Omega\mathrm{cm}^2$).

ii) open-circuit voltage (V_{OC}): at open circuit condition, $J = 0\,\mathrm{mA.cm^{-2}}$.

iii) fill factor (FF): describes the area of the J-V curve given by the point (J_m,V_m). For each point on the J-V curve, the output power may be calculated from $P_{out} = J.V$. At one point, P_{out} will reach a maximum, P_m, where $P_m = J_m.V_m$. The FF may be obtained as

$$FF = \frac{J_m V_m}{J_{SC} V_{OC}}. \tag{5.24}$$

The three above mentioned electrical parameters, J_{SC}, V_{OC}, and FF, are used to estimate the power conversion efficiency (η) of the solar cell device:

$$\eta = \frac{J_M V_M}{P_{inc}} = \frac{J_{SC} V_{OC} FF}{P_{inc}}, \tag{5.25}$$

which is the ratio between the maximum produced electrical power and incident illumination power, P_{inc}.

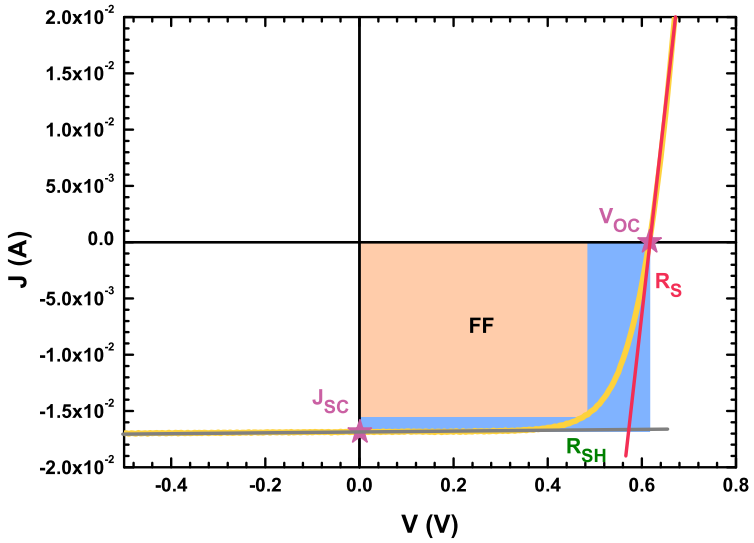

Figure 5.8: Current density-voltage curve of a generic CIGS based solar cell. The points corresponding to the V_{OC} and J_{SC} values are indicated by stars. The methods to extract FF, R_S, and R_{SH} are also schematically shown.

Experimental consideration: Completed solar cell were characterized by J-V measurements with AM1.5 illumination in a home-built system. The solar cell is illuminated and the current is measured as a function of the applied voltage.

5.4 In Summary

The studied CZTS based solar cells were fabricated in TFPR at Aveiro University following a two steps process, sulphurization of evaporated/sputtered multi-stacked precursors. We studied samples based on CZTS growth with different multi-stacked sequences sulphurized by different methods. On the other hand, the studied solar cells based on co-evaporated CIGS were fabricated according to the ÅSC solar cell baseline. Different compositions, Ga-profiles, and architectures, were implemented in the studied samples based on CIGS. The carried studies during this work are result of

cross-interpretation of several complementary techniques in order to understand the optoelectronic properties of the studied devices. For CZTS samples the studies were performed in order to understand the overall morphological and structural properties and to correlate them with the optoelectronic properties. Thus, SEM, EDS, XRD, and Raman spectroscopy techniques were used in order to obtain the information needed to correlate with the PL results. On the other hand, for CIGS based solar cells the carried studies were focused on the correlation of electrical performance with the electronic energy levels structure and the dynamics of the charge carriers. Thus, PL, EQE, and J-V were used. In the next two Chapters the presented samples will be deeply studied using the mentioned characterization techniques.

Chapter 6

CZTS based solar cells

A fundamental characterization of the defects present in the CZTS thin films and their influence on the electronic energy levels structure is presented in this Chapter throughout different studies. The combination of these results with the structural characterization and electrical performance of the devices enabled for an overview of the role of the defects in this technology.

Throughout this thesis, different issues related to fundamental properties and to technological aspects of CZTS have been identified. From the fundamental point of view, CZTS always contains some degree of structural disorder, resulting from an atomic exchange between Cu and Zn. The fact that CZTS is a quaternary compound with a narrow phase stability region, in addition to the mandatory non-stoichiometric composition for solar cells application, favours the appearance of secondary phases and greatly increases the density of defects. Thus, CZTS is characterized by a strong self-doping and high compensation [28, 302, 354]. The interaction between defects, with relevance for the donors, and the low value of the dielectric constant, will promote the appearance of electrostatic fluctuating potentials along the film [308], which may influence the electronic energy levels structure and the dynamics of the charge carriers in the material [302, 333, 409, 410]. An accurate knowledge of the electronic energy levels structure is fundamental to address the three main steps in the working process of a solar cell: absorption, charge carriers separation, and charge carriers collection. Thus, it is mandatory to cross information between the physical characterization of the materials and the growth methods in order to find new approaches that might further increase the electrical performance of the devices. PL is a well suited technique to study the effect of defects on the electronic energy levels structure, and gives important insights concerning the radiative and non-radiative electronic transitions in the material, which is very relevant for optoelectronic applications, like in PV. In this Chapter, we explore the potential of the PL technique, complemented with structural analysis, in order to study the influence of defects on the optical properties of solar cells based on CZTS. We critically analyse the recombination mechanisms in face of the performance of the solar cells.

6.1 Comparison of fluctuating potentials and donor-acceptor pair transitions in Cu-poor CZTS

In the literature, two of the models used to discuss the luminescence in Cu-poor CZTS are i) DAP transitions [411, 412, 413], and ii) transitions involving tail states created by fluctuating potentials [225, 302, 306, 354, 374, 379, 381, 414]. As discussed in Chapter 4, the origin of the radiative transition depends strongly on the doping level of the material as well as on the degree of compensation [48]. For DAP transitions, the doping level must be low and thus, the interaction between defects is not significant. Therefore, the charge carriers are located in discrete levels inside the bandgap. In the case of highly doped and strongly compensated semiconductors, a large concentration of charged defects exists. The interaction of these randomly distributed defects results in electrostatics fluctuating potentials along the film, resulting in the appearance of tails states in the bandgap. These fluctuations influence the structure of the electronic energy levels with severe consequences on the radiative transitions channels [48].

In order to understand if the Cu-poor CZTS characteristic luminescence is compatible with a lightly doped semiconductor or with a highly doped one, we studied a solar cell assuming the two aforementioned radiative transition models: DAP and fluctuating potentials.

The studied solar cell is based on a CZTS thin film deposited on a Mo-coated SLG substrate and prepared on a conventional two steps approach: i) sputtering/evaporation of $8\times$ (Zn/SnS_2/CuS) multi-stacked precursors; ii) rapid thermal processing (RTP i) [277, 281]. Atomic ratios of [Cu]/([Zn]+[Sn])= 0.81 and [Zn]/[Sn]= 0.99 were obtained by EDS.

XRD measurements were performed to evaluate the structural properties of the samples (see Fig. 6.1 a)). Several diffraction peaks are seen, including the ones from the Mo layer (40.3° and 73.4°) and from the optical window layer (SnO_2 at 26.2°). The main peaks of CZTS ((112), (204) and (312) reflections) are present. However, it is well known that these peaks may be superimposed with other phases like cubic-CTS and cubic-ZnS. CZTS and these two secondary phases, have similar structure and unit cell size, which results in the superposition of diffraction peaks from the mentioned phases. Thus, the identification of the CZTS phase was performed by the observation by the unique tetragonal peaks at 16.1°, 18.0°, 29.5°, 33.7° and 69.1° [302]. With the XRD data and according to Eq. 5.3, we estimated the lattice parameters to be $a = 5.454\,\text{Å}$ and $c = 10.95\,\text{Å}$, which allows us to calculate the ratio $c/2a = 1.004$, showing that the cell is tetragonal, and in accordance with the literature for CZTS, presented previously in Table 3.4. Furthermore, we also performed Raman spectroscopy to evaluate the presence of secondary phases. In order to overcome the discussed limited depth penetration of the laser beam in this characterization technique [28], we performed top surface and cross-sectional measurements (see Fig. 6.1 b)). No significant differences are observed between those measurements. In both cases, we can observe the CZTS vibration modes at 251.3, 287.2, 339.0, 348.2 and 366.1 cm^{-1} [302]. The peak at 302.8 cm^{-1} corresponds to CdS, since the measurements

were performed in the full device. No evidence is found for the presence of CTS and ZnS secondary phases in the scrutinized layer. The only small evidence of secondary phases are the two peaks at 215.4 and 219.5 cm^{-1}, which could be related to SnS_2 and SnS phases, respectively. However, due to its very low relative intensities and the fact that no evidences were seen in XRD, the amount of possible secondary phases in the absorber layer is at most residual.

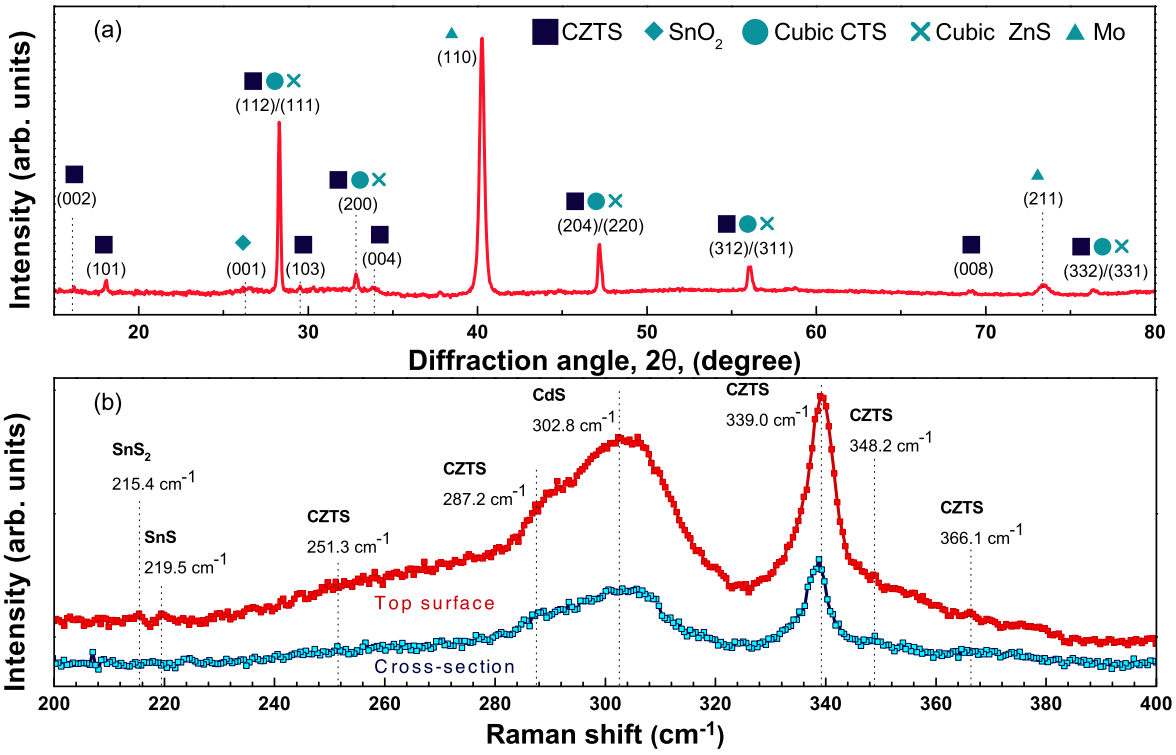

Figure 6.1: a) XRD diffractogram and b) Raman spectra measured on the top surface, and on a cross-section configuration, of a Cu-poor CZTS based solar cell.

Figure 6.2 shows the normalized PL spectra taken at 7 K and with excitation power values in the range 0.6-100 mW. The observed luminescence corresponds to a broad and asymmetric band. For an excitation power of 100 mW, the peak energy and the FWHM are ∼1.22 eV and ∼0.16 eV, respectively. On the low energy side of the luminescence, an approximate exponential decrease is observed, whereas on the high energy side, the intensity decrease is more abrupt. This band shows a deviation of ∼0.28 eV from the assumed bandgap energy (1.5 eV, at room temperature) for CZTS. The characteristics of the luminescence are close to the ones described in the literature by different authors for CZTS based samples [277, 302, 374, 381, 415].

The dependence of the PL on the excitation power allows for the discussion of the nature of the radiative transitions [344, 345]. Thus, as the excitation power increases, a blueshift of the luminescence and a slight decrease of the FWHM values occurs. This effect takes place with no significant change on the shape of the band. In order to analyse the dependence of the luminescence on the excitation power, all PL spectra were fitted with two Gaussian components, following the Gaussian model discussed

previously in Subsection 5.3.4. In Fig. 6.3 a), it is shown the dependence of the peak energy of the luminescence on the excitation power. In the literature [347, 348], this dependence is often described by Eq. 4.15. However, this model only describe the experimental points that, for the log representation in Fig. 6.3 a), are in the linear regime observed for the lower excitation power values range. In that regime, a value of $\beta = 11 \pm 1$ meV was obtained.

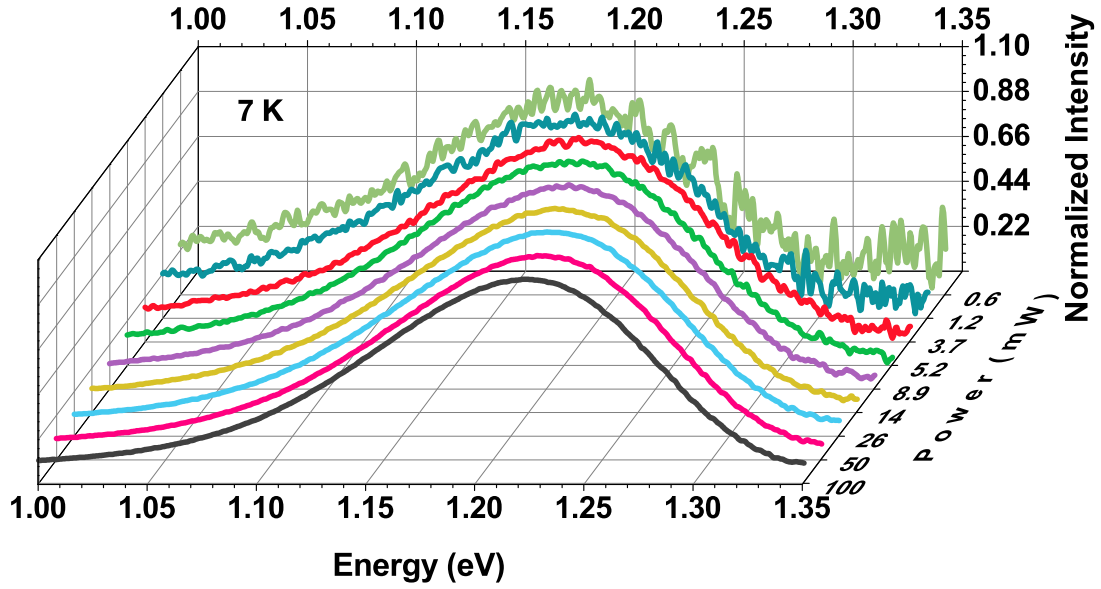

Figure 6.2: Photoluminescence spectra measured at 7 K of a Cu-poor CZTS solar cell for different values of the excitation power. The values of the PL intensity are normalized to the maximum value in each spectrum.

Assuming that the studied sample is lightly doped, and taking into account the DAP recombination model for the case of sufficiently distant pairs, a broad band is expect to be observed [339]. Following the latter assumption, Zachs and Halperin [416] proposed an analytical expression for the relation of the excitation power with the peak energy, Eq. 4.12. As is shown by the gray dashed line in Fig. 6.3 a), Eq. 4.12 is unable to describe the experimental data in the lower excitation power regime. Even if we consider valid the fit shown in Fig. 6.3 a), and assuming a value of $E_g = 1.5$ eV, an estimated value of E_D-$E_A = 2.35$ eV is achieved. A value of E_D-E_A higher than the bandgap energy has no physical meaning. Additionally, no sharp lines are observed in the high energy side of the broad band [339]. Thus, the DAP recombination model may not be able to explain the observed luminescence.

The dependence of the PL intensity on the excitation power (see Fig. 6.3 b)) may be parameterized by Eq. 4.16 [341]. The data evidences a decrease of the slope for the higher range of used excitation powers. This behaviour is commonly observed when more than two orders of magnitude are studied [341]. The deviation from Eq. 4.16 may be interpreted as a progressive saturation of the energy levels involved in the radiative recombination. The estimated value for the low (A) excitation power regime was $m_A = 1.03 \pm 0.06$, which is compatible with the values close to 1 obtained by other

authors for highly doped chalcogenide materials [102, 306, 346]. In this case, it is not straightforward the conclusion of possible localization of the two charge carriers, since the obtained value close to 1 is in the transition between the two regimes as discussed in Section 4.2.3.

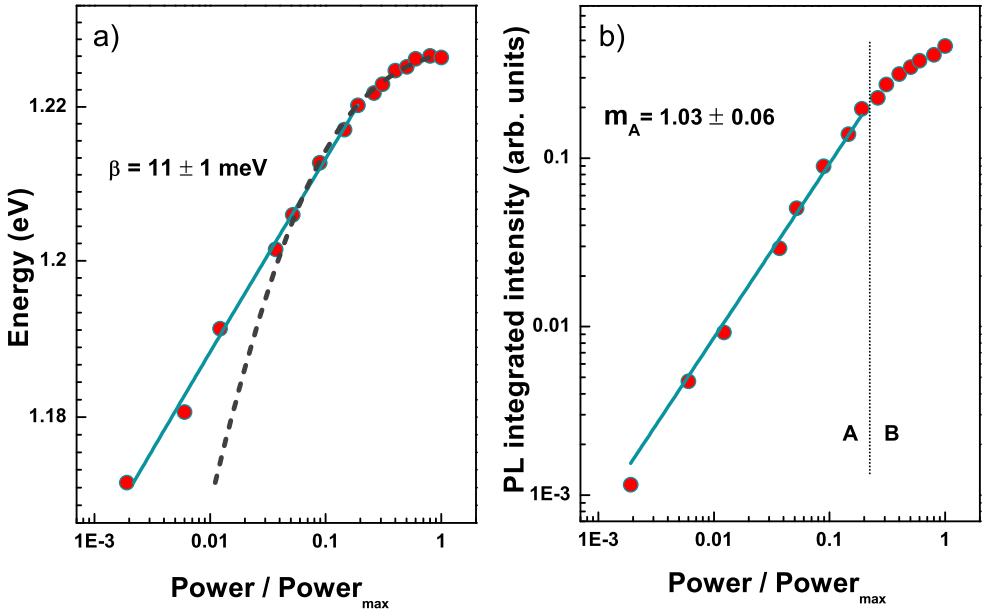

Figure 6.3: Dependence of the a) peak energy and b) PL integrated intensity of the luminescence from a Cu-poor CZTS based solar cell on the excitation power. The excitation power values were normalized to the maximum one (100 mW). The solid lines in a) and b) represent the fits of Eqs. 4.15 and 4.16, respectively, to the experimental points. The dashed line in a) corresponds to the fit of Eq. 4.12 to the experimental points. A and B in b) identifies the low and high excitation power regimes, respectively.

Previously, in the structural analysis it was discussed the possible presence of four secondary phases: CTS, ZnS, SnS and SnS_2. From these phases, CTS and SnS have bandgap values in the range (∼0.96 - 1.07 eV) [250, 257], which is lower than the value of CZTS peak energy. Thus, the expected related luminescence to those two secondary phases should present in the low energy side of the observed asymmetric band. However, we should note that for the energy range 0.8 - 1.1 eV, the detectivity of the Ge detector is high and no additional component was observed in our study (see Fig. 6.2). In fact, if the observed luminescence is composed of more than one component, with origin in different phases, it is expected a different dependence on the excitation power, which will result in a modification of the shape of the whole luminescence. This effect was not observed in this study. Concerning the other two possible secondary phases, the bandgap is much higher than the one of CZTS and no influence on the measured luminescence is expected. Therefore, PL also may contribute to the study of the structural properties, and for this particular case, it supports the conclusion from XRD and Raman spectroscopy measurements that the possible presence of those secondary phases is residual and that they have no optoelectronic effects [28].

The study of the dependence of PL on excitation power is an essential tool for the understanding of

the radiative recombination and it contributes for the distinction between transitions involving DAP and fluctuating potentials [225]. In the case of DAP transitions, it is expected that, as the excitation power increases, distant pairs become saturated and progressively closer ones will be populated, which will cause a blueshift of the luminescence according to Eq. 4.11 [339, 416]. However, this equation is unable to describe the whole set of data (see Fig. 6.3 a)). On the other hand, the dependence on the excitation power of the peak energy in highly doped semiconductors shows a strong blueshift, which may be explained by two arguments, state filling and/or screening effect, as it will be discussed bellow. The estimated value of $\beta = 11$ meV is higher than the common values found for DAP transitions reported for other semiconductors [309, 348, 417]. Furthermore, the shape of the band is clearly asymmetric, being described by an high FWHM (0.16 eV). Thus, the observed CZTS luminescence, which follows at great extent the characteristic luminescence observed by other authors [277, 302, 374, 381, 415], is typical of radiative transitions involving fluctuating potentials.

Now that we have established that the obtained CZTS luminescence is fully explained by the fluctuating potentials model, the remaining question is whether this β value of 11 meV due to state filling or screening of electrostatic fluctuating potentials. This question does not have a straightforward answer, since both phenomena should coexist and they are strongly dependent on the density of generated charge carries. Moreover, it is not clear what is the real meaning of the impact that the prevalence of one over the other phenomenon has on the optoelectronic properties of the device [346, 359]. In order to address the aforementioned question, Fig. 6.4 shows the dependence of the PL spectra on the excitation power normalized to a value on their low energy side, $\sim$1.14 eV. The two spectra measured with lower excitation power values shown in Fig. 6.2, are not considered in the following discussion due to the low signal-to-noise ratio, which hinders an accurate comparison with the remaining spectra. Increasing the excitation power, it is clear that the slop of the low energy side of the spectra remain roughly unaltered, and the high energy side progressively shifts to higher energies until it stabilizes for 100 mW. At this point, it must be noted that the low energy side of the luminescence follows the density of states of the tails states, that should decrease if the electrostatic fluctuating potentials are progressively screened. Then, a screening effect should be followed by a progressive change in the low energy side of the luminescence. Thus, the obtained result suggests that the density of states does not change significantly, as expected in the case of screening effect [346]. Thus, the blueshift may be explained by the state filling of energetically higher states considering tail states with different depth in the bandgap of the studied sample. The deeper ones are separated by longer distances and are statistically less probable. For a lower excitation power regime, populating these deeper wells is favoured. The increase of the excitation power will promote populating more shallow tails states, which have a higher density. This change from deeper to shallower tail states is reflected on a blueshift of the luminescence.

Regarding the dependence of integrated intensity on excitation power, the obtained slope ($m = 1.03 \pm 0.06$) is a transition value between the regimes from localized to non-localized charge

carriers [302, 341]. The existence of electrostatic fluctuating potentials along the film with the resulting formation of tail states within the bandgap will allow some degree of localization of the charge carriers, compatible with the estimated value of m. The observed behaviour of the luminescence supports that the radiative transitions in Cu-poor CZTS are influenced by electrostatic fluctuating potentials.

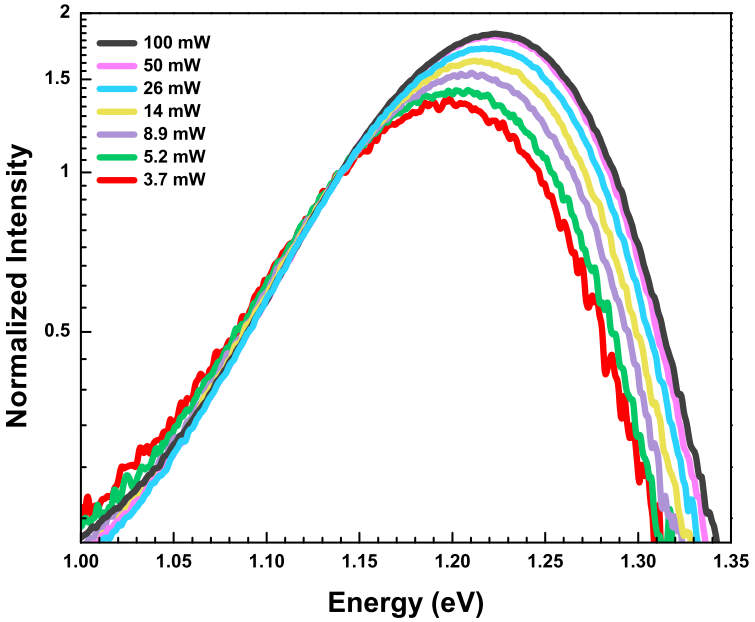

Figure 6.4: Photoluminescence spectra measured at 7 K of a Cu-poor CZTS based solar cell, for different values of the excitation power. The values of the PL intensity are normalized at the energy of ∼1.14 eV on the low energy side of the luminescence.

This study showed that PL gives strong contributions to both, structural identification and understanding of the electronic properties of CZTS. In the first case, the PL results allow us to infer that there are no evidences of secondary phases as supported by XRD and Raman spectroscopy. Concerning the radiative channels, we performed an investigation of the dependence of the PL on the excitation power and compared our results with two theoretical models: DAP transitions and fluctuating potentials. The asymmetric shape of the band, a large blueshift ($\beta = 11 \pm 1$ meV) and a m parameter ($m = 1.03 \pm 0.06$) close to 1 are compatible with a highly doped and compensated material for which the radiative transitions are influenced by the occurrence of fluctuating potentials. Clearly, our results are not in accordance with the DAP model. Thus, the influence of fluctuations was shown, discussed and proved to fully explain of the experimental observations. From this point on, radiative and non-radiative recombination channels in the studied samples will be discussed according to recombination transitions involving the fluctuating potentials model.

6.2 Recombination involving deep defects in CZTS thin films

The possible types of point defects occurring in a CZTS film, are huge due not only to the fact that we are dealing with a quaternary compound, but also due to the influence of the non-stoichiometric composition, Na doping, and an unavoidable atomic disorder on the cation sub-lattice [235]. Several theoretical works considered first-principles calculations of the enthalpic energies of formation of several types of defects, like vacancies (V_{Cu}, V_{Zn}, $\cdots$), antisites (Cu_{Zn}, Zn_{Cu}, Zn_{Sn}, $\cdots$), interstitials (Cu_i, Zn_i, $\cdots$), and complex defects involving some of the previously mentioned point defects [234, 242, 262, 287]. The results show that the enthalpy of formation is low for example, for the V_{Cu} and Cu_{Zn} defects. Regarding experimental techniques, different ones were used to tentatively identify some of the defects. In particular, PL measurements were performed by several groups and the extracted energy levels of defects involved on the radiative transitions have been compared with the calculated values [271, 302, 308, 354]. On average, all available theoretical and experimental data, point to a high probability of occurrence of different types of defects of donor and acceptor nature, in a large energy range. Despite this complex picture, the improvement of the performance of devices depends critically on the deepening of knowledge on the influence of defects on the electronic energy levels structure of the alloy [242].

Two CZTS thin films were grown by sulphurization (RTP i) of $8\times(Zn/SnS_2/CuS)$. The precursor layers were deposited on Mo-coated SLG substrates, the maximum sulphurization temperature was 550° C and the time at maximum temperature was 1 min (sample A) or 2 min (sample B). The CZTS thickness of sample A (B) was $\sim 1\,\mu$m ($\sim 0.7\,\mu$m). More details on the overall preparation of the samples are given in Section 5.1 and in Sousa *et al.* [281]. The composition ratios of the samples A (B) were $[Cu]/([Zn]+[Sn]) = 0.78$ (0.81) and $[Zn]/[Sn] = 0.87$ (0.99). Previous evaluation of the solar cells' performance revealed efficiencies of 3.1% (1.8%) for sample A (B).

In order to evaluate the crystalline phases in the absorber layer, Raman spectroscopy was performed on the surface of both solar cells. The spectra presented in Fig. 6.5 are dominated by the main vibration modes related to the CZTS kesterite phase [27, 218, 267] at 288.9 and 338.6 cm^{-1}, and reveal also the vibration mode at 304.0 cm^{-1} characteristic of the CdS phase due to measurements done in samples with the CdS layer. A few other peaks with low relative intensity are related with the CZTS phase. The possible presence of secondary phases deep in the films was tentatively investigated for both samples in a cross-section configuration. The spectra in Fig. 6.5 show a reduction of the signal-to-noise ratio, which is ascribed to a reduction of the effective excitation power on the thin film. We note that the laser spot diameter is of the order of magnitude of the thickness of the absorber layer in both samples. The observed vibration modes are roughly the same as for the measurement on the surface of the samples, suggesting that the only phase present is CZTS.

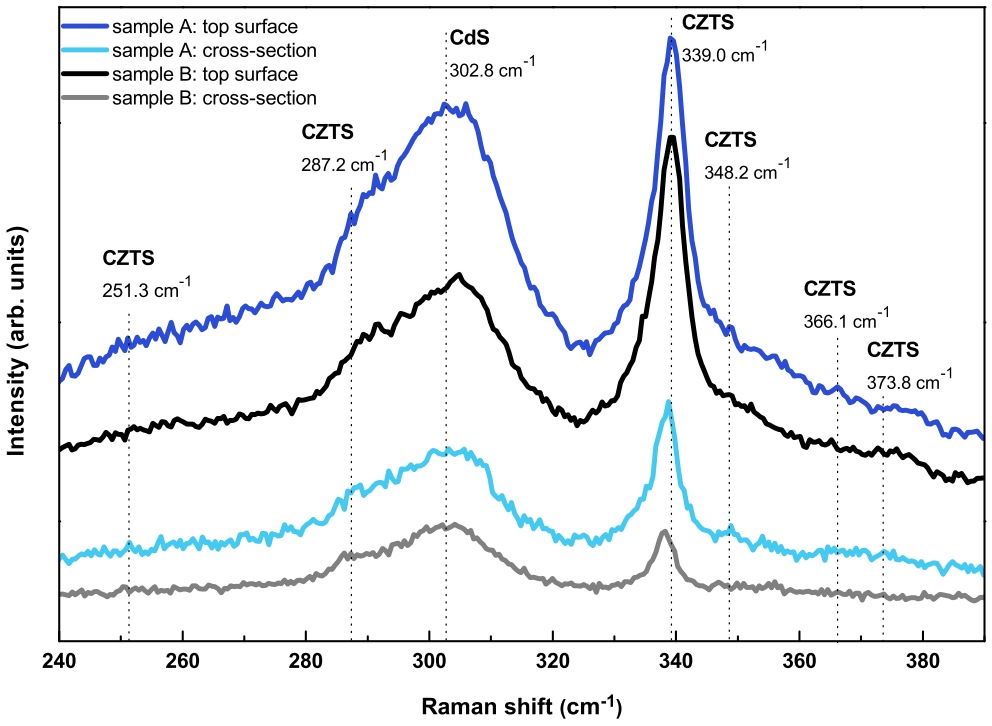

Figure 6.5: Raman spectroscopy spectra measured on the top surface of the samples and on a cross-section configuration.

The PL spectra of the two samples, measured at 7 K under equivalent experimental conditions, are presented in Fig. 6.6. The luminescence for both samples is dominated by the usual asymmetric band with peak energy at ∼1.22 eV that extends to lower energies. This band overlaps with two other bands at ∼0.92 eV and ∼1.42 eV with much lower relative intensities as shown in the inset of Fig. 6.6. Despite the necessarily different optical alignments in the measurements of the two samples, the intensity of the dominant band at 1.22 eV is clearly higher for sample A than for sample B. The study of the dominant band at 1.22 eV requires the deconvolution of the different radiative transitions through a fitting procedure. The inset in Fig. 6.6 illustrates the model considered for sample A, which is similar to the one used for sample B. The band at 1.22 eV is described by two components, the asymmetric band at 0.92 eV by other two components and the band at 1.42 eV by a fifth component. The analysis of the luminescence will be focused on the band at 1.22 eV, which originates from the CZTS phase as discussed below.

The investigation of the nature of the radiative transitions may requires the study of the influence of excitation wavelength, temperature, and excitation power on the luminescence. For the first dependence (not shown), wavelengths of 457.9 and 514.5 nm were used. No mensurable differences were observed on the shape, PL intensity and peak energy of the band. For the other two dependencies, the temperature and the excitation power values were changed in the ranges 7-280 K (for an excitation power of 100 mW), and 0.1−240 mW (at 7 K), respectively.

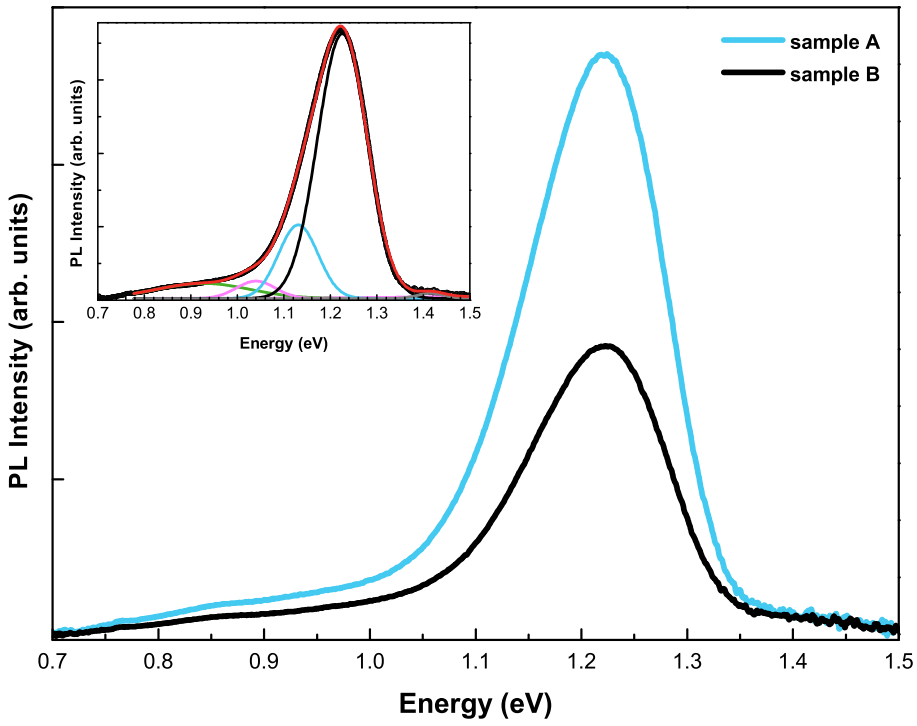

Figure 6.6: Comparison of photoluminescence spectra of both samples measured at 7 K for measurements in similar experimental conditions. The excitation wavelength was 514.5 nm with an excitation power of 120 mW. The inset illustrates the fitting model used in the analysis of the radiative transitions for sample A.

The dependencies on the temperature of both, peak energy and PL integrated intensity, of the band at 1.22 eV, are shown in Fig. 6.7. A similar behaviour was obtained for both samples: for sample A (B) a redshift of 24.7 meV (21.1 meV) is observed for the increase of the temperature in the range 7-100 K, followed by a blueshift of 32.8 meV (34.7 meV) until 280 K. The PL integrated intensity evidences a small decrease in the range 7-30 K whereas for higher temperatures, a strong thermal quenching occurs. The quenching of the PL intensity with increasing temperature can be interpreted considering the thermal activation of non-radiative channels [400]. The increase of the thermal energy will contribute to the release of charge carriers from the radiative energy state to one or more discrete excited energy states, or to a band. The discrete energy levels may describe excited states of the radiative optical center or be related to other defects present in the sample. Different models were tested according to Eq. 5.12 and the best one consisted in the lower number of de-excitation channels that describe the experimental data. For the two samples, the same model was found: two non-radiative de-excitation channels, one involving a discrete level (activation energy E_1) and another channel involving a band (activation energy E_{bx}). For sample A (B) the obtained values for E_1 and E_{bx} were 4 ± 0.3 meV (4.0 ± 0.9 meV) and 27 ± 1 meV (21 ± 4 meV), respectively. The obtained parameters from the fit of Eq. 5.12 to the data are presented in Table 6.1.

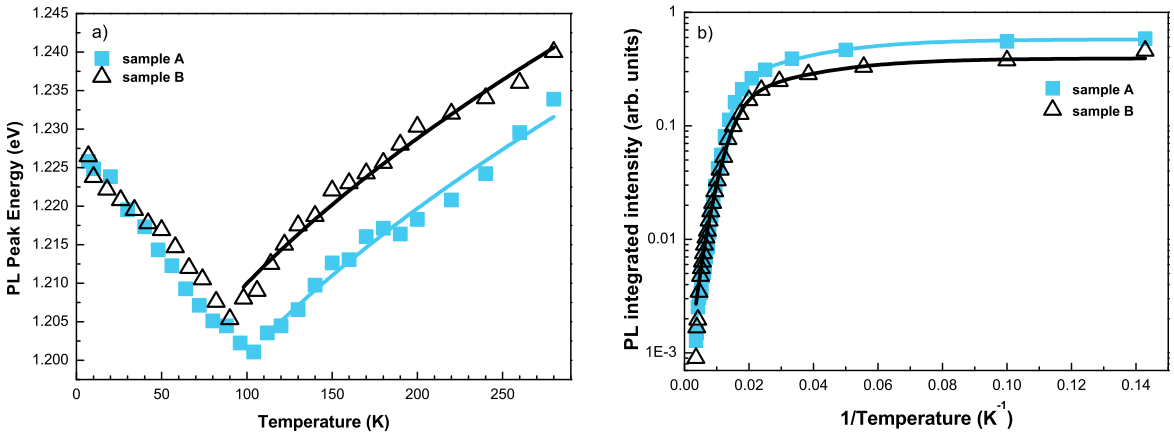

Figure 6.7: Dependence of a) the peak energy and b) the PL integrated intensity of the band at 1.22 eV on the temperature. The curves shown in a) and b) represent the fits of Eqs. 4.20 and 5.12 to the experimental points, respectively.

Table 6.1: Values of the parameters obtained in the fitting of Eq. 5.12 to the data related to the temperature dependence of the PL intensity of the band at 1.22 eV (see Fig. 6.7 b).

Sample	I_0	c_1	E_i (meV)	c_{bx}	E_{bx} (meV)
A	0.577 ± 0.004	2.6 ± 0.2	4.0 ± 0.3	3.4 ± 0.7	27 ± 1
B	0.393 ± 0.006	2.3 ± 0.9	4.0 ± 0.9	1.2 ± 0.8	21 ± 4

The dependencies on the excitation power of both, peak energy and PL integrated intensity, of the band at 1.22 eV are shown in Fig. 6.8. Again, for both samples, similar behaviours were observed. Increasing the excitation power until 80 mW, it is observed for sample A (B) a blueshift of 60.7 meV (55.0 meV), corresponding to a shift of 23.1 meV/decade (20.9 meV/decade), whereas for higher values of excitation power a redshift of 6.7 meV (6.3 meV) is observed, corresponding to a shift of 14.1 meV/decade (15.9 meV/decade), respectively. Values of the same order of magnitude were previously reported for CZTS [302, 379].

Regarding the dependence on the excitation power of the PL integrated intensity (Fig. 6.8 b), the experimental points of both samples evidence two linear regimes that can be fitted by Eq. 4.16 [341]. For sample A (B), the estimated values are $m_1 = 1.15 \pm 0.04$ (1.19 ± 0.01) and $m_2 = 0.79 \pm 0.03$ (0.64 ± 0.04), for the lower (regime 1) and higher (regime 2) excitation power values, respectively. The decrease of the estimated values for the m parameter from regime 1 to regime 2 may be ascribed to a progressive saturation of the optical centers responsible for the luminescence.

For excitation power values higher than 140 mW, we observed a negative slope. This is an unexpected behaviour, because with increasing excitation power it is expected an increase of the concentration of optical centers in the excited state, being possible to achieve a complete saturation of them. This effect will be reflected in a null slope and no reduction of the measured intensity is foreseen. The

observed redshift (Fig. 6.8 a) is explained if we assume an increase of the temperature of the thin films for the higher values of the excitation power. Indeed, a redshift was observed for the lower range of temperatures (see Fig. 6.7 a). This assumption is compatible with the low thermal conductivity of the SLG substrate, which prevents an efficient cooling of the sample. Another expected consequence of the increase of temperature is a small thermal quenching of the PL intensity, as shown by the experimental points in Fig. 6.8 b). The increase of the sample's temperature by illumination is a well known process that also occurs in solar modules.

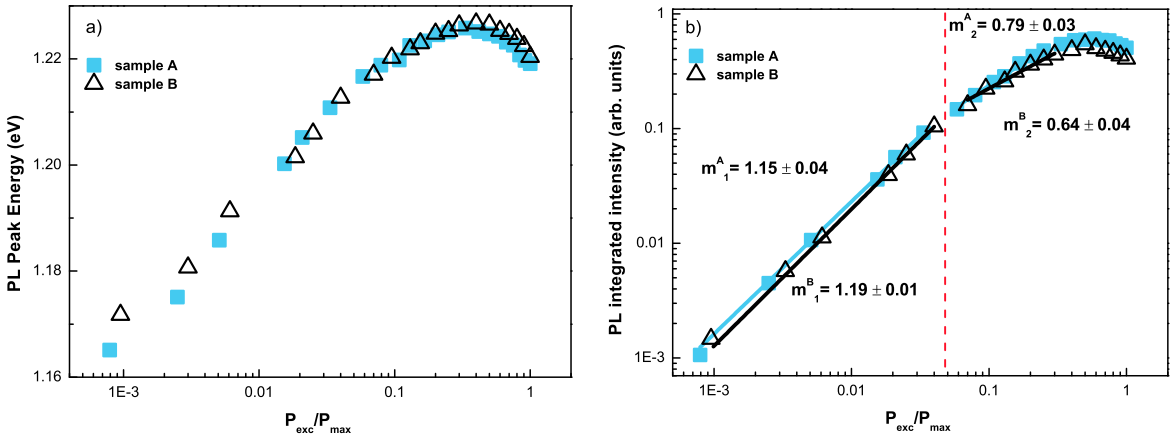

Figure 6.8: Dependence of the a) peak energy and b) PL integrated intensity of the band at 1.22 eV on the excitation power, measured at 7 K. The excitation power values were normalized to the maximum one (240 mW). The curves shown in b) represent the fit of Eq. 4.16 to the experimental points.

Concerning the observed PL, the asymmetric shape of the band at 1.22 eV remains approximately the same for the whole range of temperatures and excitation power values. In the case of the temperature dependence of the peak energy, a redshift in the range 7-100 K followed by a blueshift is observed (Fig. 6.7 a). Concerning the redshift, it cannot be ascribed to a temperature effect on the bandgap energy, because the observed shift is much higher than the one observed experimentally [418, 419]. Actually, in that work, the data showed almost no change of the bandgap energy in the range 7-100 K which is compatible with a high doping level as expected for the semiconductor [293]. The experimental behaviour in the investigated temperature range (7-280 K), is different from previous works presented in the literature in the scope of BI transitions [48, 302, 360]. Despite this, we performed a fit (not shown) of the experimental data on the low energy side of the luminescence (1.10-1.20 eV) with the theoretical equation that describes the BI transition in that range of energy values [302]. The fitting parameters for both samples gave estimated bandgap energy values of 1.27-1.30 eV, which are clearly lower than the bandgap energy values reported in the literature [14, 154, 230, 420, 421]. Due to the bandgap energy difference and the dual red and blueshift behaviour, the BI transition model does not fit into our results. Indeed, they are consistent with a TI transition as follows [342]. The lower limit (7 K) of the investigated temperature range was not low enough to allow for the observation of the predicted blueshift for values close to the absolute zero. The observed behaviour of the PL,

consisting in a shift to lower and after that to higher energy values, is only possible if the excitation rate is low enough. This behaviour is a consequence of the change of the quasi-Fermi level for electrons, that is reflected on the occupation level of donor clusters with different energy depths [342]. For temperatures higher than 112 K, FWHM increases, which is consistent with the appearance of the second type of TI transition involving electrons in shallower donor clusters (see TI_2 in Fig. 4.10). The observed blueshift can be described by Eq. 4.20 as shown by the fits in Fig. 6.7 a), being the fitting parameters $E_g^0 - I_a - \gamma_e = 1.155 \pm 0.002\,\text{eV}$ ($1.164 \pm 0.002\,\text{eV}$) and $\gamma_e = 61 \pm 5\,\text{meV}$ ($60 \pm 4\,\text{meV}$) for sample A (B). Assuming the value of $E_g^0 = 1.5\,\text{eV}$ [14, 154, 230, 420, 421], we obtain from the previous fitted parameters $I_a = 284\,\text{meV}$ (276 meV) for sample A (B), respectively. Grossberg *et al.* [271] identified a deep acceptor level with a similar ionization energy (280 meV) from an luminescence consisting in two bands ascribed by the authors to BI transitions in kesterite and disordered kesterite phases in polycrystalline CZTS films. In our work, the Raman results only give evidence for the presence of one phase (CZTS) and the PL spectra is dominated by just one band. Therefore, we assume that the dominant band at 1.22 eV is different from the luminescence observed by Grossberg *et al.* [271]. Concerning theoretical calculations, Chen *et al.* [242] proposed two defects with energy level values close to our ionization energy (V_{Zn} and Zn_{Sn}), and both have similar formation energies (0.39 and 0.36 eV, respectively), which hinders their identification. This difficulty in establishing a relation between the PL results and the defects investigated by first-principles calculations, was also highlighted by Tanaka *et al.* [379].

The temperature dependence of the PL intensity shows for lower vales of temperature a small quenching that is interpreted as the thermal activation of a non-radiative channel involving a discrete excited energy level, which is $4.0 \pm 0.3\,\text{meV}$ ($4.0 \pm 0.9\,\text{meV}$) above the radiative state in sample A (B). This lower activation energy should be related to the presence of defects that create energy levels close to the radiative states and to which the electrons can perform an electronic transition. With further increase of the temperature, a strong thermal quenching is observed which is mainly dependent on the de-excitation channel involving a band (term involving activation energy E_{bx} in Eq. 5.12). The estimated values for E_{bx} were $27 \pm 1\,\text{meV}$ ($21 \pm 4\,\text{meV}$) for sample A (B). These values corresponds to the ionization energy of the less bound charge carrier involved in the radiative transition [422]. As already discussed, the donor clusters will bind electrons just if they have a high enough number of donors. Also, the estimated values for γ_e are much lower than the ones for ionization energy of the acceptor level. So, the values for E_{bx} should correspond to the release of electrons to the percolation level.

Concerning the dependence on the excitation power of the peak energy, the observed blueshift of a few tens of meV/decade is compatible with the reported results for Cu-poor CZTS films discussed in Section 6.1. In the case of the dependence of the PL intensity (Fig. 6.8), values for the m parameter around 1 were obtained. According to Schmidt *et al.* [341], when the experimental data covers more than two orders of magnitude, which is our case, it is expected a deviation from the law in Eq. 4.16.

They also showed that with the increase of the excitation power range, the values of m decrease. The same trend is observed here. Our estimated values for m are compatible with radiative transitions involving mainly a strongly localized charge carrier (hole). Indeed, the binding energy for the electron is approximately one order of magnitude lower than the ionization energy of the acceptor level. We note that for transitions with just one localized carrier, the m values show a large spreading [341].

The investigation of the optical properties showed that the same acceptor level is the dominant defect in both samples, and the electronic levels structure are affected in a similar way by fluctuating potentials. It was shown in several works that the presence of fluctuating potentials is a limiting factor to the improvement of V_{OC} as well as of the solar cell efficiency [138, 284, 298, 423]. To decrease the influence of fluctuating potentials one would need to lower the overall density of charged defects.

For the achieved V_{OC} values of the two solar cells fabricated from samples A and B (496 and 435 mV, respectively [281]), the contribution of the electrostatic fluctuations with tens of meV is not the dominant factor responsible for the obtained V_{OC} values [284]. Indeed, the contribution of the deep acceptor (280 meV) is likely more important. In fact, for the selenide-compound, CZTSe, a similar defect level located around 130 to 200 meV was proven to be an optoelectronic active deep acceptor, which limits the performance of solar cells [304]. We should emphasize that the energy level estimated in this work is close to the value found by other authors [271]. Thus, more theoretical studies that account for the influence of both the fluctuating potentials and intrinsic lattice defects on the solar cells performance parameters, are needed. If the theoretical work would be capable of identifying the defect, then, modifications to the growth process may be suggested with, in particular, the objective to minimize the influence of the defect at 280 meV.

To summarize a detailed optical investigation by PL of two CZTS based samples was performed. Raman measurements showed that these absorber layers are dominated by the CZTS phase. No influence of the time at maximum temperature in the sulphurization step was observed on the optical properties of the CZTS based thin films. The luminescence is dominated by an asymmetric band with peak energy at 1.22 eV. The temperature and excitation power dependencies of the PL showed a strong influence of fluctuating potentials on the optical properties of the films. The radiative transitions were ascribed to a TI transition, i.e., the recombination of an electron captured by localized state in the conduction band tails and a hole localized in a deep acceptor level with ionization energy of 280 meV.

6.3 Influence of the sulphurization method on the PL of CZTS thin films

In the literature, different methods for the sulphurization of metallic precursor layers have been investigated in order to increase the control of the stoichiometry along the thin film as well as of the formation of secondary phases. Two of the most used methods are the sulphurization in a S flux [225, 277-280] or in a graphite box [220, 277, 424-427]. While in the S flux method, the sample

is exposed to an atmosphere with a constant S fraction, in the sulphurization in a graphite box the concentration of S changes along the process: increasing the temperature to values slightly higher than the one for the evaporation of S, exposes the sample to a S-rich atmosphere, and during the cooling of the sample, it is exposed to an S-poor atmosphere. It is expected that these two sulphurization methods will influence the thermodynamic of the growth and give rise to different intermediate phases, which should be reflected in the densities and type of defects created. Here, we will study the influence of density of defects on the optoelectronic properties of two solar cells based on CZTS sulphurized by two different methods.

Two solar cells with 4x (Zn/Sn/Cu) sequentially sputtered on a Mo-coated SLG substrate, were fabricated [277]. For sample A, the four periods of multi-stacked precursors were sulphurized in a tubular furnace directly exposed to a $N_2 + 5\%H_2$ flux plus S vapour. For sample B, the multi-stacked precursors were sulphurized in the same furnace, but inside a graphite box where 240 mg of high purity S pieces were placed. J-V measurements under standard test conditions provided power conversion efficiency values of 2.4% and 0.3% for the samples A and B, respectively [277].

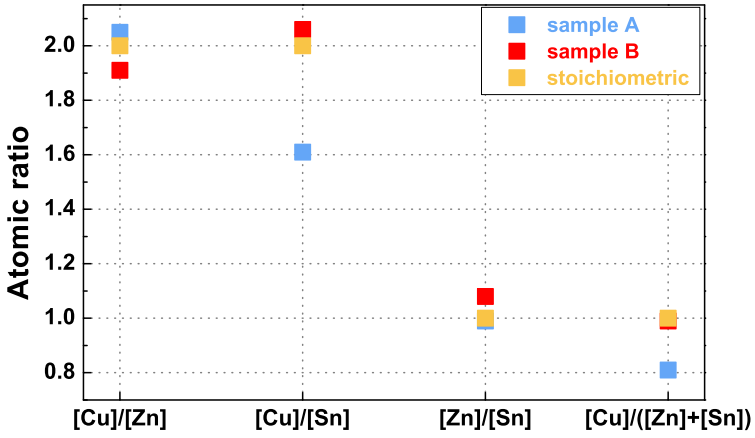

Figure 6.9: Atomic ratios of sample A and B determined by EDS measurements. The stoichiometric composition for CZTS is also shown.

The atomic ratios of the CZTS layer was investigated by EDS, and the obtained results of the two samples are shown in Figure 6.9, where they are compared with stoichiometric values. Sample A is Cu-poor and slightly Sn-rich, while in sample B all element fractions are closer to the stoichiometry. These differences in the two samples, should be related with the two sulphurization methods, since the multi-stacked metallic precursors were identical in both samples.

The different layers of the solar cells are identified in the cross-section SEM images as shown in Figure 6.10 a) and b) for samples A and B, respectively. While in sample A the absorber layer is quite compact, this is not the case for sample B. In both samples the size of the grains decrease in depth, suggesting a bilayer structure in the absorber layer. Grains with diameters of ∼0.5-1.0 μm are visible, for sample A, although smaller grains (∼0.2-0.6 μm) are observed for sample B.

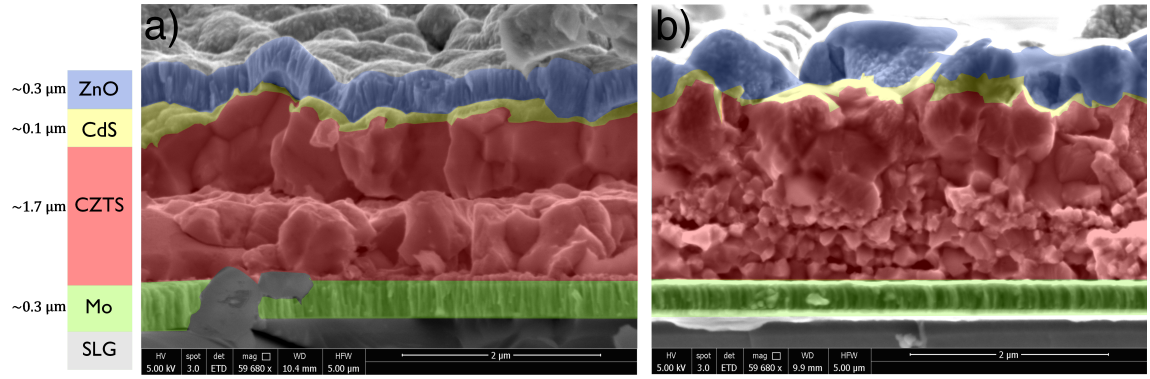

Figure 6.10: SEM images of the cross-section of CZTS solar cells showing the SLG, Mo, CZTS, CdS, and i-ZnO/ZnO:Al layers for: a) sample A; b) sample B. The estimated thickness of each layer is shown.

The structural evaluation of both samples was performed through the comparison of XRD and Raman spectroscopy measurements. Concerning XRD, the diffractograms of samples A and B are shown in Figure 6.11 a). A few peaks related with the Mo layer in the back contact of the solar cell were identified for the two samples. Both diffractograms show several diffraction peaks (16.3°, 18.2°, 23.1°, 29.6°, 36.9°, 37.9°, 44.9°, 58.9° and 69.2°) unequivocally related to the CZTS crystalline phase, which gives undebatable evidence for the formation of the CZTS. However, the origin of other peaks (28.4°, 32.9°, 47.3°, 56.1°, 76.4° and 88.0°), present in both samples, is less clear since they raise the possibility of the presence of cubic-CTS and cubic-ZnS, as discussed in Section 6.1 [27]. The contribution of Raman measurements is necessary in order to clarify this topic [27, 28]. Finally, for sample A, we must mention the observation of a diffraction peak with a high relative intensity at 15.0° and a few other peaks with much lower relative intensities, which are ascribed to hexagonal-SnS_2.

The Raman spectra for both samples, shown in Figure 6.11 b), are dominated by the CZTS related phonon modes at 288.3 and 338.0 cm^{-1}. Additional phonon modes at 252.4 and 347.1 cm^{-1}, both with small relative intensities, can also be ascribed to the CZTS crystalline phase. A phonon mode at 300.3 cm^{-1}, characteristic of the CdS phase, is also observed [27, 218, 267]. Concerning the possible presence of secondary phases, a few different positions on the surface were analysed. No other phases were identified for sample B. In the case of sample A, Figure 6.11 b) shows the Raman spectroscopy measurements for two positions. For position #1, a phonon mode at 356.0 cm^{-1}, related to the CTS, was observed, whereas for position #2, the previous CTS related phonon mode is observed in addition to a new one at 315 cm^{-1} [245], ascribed to SnS_2. Since the Raman spectroscopy is a local measurement, the presence of SnS_2 just in some positions shows that, for sample A, the scrutinized depth of the absorber layer is not homogeneous. The Raman spectroscopy results are in accordance with the XRD measurements. The presence of SnS_2 only in sample A agrees with a previous work that shows the presence of this secondary phase in CZTS with Sn-rich composition [245].

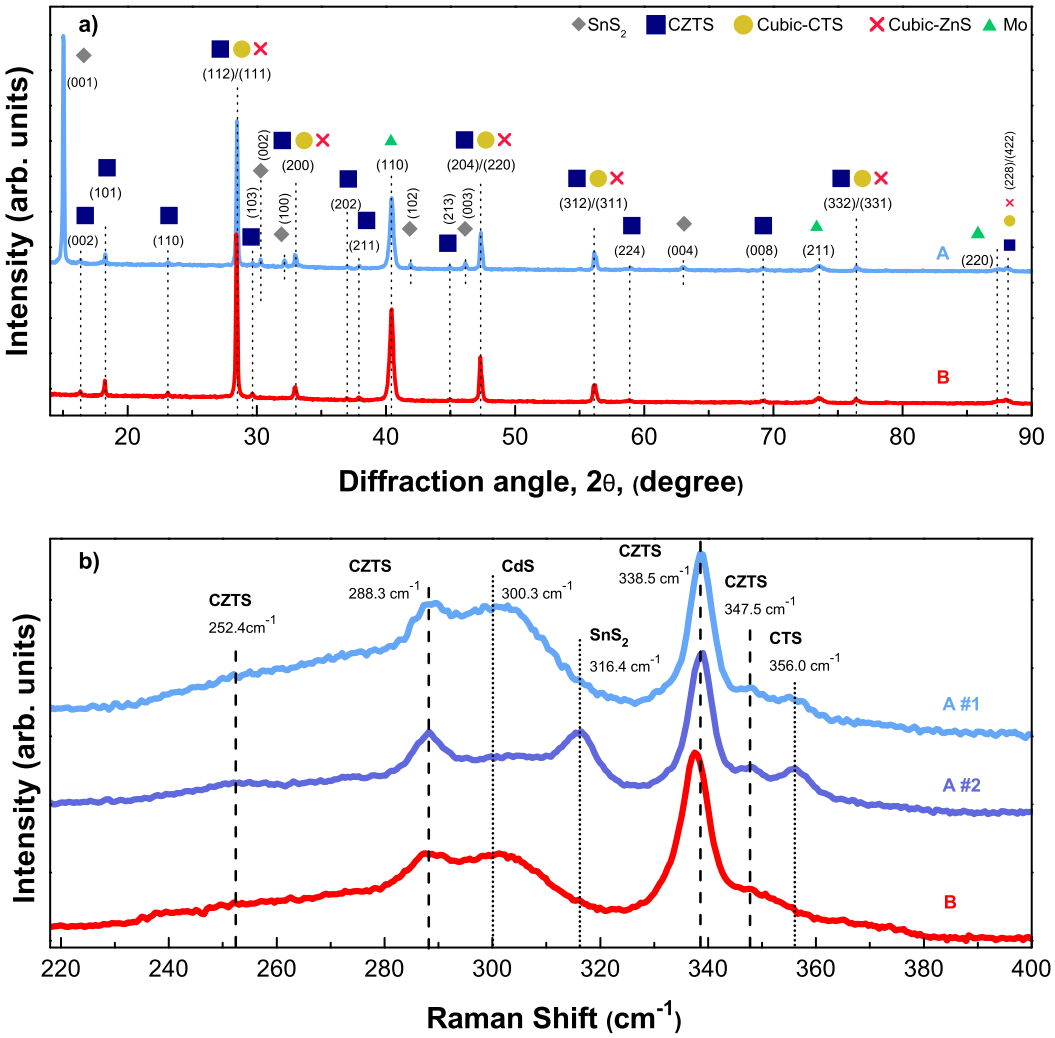

Figure 6.11: a) XRD diffractograms and b) Raman spectra measured for samples A and B. For both samples different locations were insppected and we show two different locations #1 and #2 for sample A.

Figure 6.12 a) shows the PL spectra of the two solar cells measured at 5 K, under an excitation power of 90 mW. The luminescence from sample A corresponds to a single, broad, and asymmetric band with peak energy at ∼1.32 eV. The asymmetric shape of this band becomes evident after the fit of the PL spectrum with two Gaussian components (see Figure 6.12 b)). In the case of sample B, a quite different luminescence, consisting in a broad luminescence with a low signal-to-noise ratio, was observed.

The power dependence for sample A was performed in the range 1.35–216 mW. All measured PL spectra were fitted according to the Gaussian model shown in Figure 6.12 b). For all excitation power values, the shape of the band is approximately the same and this is reflected in an almost constant ratio of the relative intensities of the two Gaussian components. Thus, we assume that the observed band is just one radiative transition, in accordance with the discussed Gaussian fitting model presented in Subsection 5.3.4 and to several reports in the literature [28, 271, 302, 306, 354, 381, 414].

This will be further discussed below. The dependence of the peak energy on the excitation power is shown in Figure 6.13 a). The increase of the excitation power until 121 mW results in a blueshift of ∼15 meV/decade, whereas for higher values, the position of the peak energy is almost constant. The dependence of the PL integrated intensity on the excitation power is shown in Figure 6.13 b). The experimental data shows two linear regimes with slightly different slopes. The two regimes (A and B) can be fitted by Eq. 4.16 [341]. The estimated values for m are 0.90 ± 0.03 and 0.50 ± 0.04 for the regime A and B, respectively. The estimated decrease of the m values should be understood as a progressive saturation of the radiative states involved in the transitions.

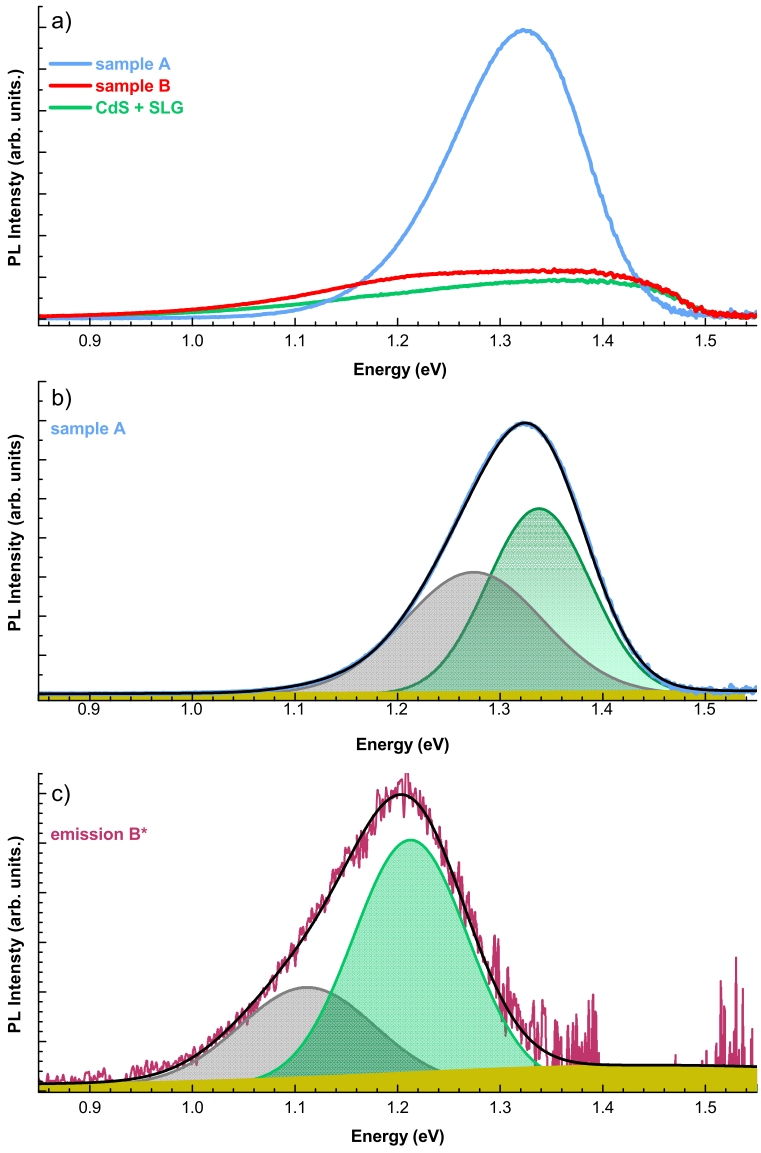

Figure 6.12: a) PL spectra measured at 5 K, under 90 mW, of samples A and B. PL spectrum of a thin CdS layer deposited on SLG, measured at 70 K under 100 mW, is also shown. b) Fitting model used in the analysis of radiative transitions for sample A. c) Fitting model used in the analysis of radiative transitions denoted by B*.

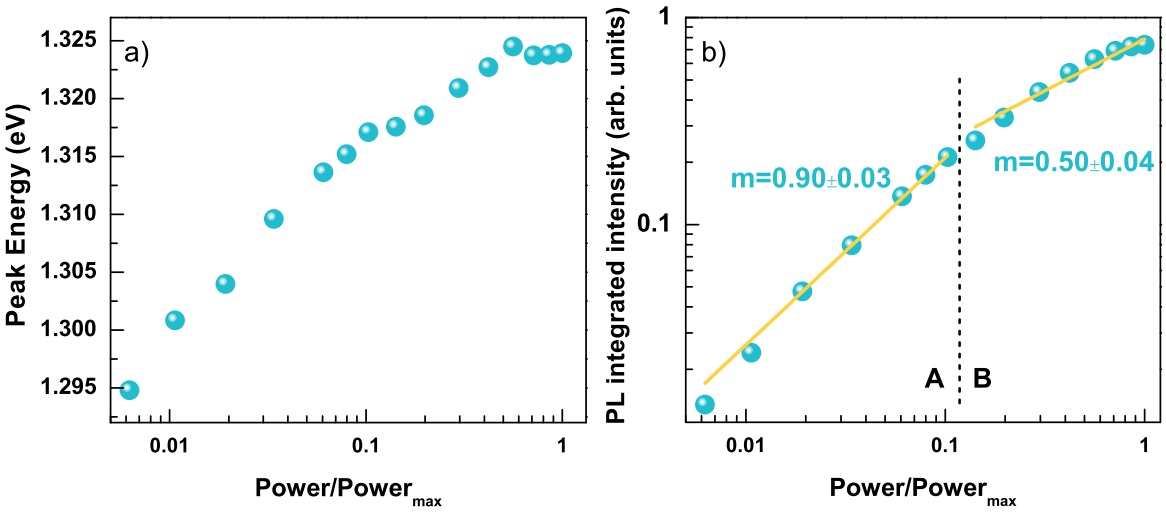

Figure 6.13: Dependence of a) peak energy and b) PL integrated intensity of the luminescence of sample A on the excitation power. The excitation power values were normalized to the maximum one (216 mW). The solid lines in b) represent the fits of Eq. 4.16 to the experimental points in the two regimes. A and B in b) identifies the low and high excitation power regimes, respectively.

We must recall that, to avoid the oxidation of the CZTS surface, the presented PL measurements were always performed in fully completed solar cells. We note that after depositing the ZnO, the PL does not change. In order to discuss qualitatively the possible influence of the buffer layer on the luminescence from both samples, PL from a thin CdS layer deposited on SLG was measured at 70 K. The latter has a quite different energy range, shape and signal-to-noise ratio from the observed luminescence from sample A as shown in Figure 6.12 a). So, we discard a significant influence of the buffer layer on the luminescence of this sample. However, the comparison between the luminescence from sample B and CdS shows evident similarities. Notwithstanding, it does not exclude the emission from the absorber layer at least in the energy range of ∼1.0-1.4 eV. A direct comparison of PL intensity from different samples should be done with caution due to the necessarily different optical alignments. Thus, only a qualitative discussion can be performed. For sample B, the result of the subtraction of the CdS PL spectrum is shown in Figure 6.12 c) and denoted as "luminescence B*". In comparison to the luminescence from sample A, it also reveals an asymmetric band with a similar shape, fitted with the same number of Gaussian curves, a much lower signal-to-noise ratio, and it is shifted to lower energies. This shift can be due to: i) the difference in the measurement temperatures of the two PL spectra; ii) the influence that a high density of grain boundaries can have in the electronic energy levels structure of the absorber layer, as discussed below.

Concerning the structural analysis for sample A, the dominant crystalline phase in the absorber layer is CZTS, with traces of SnS_2 and CTS. The bandgap values of these two secondary phases are ∼0.96 and ∼2.22-2.88 eV for CTS and SnS_2, respectively [251, 252, 253, 257]. Thus, possible radiative transitions related to CTS may be observed in the low energy side of the dominant band, whereas

for SnS_2 only very deep defects could originate mensurable radiative transitions in the energy range inspected in this study. Nevertheless, in the literature the reported SnS_2 related luminescence has a tail in the energy range ∼1.1-1.45 eV [253]. Therefore, if the observed luminescence had contributions from different crystalline phases, a modification of the shape of the luminescence with increasing excitation power is expected. Obviously, radiative transitions with origin in different phases should have different dependencies on the excitation power. Actually, no such changes were observed in the luminescence from sample A. Additionally, the implemented fitting model with two Gaussian components is similar to the ones used in literature to fit the luminescence of single CZTS phase [302, 308]. In this way, the obtained luminescence from sample A is ascribed to the CZTS. As discussed previously, a residual contribution involving deep defects on CdS cannot be excluded, but does not affect the estimated values for the blueshift of the peak energy and for the m parameter.

Regarding sample B, the luminescence is dominated by the emission from the CdS buffer layer, with a small contribution from the CZTS absorber layer (see "luminescence B*" in Figure 6.12 c)). For this sample, no secondary crystalline phases were identified in the structural analysis. The very small relative intensity of the CZTS related luminescence shows a clearly less efficient emission when compared with sample A. The penetration depth of the incident laser light is similar in both samples, because they have a similar solar cell structure and were processed in exactly the same batch of CdS and ZnO. Therefore, a higher absorption in the buffer layer in the case of sample B is not expected. A higher density of defects that create non-radiative deexcitation channels in the absorber layer should be responsible for the low signal-to-noise ratio in PL. Actually, we must recall that the EDS measurements showed that the Cu fraction is higher in sample B in contrast with sample A that is Cu-poor. Thus, the type of defects should change significantly between both samples following the differences between the two sulphurization methods. The increase of the defects density will reduce the diffusion length of charge carriers, which is reflected in a higher efficiency of the non-radiative recombination channels, and gives us a hint for a low performance of the final device. The interpretation of the optical results is compatible with electrical parameters presented by Sousa *et al.* [277]. Both samples present low values of J_{SC}, 16.5 and 11.8 mA, for samples A and B, respectively (see J_{SC}^{SQ} in Chapter 1 for comparison). Following, the argument that penetration depth of the incident laser in the PL measurements is significantly the same in both samples, we are assuming that the optical losses are roughly the same in samples A and B. Thus, the difference between the two J_{SC} values should be the result of significant differences in the efficiency of the charge carries collection. Indeed, the scrutinized CZTS region by PL should be within the SCR, and the existence of a higher density of defects, as the PL results suggest, for sample B in comparison to A, shows that sample B has a narrower SCR in comparison to sample A. Thus, in addition to the low diffusion length, the narrow SCR will deteriorate the probability of collection of the generated charge carriers in sample B, which is in accordance with the lower value of the J_{SC}. Furthermore, a huge difference was obtained in the V_{OC}, 541 and 271 mV, for samples A and B, respectively. The V_{OC} values follows the above discussion that suggest a higher impact of the

electronic losses in sample B in comparison to sample A. Indeed, an agreement between PL intensity and the performance of the device was obtained for the two samples. Thus, a low relative intensity of the luminescence related to the absorber layer is indicative for a low PV performance.

The PL discussion of the two samples suggests that the CZTS layers in both samples are highly doped and compensated. The asymmetric band, high blueshift ($\sim$15 meV/decade) and the value of $m = 0.90 \pm 0.03$, close to unity, estimated for sample A in the regime of lower excitation power values, are in accordance with the fluctuating potentials model which has been shown as the dominant radiative recombination model for CZTS [302, 308, 344, 345]. The interaction between these randomly distributed defects creates electrostatics fluctuating potentials along the semiconductor, which result in the appearance of tails states in the bandgap. Two main origins can be pointed as source of defects in CZTS: the self-doping and grain boundaries. The latter are likely locations for non-radiative recombination centers in polycrystalline thin films [198, 428] and they have been pointed out as source of limiting factors to the improvement of the V_{OC} in CZTSSe based solar cells [428-432]. Some studies point that grain boundaries in CZTSSe act as an efficient electron collection region [428, 429] whereas others found that grain boundaries promote the non-radiative recombination of photogenerated electron-hole pairs [430, 431]. Our results show smaller average grain size in sample B, in comparison with sample A (see Figure 6.10), which may be reflected in a less efficient radiative recombination of the carriers in sample B.

Two different methods (S flux and graphite box) were used for the sulphurization of identical metallic precursors. Larger average grain size and a much higher signal-to-noise ratio in the luminescence were observed for the sulphurization in S flux in comparison with the sulphurization in a graphite box. Also, a better performance of the solar cell was obtained in the first sulphurization method. Despite the presence of traces of secondary crystalline phases for the sample sulphurized in S flux, the PL is dominated by the CZTS related luminescence, whereas for the sulphurization in a graphite box a critical influence of the CdS buffer layer was observed. The dependence on the excitation power of the PL showed the presence of fluctuating potentials in the CZTS absorber layer which determines the radiative recombination channels. In addition, we also showed that the luminescence from CZTS can be superimposed by the luminescence coming from the buffer layer, which could be an issue in the interpretation of the obtained luminescence from CZTS based solar cells. Finally this study showed a clear relation between the optoelectronic properties, showing that the non-radiative recombination is in great extent harmful for the devices performance.

6.4 Influence of post-deposition annealing on the PL of CZTS thin film

From the studies presented above for solar cells based on CZTS, it is clear that the overall composition and structural properties obtained are quite satisfactory: compositions close to sate-of-art

solar cells, residual amount of secondary phases, and a morphology of samples with grains that are big enough showing compact films. However, the optoelectronic properties do not seem to follow this trend. PL showed that CZTS luminescence results from recombination mechanisms involving tails states, which is only compatible with the existence of a high density of charged defects. However, the cross information between the optical and electrical results suggests that the presence of fluctuating potentials is not the major issue, a less efficient luminescence due to non-radiative recombination or recombination involving deep defects is closely related with a poor performance of the devices. Thus, new strategies to improve the performance of CZTS based solar cells must be introduced, beyond the continuous enhancement in the CZTS growth process. Following the continuous enhancement in CIGS technology due to developments on PDT that improve the electrical performance of the solar cell [433], the same strategy have been implemented in the CZTS based solar cells [8, 434]. In this Section we will analyse the changes on the CZTS electronic levels structure after a PDA in an atmosphere of N_2.

The studied CZTS samples were grown by RTP ii of multi-stacked precursors $8\times(ZnS/SnS_2/Cu)$ deposited on Mo coated SLG. A PDA in an atmosphere of N_2, at 300 °C for 15 mins was carried out in the complete solar cell [152]. We studied two samples fabricated in the same batch, one as grown (A) and other one subject to the PDA treatment aforementioned (B).

Fig. 6.14 a) shows the PL spectra measured at 70 K, under an excitation power of 140 mW, of the solar cell with and without PDA. Prior to the thermal treatment, a broad luminescence with a low signal-to-noise ratio, is observed. The energy range and shape of this luminescence is very similar to the one measured from a CdS thin layer, deposited directly on SLG. The comparison of the two PL spectra shows that, before the PDA, mainly radiative transitions involving deep defects in CdS were observed. We must note that the excitation wavelength is close to the bandgap of the buffer layer, but allows for the optical excitation of the absorber layer as shown in the previous Sections of this Chapter [28].

After the PDA, the luminescence from the solar cell clearly changed as shown in Fig. 6.14 a). A broad and asymmetric band in the range of 0.8-1.34 eV, with maximum of intensity at ∼1.16 eV, was observed. Additionally, a higher signal-to-noise ratio was obtained. Again, the shape of the band after the treatment is close to the ones assigned in literature to Cu-poor CZTS [225, 302, 308, 344, 345, 415]. This band shows a deviation of 0.34 eV from the assumed bandgap energy at room temperature (∼1.5 eV [14, 230]) for CZTS, which is higher than the common values available in the literature, for low temperatures. This higher redshift of the luminescence may be ascribed to the higher temperature value (70 K) used for our current measurements, since it is commonly observed a redshift of the luminescence increasing the temperature up to 70 K, as shown in Section 6.2 [302, 308].

A study of the dependence on the excitation power of the peak energy was performed in the range 2-140 mW, for the solar cell after the PDA (Fig. 6.14 b)). All measured PL spectra were fitted with four Gaussian components as shown in the inset of Fig. 6.14 b). The increase of the excitation power until 100 mW, results in a blueshift of ∼18 meV/decade, whereas for higher values

the behaviour is compatible with a slope close to 0. The blueshift (∼18 meV/decade) estimated in this study, confirms the existence of fluctuating potentials in the absorber layer after the PDA treatment. A possible residual contribution from the CdS buffer layer to the measured luminescence after the thermal treatment of the solar cell may not be excluded. However, that possibility does not prevent the interpretation of the influence of the fluctuating potentials in the observed luminescence from the CZTS layer.

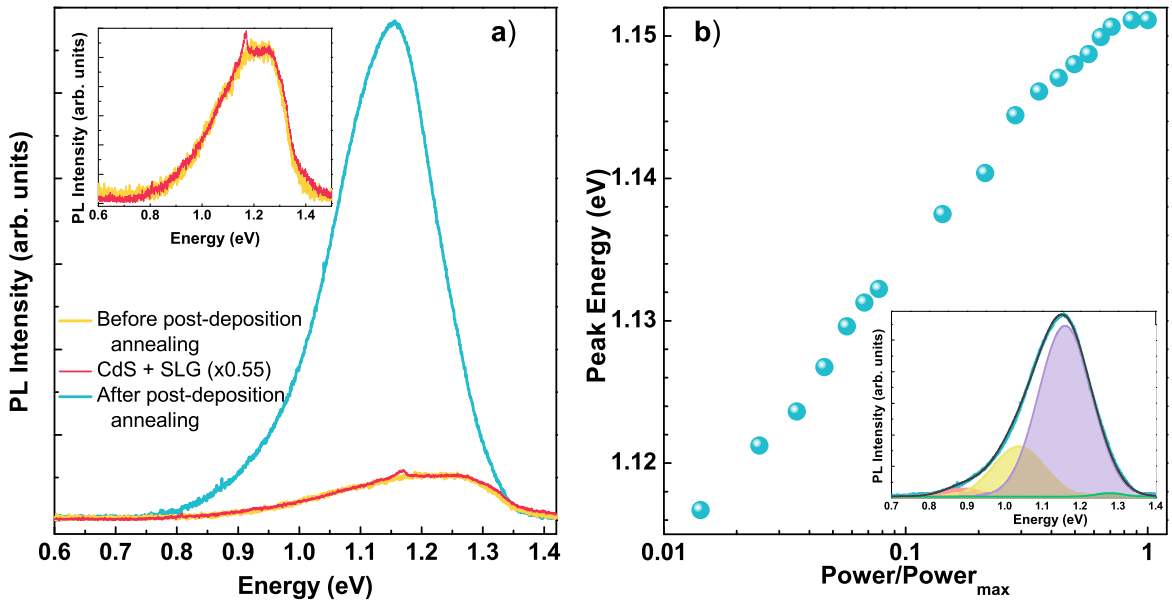

Figure 6.14: a) PL spectra measured at 70 K, under an excitation power of 140 mW, of a CZTS based solar cell before and after a thermal treatment of 15 mins at 300 ° C. A PL spectrum of a thin CdS layer deposited on SLG, measured with comparable experimental parameters, is also shown. A multiplicative factor of 0.55 for the intensity was considered for comparison purposes with the PL spectrum measured before the treatment. The small peak at 1.164 eV is related to the SLG. b) Dependence of the power of the peak energy of the luminescence on the excitation from the solar cell measured after the thermal treatment. The inset illustrates the fitting model used in the analysis of the radiative transitions for sample B.

The drastic change of the luminescence with the PDA suggests a significant change in the density of defects on the absorber layer. Previously to the PDA, the density of non-radiative channels was very high, because no luminescence related with the CZTS layer was observed. After the PDA, most of those channels are passivated which allows the observation of radiative channels in the absorber layer. The passivation of the non-radiative centers is followed by a significant enhancement in the electrical parameters on sample B as shown in Table 6.2. The X-ray photoelectron spectroscopy (XPS) results presented by Sousa *et al.* [152] suggest diffusion of Cu and Zn from the CZTS into the buffer layer and Cd from the buffer layer in to the CZTS thin film. These results suggest that the enhancement of the electrical performance of sample B may be explained by passivation of defects at the interface, where should be the majority of the ones that acted as non-radiative recombination centers in sample A. The diffusion of the atomic elements Cu, Zn, will increase the density of the V_{Cu} and V_{Zn}, respectively.

Thus, the simplest possibility is that Cd replaces those metals in the lattice. The next discussion follows qualitatively first-principles studies on Cd doping in CZTS [435, 436]. The formation energy of Cd_{Zn} substitutional defect is always lower than of Cd_{Cu}. However, the difference may fluctuate from just few meV to hundreds of meV, depending on how Cd is incorporated in the CZTS layer [435, 436]. Hence, let us discuss the two most likely passivation mechanisms:

i) Cd_{Zn}: according with the theoretical studies Cd will preferentially replace Zn, in agreement with experimental studies on Cd incorporation into CZTS [148, 435-438]. The diffusion of Cd in to CZTS surface will create a $Cu_2Zn_{1-x}Cd_xSnS_4$ alloy at the interface, CZTS/$Cu_2Zn_{1-x}Cd_xSnS_4$/CdS. The partial replacement of Zn by other atomic element have been implemented as a strategy to decrease the harmful Cu/Zn structural disorder. Thus, the decrease of CZTS self disorder may also contribute to the reduction of the interface recombination in our sample.

ii) Cd_{Cu}: in a Cu-depleted surface the formation of Cd_{Cu} donors is more likely. A high density of this substitutional donor may give rise to a buried homojunction, due to the conductivity type inversion in the CZTS surface [439, 440]. This may be the mechanism responsible for the reduction of the interface recombination. However, in CZTS, due to lower formation energy of the Cd_{Zn} than the Cd_{Cu}, the chances of establishing a buried homojunction are smaller than in CIGS [441]. Additionally, no evidences for a Cu-depleted surface were seen in the studied samples.

Additionally, according to Maeda *et al.* the [Cd_{Cu}+V_{Cu}] neutral cluster has lower formation energy than the two aforementioned substitutional defects [435]. Hence, it may also contribute as a passivation mechanism. Note that regardless of which passivation mechanism is involved, this diffusion of atomic elements will automatically reduce the Cu/Zn disorder in the surface/interface region.

Table 6.2: Extracted electrical parameters, J_{SC}, V_{OC}, FF, and η for sample A and B [152].

Sample	J_{SC} (mA.cm^{-2})	V_{OC} (mV)	FF (%)	η (%)
A	4.1	161	21.5	0.14
B	33.1	518	38.6	6.63

The changes on the CZTS electronic levels structure after a PDA in an atmosphere of N_2 were investigated. A significant change in the density of defects at the interface CZTS/CdS was observed after a PDA treatment. Despite the passivation of interface defects via the PDA, the luminescence of the sample is fully explained by the fluctuating potentials model, which shows a high density of charged defects even after the thermal treatment.

6.5 In Summary

A characterization of the defects present in the CZTS thin films and their influence on the electronic energy levels structure was carried out. Structural analysis showed that the studied absorber layers are dominated by the CZTS phase. The influence of fluctuations was shown, and fully explains the CZTS characteristic luminescence. No influence of the time at maximum temperature in the sulphurization step was observed on the optical properties of CZTS thin films. On the other hand, different sulphurization methods of identical multi-stacked precursors, led to samples with significantly different density of defects, with severe consequences on the nature of the radiative mechanisms resulting from different electronic levels' structure. The optical studies revealed, that a less efficient luminescence due to non-radiative recombination or recombination involving deep defects, are at great extent related with a poor performance of the devices. Finally, significant changes in the density of defects at the interface CZTS/CdS was observed before and after a PDA treatment.

Chapter 7

CIGS based solar cells

An experimental and theoretical investigation of the fluctuating potentials influence on the CIGS based solar cells performance is presented in this Chapter throughout different studies. The combination of optical results with the electrical performance of the devices enabled for an overview of the role defects, and in particular of fluctuating potentials in this technology.

CIGS based solar cells are the most efficient polycrystalline solar cells achieving a light to power conversion efficiency of 23.35% [7]. This remarkable electrical performance requires primarily a Cu-poor absorber composition [51, 210]. The off-stoichiometry composition, in addition to the presence of four distinct atomic elements in CIGS, the diffusion of atomic elements, namely, Na and Cd from the commonly used SLG substrate and CdS buffer layer, and the non-intentional incorporation of impurities during the growth, will promote local fluctuations in the composition and a large density of defects [174, 175]. The existence of spatial fluctuations in the composition and of an inhomogeneous doping, leads to bandgap and electrostatic fluctuating potentials, respectively [102, 188, 298, 301]. Now that CIGS based solar cells has reached a mature state, the empirical "know-how" that often contributed for improvements in this technology has clearly lost strength. So, further improvements in CIGS solar cells performance, now more than ever, depends mandatorily on the understanding of the limiting factors of the performance as well as of fundamental physical properties of the absorber layers, namely, the electronic energy levels structure and the dynamics of the charge carriers [19, 64, 101]. In this way, the investigation of fluctuating potentials is presently one of the hottest topics in the field [102, 223, 289, 290, 291, 442, 443, 444]. In this Chapter, we explore the potential of the PL technique, complemented with analysis of the sub-bandgap region of the EQE spectrum, in order to study the influence of the fluctuating potentials on the optoelectronic properties of CIGS based solar cells. We critically analyse the estimate of fluctuating potentials and its role on the electrical parameters of the studied devices.

7.1 Qualitative analysis of the amplitude of fluctuating potentials: case of CIGS:Na

In Chapter 6, we addressed the case of CZTS based solar cells and the impact that different growth conditions or PDA treatments may have on the electronic energy levels structure of the absorber layer, and in the performance of solar cells. All the recombination mechanisms discussed in CZTS, fitted in the fluctuating potentials model. Nonetheless, the poor performance of the devices was at great extent correlated with a preeminence of the non-radiative recombination mechanisms or recombination involving deep defects. In the case of the CIGS based solar cells the scenario is potentially different, and the influence of the fluctuating potentials in the performance of the devices is a hot topic in the scientific community [102, 223, 289, 290, 291, 442, 443, 444]. However, this discussion is hampered by the fact that the luminescence is often similar between samples grown with different growth parameters [102]. Thus, the luminescence analysis requires an accurate discussion to correctly depict the influence of fluctuating potentials, particularly in the case of electrostatic ones. Based on the knowledge developed in the study of CZTS based solar cells, in this Section we try to understand how accurate may be the estimation of the tails sates depth, and then, if it is valid a quantitative evaluation of the influence of fluctuating potentials. For this purpose, we studied a well known case in the literature of Na-containing and Na-free CIGS layers that present different density of charged defects that will allow us to address the influence of electrostatic fluctuating potentials.

The impact in the electric parameters of the Na incorporation ($\sim$1 at%) in the CIGS layer have been well discussed in the literature [71]. An improvement on the device performance due to a gain in V_{OC} and FF is widely obtained in Na-containing samples [445, 446]. It is widely accepted, that the improvement in those parameters is driven by an increase in the majority carriers density, due to a decrease in compensation level. There are numerous works that attempt to model the Na effect in CIGS [184, 185]. However, there is no clear conclusions regarding the mechanism behind the Na effect, due to the comparison of results between samples grown with different growth parameters and with different architectures (for example, the Na diffusion from the SLG can be blocked and intentionally promoted by a NaF layer at the rear contact) [20, 71, 76, 77].

In this work, we studied two samples: a reference one (Sample A), prepared according to standard industrial procedures and a sample grown on an Al_2O_3 substrate (Sample B), that simulates an extreme problem of insufficient Na diffusion from the substrate. Completed solar cells were characterized by J-V measurements (see Table 7.1). As observed by others authors [445, 446], significant losses in the V_{OC} and FF for sample B were obtained in comparison to sample A. On the other hand, both samples present a similar value of J_{SC}. In order to evaluate the V_{OC} losses, we extracted the bandgap energy for the two samples. The linear fit to the data in the EQE^2 vs. $h\nu$ plot, shown in Fig. 7.1 a), provided bandgap energy values of 1.08 ± 0.02 and 1.10 ± 0.06 eV for sample A and B, respectively. As expected, the diffusion of Na within the CIGS lowers the value of the bandgap energy [447]. The

difference between the V_{OC} losses of the two samples is 173 mV, which is significant, but compatible with the expected higher density of charged defects and degree of compensation in sample B in comparison to sample A. Additionally, from capacitance-voltage measurements (C-V), we can see in Table 7.1 that the lack of Na doping led to a significantly larger SCR width and to a decrease on the density of holes in comparison with the results obtained for sample A, which may be explained with a higher degree of compensation in sample B in comparison to sample A. Such results are compatible with passivation of donor defects by Na [71].

Table 7.1: Electrical and optical parameters obtained for the two samples: J_{SC}, V_{OC}, FF, and η obtained from J-V measurements; E_g obtained from EQE^2 vs. $h\nu$ plot; E_g/e-V_{OC}, W_D, and p obtained from C-V measurements.

Sample	J_{SC} ($mA.cm^{-2}$)	V_{OC} (mV)	FF (%)	η (%)	E_g (eV)	E_g/e-V_{OC} (mV)	W_D (μm)	p (cm^{-3})
A	33.73	609	72.3	14.9	1.08 ± 0.06	471	362	8.5×10^{15}
B	33.02	456	45.8	6.9	1.10 ± 0.02	644	2107	8.3×10^{13}

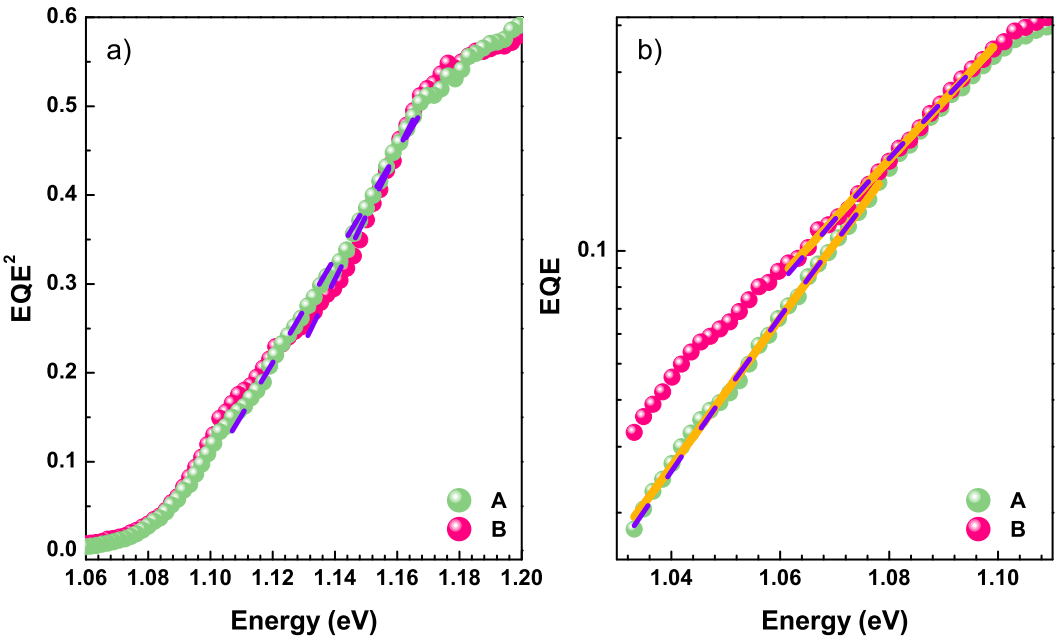

Figure 7.1: a) EQE^2 vs $h\nu$ plots for the two samples depicting a linear fit for the estimation of the bandgap energy values. b) Sub-bandgap energy range of the EQE curve for the two samples. In b) the, yellow line and the purple dashed line represent the fit of Eqs. 4.6 and 4.8 to the experimental data, respectively.

Figure 7.2 a) shows the normalized luminescence spectra of the two samples measured at 5 K, under an excitation power of 10 mW. The luminescence of sample A corresponds to a single, broad,

and asymmetric band with peak energy at ∼1.00 eV, which follows at great extent the characteristic luminescence of Cu-poor CIGS with normal Ga-profile, observed by other authors [188, 301]. In the case of the Na-free sample (B), a quite different luminescence is observed, two radiative transitions were identified as #1 and #2 with peak energy at ∼0.94 eV and ∼0.98 eV, respectively. Thus, the diffusion of Na within the absorber layer clearly changes the nature of the recombination channels. Beyond the clear differences in the shape of the two luminescences, sample B has a significantly lower signal-to-noise ratio in comparison to sample A.

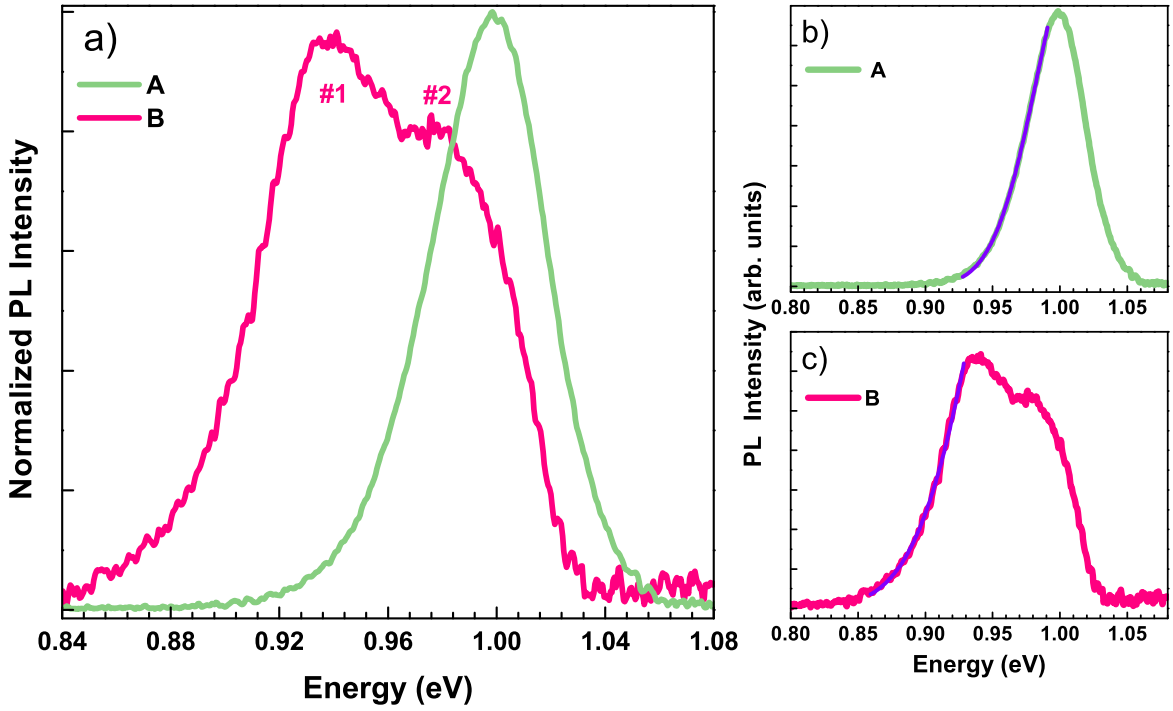

Figure 7.2: a) Normalized luminescence spectra of samples A and B measured at 5 K with an excitation power of 10 mW. PL intensity fitted by Eq. 7.1 b) in the range 0.93 to 0.99 eV and c) in the range 0.86 to 0.93 eV for the spectra presented in a) for samples A and B, respectively.

In order to understand the origin of the luminescence, its dependence on the excitation power was carried out. Fig. 7.3 shows a few PL spectra for both samples for excitation power values in the range 1 to 140 mW. In the case of the sample A, a blueshift with no significant change on the shape of the luminescence is observed, while for sample B a blueshift along with a significant change in the luminescence shape, was observed. For lower values of excitation power, the luminescence of sample B is dominated by the radiative transition of lower energies, #1, while with the increase of the excitation power the relative intensity of transition #2 starts dominating the luminescence. Thus, different Gaussian fitting models were used for the two samples in order to describe the whole dependence of the PL on the excitation power, following the fitting model discussed earlier in this thesis (Subsec. 5.3.4).

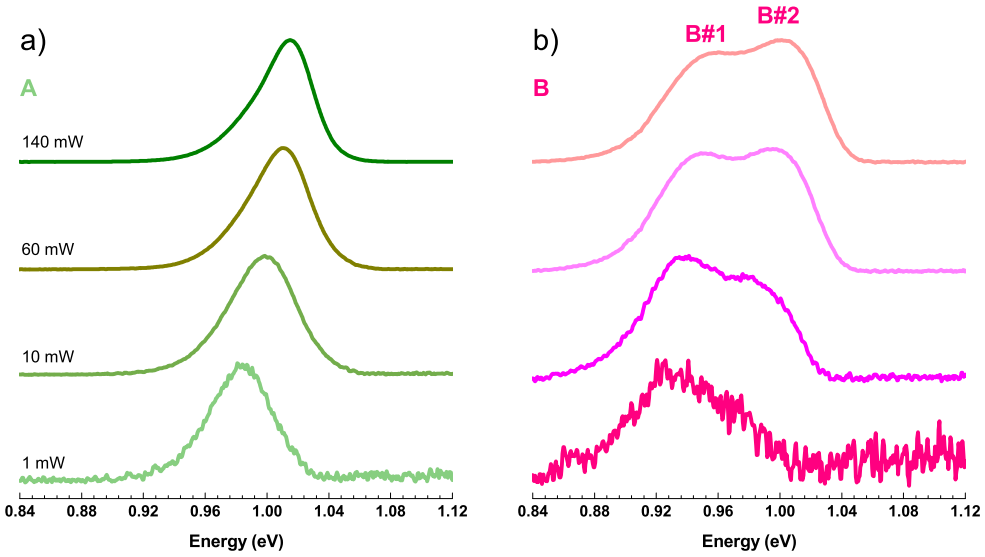

Figure 7.3: Luminescence measured at 5 K with an excitation power of 1, 10, 60, and 140 mW for a) sample A and b) sample B. The radiative transitions #1 and #2 of sample B are identified in b).

Fig. 7.4 shows the obtained dependence of the peak energy on the excitation power for the two samples. The increase of the excitation power results in a blueshift of the luminescence for both samples. From the fit of Eq. 4.15 to the dependence of the peak energy on the excitation power, a β value of 6.43 ± 0.01 meV was obtained for sample A, while for sample B we obtained β values of 5.3 ± 0.1 meV and 6.2 ± 0.2 meV for radiative transitions #1 and #2, respectively. Such values of β are compatible with the existence of fluctuating potentials in both samples. As discussed in Subsection 4.2.4, the β values should reflect the influence of the tails states in the samples. Thus, the slightly higher value of β obtained for sample A is a rather unexpected result, which is in disagreement with the obtained results from the C-V measurements, with the lower asymmetry observed in the luminescence of sample A than the observed for sample B, and also with the often reported higher degree of compensation in Na-free samples in comparison to Na-containing ones.

In the whole excitation power range, the low energy side of the luminescence in both samples is roughly the same, which according to the discussion in Section 6.1 allow the exclusion of a significant screening effect of the electrostatic fluctuating potentials. Thus, the observed blueshift follows the state filling of energetically higher states. In that way, the β value should reflect the overall of fluctuating potentials, and not only the influence of the electrostatic ones [346, 359]. The two different β values obtained for the two transitions in sample B may be understood, if we focus on the dependence of the β value on the density of states: radiative transition #1 has a lower β value, which should be related with a transition involving a higher density of states in comparison to the one available for radiative transition #2. The lower number of available states for radiative transition #2 will leads to a higher blueshift than for radiative transition #1, and compatible with two different slopes highlighted in Fig. 7.4 as 1 and 2.

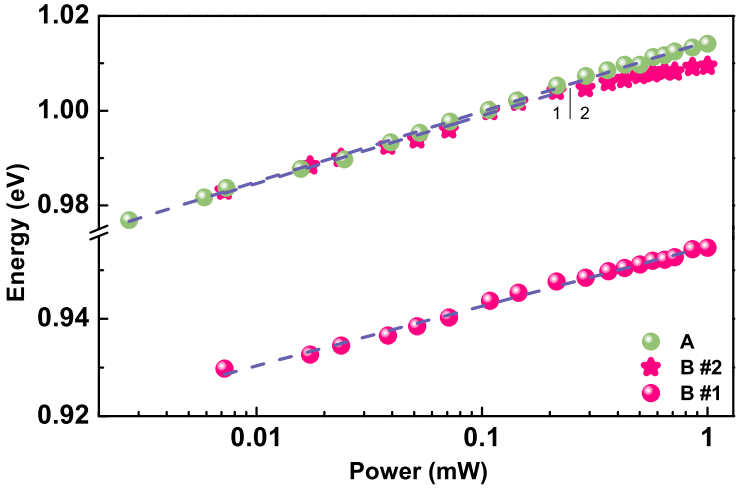

Figure 7.4: Dependence of the peak energy for the radiative transition for sample A and the two transitions #1 and #2 of sample B on the excitation power. The excitation power values were normalized to 140 mW. The dashed lines represents the fit of Eq. 4.15 to the experimental data.

The similar β values obtained for sample A and transition #2 from sample B (6.43 ± 0.01 and 6.2 ± 0.2 meV, respectively), makes it difficult to address a conclusion about the influence of the fluctuating potentials. Hence, other strategies were used to evaluate the influence of theses fluctuations, in particular the electrostatic ones, that should reflect the passivation effect that Na reportedly have in the native donor defects of CIGS [71]. A widely path used in the literature to compare the influence of the electrostatic fluctuating potentials is based on the analysis of the luminescence intensity in the low energy side [48, 302]. Different approaches assuming different type of transitions were tested according to a Gaussian (Eq. 4.13) and exponential (Eq. 4.14) models. The best model to fit the low energy side of the luminescence was the same for both samples, and follows a Gaussian model that describes the particular case of a BI type transition. Thus, the fit was done (in the ranges 0.93-0.99 eV and 0.86-0.93 eV for samples A and B, respectively) with,

$$I_{LE}(h\nu) \propto \frac{1}{\gamma_g} \exp\left(-\frac{(E_g - I_a - h\nu)^2}{2\gamma_g^2}\right). \tag{7.1}$$

For the case of a BI transition, the low energy side of the luminescence follows the density of states of the valence band, then the γ_g should reflect the overall extension of electrostatic fluctuating potentials density of states within the bandgap. We obtained γ_g values of 32.9 ± 0.2 and 50 ± 1 meV for sample A and sample B, respectively. The obtained difference between the γ_g values is clear and suggest a significantly lower influence of the electrostatic fluctuating potentials in sample A in comparison to sample B. In order to further support the latter result, we estimate the influence of the fluctuating potentials at RT, from the sub-bandgap energy range of the EQE curve. For that energy range, EQE follows the density of states of the fluctuating potentials. The sub-bandgap energy range of the EQE curve for both samples was fitted with the Urbach (Eq. 4.6) and the optimal-fluctuation (Eq. 4.8) models, that should inspect the influence of tails states with different depth in the bandgap

(see Fig. 7.1 b)). The obtained parameters E_U and γ obtained from both models are presented in Table 7.2 and support a lower influence of fluctuating potentials for sample A in comparison to sample B. Additionally, this result also back up the previous assumption of a BI type transition for the luminescence in sample A and #1 in sample B. The three used models to evaluate the influence of the fluctuating potentials, Gaussian, optimal-fluctuation, and Urbach, also provide a bandgap energy values in the scope of each model, which are presented in Table 7.2. All three models give bandgap energy values compatible with the ones extracted from the EQE^2 vs $h\nu$ plot if the errors are taken into account. The only exception is the value estimated for sample B by the Gaussian model, which is smaller than the previous one obtained at RT, does not following the expected decrease of the bandgap value with the temperature.

Table 7.2: Optical parameters obtained for the two samples: peak energy (E_p) for the observed transitions measured at 5 K, β obtained from Eq. 4.15, γ_g obtained from Eq. 7.1, γ obtained from Eq. 4.8, E_U obtained from Eq. 4.6 and $E_g(\gamma_g)$, $E_g(\gamma)$, and $E_g(E_U)$, with errors of 0.01 eV, obtained from Eq. 7.1, 4.8, and. 4.6, respectively.

Sample		E_p (eV)	β (meV)	γ_g (meV)	γ (meV)	E_U (meV)	$E_g(\gamma_g)$ (eV)	$E_g(\gamma\ )$ (eV)	$E_g(E_U\ )$ (eV)
A		1.00	6.43 ± 0.01	32.9 ± 0.2	20.14 ± 0.01	21.9 ± 0.01	1.13	1.13	1.12
B	#1	0.99	5.3 ± 0.1	50 ± 1	23.00 ± 0.02	27.6 ± 0.02	1.00	1.14	1.13
	#2	0.94	6.2 ± 0.2						

The overall of our results show a lower influence of the fluctuating potentials in sample A than in sample B, compatible with a decrease of the density of charged defects and compensation for sample A in comparison to sample B. Moreover, the optical results follow the significant improvement in the V_{OC} observed for sample A in comparison to sample B. However, from the analysis of the β value, which in the literature is a widely used parameter to evaluate the influence of fluctuating potentials, we did not obtained a clear evidence, due to the proximity between the β values obtained for sample A and for transition #2 of sample B. The low energy side of both luminescences are described by a Gaussian decay following the density of states of the valence band for deeper tails states ($R \sim r_0$). For the case of tails states scrutinized by the Gaussian model, we obtained a significant difference between the amplitude of the electrostatic fluctuating potentials in the two samples. Taking into account that the latter analysis and β values were both obtained at low temperature, and the Gaussian model used describes the particular case of a BI transition, we suggest that the lower value of β obtained for the radiative transition #1 of sample B results from a significant higher density of states related with the acceptor defect involved in that transition in comparison to the acceptor levels involved in transition B2 of sample B or the one observed for sample A.

In regard, to the analysis of the influence of the fluctuating potentials at RT, the models that best described the sub-bandgap region of the EQE, follow the density of shallower tails states ($R < r_0$) than the ones scrutinized at low temperature. The pure electrostatic optimal-fluctuation model describes

deeper tails than the empirical Urbach model (see Subsection 4.1.1). The first evidence to note is that the difference on the amplitude of the tails states between the two samples decrease significantly when we address tails states that are more close to the continuum. The qualitative character of the parameters that describe the amplitude of the fluctuating potentials is well shown by the higher values of the amplitude of tails sates obtained from the Urbach model in comparison to the ones obtained for the optimal-fluctuation one, that follows the density of states for deeper tails.

The analysis of PL and EQE results showed a lower influence of fluctuating potentials, in particular the electrostatic ones, in the Na-containing sample (A) in comparison to the Na-free one (B) compatible with the electrical and C-V results. The difference in the influence of fluctuating potentials between the two samples is significantly higher when deeper tails sates are inspected at low temperature. A significantly high density of defects may hinders an accurate proportionality of the β magnitude to the influence of the fluctuating potentials, being the correlation of the β value and the analysis of the luminescence shape necessary to discuss the impact of the fluctuating potentials in the optoelectronic properties of a material.

7.2 Influence of the Ga-profile on the PL of CIGS thin films

A wide variety of thin film growth methods has been used to fabricate CIGS based solar cells [20, 65, 203, 204]. However, co-evaporation is the most common one, allowing for the development of different schemes of deposition. Depending upon the number of stages (see Fig. 3.11), the co-evaporation method may be classified as: three-stage, two-stage, and in-line processes [65, 204, 216]. State-of-art solar cells grown by co-evaporation have been mainly obtained following a three-stage process [448, 449]. The success of this process is very much due to the inherent notch Ga-profile that will lead to a quasi-electric field, which assists the drift of free charge carriers to their respective contacts. Another advantage consists in a lower bandgap in the notch region close to the front surface, which further enhances the absorption of low energy photons [450]. However, the in-line process emerged from the need of a simple deposition method, due to the technical complexity of the three-stage process. The possibility to engineering an efficient Ga-profile by single stage process is therefore preferable from an industrial point of view. In this Section, we present a study that shows the impact on the luminescence of the two different Ga-profiles obtained by the three-stage and in-line deposition methods, in order to study possible differences in electronic energy levels structure of the samples.

The luminescence of CIGS samples with a notch Ga-profile commonly presents two clear radiative transitions, and the origin of the luminescence is associated to the minimum of the conduction band in the notch region [32, 353, 451, 452, 453], whereas for normal Ga-profile a broad luminesce is observed [102]. Since the relative amount of Ga determines the bandgap energy of the CIGS layer, mainly due to a shift in the position of the conduction band minimum, different Ga-profiles will lead to different electronic energy levels structures, and more importantly the CIGS samples with a Ga-profile will present differences in the electronic energy levels structure that will meet the changes

on the Ga content throughout the CIGS layer. Let us consider the PL process described earlier in this thesis: i) excitation, ii) thermalization, iii) diffusion, and iv) radiative recombination [64]. After excitation, charge carriers are subjected to diffusion mechanisms that allows their distribution in the sample, that in the presence of a Ga-profile, will be additionally assisted by a drift of the free charge carries in their respective bands driven by the presence of a quasi-electric field. This means that the recombination may occur in different physical places of the sample, depending on the diffusion length of the charge carriers and the properties of the quasi-electric field [51]. The existence of a bandgap profile will promote the distribution of the photogenerated charge carriers in comparison to samples with a constant bandgap. This process should be carefully taken into account in order to an accurate analysis of the luminescence in samples with bandgap profiles, since the CIGS energy levels structure will change in depth from the interface with the buffer layer to the back contact.

Two CIGS sample were prepared with different Ga-profiles: i) a three-stage sample with a typical notch Ga-profile (Sample A); and ii) an in-line sample with a normal Ga-profile, from 55% at the back to 25% at the front (Sample B). The two Ga-profiles are shown in Fig. 7.5. The samples were grown with the same overall composition of GGI = 0.4 and [Cu]/([Ga]+[In])= 0.92, and with the same solar cell architecture [51].

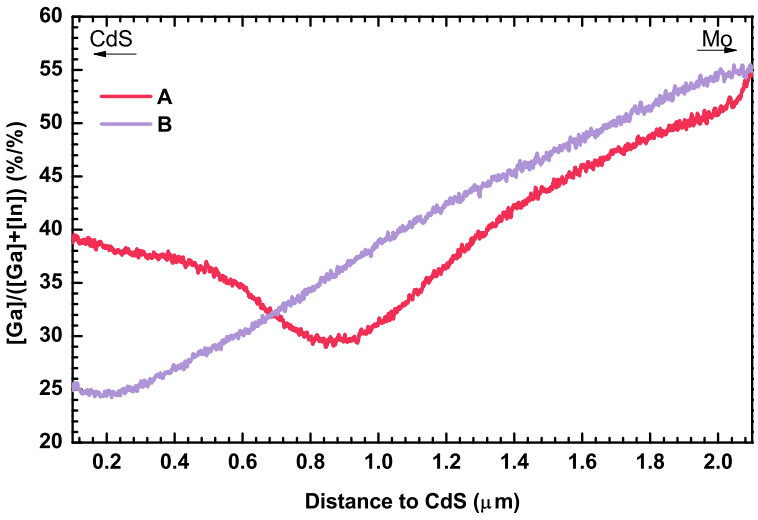

Figure 7.5: Elemental depth profile of [Ga]/([Ga]+[In]) (GGI) measured by glow discharge optical spectroscopy (GDOES) for the studied samples and with an overall GGI value of 0.4. Adapted from [51].

Normalized PL spectra for the two samples A and B, measured at ∼5 K under an excitation power of 1 mW, are shown in Fig. 7.6 a). A radiative transition at ∼1.015 eV dominates the two spectra (from now on denoted by A_1 and B_1). The fact that at low temperature the peak energy is approximately the same in both spectra, suggests the same origin for that transition in the two samples. In the case of sample A, an additional transition (A_2) at ∼1.09 eV is observed. The fitting with Gaussian components of the luminescence for both samples (Fig. 7.6 b) and c)) allow us to separate the individual contributions of the two transitions in the case of sample A and to identify

another transition (B_2) at ∼1.03 eV for sample B. For both samples the radiative transitions A_1 and B_1, are described by two components illustrated in Fig. 7.6 b) and c) by 1 and 1', whereas the radiative transitions observed for higher energies, A_2 and B_2, are solely described by one Gaussian component illustrated by 2. Despite the number of radiative transitions, both luminescence are broad and asymmetric. The shapes are characteristic of electronic transitions occurring in semiconductors with tails states in the bandgap, as we observed in Chapter 6 for the CZTS studied samples.

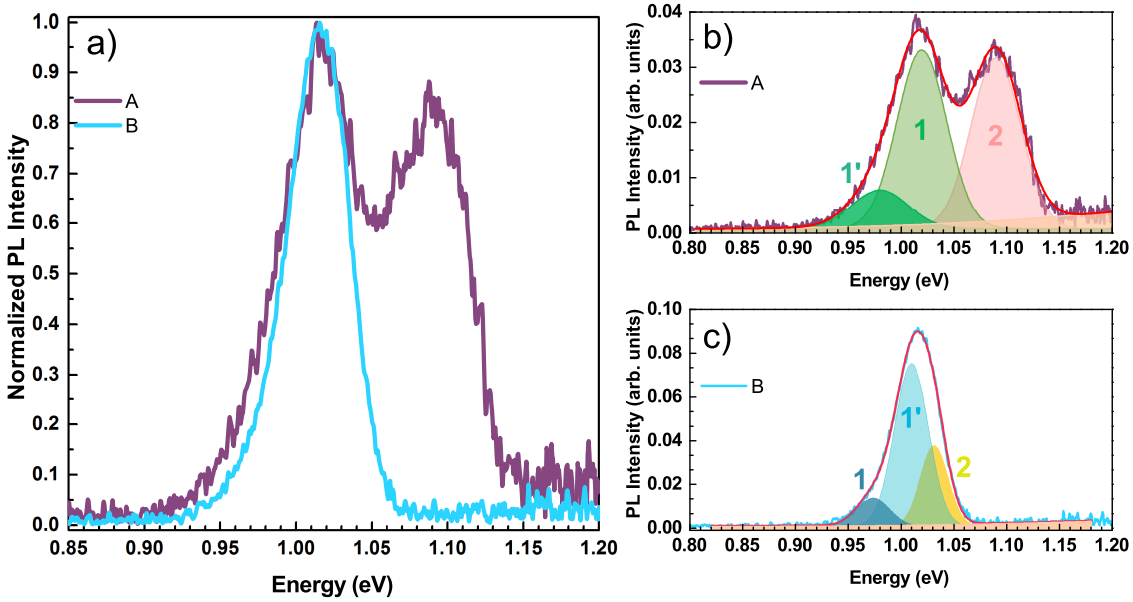

Figure 7.6: Normalized PL spectra of sample A and B measured at 5 K under an excitation power of 1 mW. The fitting models with Gaussian components are shown for b) sample A and c) sample B. Gaussian components #1 and #1′ describe the main radiative transitions denoted by A_1 and B_1, whereas only one Gaussian component describes the higher energy transition denoted by A_2 and B_2.

In Fig. 7.7 we show the dependencies of the peak energy and the PL integrated intensity of the two radiative transitions for both samples on the excitation power. A blueshift is observed for the two radiative transitions of the two samples, being the extracted β values from the fit of Eq. 4.15 to the experimental data, as shown in Fig. 7.7 a) and b), presented in Table 7.3. On average, all β values are in the range 2.9-6.4 meV, which represents a strong enough energy shift compatible with the presence of fluctuating potentials in both samples. In the particular case of transition A_2, the blueshift is mainly observed for the lower excitation power values regime, due to a decrease of the energy shift with the raise of the excitation power. The dependence of the integrated PL intensity of the two transitions in both samples on the excitation power is shown in Fig. 7.7 c) and d). For sample A, the two transitions show a different behaviour as the excitation power is increased: whereas the intensity of transition A_1 increases, the transition A_2 shows a saturation for $P > 10$ mW. In the case of sample B, the intensity of both transitions increases with the excitation power without saturation. As shown in Fig. 7.7 c) and d), the dependence of all transitions of the two samples on the excitation power were

fitted with the power law given by Eq. 4.16 [341]. The estimated values of m are shown in Table 7.3 and are distributed between ∼0.9 and ∼1.2. Therefore, they are around 1, which corresponds to a common behaviour for transitions involving fluctuating potentials.

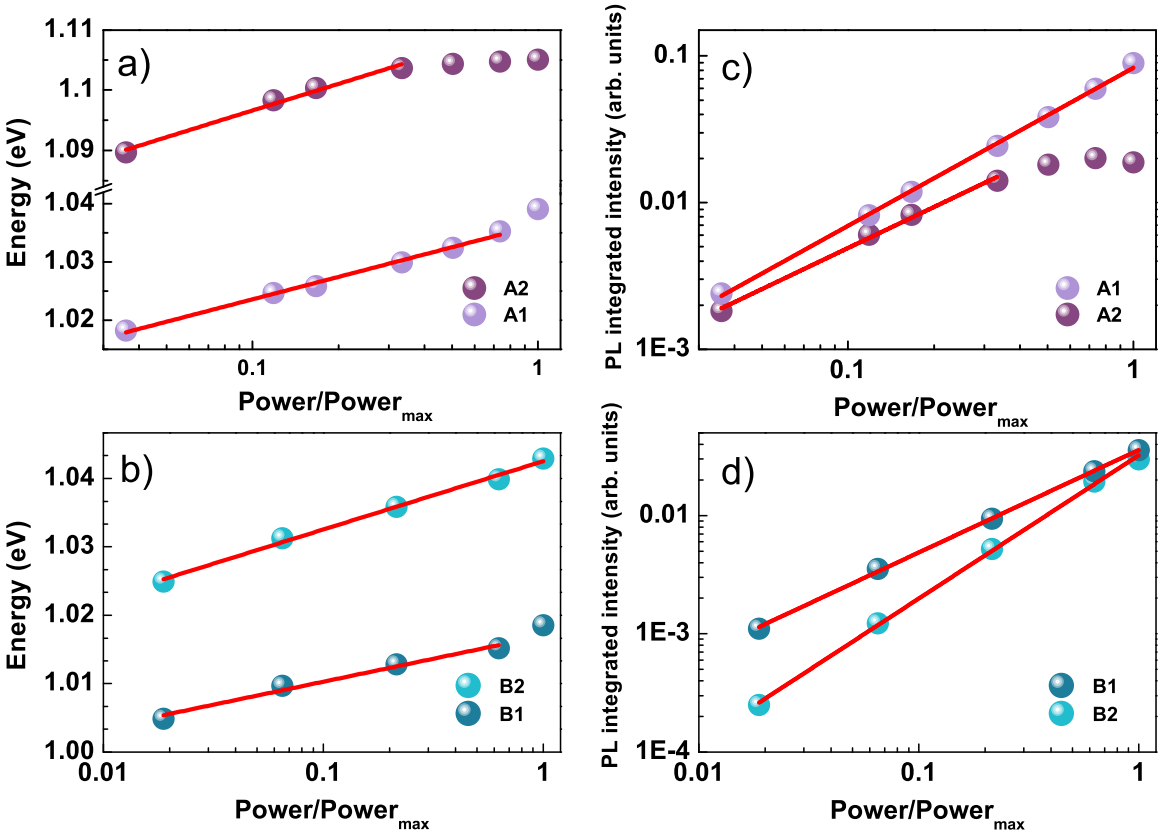

Figure 7.7: Dependence of the peak energy for transitions a) A_1 and A_2 and b) B_1 and B_2 on the excitation power. Dependence of the PL integrated intensity for transitions c) A_1 and A_2 and d) B_1 and B_2 on the excitation power. Both dependencies were performed at 5 K and excitation power values were normalized to 30 and 29 mW for sample A and B, respectively. The solid lines represent the fit to the experimental points by a)-b) Eq. 4.15 and c)-d) Eq. 4.16.

Table 7.3: Values of the peak energy (E_p), β parameter, and m parameter estimated for the two radiative transitions in sample A and B. The β and m parameters were obtained after the fit of Eqs. 4.15 and 4.16 to the experimental data in Fig.7.7 a)-b) and c)-d), respectively.

Sample	Transition	E_p (meV)	β (meV)	m
A	A_1	1.018	6.4 ± 0.2	1.08 ± 0.02
	A_2	1.090	5.6 ± 0.2	0.93 ± 0.04
B	B_1	1.001	2.9 ± 0.3	0.87 ± 0.01
	B_2	1.031	4.3 ± 0.2	1.21 ± 0.02

The dependence of the luminescence for samples A and B on temperature was studied under an

excitation power of 3.5 and 19.1 mW, respectively. Due to the low relative intensity of transition B_2 for low values of excitation power (see Fig. 7.6), a higher value was used, where both transitions have similar intensities, to allow a deeper investigation of both transitions. With the increase of temperature, the PL integrated intensity of both radiative transitions for sample B evidence a common behaviour [102, 308] consisting in a small decrease in a regime of low temperatures (5-40 K), followed by a strong reduction until the thermal quenching at ~240 K. Regarding sample A, the behaviour of the two transitions are quite different: as the temperature is raised, transition A_2 suffers a strong thermal quenching at 40 K, whereas until the same temperature the relative intensity of transition A_1 increases; for higher temperatures, A_1 suffers a strong reduction with the complete thermal quenching at 170 K. This unexpected behaviour observed for sample A is illustrated in Fig. 7.8 a), and suggests the existence of a thermal supply mechanism of carriers from the radiative states involved in transition A_2 to the ones involved in transition A_1.

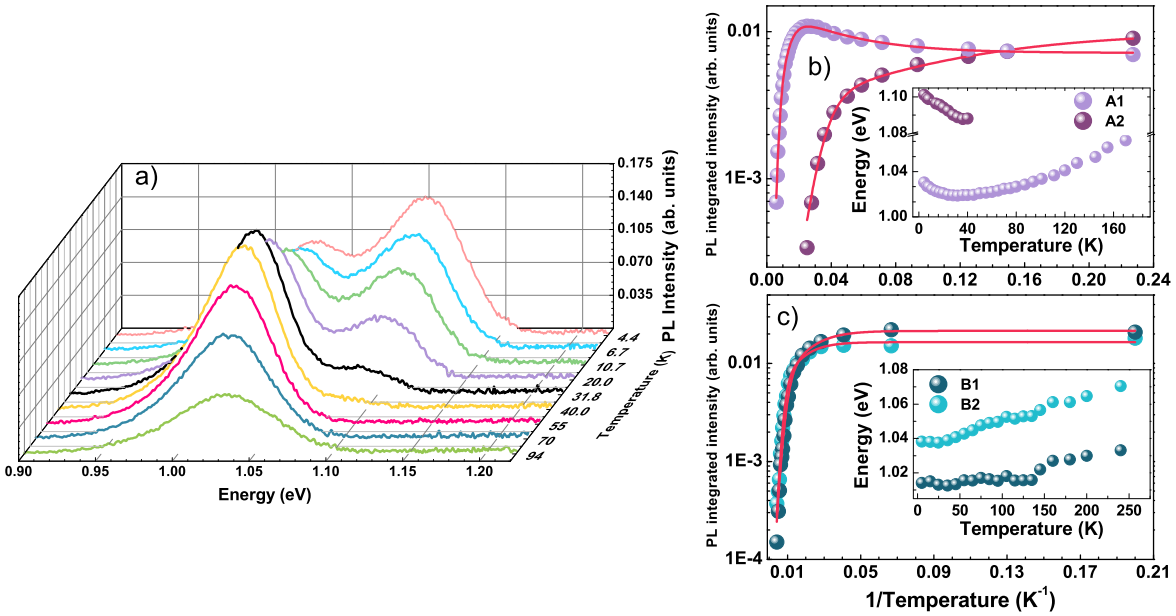

Figure 7.8: a) PL spectra for different temperatures of sample A. Dependence of the integrated intensity b), and c) (as well as peak energy, insets in b) and c)) of samples A and B on the temperature, respectively. The lines are the fit of Eq. 5.12 to the experimental data.

The dependence of the PL integrated intensity of each radiative transition may be described considering that, as temperature increases, de-excitation channels are thermally activated according to Eq. 5.12. Different models using this equation were considered. The same model provided the best fit to describe the experimental points for transitions A_2, B_1, and B_2 and considers two de-excitation

channels, one involving a discrete energy level and another one involving a band. For transition A_1, the best fit was obtained by considering one de-excitation channel involving a band, and another channel corresponding to the thermal supply of charge carriers involving shallow energy levels. The obtained parameters from the fit Eq. 5.12 to the dependence of PL integrated intensity of the four transitions on the temperature, are presented in Table 7.4. The small quenching of the luminescence for A_2, B_1, and B_2 observed at low temperatures, is compatible with the thermal activation of a non-radiative channel involving a discrete excited energy level with activation energies E_1 presented in Table 7.4. The quenching of the luminescence for all radiative transitions are associated to the de-excitation channel involving a band with activation energies of 18 ± 1, 10 ± 2, 37 ± 4, and 41 ± 13 meV for the transitions A_1, A_2, B_1, and B_2, respectively.

In the insets of Fig. 7.8 b) and c) we show the dependencies of the peak energy on the temperature of the four studied radiative transitions. For sample A, we observe a redshift for $T \lesssim 30$ K for both transitions, followed by a blueshift up to the total quenching of the luminescence of the transitions. For sample B, just a blueshift is observed. However, as discussed in Subsection 4.2.3, the magnitude of the redshift depends on the excitation power. We note that the excitation power used in sample B is approximately six times higher than the one used in sample A [301, 342, 350, 351]. The absence of the redshift at lower temperatures in sample B, is compatible with the higher value of the used excitation power according to other works presented in the literature [347, 358, 359]. Therefore we assume that the dependence of the peak energy of the studied transitions on the temperature presents a qualitatively similar behaviour. Globally, the change from the red to the blueshift happened for low enough temperatures (∼40 K,), which is lower than the usually reported (∼100 K) [32, 102, 301, 308, 347, 350].

Table 7.4: Values of the parameters obtained in the fitting of Eq. 5.12 to the experimental data in the dependence of the integrated PL intensity on the temperature for samples A and B (see Fig. 7.8 b and c)).

Sample	Band	E_1 (meV)	E_{bx} (meV)	E_{nr} (meV)
A	A1	-	18 ± 1	0.8 ± 0.5
	A2	1.2 ± 0.2	10 ± 2	-
B	B1	8 ± 1	37 ± 4	-
	B2	10 ± 2	41 ± 13	-

The shape of the luminescence of both samples, the obtained values for the β and m parameters, in addition to the redshift followed by the blueshift of the peak energy with the raise of the temperature, are compatible with the presence of fluctuating potentials on both samples, regardless the Ga-profile. However, there are several differences in the luminescence that should be related mainly with the

different Ga-profiles. Let us start by analysing the three-stages sample with a notch Ga-profile, sample A. The two close obtained E_{bx} values of 18 ± 1 and 10 ± 2 for A_1 and A_2 transitions, suggest a similar de-excitation channel is involved in the quenching of both radiative transitions. These two low energies are closer to the experimentally obtained ionization energies by other authors which they ascribed to an intrinsic shallow donor in CIGS [176]. Since, due to the low effective mass of the electrons, it is not expected that single donors form bound states for electrons. So, the de-excitation channels should involve the release of electrons from a tail in the conduction band. However, it is not straightforward to understand the earlier quenching of the transition A_2 in comparison to A_1. The complete quenching of the radiative transition A_2 at $\simeq$40 K, may be compatible with the observed dependence of the peak energy with the increase of the excitation power. For the latter dependence, two different slopes are observed, up to 10 mW a strong blueshift of the luminescence given by a β value of 5.6 meV followed by an almost no shift of the luminescence. According to the state filling effect, the first slope should be related with the filling of a small density of states, whereas the second slope should be related with the filling of a larger density of states. Regarding transitions A_1, only one slope is observed which suggests no significant changes in the density of states. At this point, we must note that an energy shift in the excitation power dependence is mainly determined by the lower density of the states involved in the radiative transition (density of states for electrons or holes). Thus, assuming the possibility of tails of the conduction band in both A_1 and A_2, we must ascribe the observed blueshift of both transitions to the low density of states describing those tails since the density of states for an acceptor band or tails in the valence band are expected to be higher [342]. Assuming that the observed radiative transitions occur in different regions of the sample, we may be able to explain the differences on the available density of sates for the two transitions. Taking into account a possible diffusion and drift of the free charge carriers throughout the sample, the latter being driven by the quasi-electric field, there are two regions where it is more likely to occur recombinations in sample A at: i) the CIGS/CdS interface, which is a highly recombinative region, and ii) the region of the notch where the minimum of the conduction band has its lowest value. The defects formation energy will depend on a commitment between the composition, and also on the Fermi energy level. The Fermi level at near the interface moves closer to the minimum of the conduction band, whereas, in the bulk of the CIGS, the Fermi level is much closer to the top of the valence band (see Fig. 3.1). However, looking to the notch Ga-profile (Fig. 7.5), in the region of lower GGI it is expect that the Fermi level approaches again the conduction band. Thus, the Fermi level closer to the conduction band in these two regions will favour the formation of the same type of defects, and the different composition in the CIGS/CdS interface region and the notch one, may lead to different densities of these defects in the two different regions. Hereupon, the dependence of A_1 and A_2 may be explained according to the following reasoning: assuming that at great extent the conduction band will follow the Ga-profile, electrons will occupy preferentially the region with lower GGI, where they recombine with holes (transition A_1); at low temperature, a fraction of electrons will recombine near the CIGS/CdS

interface (transition A_2). Assuming that, a small increase of the thermal energy will contribute to the drift in the conduction band to a region more favourable from an energy point of view, the notch region, then the carriers will contribute to transition A_1. This behaviour is fully compatible with the existence of a thermal supply mechanism of electrons from the radiative states involved in transition A_2 to the ones involved in transition A_1.

To further clarify the nature of the radiative recombination channels in sample A, it is important to estimate the bandgap at the two above regions. According to Eq. 3.1, we calculate a value of $E_g(0.295) = 1.229\,\text{eV}$ for the notch region, and a value of $E_g(0.390) = 1.294\,\text{eV}$ for the CIGS/CdS interface, while the extraction method should not be completely valid for absolutes values, the differences between the values are valid and provide for a physical meaning. It is remarkable that the difference between these two values (65 meV) is close to the difference between the peak energy of the transitions (72 meV). Thus, this result also supports that transitions A_1 and A_2 have the same nature and occur in different regions of the CIGS layer: A_1 in the notch and A_2 near the CIGS/CdS interface.

Looking now, to the spectroscopic energy difference between bandgap and peak energies in each of the two regions, we obtain the following values $E_g(0.295)$-$E_p^{A1} = 211\,\text{meV}$ and $E_g(0.390)$-$E_p^{A2} = 204\,\text{meV}$. The combination of this high energy separations of the peak energies from the respective bandgap energies, with the shallow tails states in the conduction band (18 and 11 meV for transition A_1 and A_2, respectively), suggests that both transitions involve a hole located at a deep acceptor level.

From the above discussion, the radiative transitions A_1 and A_2 that occur in the notch and near the CIGS/CdS interface, respectively, were both ascribed to a TI type transition involving the same acceptor level and similar donors cluster, i.e. a recombination of electrons trapped in tails in conduction band with holes bound to a deep acceptor level that follow the fluctuating potentials of the valence band.

Regarding sample B, the normal Ga-profile presented in Fig. 7.5 shows an in depth continuous increase of Ga, which hinders the diffusion of the electrons away from the surface and keeps them there. As a consequence, the observed transitions should come from that region characterized by an almost constant bandgap energy of around 300 nm in depth. The dependence of the luminescence on the temperature revealed E_{bx} activation energies close to each other (see Table 7.4), suggesting the same thermal activation of a de-excitation channel with the increase of the temperature, in the two transitions. The E_{bx} values are also very close to the ionization energy calculated theoretically for the V_{Cu} defect, 30 meV [173, 174]. From that, the observation of the two radiative transitions involving the same defect cannot be explained by assuming different bandgap values for each transition, as done previously for sample A. In fact, both transitions for sample B may be ascribed to a BI type transition. We must note that, for this type of transition to occur, a hole must be bound to an acceptor state. In principle, with high enough temperatures, the holes may be released to the valence band, which is reflected in the absence of luminescence. The E_{bx} activation energy parameterizes this process. In

highly doped materials, we may distinguish two types of radiative recombination involving the same acceptor level: i) when the radiative transition involves a hole located in a region of the material where the top of the valence band is located below the percolation level, and ii) when the radiative transition involves a hole located in a region of the material where the top of the valence band is located above the percolation level, being the transitions named as BI1 and BI2, respectively (see Fig. 4.9) [342]. The observation of the BI1 transition should be thermally induced, since the hole is not at the its lowest energy, unless the excitation power is high enough to fill the valence band up to energies in which the holes are below the percolation level. Thus, transitions B_1 and B_2 may be ascribe to an BI2 and BI1 type transitions, respectively.

The dependence of the peak energy, of both transitions, on the temperature corroborates the above model. As the temperature is increased, the two transitions present an almost no shift of the luminescence followed by a blueshift. For transition B_1 the blueshift is observed only for $T > 135\,K$, whereas for transition B_2 the blueshift starts for significantly lower temperatures, $T > 25\,K$. The difference after which the blueshift is observed may be understood if we take into account the occupation level of the top of the valence band by holes. In the case of transition B_1 (BI2 type transition in Fig 4.9) the holes involved have a lower energy (from the point of view of this charge carrier) than the ones in transition B_2 (BI1). Thus, with the temperature in low temperature regime ($T < 100\,K$), only the holes with higher energy may move to unoccupied states with higher energy. This is the case of the holes involved in the radiative transition B_2. A similar transition of holes to higher energy states is not possible in the case of holes involved in radiative transition B_1, since a higher amount of thermal energy is needed to the holes reach the unoccupied states.

Regarding the influence of the fluctuating potentials, sample A presents higher β values and the shape of the luminescence is slightly more asymmetric comparing with sample B, which suggests a high influence of fluctuating potentials in the former sample. However, this evidence is not reflected in the electrical parameters, since the obtained V_{OC} losses are approximately the same for the two samples (451 and 449 mV for sample A and B, respectively [51]). These results, may be related with the quite different regions inspected by the PL, consequence of the different Ga-profiles. In sample A, we inspect a region that is deeper in the bulk, whereas for sample B the luminescence comes from a surface region of the CIGS layer, close to the interface. Thus, the differences in the influence of fluctuating potentials may be just the result of different density of charged defects in the inspected regions. Remember that CIGS is dominated by bulk recombination, which may explain a higher density of charged defects detected for sample A, comparing to the region inspected in sample B.

The three-stage growth method is rather complex, in terms of industrial upscaling, than the in-line one, and since the impact of the both, growth method and Ga-profiles, in the electronic structure led at great extent to similar optoelectronic properties, the following studied samples in thesis were grown according to the in-line method.

Two samples grown by different methods, one with a notch Ga-profile (sample A) and another one

with a normal Ga-profile (sample B) were studied in this Section. For both samples, two radiative transitions were identified. For sample A, the radiative transitions A_1 and A_2 occur in the notch and near the CIGS/CdS interface, respectively, were both ascribed to a TI type transition involving the same acceptor level and similar donors clusters. For sample B, the radiative transitions B_1 and B_2 were ascribed to a BI2 and BI1 type transitions, respectively, compatible with the involvement of the V_{Cu} defect. The higher influence of the fluctuating potentials in sample A comparing to sample B was not observed in the electrical parameters of the two samples.

7.3 Metastability induced by post-deposition air annealing in CIGS thin film

The continuous enhancement in CIGS technology has followed a number of developments on PDT that improve the electrical performance of the solar cell [433]. One of the most widely used treatments is the PDA that may be performed on the absorber layer only [368, 454], on the sample after the deposition of the CdS layer [455] or on the final device [456]. The influence of PDA treatments in the CIGS optical properties has been investigated by different authors under air atmosphere [368, 457, 458]. However, it is not clear the real impact of these thermal treatments in CIGS optoelectronic properties, as we will show.

A significant decrease of the electrostatic fluctuating potentials influence on the luminescence was observed in annealed CIS and CIGS (GGI = 0.1) samples, at high temperatures (400 °C), in comparison to the obtained luminescence for the as-grown samples [368, 457]. The asymmetric and broad luminescence measured before the PDA became a structured luminescence comparable to the one observed for Cu-rich CIGS samples. The changes in the luminescence were explained by a significant decrease on the compensation, due to the passivation of donor defects induced by the thermal treatments. However, the same authors observed that an increase on the Ga content in the alloy, CIGS sample with a GGI= 0.28, hinders the passivation of the donor defects [368, 457]. Although a decrease on the compensation was also obtained after the PDA, the impact was not sufficient to cause a change in the shape of the luminescence of the CIGS sample with a GGI= 0.28 [457]. Another effect of PDA at high temperatures, is the possible formation of secondary phases, which are detrimental for the performance of the solar cell [368]. Thus, 200 °C is assumed to be the higher temperature that the solar cells may withstand without leading to a degradation in the device performance, which is the usual choice for PDA treatments [181, 198]. Nevertheless, Yakushev et al. observed an increase of the influence of fluctuating potentials on the CIGS optical properties after a PDA performed at lower temperatures (120, 140, and 160 °C) in a CIS and CIGS (GGI = 0.005) samples, which is somehow in contradiction with the previous behaviour for higher temperature values [458].

In this study, we investigate the influence of a PDA on the CIGS optical properties through the dependence of the luminescence on the excitation power. A CIGS sample with a base solar cell

structure (SLG/Mo/CIGS/CdS) was fabricated following the Ångstrom solar cell baseline (sample CIGS-ag) [140], with a composition of GGI = 0.42 and [Cu]/([In]+[Ga]) = 0.86. The sample was annealed at ∼185 °C for 30 mins in air atmosphere (sample CIGS-an). The PL was measured before (15 min) and after the PDA. In the latter, the time intervals (Δ t) between the annealing and the PL study was performed Δt = 1, 16, 64 hours. The acquisition time for a complete set of PL spectra in each excitation power dependency is low enough in comparison with the values of $\Delta\, t$.

Fig. 7.9 shows the luminescence of the sample CIGS-ag, measured at 5 K with an excitation power of 1.2 mW. The luminescence corresponds to a broad and asymmetric band in an energy range between 0.98-1.18 eV with peak energy at 1.095 eV. The energy range and shape of the luminescence are close to the ones observed for other samples presented in this thesis and to the ones ascribed to Cu-poor CIGS samples with a normal Ga-profile in the literature [102, 347].

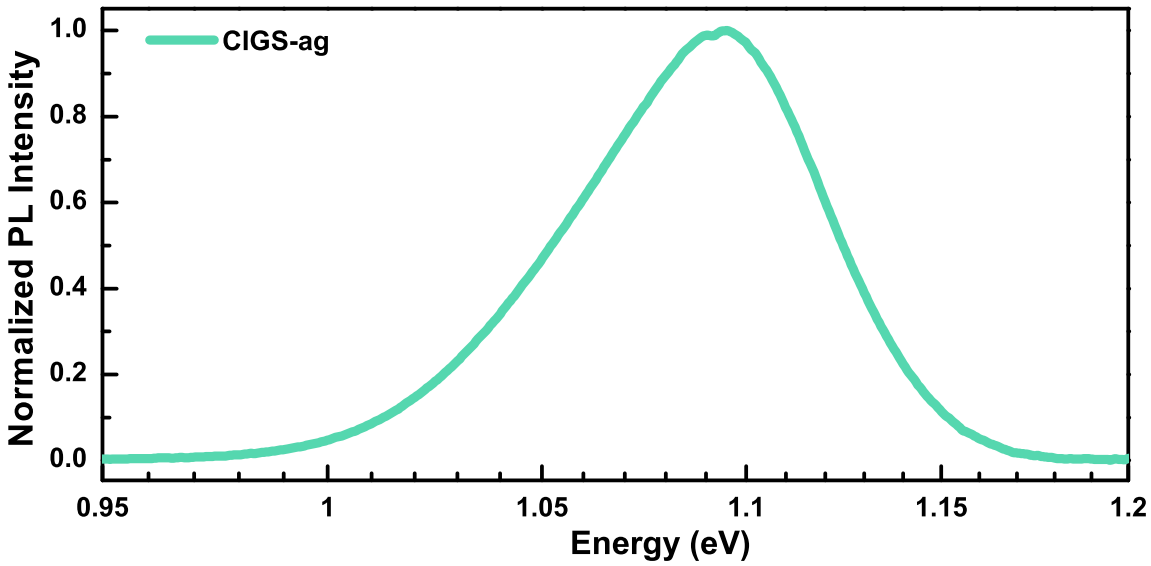

Figure 7.9: Normalized PL spectrum of the sample CIGS-ag, measured at 5 K under an excitation power of 1.2 mW.

A study of the dependence of the PL on the excitation power was carried out in a range of 0.06-3.6 mW. All measured PL spectra were fitted with two Gaussian components and the experimental behaviour evidence only one radiative transition. Based on these fits, Fig. 7.10 a) shows the dependence of the peak energy on excitation power. The fit of Eq. 4.15 to the experimental data gave an estimated β value of 7.0 ± 0.5 meV, which is an expected value for Cu-poor CIGS samples under the influence of fluctuating potentials [347]. Fig. 7.9 b) shows the dependence of the PL integrated intensity on excitation power, which may be parameterized by Eq. 4.16 [341]. The obtained m value was 0.98 ± 0.01.

The asymmetry of the luminescence in addition to the high β value, and obtained value for the slope (m) are in agreement with the presence of tail states in the bandgap in this sample.

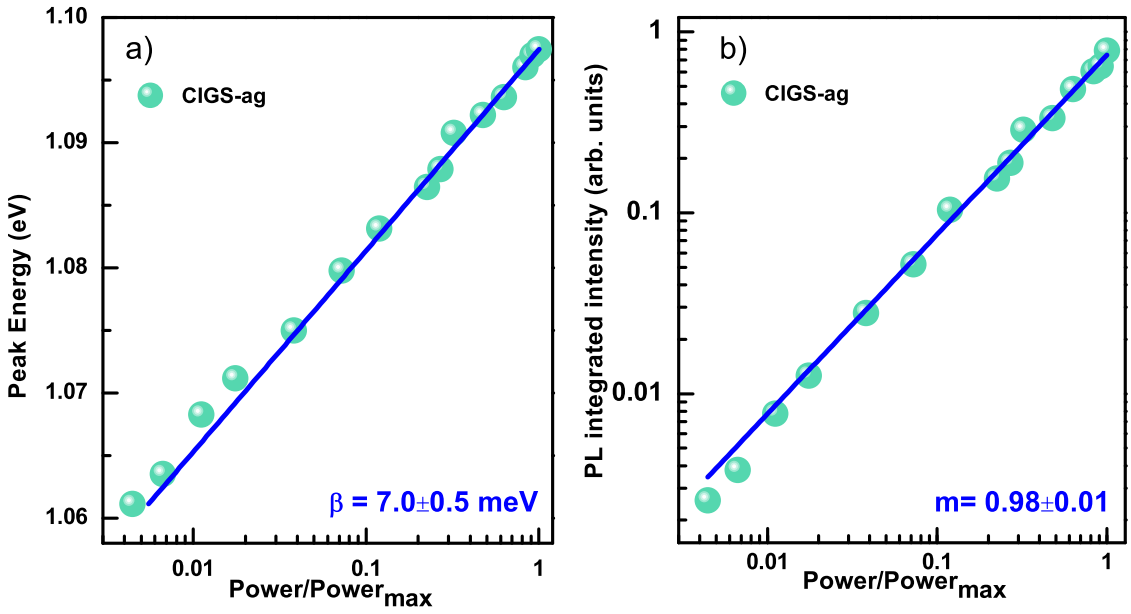

Figure 7.10: Dependence of the a) peak energy and b) PL integrated intensity on the excitation power of the luminescence for the sample CIGS-ag, measured at 5 K. The excitation power values were normalized to the highest one (3.6 mW). The solid lines in a) and b) represent the fits of Eqs. 4.15 and 4.16 to the experimental points, respectively. The estimated values for β and m parameters are shown.

Fig. 7.11 a) shows the obtained luminescence before and after the PDA for different time intervals (Δt). The luminescence measured 1 hour after the annealing is significantly redshifted ($E_p \sim 1.076$ eV) and is clearly less asymmetric than for the luminescence of the sample CIGS-ag. In particular, the asymmetry in the low energy side is less pronounced than observed prior to the annealing. The dependence of the peak energy on the excitation power, Fig. 7.11 b), reveals a β value of 5.8 ± 0.4 meV, which is lower than the value estimated for sample CIGS-ag (7.0 ± 0.5 meV). Interestingly, the luminescence measured 16 hours and 64 hours after the PDA, show a small, but progressive increase of the asymmetry and a blueshift ($E_p = 1.087$ eV for $\Delta t = 64$ hours). However, a complete "recovery" of the shape and peak energy value observed in the obtained luminescence before the PDA, was not obtained. This behaviour goes along with β values of 6.2 ± 0.8 and 6 ± 2 eV estimated for 16 and 64 hours, respectively. Concerning the m parameter, all the values estimated after the PDA (see Fig. 7.11 c)) are still close to 1.

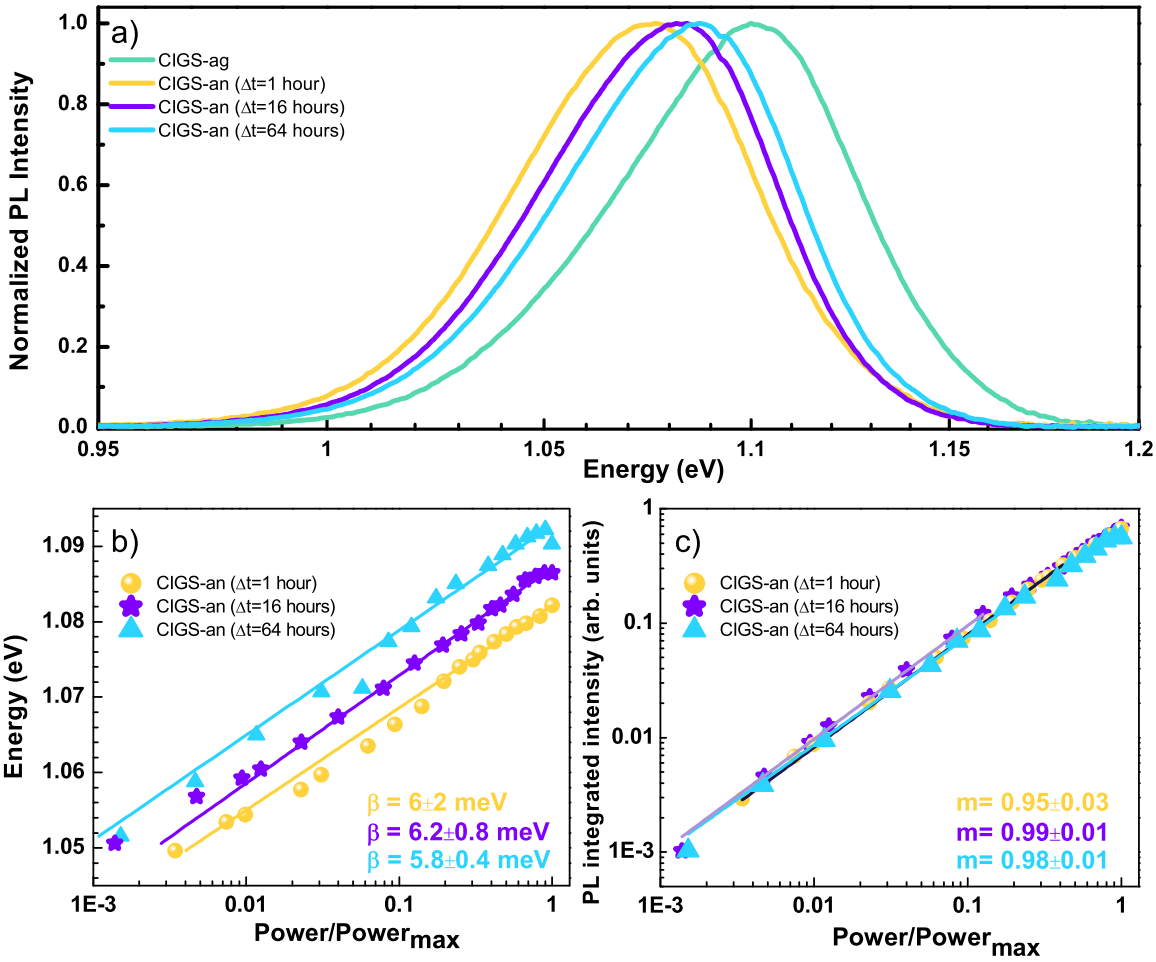

Figure 7.11: a) Normalized PL spectra of sample CIGS-ag sample and CIGS-an, measured 1, 16 and 64 hours after the PDA. The spectra were measured at 5 K under an excitation power of 36 mW. Dependence of the b) peak energy and c) PL integrated intensity on the excitation power of the sample CIGS-an for different time intervals between the PDA and the PL measurement, measured at 5 K. The excitation power values were normalized to 120, 90.5 and 95 mW for Δt = 1, 16, 64 hours, respectively. The solid lines in b) and c) represent the fits of Eqs. 4.15 and 4.16 to the experimental points, respectively. The estimated values for the β and m parameters are shown.

The above results show that the PDA at ∼185 °C for 30 mins in air atmosphere, led to notorious differences in the luminescence comparing to the as-grown sample, as follows: i) an initial redshift of the luminescence followed by a blueshift as the time interval after the annealing increases (see Table 7.5), ii) a potential change on the charged defects density, supported by the less asymmetric shape of the luminescence and a decrease of the β values, and iii) a metastable effect, which is reflected in the continuous changes on the luminescence over time.

From a theoretical point of view, the redshift of the luminescence after the PDA may be explained by: i) an increase of the influence of the fluctuating potentials, ii) a radiative transition involving deeper states than the ones involved in the luminescence of sample CIGS-ag, iii) a decrease of the

bandgap energy induced by a strong enough change in the density and type of defects, and iv) a combination of the previous points. The less asymmetric shape of the luminescence obtained after the PDA combined with the lower value of β in comparison to one obtained for the sample CIGS-ag are not compatible with an increase of the fluctuating potentials. A radiative transition involving deeper sates may be considered. However, this assumption alone does not explain the progressive blueshift observed after the PDA. Thus, a thermally induced metastable decrease of the bandgap energy in the PL scrutinized region followed by a progressive "reversion" to the equilibrium configurations, should be the main reason for the redshift of the luminescence followed by the progressive blueshift.

Table 7.5: Values of the peak energy (E_p) and parameters obtained in the fitting of Eqs. 4.15 and 4.16 to the experimental points for samples CIGS-ag and CIGS-an. Fore sample CIGS-an, the parameters are shown for the different time intervals (Δt) between the PDA and the PL measurement.

	CIGS-ag	CIGS-an	CIGS-an	CIGS-an
Δt		1 hour	16 hours	64 hours
E_p (eV)	1.100	1.076	1.082	1.087
β (mev)	7.0±0.5	5.8±0.4	6.2±0.8	6.0±2
m	0.99±0.04	0.98±0.01	0.99±0.01	0.95±0.03

There are a large number of studies reporting light and bias induced metastability effects in CIGS thin films and CIGS/CdS interface [177, 178, 459]. The light induced metastability effect is often observed after a two step procedure, a prior annealing in dark at ∼330 K (∼57 °C) for extended hours to achieve a relaxed state, followed by a light (red, blue, or white)[1] soaking at RT with 1-Sun of equivalent excitation density (see Table 5.6) [20, 460, 461]. The samples return to their original state after storage in the dark [178]. In our study, we clearly induced the studied sample into a relaxed state, since the ∼185 °C used for the thermal treatment was higher than the threshold temperature needed to obtain such a state, and consequently to observe the metastable effect [20]. However, the studied sample was not exposed to light soaking at RT, since the dependence on the excitation power was studied at 5 K. Moreover, it is widely accepted that the red light soaking brings an increase on the density of the majority charge carriers, that according to Lany and Zunger (L-Z model) may be explained by the amphoteric behaviour of the divacancy complex [V_{Cu}-V_{Se}] that goes from donor to acceptor upon light soaking [177-181]. Even if we consider that the absorbed light may have an active role in the observed metastable effect, these changes of the defects distribution, from donor to acceptor are able to explain the decrease of the influence of the fluctuating potentials, by a decrease on the compensation. However, they do not explain the observed shift of the luminescence after the PDA. Thus, the metastable effect observed in this study is not fully explained by the framework of L-Z model.

[1] Red light is mainly absorbed in the CIGS absorber layer, while blue light is mainly absorbed in the CdS buffer layer. The 514.5 nm line used as excitation source fits mainly the red light condition.

Let us consider the atomic species migration, looking with particular care for the case of Cu diffusion, and explain why this may be the best explanation to the observed effect. The studied CIGS based sample (SLG/Mo/CIGS/CdS) consists in four layers containing seven main constituent elements (Mo, Cu, In, Ga, Se, Cd, and S) in addition to the Na that diffuse to the CIGS layer. This scenario enhances a complex chemical system that, with increasing temperature, will favour the alteration of the in-depth distribution of some of the aforementioned elements in the CIGS layer, resulting in the modification of the type and density of defects present in the CIGS layer after annealing. At this point, we must note that, due to the penetration depth of the incident photons and driven by the normal Ga-profile, PL is able to inspect a region of the CIGS close to the CdS, which is a Cu depleted region. Additionally the progressive change of the luminescence after the PDA was not promoted by temperatures higher than RT. Then a possible diffusion of the elements should happen at RT. It is well known, that the Cu ions are mobile in CIGS at RT with a diffusion constant of 10^{-13} to $10^{-10}\,\mathrm{cm}^2/\mathrm{s}$ [181]. Thus the temperature will necessarily promote the diffusion of Cu from the bulk of the CIGS layer into the surface region, which will lead to a decrease in bandgap values in the former region, which is compatible with the observed redshift of the luminescence. Then, as the time after the PDA goes by, and considering that the Cu moves as a positive ion (Cu_i) and its distribution is favoured by the built-in electric field in the SCR and the quasi-electric field created by the Ga-profile, the assisted drift will promote the return of Cu to the bulk of the CIGS [181]. Hereupon, the diffusion of Cu to the top of the CIGS layer will lead to a decrease of the bandgap energy, compatible with the observed redshift of the luminescence, and its capability to diffuse at room temperature, in addition to its assisted drift, explains the progressive reversion to an equilibrium configuration, that should be different to the one existent before the PDA, since, for instance the occupation from Cu of V_{Cu} will be energetically favourable, which is also compatible to the Le Chatelier's principle[2]. The change in the defects nature will have impact in the influence of the electrostatic fluctuating potentials, that decreased after the PDA, then over time start to increased again. However, it was not possible to associate this effect to a particular mechanism, in this case we associate the observed changes in the fluctuating potentials to an overall rearrangement in the defects nature promoted by the diffusion of the elements followed by the readjusts predicted by the Le Chatelier's principle.

In this study, we investigate the influence of a PDA at 185 °C in air on the CIGS optical properties over the time after the thermal treatment. Notorious changes in the peak position and shape of the luminescence was observed after the PDA comparing with the luminescence obtained for the as-grown sample. The above changes are at least partially reversible, and after a certain time the sample tends to return to a chemical stable state, showing a metastable behaviour. We suggested that the metastable effect may be explained by taking into account the diffusion of the atomic species, being the observed shift of the luminescence at great extent explained by Cu diffusion. The variation of the

[2]Le Chatelier's principle: when a system at equilibrium for a long period of time is subjected to a change in the temperature, then the system will readjusts itself and a new equilibrium is established, which will be different from old equilibrium.

influence of the fluctuating potentials after the PDA may also be explained considering the diffusion and subsequent readjustment of the chemical species presents in the PL scrutinized region.

7.4 Influence of CdS and ZnSnO buffer layers on the PL of CIGS thin films

The Center for Solar Energy and Hydrogen Research Baden-Württemberg, ZSW, achieved similar values of power conversion efficiency, 22.6% for CdS based devices and 21.0% for Cd-free based ones [448, 462]. This impressive result together with the need, for replacing the toxic CdS layer in the CIGS solar cell architecture, emphasizes the need to study alternatives to CdS and the influence of the buffer layer on the CIGS/buffer layer interface properties. Zinc compounds are very promising candidates, being non-toxic and highly transparent at short wavelengths due to their high bandgap values [463]. Among the Zn compounds, the ZnSnO has demonstrated a great potential [140]. ZnSnO has the intrinsic properties required for an ideal buffer layer and can be successfully grown by vacuum compatible techniques, e.g. ALD [140]. In previous works, it was shown that by changing the Sn fraction and the deposition temperature, it is possible to change the bandgap energy in the range 3.2-3.7 eV, mainly through the position of the conduction band edge [114, 139, 141, 143, 464]. In this way, ZnSnO may be used to achieve a suitable conduction band alignment with CIGS and i-ZnO [139]. Nevertheless, one of the open questions about this buffer layer is its influence on the optical properties of the CIGS and of the CIGS/buffer layer interface.

In this study, we investigate the influence of the buffer layer on the CIGS by using PL as a probing tool for the defects in CIGS and in the CIGS/buffer layer interface. A CIGS thin film was deposited on Mo coated soda lime glass using a in-line co-evaporation method [140]. The CIGS film was split in two pieces to allow for the deposition of different buffer layers: CdS (sample A) and ZnSnO (sample B). The CdS was deposited by CBD and the $Zn_{0.8}Sn_{0.2}O_y$ layer was deposited by ALD. For the considered Sn fraction and the deposition parameters of the ZnSnO buffer layer (see Section 5.2), the conduction band line-up at the heterointerface CIGS/ZnSnO should be similar to that of CIGS/CdS [114]. Thus, a similar band alignment for both buffer layers is ensured.

Fig. 7.12 shows the luminescence of the two samples measured at 10 K and with an excitation power of 3.6 mW. For both samples, the luminescence is a broad and asymmetric band in the range of ∼0.97-1.18 eV, with maximum of intensity at ∼1.09 eV. The difference between the relative intensities of the luminescence should be regarded with caution due to the necessarily different experimental optical alignments for both samples.

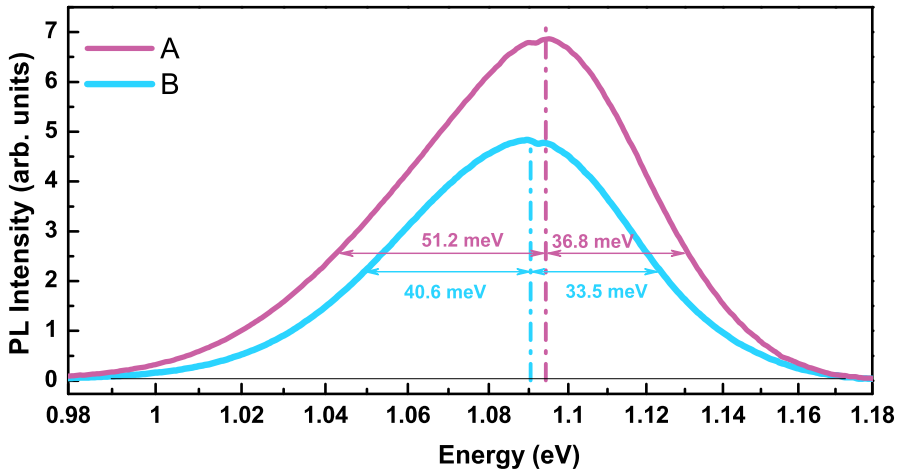

Figure 7.12: PL spectra of sample A (CIGS/CdS) and sample B (CIGS/ZnSnO) measured at 10 K, and with an excitation power of 3.6 mW. The vertical dashed lines indicate the maximum of the luminescence.

The asymmetry of the band may be visually represented by the width at half maximum as displayed in Fig. 7.12. Each luminescence spectrum was fitted with three Gaussian components. The shape of the emission bands was approximately the same for all measured spectra in both dependencies (excitation power and temperature). In fact, the shape is characteristic of electronic transitions occurring in semiconductors with high concentrations of charged defects, that create electrostatic fluctuating potentials along the material [48, 308, 368, 417, 465]. Thus, the three Gaussian components used in the fits describe the asymmetry of the observed luminescence and should not be considered as independent radiative transitions as also done previously in this thesis. The following experimental results and their discussion supports this interpretation.

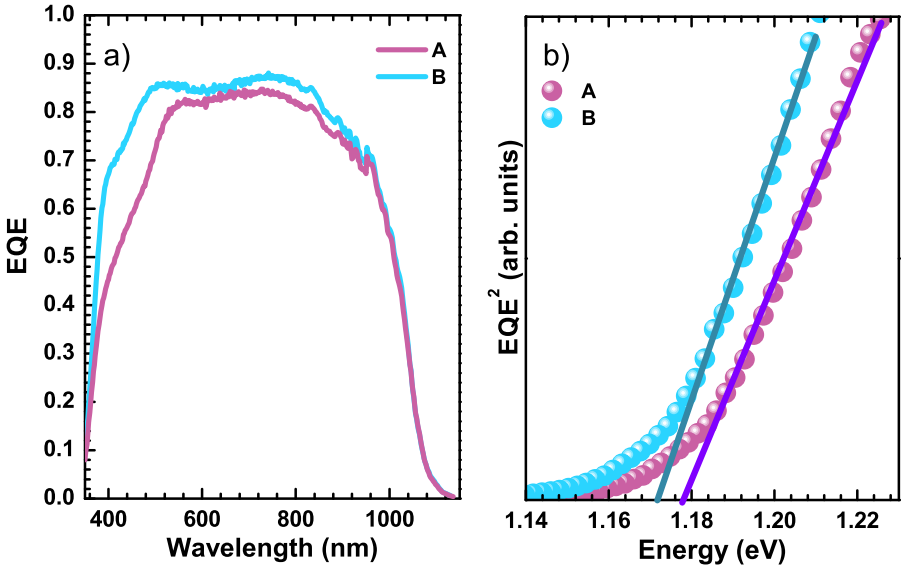

Figure 7.13: a) EQE and b) EQE^2 vs. $h\nu$ plots for the two samples. The solid lines depict the linear fit for the estimation of the bandgap energy values.

For sample A, a slight blueshift (4.5 meV) of the luminescence and a higher asymmetry in the low energy side of the emission are observed, when compared with sample B. A change in the position of the emission may be related with a change of the density of defects or with a change of the bandgap energy. The first case will be addressed later in this Section. Concerning the possibility of a change of the bandgap energy, EQE measurements results are shown in Fig. 7.13 a). The linear fit to the data in the EQE^2 vs. $h\nu$ plot, shown in Fig. 7.13 b), provides for a value of 1.178 eV for sample A and a lower value of 1.172 eV for sample B. This difference of ~6 meV in the bandgap energy of the two samples is compatible with the experimental observed blueshift.

We note that the absorption of the used incident laser light almost do not occurs at the buffer layers, because the incident photons (514.5 nm) have a slightly lower energy than the bandgap energy values of the two materials, 2.4-2.5 [112] and 3.2-3.7 eV [139] for CdS and ZnSnO, respectively. Nevertheless, complementary measurements with a different wavelength, 632.8 nm, with spot diameter of ~1 mm, was performed. In this case, no absorption is expected in the buffer layer. Additionally, a different equipment Bruker Vertex 80v FTIR spectrometer, was used, being the samples measured at 70 K. The as-measured spectra for both, excitation wavelengths and samples, are shown in Fig. 7.14.

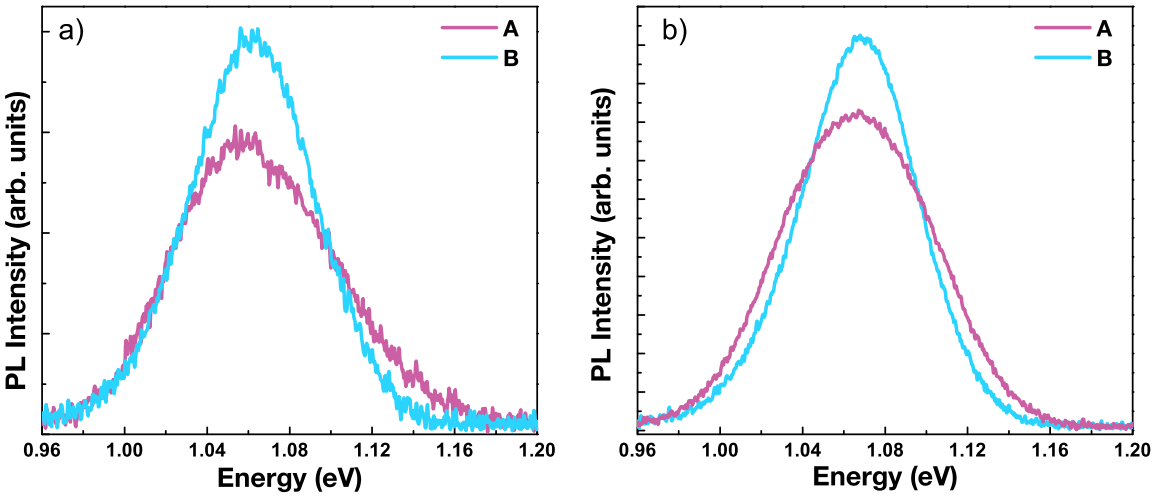

Figure 7.14: PL spectra of sample A and B for an excitation wavelength of a) 514.5 and b) 632.8 nm measured at 70 K, with an excitation power of ~6.5 mW showing an identical behaviour. The measurements were performed in a Bruker Vertex 80v FTIR spectrometer.

No significant changes in the studied emission of both samples were observed in comparison with the previous measurements performed with the excitation wavelength of 514.5 nm in the Bruker IFS 66v FTIR spectrometer. That comparison allow us to conclude that the luminescence of sample A is not affected by the low absorption in the CdS buffer layer and relate the luminescence with the CIGS absorber layer. Fig. 7.14 shows a slightly lower signal-to-noise ratio for sample A in comparison with sample B, independently of the excitation wavelength, which is not in accordance with the

observed luminescence at 10 K (see Fig. 7.12). This behaviour was expected due to the dependence on temperature of the PL integrated intensity, that will be discussed later in this Section. Having guaranteed that the excitation wavelength has no significant influence on the luminescence, both excitation power and temperature were performed with the the 514.5 nm laser line.

Fig. 7.15 a) presents the increase of the excitation power until 3.6 and 19.6 mW, which results in a blueshift of 13.5 ± 0.2 and 10.5 ± 0.5 meV/decade for sample A and B, respectively. Such high blueshift values may be explained in the scope of the fluctuating potentials model [301, 302]. Concerning the dependence of the PL integrated intensity on the excitation power (see Fig. 7.15 b)), the experimental points were fitted with Eq. 4.16. The estimated m values are 0.98 ± 0.01 and 0.99 ± 0.04 for sample A and B, respectively.

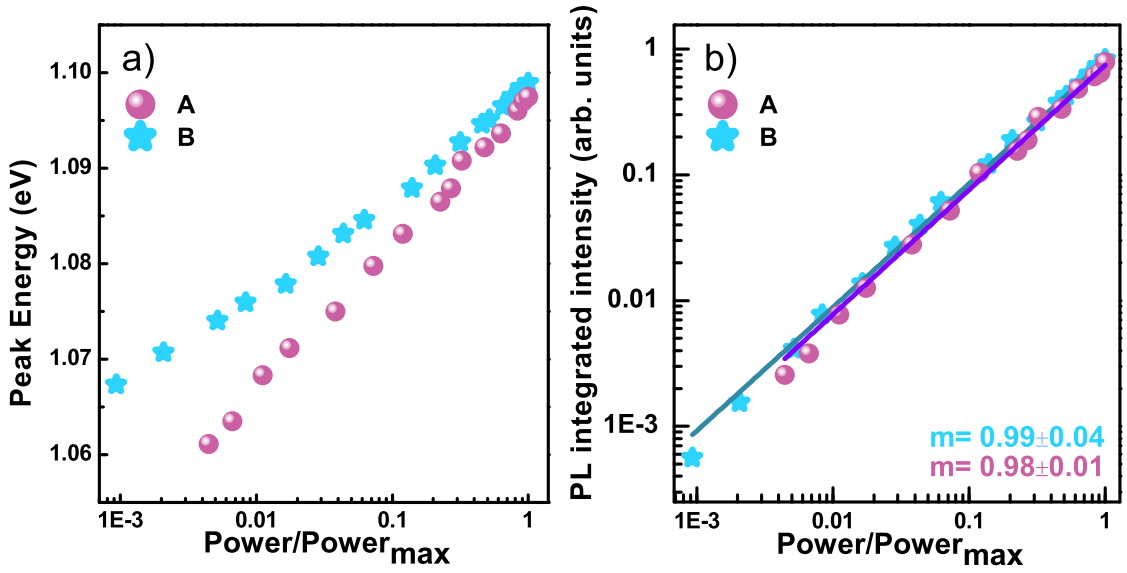

Figure 7.15: Dependence of the a) peak energy and b) PL intensity on the excitation power for both samples. The excitation power values were normalized to 3.6 and 19.6 mW for sample A and B, respectively. The solid lines in b) represent the fit to the experimental points by Eq. 4.16.

.

Fig. 7.16 shows for both samples, the dependencies of the peak energy and PL integrated intensity on the temperature, for an excitation power of 3.6 mW. By increasing the temperature to ~90 K, it is observed a redshift of 59 ± 1 and 39 ± 1 meV for sample A and B, respectively. This observation cannot be explained with a shrinkage of the bandgap. For $T \gtrsim 90$ K, a strong blueshift of the peak energy (72 ± 1 meV) is observed for the ZnSnO containing sample B. The experimental points suggest a compatible behaviour for sample A. However, for this sample the thermal quenching of the PL at ~100 K (~160 K for the ZnSnO sample) prevents its confirmation.

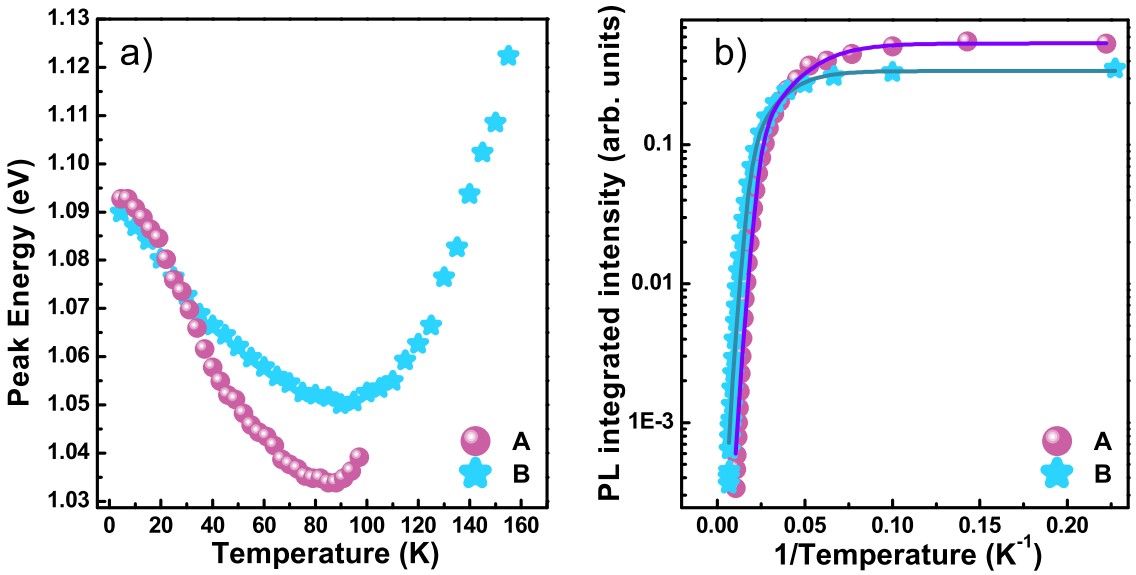

Figure 7.16: Dependence of a) peak energy and b) PL integrated intensity on the temperature in both samples, under an excitation power of 3.6 mW. The solid lines in b) represent the fit to the experimental points by Eq. 5.12.

The temperature dependence of the PL integrated intensity was investigated by considering different models for the thermal activation of non-radiative de-excitation mechanisms. The best model is the one that describes the experimental data with the lower number of de-excitation channels as well as the lower error associated to the estimated parameters (see Table 7.6), and it is described by two de-excitation channels, one involving a discrete energy level and another one involving a band according with Eq. 5.12. The same model provides the best fit for both samples. In the low temperature range (∼4.5-22 K), a small quenching of the PL is observed, which is interpreted as the thermal activation of a non-radiative channel involving a discrete excited energy level. The estimated activation energies E_1 are 6.6 ± 0.4 meV and 5.2 ± 0.3 meV for sample A and B, respectively. These low activation energy values should be related with the presence of defects that create energy levels close in energy to the radiative states. In the high temperature region, activation energies of 28.9 ± 0.6 and 28.3 ± 0.6 meV were estimated for sample A and B, respectively. The similarity of the activation energies for both samples in each non-radiative de-excitation channel suggests that the same mechanisms are responsible for the thermal quenching in both cases. These results support the assumption that the emission in both samples comes mainly from the CIGS layer.

Table 7.6: Values of the parameters obtained in the fitting of Eq. 5.12 to the experimental data of the dependence on the temperature of the PL intensity for samples A and B (see Fig. 7.16 b)).

Sample	I_0	c_1	E_i (meV)	c_{bx}	E_{bx} (meV)
A	0.538 ± 0.006	13 ± 2	5.2 ± 0.3	293 ± 10	28.9 ± 0.6
B	0.340 ± 0.004	9 ± 2	6.6 ± 0.4	25 ± 5	28.3 ± 0.6

The results show clear evidence for a strong influence of fluctuating potentials in the recombination channels in both samples and cannot be explained if typical flat bands are assumed. A few reasons can be pointed out: i) the luminescence of both samples shows an evident asymmetry (see Fig. 7.12); ii) with the increase of excitation power a strong blueshift of the peak position is observed (see Fig. 7.15 a)); iii) the dependence of the intensity on the excitation power gives m values close to 1; iv) with the increase of temperature, a strong redshift followed by a blueshift is observed (see Fig. 7.16 a)). All these experimental results are strong evidences that support the influence of electrostatic fluctuating potentials on the luminescence. Concerning case iv), the results do not follow the theoretical behaviour expected for a semiconductor: absence of energy shift or slight blueshift in the low temperature regime, and a decrease of the bandgap energy for $T \gtrsim 100\,\mathrm{K}$ [418, 466-469]. The experimental results also suggest a higher influence of the electrostatic fluctuating potentials in the CdS sample (A): the asymmetry and the shifts with excitation power and with temperature are higher for the sample A in comparison with sample B. Thus, we assume a higher density of defects on sample A in the CIGS near-interface and/or the CIGS/buffer layer interface, following the previous discussion concerning the presence of a normal Ga-profile. Additionally, the thermal quenching of the luminescence in the case of sample A occurs for a lower temperature, which may be explained by the presence of a higher density of defects involved in the non-radiative de-excitation channels. The occurrence of a higher influence of electrostatic fluctuating potentials in sample A cannot explain the observed blueshift of the luminescence in that sample in comparison with the ZnSnO one. Actually, an increase of fluctuating potentials should be reflected in a redshift if the same bandgap is assumed in both CIGS layers. Thus, the observed blueshift is attributed to an increase of the bandgap in the near-interface layer of the CIGS scrutinized by the PL, in accordance with the EQE results of Fig. 7.13 b).

As discussed in Subsection 4.2.3 [48, 308], even in the presence of electrostatic fluctuating potentials, acceptor defects participate on the radiative recombination mechanisms. Our dependence on the temperature of the PL intensity revealed the thermal activation of a de-excitation channel corresponding to the release of a charge carrier from the radiative state to a band. The estimated activation energies (E_{bx}) for both samples are in the range 28-29 meV and close to the ionization energy calculated theoretically for the V_{Cu}, 30 meV, which is vastly assumed as the dominant acceptor defect in Cu-poor CIGS [173, 174]. Thus, the apparently higher PL intensity at low temperatures observed for the CdS sample may be tentatively related with a higher concentration of the V_{Cu} defect since for radiative defects, higher concentrations will lead to higher PL intensity. Concerning the slight blueshift of the luminescence at low temperature, observed for the CdS sample (see Fig. 7.12), a higher concentration of the V_{Cu} defect is in perfect agreement with the observation of the slightly higher bandgap energy of the CdS sample since an increase on V_{Cu} concentration is compatible with a Cu-deplected region for which it is expected an higher value of the bandgap [470]. Since the same CIGS piece was used for the two buffer layer depositions, it is safe to say that it was the CdS processing that caused an increase of the V_{Cu} concentration. This is in agreement with reports that during

the CBD process there is some Cu-leeching from the CIGS film into the bath [471, 472] providing the CIGS/CdS sample with a higher V_{Cu} defect density than the ZnSnO sample B, and thus explaining our results.

Having explored the difference in the peak position of the luminescence, we now focus on the influence of electrostatic fluctuating potentials on the electronic structure. The different behaviour of the fluctuating potentials between the two samples could be related to a change in the density and/or type of charged defects and, more specifically, to a change in the compensation level due to a modification of the density of donors at the near-interface layer of the CIGS absorber layer. Indeed, as already mentioned in Section 7.1 if a diminishing of the density of donors occurs, it will contribute to a reduction of the fluctuating potentials due to a lower compensation level. The properties of the absorber layer and its interface with the buffer layer are critically influenced by the deposition method of the latter and by its chemical composition, as shown previously [137, 473]. Therefore, many different effects can cause a reduction in the donor concentration. A few differences should be analysed, namely: i) different chemical composition of the buffer layer; ii) different deposition temperatures; and iii) different deposition methods.

Concerning the chemical composition of the buffer layer, it is well known that Cd is able to diffuse into the CIGS, where it creates a donor defect, Cd_{Cu} [474, 475]. The creation of donors in the CIGS will contribute to a higher compensation level and to an increase of the density of ionized defects. In the case of the ZnSnO buffer layer, no experimental results are available showing if there is diffusion of atomic species from the ZnSnO layer to the CIGS. We believe that the formation of the Cd_{Cu} defect is the dominant mechanism that explains the different influence of fluctuating potentials in the two samples. Furthermore, for case ii), a possible contribution could also come from the difference between the deposition temperatures in the two methods, ALD uses a substrate temperature of 120 ° C which is higher than the CBD one (60 ^{o}C). Due to the low formation enthalpy of some point defects in CIGS, an increase of the deposition temperature of the buffer layer can promote a significant change of the total density of defects and their types [173, 174]. As discussed in Sec. 7.3, it is well known that Cu is a mobile element in CIGS at low temperatures such as 80 ° C [198]. Other elements, like Na and K, are also extremely mobile and any change in the concentration of an element will cause significant changes to the defect properties of the semiconductor. However, in this case the precise identification of donors would require a detailed XPS analysis comparing both samples. On case iii), the differences to the deposition process, we can highlight that for the CdS deposition, the CIGS surface will be directly exposed to the CBD solution, whereas for the ZnSnO the CIGS surface will be exposed to the ALD precursors, DEZn, TDMASn and water vapour. On one hand, the CBD process is beneficial for the performance of the solar cell [198, 202, 476] due to restoring the positive defects at the CIGS/buffer interface through the removal of O in the surface In-O bonds [137]. On the other hand during the CBD, there is the removal of Na due to its solubility in water [76]. Subsequently, in the case of the deposition of ZnSnO, there is neither a supply of ammonia to remove surface oxides nor a solution

that rinses Na from the surface. With regards to Na, its main effect on the CIGS is the passivation of donor defects, as discussed in Section 7.1 [394, 477]. The maintenance of O and Na at the surface contributes to the existence of a lower density of donor defects by passivation of V_{Se} defects and, thus to a lower influence of electrostatic fluctuating potentials in the ZnSnO sample [198, 202].

In spite of the positive effect attributed to the CBD process on the electrical performance of solar cells, the ALD of ZnSnO reveals to reduce the effect of electrostatic fluctuating potentials on the CIGS luminescence.

This study showed a reduction of electrostatic fluctuating potentials in the CIGS/ZnSnO sample in comparison with the CIGS/CdS one, showing that the choice of the buffer layer, together with its deposition process, changes the properties of the CIGS absorber. Also, it shows that the ZnSnO semiconductor is a promising buffer layer for CIGS based solar cells. The lower influence of electrostatic fluctuating potentials in the ZnSnO sample compared with the CdS one was discussed and three major candidates for this difference were identified: i) Cd_{Cu} donor defects present in the CdS sample; ii) increased modification of types and densities of defects, including ion mobility, in the ZnSnO sample due to the higher substrate deposition temperature and iii) effects of exposing the CIGS surface to the aggressive CBD solution in the CdS sample. These conclusions should be kept in mind when designing buffer layer materials and/or choosing their deposition methods.

7.5 Influence of back contact passivation on the PL of CIGS ultrathin films

Ultrathin devices are believed to be the forward step to take on CIGS technology. From an economic point of view, a reduction in the material cost and production time are of great interest for the industry. Additionally, a reduction on the path for the generated charge carriers to reach contacts, may lead to a decrease in bulk recombination losses [109]. However, the architecture of ultrathin devices raises new issues concerning absorption and electronic transport, requiring an enhancement of the interfaces quality due to the increased charge carrier density at the contacts. Thus, keeping the same architecture with an ultrathin CIGS layer, results in a deterioration of the electrical parameters, mainly when the thickness reaches values below $1\,\mu$m [107, 108]. This effect is mainly attributed to increased optical losses and recombination at the back contact. In order to address the latter issue, it has been demonstrated that the back interface may be effectively passivated by an Al_2O_3 nanopatterned layer forming a point contact structure [44, 105, 106]. Such passivation layer may lead to three advantageous effects [44]: i) chemical passivation, ii) field effect passivation, and iii) increased reflection at the back contact.

In this Section we will focus our attention on the effect, i) which will lead to a decrease of the

interface defect density [44]. Thus, we expect to observe an influence of the Al_2O_3 nanopatterned layer on the optical properties of the CIGS caused by a change in the density of the charged defects.

Two ultrathin solar cells were prepared: i) a reference solar cell with the standard CIGS solar cell structure (Sample A); ii) a solar cell with an Al_2O_3 nanopatterned layer in-between the Mo and the CIGS (see Fig. 7.17), the so-called passivation layer (sample B). The ultrathin CIGS absorber layer is 350 nm thick, so that the effects of back interface recombination have a strong impact on the cell performance. Both samples were grown with flat Ga-profiles, in order to avoid complementary back surface passivation effects by the quasi-electric field that comes up with the Ga-profile. Note that with the exception of the passivation layer, all the solar cell fabrication was exactly the same for both samples. Hence, the possible differences in the level of fluctuating potentials should be related with differences on the electrostatic ones between the two samples.

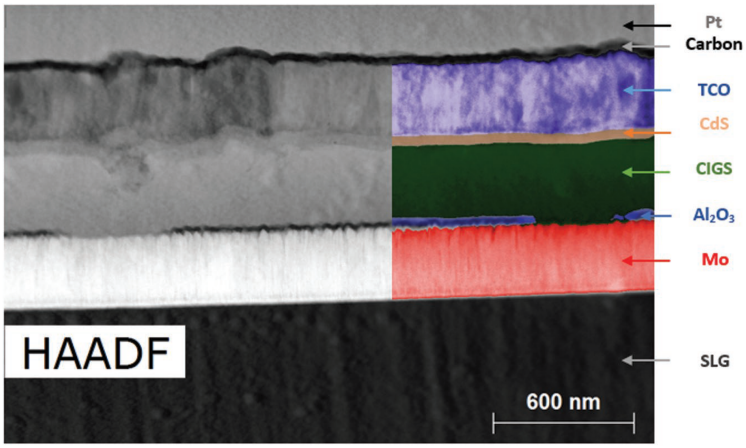

Figure 7.17: Cross section high angle annular dark-field transmission electron microscope image of the passivated solar cell. The dark layer in-between the Mo layer and the CIGS layer is the Al_2O_3 passivation layer. The observed openings on this Al_2O_3 layer are the nanopatterned point contacts. Adapted from [44].

The normalized PL spectra of the two solar cells, measured at 7 K under an excitation power of 29 mW are presented in Figure 7.18 a). Two broad and asymmetric bands with a maximum intensity at 1.07 and 1.06 eV are observed for sample A and B, respectively. Broad luminescence is typical of Cu-poor CIGS polycrystalline solar cells [102, 301]. However, for the case of sample A the luminescence is significantly broader (FWHM∼83 meV) than that obtained for sample B (FWHM∼60 meV). Additionally, sample A also shows a larger asymmetry in the low energy side of the spectrum, suggesting a higher influence of charged defects in this sample than in sample B. The inset of Fig 7.18 a) shows the two non-normalized spectra for sample A and B, a notorious high signal-to-noise ratio may be observed for sample A than for sample B. The luminescence of both samples shows strong evidences of more than one radiative transitions. Three transitions were identified in both samples (#1, #2,

and #3). Figure 7.18 b) and c) show the Gaussian fitting model implemented for sample A and B, respectively. The luminescence from sample A is described by 5 Gaussian components as follows, the Gaussian components 1 is ascribed to the main radiative transition #1, whereas $2'$ and $2''$ to the lower energy transition and $3'$ and $3''$ to the higher energy transition. On the other hand, four Gaussian components are enough to describe the luminescence from sample B, the Gaussian components 1 and $1'$ are ascribed to the main radiative transition #1, whereas 2 and 3 to the lower and higher energy transitions, respectively. We will focus our attention in the main radiative transition #1. Thus, in order to better understand the impact of the Al_2O_3 nanopatterned passivation layer in the electronic energy levels structure of the CIGS, we will study the dependencies of transition #1 on the excitation power and temperature.

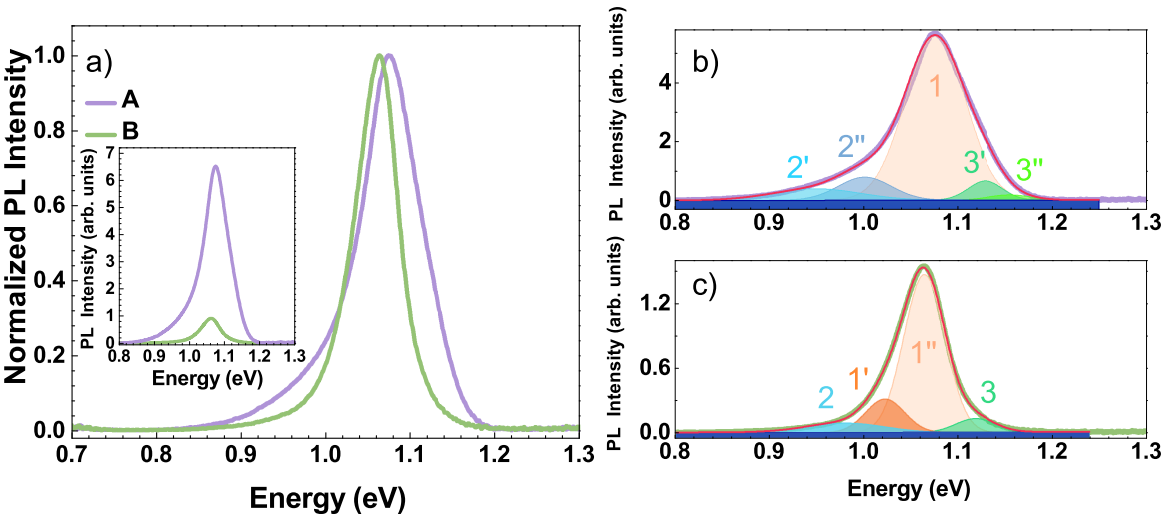

Figure 7.18: a) Normalized PL spectra of samples A and B, measured at 6 K, with an excitation power of 29 mW. The inset shows the non-normalized spectra of samples A and B presented in a). The fitting models with Gaussian components for samples A and B are presented in b) and c). b) Gaussian components 1 is ascribed to the main radiative transition, whereas $2' + 2''$ and $3' + 3''$ to the lower and higher energy transitions in sample A, respectively. c) the Gaussian components 1 and $1'$ are ascribed to the main transition, whereas 2 and 3 to the lower and higher energy transitions in sample B, respectively.

Fig. 7.19 a) and b) show the dependence of the peak energy and integrated PL intensity for transition #1 on the excitation power, respectively. From the fit of Eq. 4.15 to the dependence of the peak energy on the excitation power we obtained β values of 9.2 ± 0.1 and 6.2 ± 0.1 meV for sample A and B, respectively. Concerning the dependence of the PL integrated intensity on excitation power, the experimental points were fitted with Eq. 4.16. The estimated m values were 0.98 ± 0.01 and 0.99 ± 0.04 for sample A and B, respectively. These m values close to 1 are compatible with recombination involving tails states, as have been obtained for others CIGS samples studied in this

thesis.

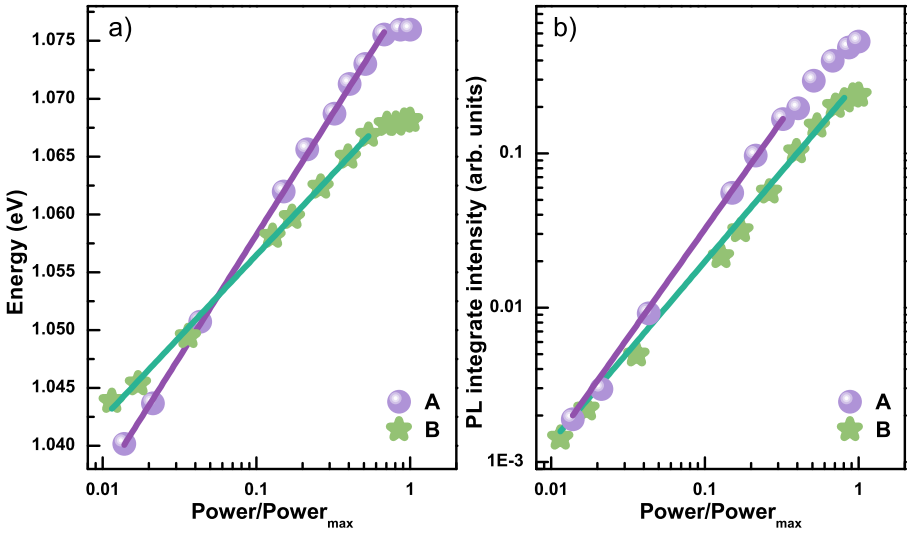

Figure 7.19: Dependence of a) peak energy and b) PL integrated intensity for transition #1 of sample A and B on the excitation power, measured at 6 K. The excitation power values were normalized to 29.2 and 36.2 mW for sample A and B, respectively. The solid lines represent the fit to the experimental points by a) Eq. 4.15 and b) Eq. 4.16.

Fig. 7.20 shows the dependence of the peak energy and PL integrated intensity for transition #1 on the temperature, under an excitation power of 29 mW. From ∼5 K to ∼75 K it is observed a well behaved redshift of 41 ± 1 and 38 ± 1 meV for samples A and B, respectively. For temperatures higher than the ∼75 K an overall non-monotonous redshift for both samples is observed up to the complete thermal quenching of the luminescence at 114 K and 106 K for samples A and B, respectively. Note that the non-monotonous trend observed for higher temperatures is not related with difficulties in the Gaussian model implementation, since the signal-to-noise ratio and shape of both luminescences are quite well defined.

The dependence of the PL integrated intensity on the temperature was investigated by considering different models for the thermal activation of non-radiative de-excitation mechanisms. The best model is described by two de-excitation channels, one involving a discrete energy level and another one involving a band according to Eq. 5.12. The same model provides the best fit for both samples, and the obtained parameters are presented in Table 7.7. It considers in the low temperature range (∼6-17 K), a small quenching of the luminescence, which is interpreted as the thermal activation of a non-radiative channel involving a discrete excited energy level with activation energies E_1 of 4.2 ± 0.2 meV and 2.9 ± 0.2 meV for samples A and B, respectively. In the high temperature region, activation energies of 33 ± 4 and 11.2 ± 0.7 meV were estimated for sample A and B, respectively. Activation energy values of 11 and 33 meV are close to other activation energy values already presented in this thesis (Sections 7.2 and 7.4) for different CIGS based samples. Thus, this may suggest that the existence of dominant mechanisms responsible for the thermal quenching in CIGS based samples, which are the

same in ultrathin and thick absorbers. Indeed, both activation energies have been already tentatively related to conduction band tails involving donor clusters and the V_{Cu} acceptor defect. Note that, besides the importance of the identification of common radiative channels in different CIGS samples, the reproducibility in the obtained activation energies in significantly different CIGS, supports the approach used in the implemented Gaussian fitting models.

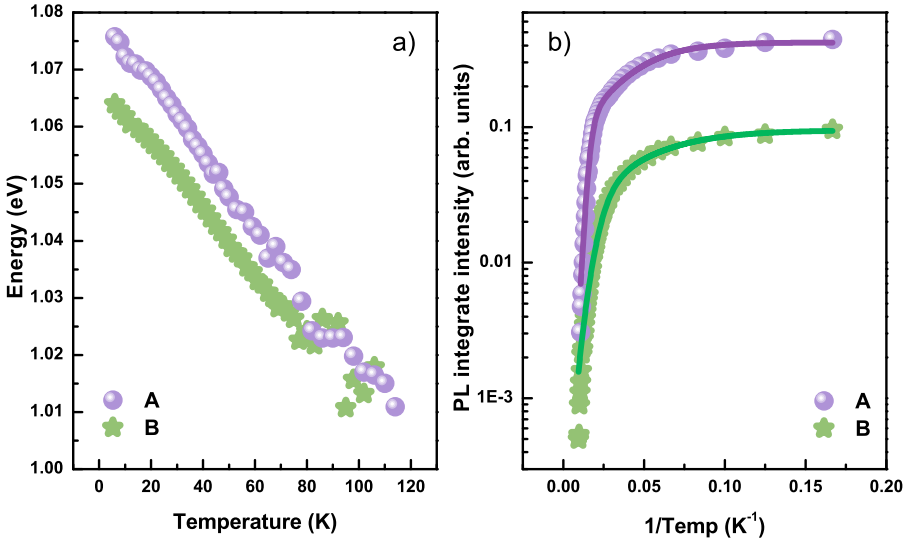

Figure 7.20: Dependence of a) peak energy and b) PL integrated intensity for transition #1 on the temperature in both samples, under an excitation power of 29 mW. The solid lines represent the fit to the experimental points by Eq. 5.12.

Table 7.7: Values of the parameters obtained in the fitting of Eq. 5.12 to the data related to the temperature dependence of the PL integrated intensity for transition #1 (see Fig. 7.20 b)).

Sample	I_0	c_1	E_i (meV)	c_{bx}	E_{bx} (meV)
A	0.421 ± 0.005	5.4 ± 0.4	4.2 ± 0.2	4 ± 2	33 ± 4
B	0.095 ± 0.001	3.3 ± 0.4	2.9 ± 0.2	0.18 ± 0.02	11.2 ± 0.7

The shape of the luminescence of sample A is notoriously broader and asymmetric than the luminescence obtained for sample B. In addition, the β value obtained for sample A was significantly higher regarding the one obtained for sample B. Since the CIGS layer is nominally the same, the changes observed in luminescence must be related with the chemical passivation of the back surface of the absorber layer. With the used excitation wavelength, 514.5 nm, penetration depth of the incident photons, 70 nm, is smaller than the CIGS thickness, 350 nm. However, due to the CIGS high diffusion length of the generated charge carriers, we will be able to detect possible differences in the

electronic structure between the two samples, necessarily caused by the presence of the passivation layer in sample B. The above results support the existence of an effective chemical passivation effect due to the Al_2O_3 nanopatterned layer, since the experimental evidences suggests an higher influence of the electrostatic fluctuating potentials caused by a higher density of charged defects in sample A in comparison to sample B. The PL results are supported by the obtained electrical parameters, that show a notorious improvement in the V_{OC} value from 538 to 627 mV and in the J_{SC} value from 19.29 to 21.56 $mA.cm^{-2}$ for sample A to B, respectively [44]. These improvements are compatible with the passivation of recombination centers in sample B, that will improve directly the V_{OC} and the collection of the generated charge carriers leading to a higher J_{SC} value.

At this point, it is relevant to discuss the bandgap energy values for the two samples. A similar bandgap value was estimated for both samples, 1.17 ± 0.01 eV, according to a linear fit to the data in the EQE^2 vs. $h\nu$ plot (not shown). Also, no significant difference in the peak energy of transition #1 is observed between the two samples. Both experimental evidences are compatible with the fact that the CIGS layer in both samples is nominally equivalent. Regarding the nature of transition #1 in the two samples, the temperature dependence gave activation energies for the de-excitation mechanism involving a band that are close to the values obtained for other set of samples studied in this thesis. Indeed, for sample A, the value is compatible with the involvement of the V_{Cu} acceptor defect, whereas for sample B, a lower value was estimated, which suggest the involvement of tails states in the conduction band. Due to close magnitude of the two redshifts observed until 75 K, and more important, the non-monotonous behaviour observed in the two samples for temperatures higher than 75 K, the recombination of the two studied radiative transitions could have a common origin, which we tentatively relate with the V_{Cu} acceptor defect. Then, the radiative transition #1 for sample A is associated to a BI recombination and for sample B, a TI recombination, involving the same impurity band associated to the V_{Cu} defect. Despite the necessary caution needed to analyse the luminescence intensity, as already stated in this thesis, the overall lower intensity obtained for sample B may be explained by a lower density of radiative defects comparing to the ones existent in sample A. This behaviour may possibly be related to a higher density of the V_{Cu} defect in sample A and compatible with the passivation of those in sample B. This result is not compatible with the observed behaviour for CZTS passivated sample studied in Section 6.4, that presented a significant improvement in the PL intensity after the PDA, which suggests a much more efficient passivation of the non-radiative centers in CZTS than in CIGS, compatible with the higher density of non-radiative centers in the CZTS studied samples comparing to the one presented in the CIGS. However, it is in agreement with the results from Section 7.4 where we observed a lower PL intensity in the CIGS sample with the ZTO buffer layer with an lower density of defects as we observed in this study, both due to a passivation of radiative defects.

Two ultrathin CIGS based solar cells were studied in this Section. The PL dependencies on the excitation power and temperature indicate an influence of electrostatic fluctuating potentials in the

optical properties of both samples. This study showed a reduction of the electrostatic fluctuating potentials in the Mo/Al_2O_3/CIGS based sample in comparison with the Mo/CIGS one, showing an effective chemical passivation of the charged defects promoted by the Al_2O_3 nanopatterned passivation layer. Despite, the lower density of charged defects present in the passivated sample, both the results suggest that luminescence present a radiative transition involving the same V_{Cu} acceptor defect. The PL results are in accordance with the electrical parameter values obtained for both ultrathin CIGS samples.

7.6 Evidences of limiting effects of fluctuating potentials on V_{oc} of CIGS thin film solar cells

The investigation of the impact of the fluctuating potentials in the performance of the solar cells is presently an open issue in the scientific community [102, 223, 289, 290, 291, 442, 443, 444]. Experimental studies suggest different types of fluctuating potentials and gave different amplitudes of the tails states [32, 131, 175, 298, 301, 442], but few works with comparison of the impact of different types of fluctuating potentials, are available [223, 290, 291]. The balance between the increase of thermal generation and recombination rate due to tails states, reduces the efficiency limit established in the SQ model [11]. Additionally, no agreement exists concerning its influence at RT for CIGS based solar cells. As already discussed, the presence of fluctuating potentials is a limiting factor to the improvement of the V_{OC} and the solar cell efficiency, η [284, 298]. On the other hand, some authors claim for both Cu-poor CIS and CGS, the reduction of the amplitude of the fluctuating potentials to a few meV at RT with negligible effects in solar cell performance [359].

In following study, we calculated the fluctuating potentials influence in the V_{OC} deficit for CIGS based solar cells according to extensions to the SQ model and compare the predictions with experimental results. A series of three Cu-poor CIGS solar cells were grown with different Cu fraction, in order to attain different amplitude of fluctuating potentials. Thus, a set of three Cu-poor CIGS solar cells were fabricated following a modified version of the Ångstrom solar cell baseline [140]. The composition of the CIGS films was determined by X-ray fluorescence (XRF) performed in a Panalytical Epsilon 5 spectrometer. Flat evaporation rates were used to achieve Cu-poor samples with metallic ratio of [Cu]/([Ga]+[In]) = 0.53, 0.71, and 0.84 (from now on denoted by samples Cu53, Cu71, and Cu84, respectively). The GGI ratio was fixed to 0.3, without any Ga-profile. The thickness W of the CIGS layers were obtained by stylus perfilometry and are 1.82, 1.88, and 2.07 μm for samples Cu53, Cu71, and Cu84, respectively.

Let us consider the SQ model discussed in Chapter 1, and the fact that this model assumes a step function for the absorptance $a(h\nu)$ of the absorber layer, i.e., $a(h\nu) = 1$ for $h\nu \geq E_g$ and $a(h\nu) = 0$ below this energy value. Thus, the J_{SC} and J_0 values given by Eqs. 1.1-1.2, respectively, depend

essentially on one input parameter related to the absorber layer (i.e., E_g), which makes this model quite simple if we think in the overall solar cell complexity and process of operation, briefly addressed in Chapter 2. However, the SQ model provides a powerful starting point to address loss mechanisms other than radiative recombination [24, 138, 442, 444, 478, 479]. Thus, we will propose extensions to the SQ model based on the Urbach, optimal-fluctuation, and bandgap models, previously discussed in Subsection 4.2.1, in order to discuss the impact of different types of fluctuating potentials in the solar cell electrical parameters in the framework of different theoretical models. We should note that these extensions are also simple models that ignore other loss mechanisms existing in real solar cells, since the aim is to isolate the role of electrostatic and bandgap types of fluctuations from the other loss mechanisms.

As discussed in Chapter 4, fluctuating potentials extend the density of states into the bandgap violating the SQ assumption of a step-function absorptance in which $a(h\nu) = 0$ for $h\nu < E_g$. Thus, changes in absorptance that reproduce the sub-bandgap absorption coefficient $\alpha(h\nu)$ are needed. In fact, as presented in Subsection 4.2.1 several theoretical approaches based on different sources of fluctuating potentials gave explicit functions for absorption edge in the sub-bandgap region [175, 298, 314, 315, 317], namely: i) Urbach model, ii) optimal-fluctuation theory, and iii) a Gaussian approach that describe the bandgap fluctuations. The existence of explicit functions for the absorption coefficient in models that deal just with one type of fluctuating potentials (Eqs. 4.8 and 4.10), allows the investigation of separate contributions on solar cell electrical parameters. In the following, we start by addressing different approaches to obtain $a(h\nu)$.

For the Urbach model, we adapt the approach of Jean *et al.* [442] to a planar solar cell, and assume zero front reflectance and total reflection on the rear side. Thus, the absorptance follows the Lambert-Beer's law and is described by Eq. 2.2, being $\alpha(h\nu)$ given by Eq. 4.6 [23, 24, 25]. In the case of electrostatic fluctuating potentials, we also adapt the approach of Jean *et al.* [442]. For $h\nu < E_g$, $a(h\nu)$ was modeled for a planar solar cell and the total $a(h\nu)$ is

$$a(h\nu) = \begin{cases} 1 - \exp[-2\alpha(h\nu)W], \ h\nu < E_g \\ 1, \ h\nu \geq E_g \end{cases} \tag{7.2}$$

where $\alpha(h\nu)$ is given by Eq. 4.8. For the previous two models, the value of $\alpha_0 = 1.24{\times}10^4$ can be estimated by fitting experimental $\alpha(h\nu)$ values with a semi-empirical expression valid for $E > E_g$ given Eq. 2.4, as discussed in Subsection 2.2 [20].

Finally, in comparison with the electrostatic fluctuating potentials, for the bandgap ones, $a(h\nu)$ must take into account that spatial fluctuations in the composition will cause local changes in the bandgap, which should be reflected on the modulation of $a(h\nu)$ below and above E_g. Rau and Werner presented an absorptance dependence on σ as follows [138]

$$a(h\nu) = \frac{1}{2} \ \mathrm{erfc}\left(\frac{E_g^{mean} - h\nu}{\sigma\sqrt{2}}\right). \tag{7.3}$$

There is an important difference between the previous three theoretical models. Whereas, models ii) and iii) focus on particular types of fluctuating potentials, the Urbach model (model i)), reflects the influence of shallow tail states, but it is not clear if this model is able to distinguish the different type of fluctuating potentials, since it is an empirical model. The impact of the fluctuating potentials described by the Urbach model in the performance of the solar cell may be discussed by replacing the step-function $a(h\nu)$, proposed by SQ, by Eq. 2.2 in Eqs. 1.1-1.2, to obtain J_0^{Urbach} and J_{SC}^{Urbach}, respectively. The remaining solar cell electrical parameters are obtained following the usual procedure. Furthermore, to study the balance of the influence of electrostatic fluctuating potentials and bandgap ones, $a(h\nu)$ is given by Eq. 7.2 and Eq. 7.3, respectively. The comparison of the SQ electrical parameters, which set the upper limit, with the ones obtained by the SQ extensions, allow us to discuss the losses induced by fluctuating potentials and, more important, to discuss the contribution given by the two different types of fluctuating potentials. After this theoretical discussion, we will present our optical and electrical experimental results in order to apply the SQ extension models to real solar cells.

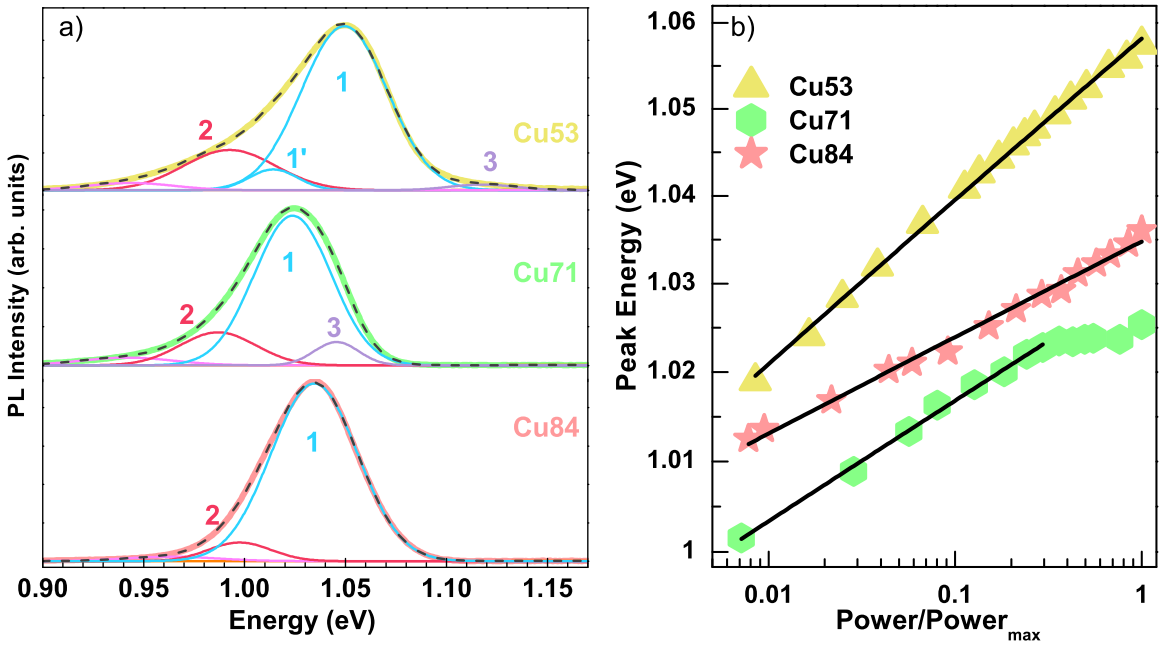

Figure 7.21: a) PL spectra of samples Cu53, Cu71, and Cu84, measured at 7 K, with an excitation power of 10 mW. The fitting models with Gaussian components are shown for each sample. Gaussian components 1 and 1′ are ascribed to the main transition, whereas 2 and 3 to the lower and higher energy transitions, respectively. b) Dependence of peak energy of transition #1 on the normalized excitation power for the three samples. The solid lines represents the fit of Eq. 4.15 to the experimental data.

Fig. 7.21 a) shows the PL spectra of the three samples measured at 7 K with an excitation power of 10 mW. For all Cu fractions the luminescence is broad and asymmetric, showing strong evidence of more than one radiative transition. Two transitions are identified for the sample Cu84 (#1 and #2), while for samples Cu71 and Cu53 a third transition (#3) is observed at higher energies. Transitions

#2 and #3 are described by one Gaussian component in all samples. Regarding transition #1, it is well described by just one Gaussian component in samples Cu73 and Cu84. However, in order to use the same fitting model throughout the dependence of the luminescence on excitation power from sample Cu53, a second Gaussian component (denoted by $1'$ in Fig. 7.21 a)) is needed. All transitions follow the same dependence on the excitation power for each sample, which allow us to focus on the main radiative transition (#1) as it is representative of the experimental behaviour of the whole luminescence.

The peak energy of transition #1 is shown in Table 7.8, for each sample. No straightforward dependence on Cu fraction is observed. Two factors may be responsible by a shift in energy of the luminescence between samples: a change of the bandgap energy and/or a change in the influence of fluctuating potentials, as a consequence of different density of charged defects, and structural inhomogeneities [102, 173, 175]. However, none of them alone may explain the experimental trend as shown in the following. To address the first issue, EQE measurements were performed. The linear fit to the data in the EQE^2 vs. $h\nu$ plot, shown in Fig. 7.22 a), provided bandgap energy values of 1.20 ± 0.10, 1.14 ± 0.05, and 1.10 ± 0.02 eV for samples Cu53, Cu71, and Cu84 , respectively. As expected, the bandgap energy decreases with the increase of the Cu fraction, due to the increment in the repulsive interaction between Cu-3d and Se-4p states, which defines primarily the maximum of the valence band in CIGS [173, 480, 481]. However, the obtained dependence of bandgap on the Cu fraction does not follow the one observed for the energy shift of the peak energy (see Table 7.8). Now, we focus on the possible influence of fluctuating potentials on the energy shift of the luminescence, starting by studying the dependence of the luminescence on excitation power. As the excitation power increases, a blueshift of the emission is observed for all samples, as shown in Fig. 7.21 b). In the literature, the dependence of the peak position on the excitation power is often described by the relation given by Eq. 4.15 [344, 345, 346, 348]. We note that β parameter reflects the amplitude of the overall fluctuating potentials, as discussed by Yu [348]. Estimated β values of 8.1 ± 0.1, 5.8 ± 0.1, and 4.7 ± 0.1 meV for samples Cu53, Cu71 and Cu84, respectively, were obtained. Such high β values, as already stated, are compatible with the existence of fluctuating potentials [102, 344, 345, 346, 348]. The decrease of β with the increase of the Cu fraction, is in accordance with the proposed aim to grow a set of CIGS solar cells with different influence of fluctuating potentials. Nevertheless, the monotonous trend of estimated β do not follow the experimental behaviour. Thus, the energy shift of the luminescence should reflects both previous factors.

Table 7.8: Composition, optical and electrical parameters obtained for the three samples. [Cu]/([Ga]+[In]) (CGI) and [Ga]/([Ga]+[In]) (GGI) ratios, peak energy for transition #1 ($E_{p\#1}$) and β estimated from PL spectra, bandgap energy (E_g) obtained from EQE^2 vs. $h\nu$ plot, and J_{SC}, V_{OC}, FF, and η estimated from the J-V curves. The calculated V_{OC} losses (E_g/e-V_{OC}) are shown.

Sample	CGI	GGI	$E_{p\#1}$ (eV)	E_g (eV)	β (meV)	J_{SC} (mA.cm^{-2})	V_{OC} (mV)	FF (%)	η (%)	E_g/e-V_{OC} (mV)
Cu53	0.53	0.31	1.049 ± 0.001	1.20 ± 0.10	8.1 ± 0.1	30.04 ± 0.24	502 ± 12	70.4 ± 0.6	10.5 ± 0.3	700
Cu71	0.71	0.30	1.024 ± 0.001	1.14 ± 0.05	5.8 ± 0.1	31.82 ± 0.49	570 ± 10	76.3 ± 3.9	13.8 ± 0.9	570
Cu84	0.84	0.30	1.035 ± 0.001	1.10 ± 0.02	4.7 ± 0.1	32.30 ± 0.26	600 ± 5	77.4 ± 0.9	15.1 ± 0.3	500

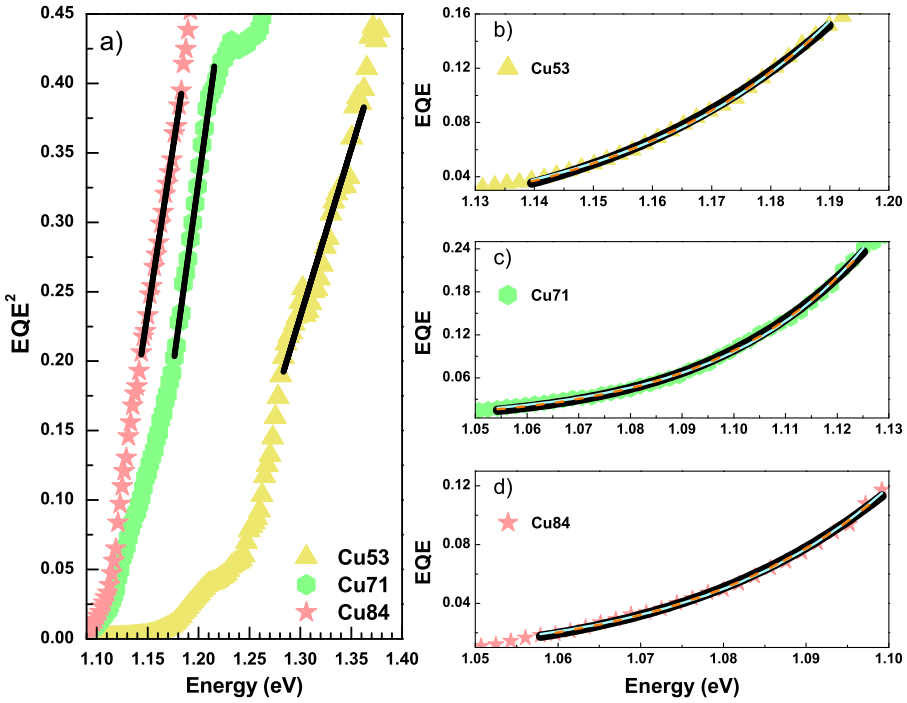

Figure 7.22: a) EQE^2 vs. $h\nu$ plots for the three samples depicting a linear fit for the estimation of the bandgap energy values. b), c), and d) sub-bandgap energy range of the EQE curve for samples Cu53, Cu71, and Cu84, respectively. The black solid, cyan solid, and orange dashed lines represent the fit of Eqs. 4.10, 4.6, and 4.8, respectively, to the experimental data.

The temperatures range in the PL study is far from the operation temperatures of the solar cells. Thus, it is important to correlate the existence of fluctuating potentials at low temperature with its possible existence at RT. In this way, we studied the sub-bandgap energy range of the EQE curve (measured at RT). For that energy range, EQE is proportional to the absorption coefficient and follows the density of states of fluctuating potentials. Following the above discussion of the SQ extensions, the sub-bandgap energy range of the EQE curve for samples Cu53, Cu71, and Cu84 were fitted with Eqs. 4.6, 4.8, and 4.10 (see Figs. 7.22 b), c), and d)), being the obtained parameters that describe the amplitude of fluctuating potentials presented in Table 7.9. The obtained E_U values are in agreement with the ones previously reported for CIGS [36, 325, 326, 328, 335]. Also, the observed decrease of the estimated E_U values with the increase of Cu fraction, is in accordance with the work of Sioda et al. [335] in which a series of samples with different Cu fractions was evaluated. However, in that work the Cu fraction range was smaller than our, and closer to the stoichiometry. The obtained γ values (electrostatic fluctuating potentials) decrease with the increase of the Cu fraction, and are also in agreement with the ones shown by other authors [298, 301]. Dirnstorfer et al. [301] showed a similar behaviour for γ for a different Cu fraction range. Lastly, our estimated σ values (bandgap fluctuating potentials), also decrease with the increase of the Cu fraction, and are higher than reported ones [298].

The presented theoretical models do not provide absolute values for the amplitude of fluctuating potentials. Indeed, in Table 7.9, E_U values are higher than the ones obtained for γ, which reflects the

Table 7.9: Values of E and E_U, E_g and γ, and E_g^{mean} and σ, obtained from the fits of Eqs. 4.6, 4.8, 4.10 to the sub-bandgap energy range of the EQE curve, respectively.

Sample	Urbach Model		Optimal-Fluctuation Theory		Bandgap Fluctuations	
	E (eV)	E_U (meV)	E_g (eV)	γ (meV)	E_g^{mean} (eV)	σ (meV)
Cu53	1.256 ± 0.001	35.5 ± 0.2	1.278 ± 0.001	32.2 ± 0.2	1.26 ± 0.03	68 ± 7
Cu71	1.164 ± 0.001	27.4 ± 0.2	1.179 ± 0.001	24.3 ± 0.2	1.22 ± 0.03	65 ± 5
Cu84	1.149 ± 0.001	22.9 ± 0.2	1.165 ± 0.001	21.4 ± 0.3	1.18 ± 0.06	54 ± 10

qualitative nature of these parameters, since the exponential function that describes the Urbach model should deal with shallower tails states than the ones described by the 5/4 power law, in the scope of the optimal-fluctuation theory. Thus, E_U, γ, and σ values should not be directly ascribed to the effective amplitude of tail states, being only possible to compare their values inside each particular model. Moreover, values obtained from different experimental techniques, even being equivalents, should not be compared straightforward, as showed by Malerba et al. [324]. Regardless of the used theoretical model, the fitting parameters that are proportional (or correspond) to the bandgap energy, decreases with the increase of the Cu fraction, following the behaviour of the assumed effective bandgap energy values.

The dependence on the Cu fraction of E_U and γ (both estimated at RT) follows the same dependence of β (estimated at low temperature), whereas σ deviates somehow from that trend. This is an important result due to the differences in physical and mathematical approaches used in Urbach model and optimal-fluctuation theory models, and also by considering the different temperatures at which the measurements were taken. Thus, our results strongly suggest that temperature is not a limiting factor for the discussion of the influence of fluctuating potentials, which follows the no significant dependence of E_U on the temperature observed by other authors, for CIS and Cu-poor CIGS [328, 335, 336].

The electrical characterization of the solar cells is summarized in Table 7.8. The increase of Cu fraction lead to an improvement of 2.26 mA.cm^{-2} in the J_{SC}, 98 mV in the V_{OC}, and of 7% in the FF, resulting in a 4.6% higher light to power conversion efficiency for sample Cu84 in comparison to the Cu53 one. Thus, all electrical parameters, as well as the performance of the solar cells, improve with the increase of Cu fraction. This behaviour is in accordance with the [Cu]/([In]+[Ga]) ratio values (0.88-0.92) reported in the literature for the best solar cells [204].

In Fig. 7.23 a), both the experimental (J_{SC}^{exp}) and the upper theoretical (J_{SC}^{SQ}) J_{SC} values, are plotted as a function of the estimated bandgap energy values. As expected, the obtained J_{SC}^{exp} for the three samples are lower than the maximum theoretical ones, and follow the theoretical trend. The inset in Fig. 7.23 a) show the dependence of J_{SC}^{exp}/J_{SC}^{SQ} ratio on the bandgap energy. It must be noted that, despite the improvement of 2.26 mA.cm^{-2} in J_{SC}^{exp} with the increase of Cu fraction, the J_{SC} losses in comparison to J_{SC}^{SQ} are lower for the sample Cu53 and increase with the increase

of the Cu fraction. This result suggests that the improvement in the performance of the solar cells with the increase of the Cu fraction are not related with an effective improvement in J_{SC}. At this point, we must note that the correlation of the J_{SC}^{exp} with the impact of the fluctuating potentials is not straightforward. A decrease in the density of defects will potentially increase the diffusion length and the space charge region, which contributes to an increase of the collection function. Nevertheless, such a decrease of the density of defects will create smaller fluctuating potentials that contribute to less absorption bellow the bandgap energy. Thus, any correlation must be only qualitative.

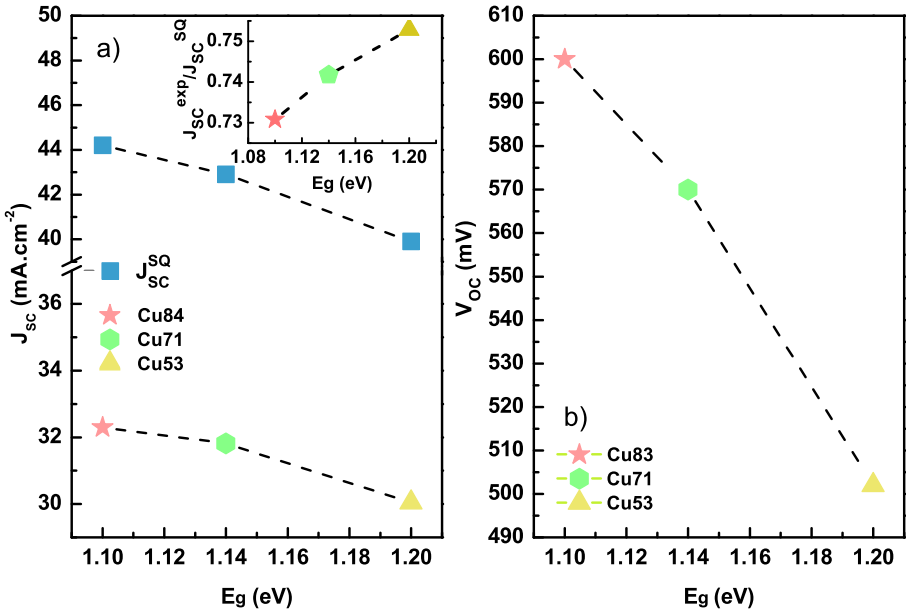

Figure 7.23: Dependence of a) J_{SC}^{exp}, J_{SC}^{SQ} and b) V_{OC} on the bandgap energy. The inset in a) shows the dependence of J_{SC}^{exp}/J_{SC}^{SQ} ratio on the bandgap energy.

Fig. 7.23 b) shows the dependence of the V_{OC} on the bandgap energy. Theoretically, it is expected that V_{OC} follows the bandgap. However, this is not the case for the studied samples. Among others, different factors contribute to the V_{OC} losses: i) the presence of fluctuating potentials; ii) native point defects inside the bandgap; iii) the presence of secondary phases with a bandgap value lower than the one of CIGS; iv) the polycrystalline character of the absorber layer, which will favour the diminishing of the lifetime of photogenerated carriers and, consequently, of their collection; v) interface recombination; vi) misalignments of energy bands at interfaces between the different solar cell layers. Indeed, almost all of these limiting factors are related to the presence of defects. We note that, a high density of defects may strongly reduce V_{OC}, while J_{SC} may be less affected [20]. Indeed, we showed a decrease in the density of defects as the Cu fraction increases, which is compatible with lower influence of fluctuating potentials in sample Cu84. Thus, in order to evaluate the importance of fluctuating potentials in the deterioration of the V_{OC} parameter, the V_{OC} losses are plotted in Fig. 7.24. Additionally, similar plots of the estimated β, γ, E_U, and σ values are included. As noted previously, the absolute values of these parameters cannot be compared between each other, and only

values of a particular parameter (for a particular model) may be compared between samples in the same experiment. In order to allow such comparison, in Fig. 7.24 we did match the experimental values estimated for the different models used, for the samples with the extreme Cu fraction. β and E_U reflect the amplitude of fluctuating potentials of different origins (electrostatic, bandgap, thermal vibration,...) in the sample. Our results show that β and E_U are the parameters that best describe experimental V_{OC} losses. Moreover, the obtained γ values also follow quite well the experimental V_{OC} loss, despite they only characterizes the amplitude of electrostatic fluctuating potentials. Finally, for σ values, which reflects only the bandgap fluctuations, the behaviour is significantly different. Thus, our results shows unequivocally: i) fluctuating potentials is a deciding factor for the V_{OC} losses; ii) the electrostatic fluctuating potentials is in a higher degree of correlation with experimental data than the bandgap fluctuations.

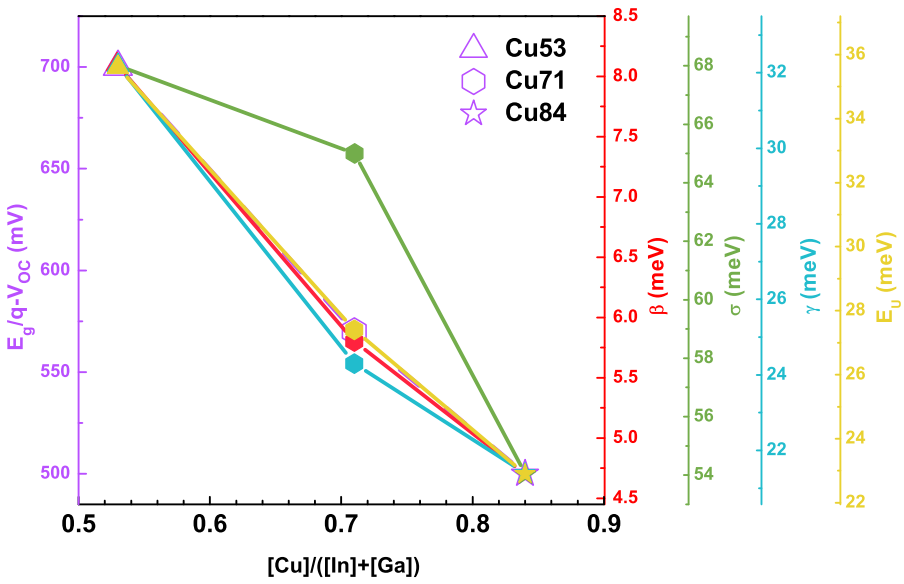

Figure 7.24: V_{OC} losses and parameters (β, σ, γ, and E_U) proportional to fluctuating potentials for each sample.

The solar cell basic principles of operation may be overview as three steps process: i) absorption of light and generation of electron-hole pair; ii) separation of the electron-hole pair; and iii) collection of the electron and hole in the opposite contacts. Fluctuating potentials should have impact in all three process. However, with the SQ extensions proposed in this study, we just focus in process i). We calculated the electrical parameters given by the SQ model as well as its extensions. As first step, the absorptance must be evaluated for all models according to Eqs. 2.2, 7.2, 7.3, being the relevant parameters in Tables 7.8 and 7.9. Additionally a α_0 value of 1.24×10^4 cm^{-1} was used in the Urbach model and optimal-fluctuation theory following the discussion presented in Section 2.2. In Fig. 7.25, we illustrate for sample Cu84 (E_g=1.10 eV) the energy dependence of the absorptance for all theoretical models. We note that for the optimal-fluctuation theory and Urbach model, the correction to the SQ absorptance occurs only in the sub-bandgap energy range, whereas for the bandgap fluctuating

potentials model, the correction is centred in the bandgap energy value. Thus, from the obtained energy dependence of the absorptance, we may stand that the Urbach model should follow at great extent the influence of the electrostatic fluctuating potentials.

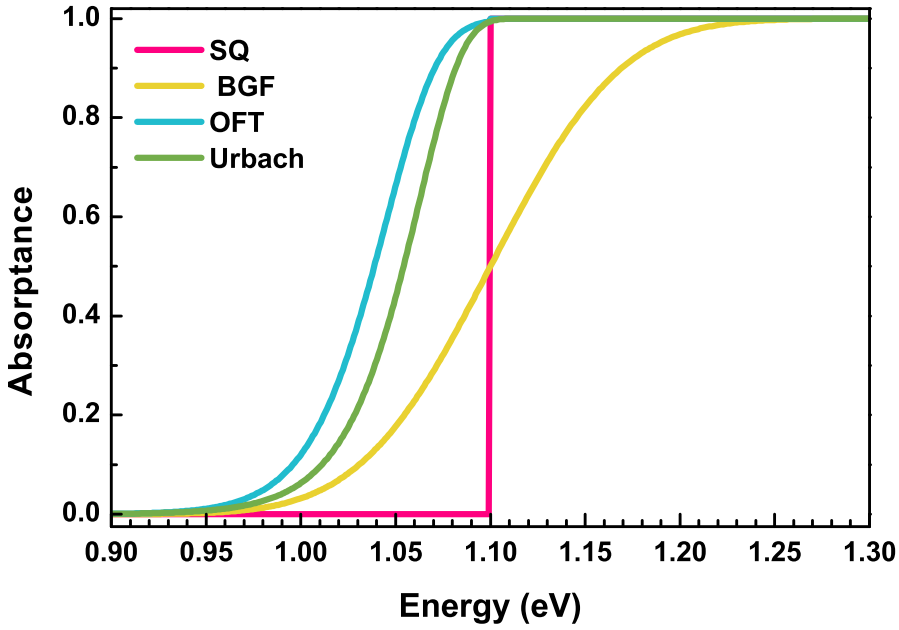

Figure 7.25: Calculated absorptance spectra for sample Cu84, considering SQ, bandgap fluctuations (BGF), optimal-fluctuation theory (OFT), and Urbach models. A value of $\alpha_0 = 1.24 \times 10^4$ cm^{-1} was estimated using the data of Paulson et al. [26].

Hereupon, the resulting electrical parameters are calculated from the theoretical models, and presented in Table 7.10. A few trends may be identified. On average, for all samples, the J_{SC}^{SQ} and J_0^{SQ} values are lower than the similar ones estimated by the SQ extensions. This rather unexpected observation may be understood by combining the absorption of photons below the bandgap energy with the shape of the solar spectrum, which can result in more photons being collected and thus, contributing to the photocurrent. However, this result is compatible with the impact of the fluctuating potentials in J_{SC}, as discussed above. Indeed, the optimal-fluctuation theory model, is the one for which the absorptance extends to lower energy values (see Fig. 7.25), resulting in more total absorption of photons and providing the highest J_{SC} values of all. Concerning the V_{OC} values, for the SQ extensions, a significant and expected reduction is observed when fluctuating potentials are taken into account. The V_{OC} losses are more notorious for sample Cu53 and decreases with the increase of the Cu fraction.

Table 7.10: J_{SC}, J_0, V_{OC} and E_g/e-V_{OC} values calculated from SQ, optimal-fluctuation theory (OFT), bandgap fluctuations (BGF), and Urbach models. The values of E_g (see Table 7.8) are also shown for each sample. α_0 was estimated by fitting Eq. 2.3 to the absorption coefficient data of Paulson et al. [26].

Sample	E_g	Model	J_{SC} (mA.cm^{-2})	J_0 (mA.cm^{-2})	V_{OC} (mV)	E_g/e-V_{OC} (mV)
Cu53	1.20 ± 0.10	SQ	39.97	4.23x10^{-15}	951	249
		BGF	40.02	9.94x10^{-14}	869	331
		OFT	43.92	2.86x10^{-12}	785	415
		Urbach	43.24	9.41x10^{-11}	694	506
Cu71	1.14 ± 0.05	SQ	42.89	3.84x10^{-14}	896	244
		BGF	42.53	6.88x10^{-13}	821	319
		OFT	45.17	1.98x10^{-12}	795	345
		Urbach	44.79	4.87x10^{-12}	772	368
Cu84	1.10 ± 0.02	SQ	44.23	1.71x10^{-13}	858	242
		BGF	44.12	1.24x10^{-12}	807	293
		OFT	46.45	4.68x10^{-12}	774	326
		Urbach	45.81	3.88x10^{-12}	778	322

In Fig. 7.26 we compare the calculated V_{OC} losses with the experimental values, following the same approach used to build Fig. 7.24. We observe that the V_{OC} losses calculated by: i) the SQ model, follow quite well the experimental ones; ii) the Urbach and optimal-fluctuation theory models, follow reasonably well the experimental values; iii) the bandgap fluctuations model, reveal a disagreement. These observations are highly compatible with the experimental results (see Fig. 7.24). At this stage, we must stress that the main differences between the three samples are the bandgap energy values and the influence of fluctuating potentials in each one. In the SQ model, only the first issue is addressed, whereas both issues are included in the Urbach and optimal-fluctuation theory models. The fact that SQ model closely describes of the experimental values in Fig. 7.26, is expected because it is well known that this model describes quite well the basic principles of operation of a solar cell. In addition, this agreement validates the approach to use the SQ model as a starting step for the study of other loss mechanisms rather than just the radiative ones as proposed in the SQ model. Nevertheless, the calculated V_{OC} losses using the SQ model (Table 7.10) are the ones more deviated from the experimental losses. Regarding the extensions to the SQ model, the inclusion of fluctuating potentials revealed that just for the case of Urbach and optimal-fluctuation theory models, the experimental trend can be described. For the bandgap fluctuations model, the disagreement is quite evident and unexpected. Different factors may be contributing to this behaviour: i) negligible influence of the bandgap fluctuations in comparison to the electrostatic one; ii) EQE and PL measurements are not sensitive enough to the bandagap fluctuating potentials, which is questionable, because the two experimental techniques have different physical principles; iii) the theoretical model needs improvements to better describe this

type of fluctuations.

Finally, the fact that the V_{OC} losses calculated by the optimal fluctuating theory and Urbach models, followed the experimental values for the γ and E_U parameters, shows that the approximation to a planar solar cell, as well as the proposed $a(h\nu)$ are good approximations to evaluate the impact of the fluctuating potentials on solar cells. As discussed above, many factors may and likely do contribute to the V_{OC} losses. Even though we cannot fully account for the experimental V_{OC} losses, our results support the experimental correlation between them and the presence of fluctuating potentials.

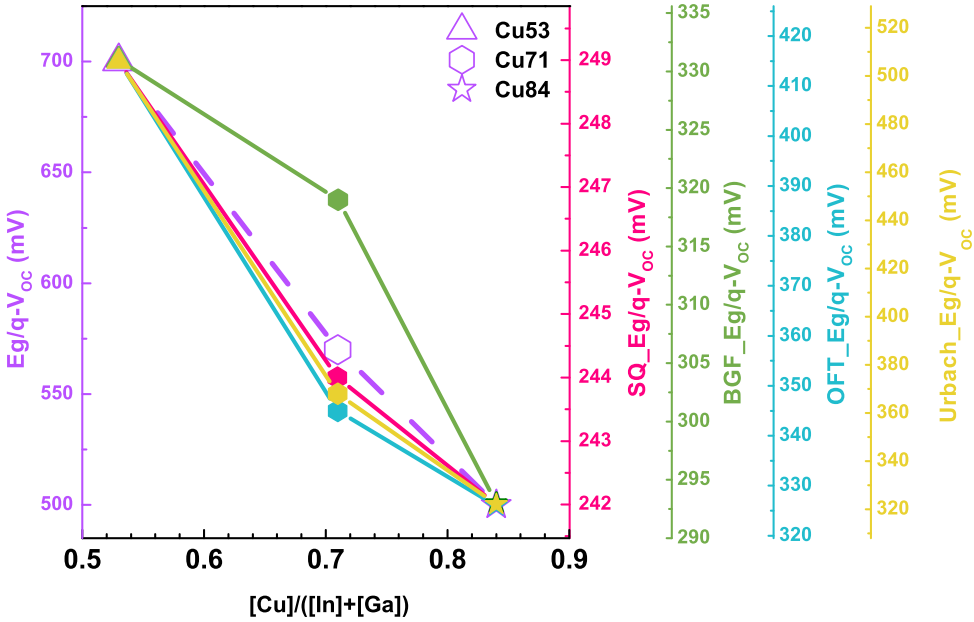

Figure 7.26: V_{OC} losses obtained experimentally and calculated considering Shockley-Queisser, bandgap fluctuations, optimal-fluctuation theory, and Urbach models, for each sample.

In this study, we have shown strong evidences based on a theoretical approach and experimental results, that the V_{OC} losses of CIGS solar cells are correlated with the amount of fluctuating potentials in the absorber layer. Evidences for a lower influence of bandgap fluctuating potentials, in comparison with electrostatic ones, were found. Furthermore, the fluctuations estimated from low temperature PL measurements, which are very sensitive to the general influence of defects in semiconductors, are in accordance with standard EQE measurements at RT.

7.7 In Summary

An experimental and theoretical investigation of the role of fluctuating potentials in the CIGS optoelectronic properties was carried out throughout different studies. As for CZTS based solar cells, the influence of fluctuating potentials was shown, and fully explains the CIGS characteristic luminescence. Although in CIGS, contrary to CZTS, the fluctuations seem to be a high limitation of the solar cell performance, different studies pointed that fluctuating potentials analysis should

be qualitative. The study of different set of CIGS samples led to the identification of two main non-recombination de-excitation channels: one involving the conduction band tails involving donor clusters and other compatible with the V_{Cu} acceptor defect.

A cross analysis of the PL results obtained at low temperature with the sub-bandgap region of the EQE spectra obtained at RT, showed a lower influence of the fluctuating potentials in a Na-containing sample in comparison to a Na-free one. Such result is in accordance with the expected effect of Na reported in the literature. The impact of different Ga-profiles in the nature of the CIGS recombination channels was observed, highlighting the importance of understanding the effect of the Ga-profile on charge dynamics. Notorious changes in the luminescence after a PDA comparing with the one obtained for the as-grown sample were obtained. The above changes are at least partially reversible, and after a certain time the sample tends to return to a stable state. A reduction of electrostatic fluctuating potentials in the CIGS/ZnSnO sample in comparison with the CIGS/CdS one, corroborates that the choice of the buffer layer, together with its deposition process, changes the properties of the CIGS layer. An effective chemical passivation of the charged defects promoted by the Al_2O_3 nanopatterned passivation layer led to a decrease of the electrostatic fluctuating potentials in the Mo/Al_2O_3/CIGS sample in comparison with the Mo/CIGS one. We showed by theoretical calculations and experimental evidences, a higher degree of correlation of electrostatic fluctuating potentials with the V_{OC} losses, in comparison with bandgap fluctuations. Finally, we showed the influence of fluctuating potentials not just at low temperature, but also at RT.

Chapter 8

Conclusions

An overview of the studies carried out in this thesis and final conclusions, followed with new ideas for further work, are presented in this Chapter.

8.1 Results overview

In this thesis, a deep study of the influence of defects on the optoelectronic properties of two semiconductors with high potential for photovoltaic application, Cu_2ZnSnS_4 (CZTS) and Cu(In, Ga)Se_2 (CIGS), was carried out. For CZTS based solar cells, we studied the optical properties of the CZTS absorber layer, in three series of samples that include: i) a minor change on the time of maximum temperature of the sulphurization; ii) a change on the sulphurization method; iii) a post-deposition annealing. These studies were selected as the CZTS preparation is still challenging and a lack of the understanding of its effects is still missing in the literature. For CIGS based solar cells three major topics were addressed: i) optoelectronic characterization of solar cells with the conventional architecture, ii) optoelectronic characterization of solar cells that explore new architectures; iii) influence of defects on the limiting factors on the performance of the device through an experimental and theoretical study. For CIGS, the technology is more mature, hence the topics that were studied reflect the need to continue to improve in terms of current limitations and novel solar cell materials/architectures. In general, the work explored the potential of the photoluminescence technique, complemented with other optical, morphological, structural, and electrical analyses, with the main focus being the one of providing relevant optoelectronic information for device optimization.

In CZTS based solar cells, the measured luminescence was fully explained by the fluctuating potentials model in contrast to donor-acceptor pairs recombination models proposed by other authors. The luminescence results give evidence for a state filling effect and do not support a screening one. No influence was observed on the optical properties of the CZTS thin films subjected to different times (1

and 2 minutes) of maximum temperature of sulphurization. Moreover, the presence of a deep acceptor defect (∼280 meV) was shown. The sulphurization of identical multi-stacked precursors in a S flux or in a graphite box methods, led to significantly different density of defects on the CZTS layer, with severe consequences on the nature of the de-excitation mechanisms resulting from different electronic levels structure. Finally, a drastic change of the luminescence after the post-annealing treatment suggests a significant change in the density of defects at the interface CZTS/CdS. CZTS based solar cells present serious recombination issues that go far beyond the existence of fluctuating potentials. The optical studies revealed, that a less efficient luminescence due to non-radiative recombination or recombination involving deep defects, is at great extent related with a poor performance of the devices.

As obtained from previous solar cells, the influence of fluctuating potential was shown, and fully explained the CIGS characteristic luminescence. However, the parameters that describe the influence of the fluctuating potentials revealed a qualitative, instead of a quantitative, character. The optical results showed the relevant role of Na in the reduction of these fluctuations. Such observation is another proof towards the hypothesis that the dominant effect of Na in CIGS is to passivate donors. A clear influence of the Ga-profile, in the CIGS luminescence was observed. For a CIGS absorber with a notch Ga-profile, two radiative transitions were identified, involving the same acceptor level and similar donors cluster, which were ascribed to the notch and to the near region of the CIGS/CdS interface. For a CIGS absorber with a normal Ga-profile, also two radiative transitions involving an acceptor with an ionization energy that might be compatible with the V_{Cu} defect were observed. The CIGS optical properties for different time intervals after the post-deposition annealing, showed notorious changes in the peak position and shape of the luminescence in comparison to the luminescence before the treatment. This is an observation very relevant as PV modules under operation might suffer of similar effects due to they warm-up during sunlight, hence the understanding of this effect is important. The above changes were at least partially reversible, and with time the sample tends to return to a stable state. The observed metastable effect is compatible with diffusion of Cu to the CIGS surface, followed in the return to its chemical stable position. A reduction of electrostatic fluctuating potentials in the CIGS/ZnSnO sample in comparison with the CIGS/CdS one, showed that the choice of the buffer layer, together with its deposition process, changes the bulk CIGS properties and also CIGS/buffer layer interface properties. These results support that ZnSnO is a promising buffer layer for CIGS based solar cells, but further optimization is required. The chemical passivation of defects at the back interface promoted by an Al_2O_3 nanopatterned passivation layer in a ultrathin CIGS layer was also observed. The sample based on Mo/Al_2O_3/CIGS presented a lower influence of fluctuating potentials than the sample based on Mo/CIGS. Despite, the lower density of charged defects present in the passivated sample, the luminescence in both samples can be interpreted as a radiative transition involving the V_{Cu} acceptor defect. By theoretical and experimental analysis, we showed a higher degree of correlation of electrostatic fluctuating potentials with V_{OC} losses, in

comparison with bandgap fluctuations. Finally, the influence of fluctuating potentials not just at low temperature, but also at RT was demonstrated. In fact, an overall correlation of the influence of the fluctuating potentials, studied by optical measurements, with the electrical parameters of the devices were obtained for different series of CIGS based solar cells. Globally, the results from the CIGS based samples led to the identification of two main recombination de-excitation channels: one involving shallow donors cluster and another compatible with the V_{Cu} defect.

The role defects in the two studied materials are crucial, since: firstly, they determine their self-doping capability as p-type semiconductors, which make CZTS and CIGS suitable for application to solar cells based on pn-heterojunctions; and secondly, their optoelectronic properties are governed by a highly complex electronic energy levels structure due to the existence of a large diversity of native point defects which makes them highly doped and compensated semiconductors. This is yet not fully understood by the PV community that still faces these materials as standard semiconductors despite of the very different mechanisms that rule highly doped and compensated semiconductors. The impact of fluctuating potentials as a limitative factor to the studied solar cells performance is significantly different on CZTS and CIGS based solar cells and naturally reflects the development of each technology. CZTS presents serious recombination issues that are significantly more critical to the performance of the device, then the existence of fluctuating potentials. On the other hand for CIGS, the influence of the fluctuating potentials and the performance of the solar cells are correlated most of the time.

8.2 Suggestions for further work

After an overview on the obtained results for CZTS and CIGS based solar cells, there are several approaches that may be implement in order to a further understand some of the results obtained in this thesis and for future development of thin film solar cells.

i) An accurate distinction and identification of the localization of the main recombination mechanism in the CZTS based solar cells, by complemented PL results with measurements that allow for a more complete study such as: dependence of the V_{OC} on the temperature to identify band alignment problems, time resolved photoluminescence to estimate carrier lifetime considering the models described here, kelvin probe force microscopy to identify grain boundaries properties, just to name a few. Furthermore, it is essential that the quality of the material improves and that the deep defects identified here are passivated for solar cells to increase significantly its performance.

ii) Investigation of new dielectric material and, point contacts design in order to enhance even further the chemical passivation at the back contact of the CIGS layer. The cross information obtained by PL results and time resolved photoluminescence would give some insights in order to understand back surface recombination velocity.

iii) The observed metastable effect may have an important role in the performance of the modules that are exposed to high temperatures. The identification of the mechanisms responsible for this behaviour and threshold temperature will be an important knowledge for the CIGS technology. From a fundamental point of view, the exploitation of this effect in CIGS samples with flat Ga-profiles can be helpful to understand the Cu diffusion dynamics.

iv) Light- and heavy-element alkali PDT, i.e. potassium fluoride and rubidium fluoride PDTs, have boosted the CIGS solar cells performance. The study of the impact of these treatments on the optical properties of the CIGS and CIGS/buffer layer would be an important study to be carried out. Moreover, and since we obtained good optoelectronic properties for the CIGS/ZnSnO interface, the study of the impact of the aforementioned PDTs in this interface, would be an interesting study in order to be one step closer to replace the CdS as buffer layer.

v) To continue the evaluation of the impact of fluctuating potentials on the limiting factors of the performance of CIGS based solar cells for different Ga-profiles and state-of-art solar cells. There is still room for improvement in CIGS solar cells considering that the effect of the fluctuation can still be reduced. For this, the community also needs to look at these materials as what they are: complex multinary highly doped and compensated semiconductors, very different from textbook typical mono or dual element materials.

Bibliography

[1] Paris agreement, December 2015. UNTC XXVII 7.d.

[2] International Energy Agency. Global energy and co_2 status report 2017, March 2018.

[3] Renewable Energy Policy Network for the 21st Century REN21. Renewables 2018, global status report, 2018.

[4] A. Polman, M. Knight, E. C. Garnett, B. Ehrler, and Wim C. Sinke. *Science*, 352:307, 2016.

[5] ISE Fraunhofer Institute for Solar Energy Systems. Photvoltaics report, August 2018.

[6] M. A. Green, Y. Hishikawa, E. D. Dunlop, D. H. Levi, J. Hohl-Ebinger, and A. W. Y. Ho-Baillie. *Prog. Photovoltaics*, 26:427, 2018.

[7] Solar Frontier, Press Release, Japan, January 17, 2019.

[8] C. Yan, J. Huang, K. Sun, S. Johnston, Y. Zhang, H. Sun, A. Pu, M. He, F. Liu, K. Eder, L. Yang, J. M. Cairney, N. J. Ekins-Daukes, Z. Hameiri, J. A. Stride, S. Chen, M. A. Green, and X. Hao. *Nat. Energy.*, 3:764, 2018.

[9] Y. S. Lee, T. Gershon, O. Gunawan, T. K. Todorov, T. Gokmen, Y. Virgus, and S. Guha. *Adv. Energy Mater.*, 5:1401372, 2015.

[10] W. Wang, M. T. Winkler, O. Gunawan, T. Gokmen, T. K. Todorov, Y. Zhu, and D. B. Mitzi. *Adv. Energy Mater.*, 4:1301465, 2014.

[11] W. Shockley and H. J. Queisser. *J. Appl. Phys.*, 32:510, 1961.

[12] T. Kirchartz and U. Rau. Introduction to thin-film photovoltaics. In D. Abou-Ras, T. Kirchartz, and U. Rau, editors, *Advanced Characterization Techniques for Thin Film Solar Cells*. Willey, Berlin, 2011.

[13] NREL. Reference solar spectral irradiance: Air mass 1.5, astm g173-03. https://www.nrel.gov/grid/solar-resource/spectra-am1.5.html.

[14] C. Persson. *J. Appl. Phys.*, 107:053710, 2010.

[15] T. Kato, J. Wu, Y. Hirai, H. Sugimoto, and V. Bermudez. *IEEE J. Photovoltaics*, 9:325, 2018.

[16] D. A. Neamen. *Semiconductor Physics and Devices-Basic Principles*. McGraw-Hill, New York, 2003.

[17] S. Sze and K. Ng. *Physics of Semiconductor Devices*. John Wiley & Sons, New Jersey, 2007.

[18] A. L. Fahrenbrunch and R. H. Bube. *Fundamentals of solar cells, Photovoltaics solar energy conversion*. Academic Press, New York, 1983.

[19] P. Würfel. *Physics of Solar cells, from principles to new concepts*. Wiley, Berlim, 2005.

[20] R. Scheer and H. W. Schock. *Chalcogenide Photovoltaics Physics, Technologies, and Thin Film Devices*. Wiley-VCH, Berlim, 2011.

[21] S. S. Hegedus and W. N. Shafarman. *Prog. Photovoltaics*, 12:155, 2004.

[22] E. Hecht. *Optics*. Addison Wesley, San Francisco, 4 edition, 2002.

[23] C. Ulbrich, S. Fahr, J. Üpping, M. Peters, T. Kirchartz, C. Rockstuhl, R. Wehrspohn, A. Gombert, F. Lederer, and U. Rau. *Phys. status solidi (a)*, 205:2831, 2008.

[24] T. Kirchartz and U. Rau. *Adv. Energy Mater.*, 8:1703385, 2018.

[25] B. Blank, T. Kirchartz, S. Lany, and U. Rau. *Phys. Rev. Applied*, 8:024032, 2017.

[26] P. D. Paulson, R. W. Birkmire, and W. N. Shafarman. *J. Appl. Phys.*, 94:879, 2003.

[27] P. A. Fernandes, P. M. P. Salomé, and A. F. da Cunha. *J. Alloys Compd.*, 509:7600, 2011.

[28] P. M. P. Salomé, P. A. Fernandes, J. P. Leitão, M. G. Sousa, J. P. Teixeira, and A. F. da Cunha. *J. Mater. Sci.*, 49:7425, 2014.

[29] K. Ito. Physical properties: Compiled experimental data. In K. Ito, editor, *Copper Zinc Tin Sulfide-Based Thin-Film Solar Cells*. John Wiley and Sons, West Sussex, 2015.

[30] P. W. Li, R. A. Anderson, and R. H. Plovnick. *J. Phys. Chem. Solids*, 40:333, 1979.

[31] I. Repins, M. Contreras, M. Romero, Y. Yan, W. Metzger, J. Li, S. Johnston, B. Egaas, C. DeHart, J. Scharf, B. E. McCandless, and R. Noufi. In *33rd IEEE Photovoltaic Specialists Conference 2008*, page 1, 2008.

[32] S. A. Jensen, S. Glynn, A. Kanevce, P. Dippo, J. V. Li, D. H. Levi, and D. Kuciauskas. *J. Appl. Phys.*, 120:063106, 2016.

[33] J. V. Li, S. Grover, M. A. Contreras, K. Ramanathan, D. Kuciauskas, and R. Noufi. *Sol. Energy Mater. Sol. Cells*, 124:143, 2014.

[34] W. K. Metzger, I. L. Repins, and M. A. Contreras. *Appl. Phys. Lett.*, 93:022110, 2008.

[35] B. Shin, O. Gunawan, Y. Zhu, N. A. Bojarczuk, S. J. Chey, and S. Guha. *Prog. Photovoltaics*, 21:72, 2013.

[36] M. M. Islam, M. A. Halim, T. Sakurai, N. Sakai, T. Kato, H. Sugimoto, H. Tampo, H. Shibata, S. Niki, and K. Akimoto. *Appl. Phys. Lett.*, 106:243905, 2015.

[37] K. Sun, C. Yan, J. Huang, K. Sun, H. Sun, L. Jiang, X. Deng, J. Stride, X. Hao, and F. Liu. *J. Alloys Compds*, 750:328, 2018.

[38] I. L. Repins, H. Moutinho, S. G. Choi, A. Kanevce, D. Kuciauskas, P. Dippo, C. L. Beall, J. Carapella, C. DeHart, B. Huang, and S. H. Wei. *J. Appl. Phys.*, 114:084507, 2013.

[39] T. Gokmen, O. Gunawan, and D. B. Mitzi. *J. Appl. Phys.*, 114:114511, 2013.

[40] T. K. Todorov, J. Tang, S. Bag, O. Gunawan, T. Gokmen, Y. Zhu, and D. B. Mitzi. *Adv. Energy Mater.*, 3:34, 2013.

[41] J. Li, H. Wang, M. Luo, J. Tang, C. Chen, W. Liu, F. Liu, Y. Sun, J. Han, and Y. Zhang. *Sol. Energy Mater. Sol. Cells*, 149:242, 2016.

[42] K-J Yang, D-H Son, S-J Sung, J-H Sim, Y-I Kim, S-N Park, D-H Jeon, J-S Kim, D-K Hwang, C-W Jeon, D. Nam, H. Cheong, J-K Kang, and D-H Kim. *J. Mater. Chem. A*, 4:10151, 2016.

[43] C. J. Hages, A. Redinger, S. Levcenko, H. Hempel, M. J. Koeper, R. Agrawal, D. Greiner, C. A. Kaufmann, and T. Unold. *Adv. Energy Mater.*, 7:1700167, 2017.

[44] P. M. P. Salomé, B. Vermang, R. Ribeiro-Andrade, J. P. Teixeira, J. M. V. Cunha, M. J. Mendes, S. Haque, J. Borme, H. Águas, E. Fortunato, R. Martins, Juan C. González, J. P. Leitão, P. A. Fernandes, M. Edoff, and S. Sadewasser. *Adv. Mat. Interfaces*, 5:1701101, 2018.

[45] W. Shockley and W. T. Read. *Phys. Rev.*, 87:835, 1952.

[46] R. N. Hall. *Phys. Rev.*, 87:387, 1952.

[47] A. Alkauskas, C. E. Dreyer, J. L. Lyons, and C. G. Van de Walle. *Phys. Rev. B*, 93:201304, 2016.

[48] A. P. Levanyuk and V. V. Osipov. *Phys. Usp.*, 24:187, 1981.

[49] S. Kim, J-S. Park, and A. Walsh. *ACS Energy Letters*, 3:496, 2018.

[50] S. Grover, J. V. Li, D. L. Young, P. Stradins, and H. M. Branz. *Appl. Phys. Lett.*, 103:093502, 2013.

[51] P. M. P. Salomé, V. Fjällström, P. Szaniawski, J. P. Leitão, A. Hultqvist, P. A. Fernandes, J. P. Teixeira, B. P. Falcão, U. Zimmermann, A. F. da Cunha, and M. Edoff. *Prog. Photovoltaics*, 23:470, 2014.

[52] R. Scheer. *J. Appl. Phys.*, 105:104505, 2009.

[53] A. Crovetto and O. Hansen. *Sol. Energy Mater. Sol. Cells*, 169:177, 2017.

[54] D. Hironiwa, N. Sakai, T. Kato, H. Sugimoto, Z. Tang, J. Chantana, and T. Minemoto. *Thin Solid Films*, 582:151, 2015.

[55] C. J. Hages, N. J. Carter, R. Agrawal, and T. Unold. *J. Appl. Phys.*, 115:234504, 2014.

[56] K-J. Yang, J-H. Sim, D-H. Son, D-H. Jeon, D-K. Hwang, D. Nam, H. Cheong, SY. Kim, J. Kim, D-H. Kim, and J-K. Kang. *J Ind Eng Chem.*, 45:78, 2017.

[57] M. Turcu and U. Rau. *Thin Solid Films*, 431-432:158, 2003.

[58] O. Gunawan, T. K. Todorov, and D. B. Mitzi. *Appl. Phys. Lett.*, 97:233506, 2010.

[59] K. Wang, O. Gunawan, T. Todorov, B. Shin, S. J. Chey, N. A. Bojarczuk, D. Mitzi, and S. Guha. *Appl. Phys. Lett.*, 97:143508, 2010.

[60] D. B. Mitzi, O. Gunawan, T. K. Todorov, K. Wang, and S. Guha. *Sol. Energy Mater. Sol. Cells*, 84:1421, 2011.

[61] K. Kaur, N. Kumar, and M. Kumar. *J. Mater.Chem. A*, 5:3069, 2017.

[62] T. Taskesen, J. Neerken, J. Schoneberg, D. Pareek, V. Steininger, J. Parisi, and L. Gütay. *Adv. Energy Mater.*, 8:1703295, 2018.

[63] A. Redinger, M. Mousel, M. H. Wolter, N. Valle, and S. Siebentritt. *Thin Solid Films*, 535:291, 2013.

[64] L. Pavesi and M. Guzzi. *J. Appl. Phys.*, 75:4779, 1994.

[65] U. Rau and H. W. Schock. Cu(in,ga)se_2 and related solar cells. In M. D. Archer and M. A. Green, editors, *Series on Photoconversion of Solar Energy: Clean electricity from photovoltaics*. Imperial College Press, London, 2015.

[66] T. Minemoto, T. Matsui, H. Takakura, Y. Hamakawa, T. Negami, Y. Hashimoto, T. Uenoyama, and M. Kitagawa. *Sol. Energy Mater. Sol. Cells*, 67:83, 2001.

[67] S.-H. Wei and A. Zunger. *Appl. Phys. Lett.*, 63:2549, 1993.

[68] A. Niemegeers, M. Burgelman, and A. De Vos. *Appl. Phys. Lett.*, 67:843, 1995.

[69] M. Gloeckler and J. R. Sites. *Thin Solid Films*, 480-481:241, 2005.

[70] J. Lindah. Atomic layer deposition of zinc tin oxide buffer layers for cu(in,ga)se2 sollar cells. Master's thesis, Uppsala University, 2015.

[71] P. M. P. Salomé, H. Rodriguez-Alvarez, and S. Sadewasser. *Sol. Energy Mater. Sol. Cells*, 143:9, 2015.

[72] J. V. Li, D. Kuciauskas, M. R. Young, and I. L. Repins. *Appl. Phys. Lett.*, 102:163905, 2013.

[73] S. Sahayaraj, G. Brammertz, B. Vermang, T. Schnabel A. Mule, M. Meuris, J. Vleugelse, and J. Poortmans. *J. Mater. Chem. A*, 6:2653, 2018.

[74] T. Gershon, B. Shin, N. Bojarczuk, M. Hopstaken, D. B. Mitzi, and S. Guha. *Adv. Energy Mat.*, 5:1400849, 2014.

[75] P. M. P. Salomé, V. Fjällström, A. Hultqvist, and M. Edoff. *IEEE J. Photovoltaics*, 3:509, 2013.

[76] P. Reinhard, B. Bissig, F. Pianezzi, E. Avancini, H. Hagendorfer, D. Keller, P. Fuchs, M. Döbeli, C. Vigo, P. Crivelli, S. Nishiwaki, S. Buecheler, and A. N. Tiwari. *Chem. Mater.*, 27:5755, 2015.

[77] Y. Sun, S. Lin, W. Li, S. Cheng, Y. Zhang, Y. Liu, and W. Liu. *Engineering*, 3:452, 2017.

[78] S. Niki, M. Contreras, I. Repins, M. Powalla, K. Kushiya, S. Ishizuka, and K. Matsubara. *Prog. Photovoltaics*, 18:453, 2010.

[79] W. Li, X. Yan, A. G. Aberle, and S. Venkataraj. *Curr. Appl. Phys.*, 17:1747, 2017.

[80] A. Chirilă, P. Reinhard, F. Pianezzi, P. Bloesch, A. R. Uhl, C. Fella, L. Kranz, D. Keller, C. Gretener, H. Hagendorfe, D. Jaeger, R. Erni, S. Nishiwaki, S. Buecheler, and A. N. Tiwari. *Nat. Mater.*, 12:1107, 2013.

[81] A. Chirilă, S. Buecheler, F. Pianezzi, P. Bloesch, C. Gretener, A. R. Uhl, C. Fella, L. Kranz, J. Perrenoud, S. Seyrling, R. Verma, S. Nishiwaki, Y. E. Romanyuk, G. Bilger, and A. N. Tiwari. *Nat. Mater.*, 10:857, 2011.

[82] W. Thongkham, A. Pankiew, K. Yoodee, and S. Chatraphorn. *Sol. Energy*, 92:189, 2013.

[83] F. Pianezzi, A. Chirilă, P. Bösch, S. Seyrling, S. Buecheler, L. Kranz, C. Fella, and A. N. Tiwari. *Prog. Photovoltaics*, 20:253, 2013.

[84] C. Jakapan, H. Daisuke, W. Taichi, T. Seiki, and M. Takashi. *Prog. Photovoltaics*, 24:990, 2016.

[85] I. Becerril-Romero, L. Acebo, F. L. Oliva, V. Izquierdo-Roca, S. López-Marino, M. Espídola-Rodríguez, M. Neuschitzer, Y. Sánchez, M. Placidi, A. P'erez-Rodríguez, E. Saucedo, and P. Pistor. *Prog. Photovoltaics*, 26:55, 2017.

[86] S. López-Marino, Y. Sánchez, M. Espídola-Rodríguez, X. Alcobé, H. Xie, M. Neuschitzer, I. Becerril, S. Giraldo, M. Dimitrievska, M. Placidi, L. Fourdrinier, V. Izquierdo-Roca, A. Pérez-Rodríguez, and E. Saucedo. *J. Mater. Chem. A*, 4:189, 2016.

[87] T. Todorov, J. Olenick, K. AOlenick, O. Gunawan, T. Gershon, C. Sturdevant, Yun Seog Lee, Liang yi Chang, and S. Guha. In *42nd Photovoltaic Specialist Conference 2015*, pages 1–3, 2015.

[88] J. H. Scofield, A. Duda, D. Albin, B. L. Ballard, and P. K. Predecki. *Thin Solid Films*, 260:26, 1995.

[89] P. M. P. Salomé, J. Malaquias, P. A. Fernandes, and A. F. da Cunha. *J. Phys. D: Appl. Phys.*, 43:345501, 2010.

[90] P. M. P. Salomé, V. Fjallstrom, A. Hultqvist, P. Szaniawski, U. Zimmermann, and M. Edoff. *Prog. Photovoltaics*, 22:83, 2014.

[91] T. Wada, N. Kohara, S. Nishiwaki, and T. Negami. *Thin Solid Films*, 387:118, 2001.

[92] N. Kohara, S. Nishiwaki, Y. Hashimoto, T. Negami, and T. Wada. *Sol. Energy Mater. Sol. Cells*, 67:209, 2001.

[93] D. Abou-Ras, G. Kostorz, D. Bremaud, M. Kälin, F. V. Kurdesau, A. N. Tiwari, and M. Döbeli. *Thin Solid Films*, 480-481:433, 2005.

[94] K. Orgassa, H. W. Schock, and J. H. Werner. *Thin Solid Films*, 431-432:387, 2003.

[95] J. J. Scragg, J. T. Wätjen, M. Edoff, T. Ericson, T. Kubart, and C. Platzer-Björkman. *J. Am. Chem. Soc.*, 134:19330, 2012.

[96] G. Altamura, L. Grenet, C. Roger, F. Roux, V. Reita, R. Fillon, H. Fournier, S. Perraud, and H. Mariette. *J. Renew. Sustain. Energy*, 6:011401, 2014.

[97] B. Shin, Y. Zhu, N. A. Bojarczuk, S. Jay Chey, and S. Guha. *Appl. Phys. Lett.*, 101:053903, 2012.

[98] F. Liu, K. Sun, W. Li, C. Yan, H. Cui, L. Jiang, X. Hao, and M. A. Green. *Appl. Phys. Lett.*, 104:051105, 2014.

[99] H. Guo, C. Ma, K. Zhang, X. Jia, X. Wang, N. Yuan, and J. Ding. *Sol. Energy Mater. Sol. Cells*, 175:20, 2018.

[100] M. Turcu, O. Pakma, and U. Rau. *Appl. Phys. Lett.*, 80:2598, 2002.

[101] M. Turcu and U. Rau. Recombination mechanisms in cu(in,ga)(se,s)$_2$ solar cells. In S. Siebentritt and U. Rau, editors, *Wide-Gap Chalcopyrites*. Springer, Berlin, 2006.

[102] P. M. P. Salomé, J. P. Teixeira, J. Keller, T. Torndahl, S. Sadewasser, and J. P. Leitão. *IEEE J. Photovoltaics*, 7:670, 2017.

[103] T. Dullweber, O. Lundberg, J. Malmström, M. Bodegård, L. Stolt, U. Rau, H.W. Schock, and J. H. Werner. *Thin Solid Films*, 387:11, 2001.

[104] S. M. Schleussner, T. Törndahl, M. Linnarsson, U. Zimmermann, T. Wätjen, and M. Edoff. *Prog. Photovoltaics*, 20:284, 2011.

[105] B. Vermang, Viktor Fjällström, Jonas Pettersson, P. Salomé, and Marika Edoff. *Sol. Energy Mater. Sol. Cells*, 117:505, 2013.

[106] B. Vermang, J. T. Wätjen, V. Fjällström, F. Rostvall, M. Edoff, R. Gunnarsson, I. Pilch, U. Helmersson, R. Kotipalli, F. Henry, and D. Flandre. *Thin Solid Films*, 582:300, 2015.

[107] O. Lundberg, M. Bodegård, J. Malmström, and L. Stolt. *Prog. Photovoltaics*, 11:77, 2002.

[108] A. Duchatelet, E. Letty, S. Jaime-Ferrer, P.-P. Grand, F. Mollica, and N. Naghavi. *Sol. Energy Mater. Sol. Cells*, 162:114, 2017.

[109] N. Naghavi, F. Mollica, J. Goffard, J. Posada, A. Duchatelet, M. Jubault, F. Donsanti, A. Cattoni, S. Collin, P. P. Grand, J. J. Greffet, and D. Lincot. *Thin Solid Films*, 633:55, 2017.

[110] W. Witte, S. Spiering, and D. Hariskos. *Vakuum in Forschung und Praxis*, 26:23, 2014.

[111] N. Naghavi, D. Abou-Ras, N. Allsop, N. Barreau, S. Bücheler, A. Ennaoui, C.-H. Fischer, C. Guillen, D. Hariskos, J. Herrero, R. Klenk, K. Kushiya, D. Lincot, R. Menner, T. Nakada, C. Platzer-Björkman, S. Spiering, A. N. Tiwari, and T. Törndahl. *Prog. Photovoltaics*, 18:411, 2010.

[112] J. M. Doña and J. Herrero. *J. Electrochem. Soc.*, 144:4091, 1997.

[113] M. Mezher, R. Garris, L. M. Mansfield, K. Horsley, L. Weinhardt, D. A. Duncan, M. Blum, S. G. Rosenberg, M. Bär, K. Ramanathan, and C. Heske. *Prog. Photovoltaics*, 24:1142, 2016.

[114] M. Kapilashrami, C. X. Kronawitter, T. Törndahl, J. Lindahl, A. Hultqvist, W.-C. Wang, C.-L. Chang, S. S. Mao, and J. Guo. *Phys. Chem. Chem. Phys.*, 14:10154, 2012.

[115] T. Törndahl, E. Coronel, A. Hultqvist, C. Platzer-Björkman, K. Leifer, and M. Edoff. *Prog. Photovoltaics*, 17:115, 2009.

[116] S. Spiering, L. Bükert, D. Hariskos, M. Powalla, B. Dimmler, C. Giesen, and M. Heuken. *Thin Solid Films*, 517:2328, 2009.

[117] K. Kim, L. Larina, J. H. Yun, K. H. Yoon, H. Kwon, and B. T. Ahn. *Phys. Chem. Chem. Phys.*, 15:9239, 2013.

[118] C. Yan, F. Liu, K. Sun, N. Song, J. A. Stride, F. Zhou, X. Hao, and M. Green. *Sol. Energy Mater. Sol. Cells*, 144:700, 2016.

[119] K. Sun, C. Yan, F. Liu, J. Huang, F. Zhou, J. A. Stride, M. Green, and X. Hao. *Adv. Energy Mater.*, 6:1600046, 2016.

[120] T. Ericson, F. Larsson, T. Törndahl, C. Frisk, J. Larsen, V. Kosyak, C. Högglund, S. Li, and C. Platzer-Björkman. *Solar RRL*, 1:1700001, 2017.

[121] J. Li, X. Liu, W. Liu, L. Wu, B. Ge, S. Lin, S. Gao, Z. Zhou, F. Liu, Y. Sun, J. Ao, H. Zhu, Y. Mai, and Y. Zhang. *Solar RRL*, 1:1700075, 2016.

[122] R. Barkhouse, D. Aaron, R. Haight, N. Sakai, H. Hiroi, H. Sugimoto, and D. B. Mitzi. *Appl. Phys. Lett.*, 100:193904, 2012.

[123] J. Y. Park, R. B. V. Chalapathy, A. C. Lokhande, C. W. Hong, and J. H. Kim. *J. Alloys Compd.*, 695:2652, 2017.

[124] D. Hironiwa, N. Matsuo, J. Chantana, N. Sakai, T. Kato, H. Sugimoto, and T. Minemoto. *Phys. Status Solidi A*, 212:2766, 2015.

[125] R. Klenk. *Thin Solid Films*, 387:135, 2001.

[126] D. Abou-Ras, G. Kostorz, A. Romeo, D. Rudmann, and A. N. Tiwari. *Thin Solid Films*, 480:118, 2005.

[127] J.-F. Han, C. Liao, L.-M. Cha, T. Jiang, H.-M. Xie, K. Zhao, and M.-P. Besland. *J. Phys. Chem. Solids*, 75:1279, 2014.

[128] A. Niemegeers, M. Burgelman, R. Herberholz, U. Rau, D. Hariskos, and H.-W. Schock. *Prog. Photovoltaics*, 6:407, 1998.

[129] M. Morkel, L. Weinhardt, B. Lohmüller, C. Heske, E. Umbach, W. Riedl, S. Zweigart, and F. Karg. *Appl. Phys. Lett.*, 79:4482, 2001.

[130] L. Kronik, L. Burstein, M. Leibovitch, Yoram Shapira, D. Gal, E. Moons, J. Beier, G. Hodes, David Cahen, D. Hariskos, R. Klenk, and H.-W. Schock. *Appl. Phys. Lett.*, 67:1405, 1995.

[131] P. M. P. Salomé, R. Ribeiro-Andrade, J. P. Teixeira, J. Keller, T. Törndahl, N. Nicoara, M. Edoff, J. C. González, J. P. Leitão, and S. Sadewasser. *IEEE J. Photovoltaics*, 7:858, 2017.

[132] T. Nakada and A. Kunioka. *Appl. Phys. Lett.*, 74:2444, 1999.

[133] C. Heske, D. Eich, R. Fink, E. Umbach, T. van Buuren, C. Bostedt, L. J. Terminello, S. Kakar, M. M. Grush, T. A. Callcott, F. J. Himpsel, D. L. Ederer, R. C. C. Perera, W. Riedl, and F. Karg. *Appl. Phys. Lett.*, 74:1451, 1999.

[134] J. B. Varley and V. Lordi. *J. Appl. Phys.*, 116:063505, 2014.

[135] M. J. Furlong, M. Froment, M. C. Bernard, R. Cortés, and A. N. Tiwari. *J. Cryst. Growth*, 193:114, 1998.

[136] L. Weinhardt, O. Fuchs, D. GroB, G. Storch, E. Umbach, N. G. Dhere, A. A. Kadam, S. S. Kulkarni, and C. Heske. *Appl. Phys. Lett.*, 86:062109, 2005.

[137] K. Ramanathan, F. S. Hasoon, S. Smith, D. L. Young, and M. A. *J. Phys. Chem. Solids*, 64:1495, 2003.

[138] U. Rau and J. H. Werner. *Appl. Phys. Lett.*, 84:3735, 2004.

[139] J. Lindahl, J. Keller, O. Donzel-Gargand, P. Szaniawski, M. Edoff, and T. Törndahl. *Sol. Energy Mater. Sol. Cells*, 144:684, 2016.

[140] J. Lindahl, U. Zimmermann, P. Szaniawski, T. Törndahl, A. Hultqvist, P. M. P. Salomé, C. Platzer-Björkman, and M. Edoff. *IEEE J. Photovoltaics*, 3:1100, 2013.

[141] J. Lindahl, C. Hägglund, J. T. Wätjen, M. Edoff, and T. Törndahl. *Thin Solid Films*, 586:82, 2015.

[142] W. Niu, X. Li, S. K. Karuturi, D. W. Fam, H. Fan, S. Shrestha, L. H. Wong, and A. I. Y. Tok. *Nanotechnology*, 26:064001, 2015.

[143] Y. S. Lee, J. Heo, S. C. Siah, J. P. Mailoa, R. E. Brandt, S. B. Kim, R. G. Gordon, and T. Buonassisi. *Energy Environ. Sci.*, 6:2112, 2013.

[144] A. Hultqvist, C. Platzer-Björkman, U. Zimmermann, M. Edoff, and Tobias Törndahl. *Prog. Photovoltaics*, 20:883, 2012.

[145] P. Salomé, J. Keller, T. Törndahl, J. Teixeira, N. Nicoara, R. Ribeiro Andrade, D. Stroppa, J. González, M. Edoff, J. P. Leitao, and S. Sadewasser. *Sol. Energy Mater. Sol. Cells*, 159:272, 2017.

[146] S. Siebentritt. *Thin Solid Films*, 535:1, 2013.

[147] A. Crovetto, M. L. N. Palsgaard, T. Gunst, T. Markussen, K. Stokbro, M. Brandbyge, and O. Hansen. *Appl. Phys. Lett.*, 110:083903, 2017.

[148] A. Crovetto, A. Cazzaniga, R. Bolt Ettlinger, J. Schou, and O. Hansen. *Sol. Energy Mater. Sol. Cells*, 187:233, 2018.

[149] C. Platzer-Björkman, C. Frisk, J. K. Larsen, T. Ericson, S.-Y. Li, J. J. S. Scragg, J. Keller, F. Larsson, and T. Törndahl. *Appl. Phys. Lett.*, 107:243904, 2015.

[150] P. Jackson, R. Würz, U. Rau, J. Mattheis, M. Kurth, T. Schlötzer, G. Bilger, and J. H. Werner. *Prog. Photovoltaics*, 15:507, 2007.

[151] M. A. Martínez, J. Herrero, and M. T. Gutiérrez. *Sol. Energy Mater. Sol. Cells*, 45:75, 1997.

[152] M. G. Sousa, A .F. da Cunha, J. P. Teixeira, J. P. Leitao, G. Otero-Irurueta, and M. K. Singh. *Sol. Energy Mater. Sol. Cells*, 170:287, 2017.

[153] D. S. Su and S.-H. Wei. *Appl. Phys. Lett.*, 74:2483, 1999.

[154] S. Chen, X. G. Gong, A. Walsh, and S.-H. Wei. *Appl. Phys. Lett.*, 94:041903, 2009.

[155] S.-H. Wei, S. B. Zhang, and A. Zunger. *Phys. Rev. B*, 59:R2478, 1999.

[156] S. Schorr. *Thin Solid Films*, 515:5985, 2007.

[157] S. Chen, X. G. Gong, A. Walsh, and S.-H. Wei. *Phys. Rev. B*, 79:165211, 2009.

[158] J. E. Jaffe and A. Zunger. *Phys. Rev. B*, 28:5822, 1983.

[159] C. Persson. *Appl. Phys. Lett.*, 93:072106, 2008.

[160] C-H Chang, S-H Wei, W. Johnson, R. Bhattacharya, B. Stanbery, T. Anderson, and R. Duran. *Japanese J. Appl. Phys.*, 39:411, 2000.

[161] B. J. Stanbery, S. Kincal, S. Kim, C. H. Chang, S. P. Ahrenkiel, G. Lippold, H. Neumann, T. J. Anderson, and O. D. Crisalle. *J. Appl. Phys.*, 91:3598, 2002.

[162] J. Lażewski, H. Neumann, K. Parlinski, G. Lippold, and B. J. Stanbery. Lattice dynamics of cuau-ordered $cuinse_2$. *Phys. Rev. B*, 68:144108, 2003.

[163] O. Madelung. *Semiconductors: Data Handbook*. Springer-Verlag Berlin Heidelberg, 3 edition, 2004.

[164] H. W. Spiess, U. Haeberlen, G. Brandt, A. Räuber, and J. Schneider. *Phys. Status Solidi (b)*, 62:183, 1974.

[165] M. I. Alonso, M. Garriga, C. A. Durante Rincón, E. Hernández, and M. León. *Appl. Phys. A*, 74:659, 2002.

[166] J. E. Jaffe and A. Zunger. *Phys. Rev. B*, 27:5176, Apr 1983.

[167] S.-H. Wei and A. Zunger. *J. Appl. Phys.*, 78:3846, 1995.

[168] J. C. Mikkelsen. *J. Electron. Mater.*, 10:541, 1981.

[169] J.K. Larsen. Inhomogeneities in epitaxialcalchopyrites studied by photoluminescence. Master's thesis, Université du Lusembour, 2011.

[170] W. Bollmann. *Crystal Defects and Crystalline Interfaces.* Springer-Verlag Berlin Heidelberg, 1970.

[171] Karl W. Böer. *Handbook of the Physics of Thin-Film Solar Cells.* Springer-Verlag Berlin Heidelberg, 2013.

[172] D. Abou-Ras and *et al. Phys. Status Solidi*, 10:363, 2016.

[173] S. B. Zhang, S.-H. Wei, Alex Zunger, and H. Katayama-Yoshida. *Phys. Rev. B*, 57:9642, 1998.

[174] S-H. Wei, S. B. Zhang, and A. Zunger. *Appl. Phys. Lett.*, 72:3199, 1998.

[175] J. Mattheis, U. Rau, and J. H. Werner. *J. Appl. Phys.*, 101:113519, 2007.

[176] J. Pohl and K. Albe. *Phys. Rev. B*, 87:245203, 2013.

[177] S. Siebentritt and T. Rissom. *Applied Physics Letters*, 92:062107, 2008.

[178] T. Eisenbarth, R. Caballero, M. Nichterwitz, C. A. Kaufmann, H-W. Schock, and T. Unold. *J. Appl. Phys.*, 110:094506, 2011.

[179] S. Lany and A. Zunger. *J. Appl. Phys.*, 100:113725, 2006.

[180] S. Lany and A. Zunger. *Phys. Rev. Lett.*, 100:016401, 2008.

[181] J.-F. Guillemoles, L. Kronik, D. Cahen, U. Rau, A. Jasenek, and H.-W. Schock. *J. Phys. Chem. B*, 104:4849, 2000.

[182] J. V. Li, D. Kuciauskas, M. R. Young, and I. L. Repins. *Appl. Phys. Lett.*, 103:029901, 2013.

[183] A. Mule, B. Vermang, M. Sylvester, G. Brammertz, S. Ranjbar, T. Schnabel, N. Gampa, M. Meuris, and J. Poortmans. *Thin Solid Films*, 633:156, 2017.

[184] S-H. Wei, S. B. Zhang, and A. Zunger. *Journal of Applied Physics*, 85:7214, 1999.

[185] L. Kronik, D. Cahen, and H. W. Schock. *Adv. Mater.*, 10:31, 1999.

[186] C. Rincón, J. González, and G. Sánchez Pérez. *J. Appl. Phys.*, 54:6634, 1983.

[187] G. Dagan, F. Abou-Elfotouh, D. J. Dunlavy, R. J. Matson, and D. Cahen. *Chem. Mater.*, 2:286, 1990.

[188] A. Bauknecht, S. Siebentritt, J. Albert, and M. Ch. Lux-Steiner. *J. Appl. Phys.*, 89:4391, 2001.

[189] S. Siebentritt and S. Schuler. *J. Phys. Chem. Solids*, 64:1621, 2003.

[190] G. Massé and E. Redjai. *J. Appl. Phys.*, 56:1154, 1984.

[191] T. Walter, R. Herberholz, C. Müller, and H. W. Schock. *J. Appl. Phys.*, 80:4411, 1996.

[192] U. Reislöhner, H. Metzner, and C. Ronning. *Phys. Rev. Lett.*, 104:226403, 2010.

[193] Q. Cao, O. Gunawan, M. Copel, K. B. Reuter, S. J. Chey, V. R. Deline, and D. B. Mitzi. *Adv. Energy Mater.*, 1:845, 2011.

[194] D. Schmid, M. Ruckh, F. Grunwald, and H. W. Schock. *J. Appl. Phys.*, 73:2902, 1993.

[195] D. Schmid, M. Ruckh, and H. W. Schock. *Appl. Surf. Sci.*, 103:409, 1996.

[196] M. J. Romero, K. M. Jones, J. AbuShama, Y. Yan, M. M. Al-Jassim, and R. Noufi. *Appl. Phys. Lett.*, 83:4731, 2003.

[197] Y. Yan, K. M. Jones, J. Abushama, M. Young, S. Asher, M. M. Al-Jassim, and R. Noufi. *Appl. Phys. Lett.*, 81:1008, 2002.

[198] U. Rau, D. Braunger, R. Herberholz, H. W. Schock, J.-F. Guillemoles, L. Kronik, and David Cahen. *J. Appl. Phys.*, 86:497, 1999.

[199] A. Niemegeers, M. Burgelman, R. Herberholz, U. Rau, D. Hariskos, and H.-W. Schock. *Prog. Photovoltaics*, 6:407, 1998.

[200] D. Cahen and R. Noufi. *Appl. Phys. Lett.*, 54:558, 1989.

[201] D. Cahen and R. Noufi. *Solar Cells*, 30:53, 1991.

[202] L. Kronik, U. Rau, J.-F. Guillemoles, D. Braunger, H.-W. Schock, and D. Cahen. *Thin Solid Films*, 361:353, 2000.

[203] A. Romeo, M. Terheggen, D. Abou-Ras, D. L. Bätzner, F.-J. Haug, M. Kälin, D. Rudmann, and A. N. Tiwari. *Prog. Photovoltaics*, 12:93, 2004.

[204] J. Ramanujam and U. P. Singh. *Energy Environ. Sci.*, 10:1306, 2017.

[205] T. Feurer, P. Reinhard, E. Avancini, B. Bissig, J. Löckinger, P. Fuchs, R. Carron, T. P. Weiss, J. Perrenoud, S. Stutterheim, S. Buecheler, and A. N. Tiwari. *Progress in Photovoltaics: Research and Applications*, 25:645, 2017.

[206] H. Yildirim and A. Peksoz. *Thin Solid Films*, 631:34, 2017.

[207] Y. Qu, G. Zoppi, and N. S. Beattie. *Sol. Energy Mater. Sol. Cells*, 158:130, 2016.

[208] V.G. Rajeshmon, M.R. Rajesh Menon, C. Sudha Kartha, and K.P. Vijayakumar. *J. Anal. Appl. Pyrolysis*, 110:448, 2014.

[209] C. J. Hibberd, E. Chassaing, W. Liu, D. B. Mitzi, D. Lincot, and A. N. Tiwari. *Prog. Photovoltaics*, 18:434, 2010.

[210] R. Noufi, R. Axton, C. Herrington, and S. K. Deb. *Appl. Phys. Lett.*, 45:668, 1984.

[211] J.R. Tuttle, D.S. Albin, and R. Noufi. *Solar Cells*, 30:21, 1991.

[212] Billy J. Stanbery. *Crit. Rev. Solid State Mater. Sci.*, 27:73, 2002.

[213] N. Barreau, J. Lähnemann, F. Couzinié-Devy, L. Assmann, P. Bertoncini, and J. Kessler. *Sol. Energy Mater. Sol. Cells*, 93:2013, 2009.

[214] D. J. Dwyer, S. B. Schujman, J. A. Novak, D. J. Metacarpa, and P. Haldar. In *2013 IEEE 39th Photovoltaic Specialists Conference (PVSC)*, page 1957, June 2013.

[215] A. M. Gabor, J. R. Tuttle, D. S. Albin, M. A. Contreras, R. Noufi, and A. M. Hermann. *Appl. Phys. Lett.*, 65:198, 1994.

[216] Udai P. Singh and Surya P. Patra. *Int. J. of Photoenergy*, 2010:1, 2010.

[217] J. R. Tuttle, M. A. Contreras, T. J. Gillespie, K. R. Ramanathan, A. L. Tennant, J. Keane, A. M. Gabor, and R. Noufi. *Prog. Photovoltaics*, 3:235, 1995.

[218] A. Khare, B. Himmetoglu, M. Johnson, D. J. Norris, M. Cococcioni, and E. S. Aydil. *J. Appl. Phys.*, 111:083707, 2012.

[219] S. Schorr. *Thin Solid Films*, 515:5985, 2007.

[220] J. J. Scragg, T. Kubart, J. T. Wätjen, T. Ericson, M. K. Linnarsson, and C. Platzer-Björkman. *Chem. Mater.*, 25:3162, 2013.

[221] M. Tovar S. Schorr, H. J. Hoebler. *Eur. J. Mineral*, 19:65, 2007.

[222] J. J. S. Scragg, L. Choubrac, A. Lafond, T. Ericson, and C. Platzer-Björkman. *Appl. Phys. Lett.*, 104:041911, 2014.

[223] S. Bourdais, C. Choné, B. Delatouche, A. Jacob, G. Larramona, C. Moisan, A. Lafond, F. Donatini, G. Rey, S. Siebentritt, A. Walsh, and G. Dennler. *Adv. Energy Mat.*, 6:1502276, 2016.

[224] J. Paier, R. Asahi, A. Nagoya, and G. Kresse. *Phys. Rev. B*, 79:115126, 2009.

[225] J. P. Leitao, N. M. Santos, P. A. Fernandes, P. M. P. Salomé, A. F. da Cunha, J. C. González, and F. M. Matinaga. *Thin Solid Films*, 519:7390, 2011.

[226] G. S. Babu, Y. B. K. Kumar, P. U. Bhaskar, and V. S. Raja. *Semicond. Sci. Technol.*, 23:085023, 2008.

[227] R. A. Wibowo, E. S. Lee, B. Munir, and K.H. Kim. *Phys. Satus Solidi (a)*, 204:3373, 2007.

[228] S. Botti, D. Kammerlander, and M. A. L. Marques. *Appl. Phys. Lett.*, 98:241915, 2011.

[229] Y. Zhang, X. Yuan, X. Sun, B-C. Shih, P. Zhang, and W. Zhang. *Phys. Rev. B*, 84:075127, 2011.

[230] J.-S. Seol, S.-Y. Lee, J.-C. Lee, H.-D. Nam, and K.-H. Kim. *Sol. Energy Mater. Sol. Cells*, 75:155, 2003.

[231] H. Katagiri, K. Saitoh, T. Washio, H. Shinohara, T. Kurumadani, and S. Miyajima. *Sol. Energy Mater. Sol. Cells*, 65:141, 2001.

[232] N. Nakayama and K. Ito. *Appl. Surf. Sci.*, 92:171, 1996.

[233] J. Zhang, L. Shao, Y. Fu, and E. Xie. *Rare Met. Mater. Eng.*, 25:315, 2006.

[234] S. Chen, A. Walsh, J.-H. Yang, X. G. Gong, L. Sun, P.-X. Yang amd J.-H. Chu, and S.-H. Wei. *Phys. Rev. B*, 83:125201, 2011.

[235] A. Walsh, S. Chen, S.-H. Wei, and X.-G. Gong. *Adv. Energy Mater.*, 2:400, 2012.

[236] S. Levcenco, D. Dumcenco, Y.P. Wang, Y.S. Huang, C.H. Ho, E. Arushanov, V. Tezlevan, and K.K. Tiong. *Optical Materials*, 34:1362, 2012.

[237] C. Persson H. Zhao. *Thin Solid Films*, 519:7508, 2011.

[238] S. Ahn, S. Jung, J. Gwak, A. Cho, K. Shin, K. Yoon, D. Park, H. Cheong, and J. H. Yun. *Appl. Phys. Lett.*, 97:021905, 2010.

[239] J. Vidal, S. Botti, P. Olsson, J.-F. Guillemoles, and L. Reinin. *Phys. Rev. Lett.*, 104:056401, 2010.

[240] S. Siebentritt and S. Schorr. *Prog. Photovoltaics*, 20:512, 2012.

[241] L. Choubrac, A. Lafond, C. Guillot-Deudon, Y. Moëlo, and S. Jobic. *Inorg. Chem.*, 51:3346, 2012.

[242] S. Chen, J.-H. Yang, X. G. Gong, A. Walsh, and S.-H Wei. *Phys. Rev. B*, 81:245204, 2010.

[243] S. Chen, X. G. Gong, A. Walsh, and S.-H. Wei. *Appl. Phys. Lett.*, 96:021902, 2010.

[244] P. Sarker, M. M. Al-Jassim, and M. N. Huda. *J. Appl. Phys.*, 117:035702, 2015.

[245] P. A. Fernandes, P. M. P. Salomé, and A. F. da Cunha. *Thin Solid Films*, 517:2519, 2009.

[246] I. D. Olekseyuk, I. V. Dudchak, and L. V. Piskach. *J. Alloys Compd.*, 368:135, 2004.

[247] A. D. Collord, H. Xin, and H. W. Hillhouse. *IEEE J. Photovoltaics*, 5:288, 2015.

[248] L. E. V. Rios, K. Neldner, G. Gurieva, and S. Schorr. *J. Alloys Compd.*, 657:408, 2016.

[249] D. Zimmer, J. Ruiz-Fuertes, L. Bayarjargal, E. Haussühl, B. Winkler, J. Zhang, C. Q. Jin, V. Milman, E. Alig, and L. Fink. *Phys. Rev. B*, 96:054108, 2017.

[250] A. Schneikart, H-J. Schimper, A. Klein, and W. Jaegermann. *J. Phys. D: Appl. Phys.*, 46:305109, 2013.

[251] G. Domingo, R. S. Itoga, and C. R. Kannewurf. *Phys. Rev.*, 143:536, 1966.

[252] C. D. Lokhande. *J. Phys. D: Appl. Phys.*, 23:1703, 1990.

[253] N. G. Deshpande, A .A. Sagade, Y. G. Gudage, C. D. Lokhande, and R. Sharma. *J. Alloys Compd.*, 436:421, 2007.

[254] D. Avellaneda, M. T. S. Nair, and P. K. Nair. *J. Electrochem. Soc.*, 157:D346, 2010.

[255] Q. Chen, X. Dou, Z. Li, Y. Ni, J. Chen, F. Zhou, Y. Yamaguchi, and S. Zhuang. *Optik*, 125:3217, 2014.

[256] X a. Chen, H. Wada, A. Sato, and M. Mieno. *J. Solid State Chem.*, 139:144, 1998.

[257] P. A. Fernandes, P. M. P. Salomé, and A. F. da Cunha. *J. Phys. D: Appl. Phys.*, 43:215403, 2010.

[258] Y-T. Zhai, S. Chen, J-H. Yang, H-J. Xiang, X-G. Gong, A. Walsh, J. Kang, and S-H. Wei. *Phys. Rev. B*, 84:075213, 2011.

[259] M. Bouaziz, M. Amlouk, and S. Belgacem. *Thin Solid Films*, 517:2527, 2009.

[260] M. Altosaar, J. Raudoja, K. Timmo, M. Danilson, M. Grossberg, J. Krustok, and E. Mellikov. *Phys. Status Solidi A*, 205:167, 2008.

[261] A. Nagoya, R. Asahi, R. Wahl, and G. Kresse. *Phys. Rev. B*, 81:113202, 2010.

[262] T. Maeda, S. Nakamura, and T. Wada. *Japanese J. Appl. Phys.*, 50:04DP07, 2011.

[263] S. Chen, A. Walsh, X-G. Gong, and S-H. Wei. *Adv. Mater.*, 25:1522, 2013.

[264] A.-J. Cheng, M. Manno, A. Khare, C. Leighton, S. A. Campbell, and E. S. Aydil. *J. Vac. Sci. Technol., A*, 29:051203, 2011.

[265] P. Y. Yu and M. Cardona. *Fundamentals of Semiconductors*. Springer, Berlin, 3rd edition, 2001.

[266] M. Himmrich and H. Haeuseler. *Spectrochim. Acta, Part A*, 47:933, 1991.

[267] Tanju Gürel, Cem Sevik, and Tahir Çağin. *Phys. Rev. B*, 84:205201, 2011.

[268] H. Yoo and J. Kim. *Thin Solid Films*, 518:6567, 2010.

[269] P. A. Fernandes, P. M. P. Salomé, and A. F. da Cunha. *Thin Solid Films*, 517:2519, 2009.

[270] X. Fontané, V. Izquierdo-Roca, E. Saucedo, S. Schorr, V.O. Yukhymchuk, M.Ya. Valakh, A. Pérez-Rodriguez, and J.R. Morante. *J. Alloys Compd.*, 539:190, 2012.

[271] M. Grossberg, J. Krustok, J. Raudoja, and T. Raadik. *Appl. Phys. Lett.*, 101:102102, 2012.

[272] F. Jiang, S. Ikeda, T. Harada, and M. Matsumura. *Adv. Energy Mater.*, 4:1301381, 2013.

[273] G. Larramona, S. Bourdais, A. Jacob, C. Choné, T. Muto, Y. Cuccaro, B. Delatouche, C. Moisan, D. P'er'e, and G. Dennler. *J. Phys. Chem. Lett.*, 5:3763, 2014.

[274] S. Zhuk, A. Kushwaha, T. K.S. Wong, S. Masudy-Panah, A. Smirnov, and G. K. Dalapati. *Sol. Energy Mater. Sol. Cells*, 171:239, 2017.

[275] A. V. Moholkar, S. S. Shinde, A. R. Babar, K-U. Sim, Y b. Kwon, K. Y. Rajpure, P. S. Patil, C. H. Bhosale, and J. H. Kim. *Sol. Energy*, 85:1354, 2011.

[276] A. Weber, R. Mainz, and H. W. Schock. *J. Appl. Phys.*, 107:013516, 2010.

[277] M. G. Sousa, A. F. da Cunha, P. M. P. Salomé, P. A. Fernandes, J. P. Teixeira, and J. P. Leitão. *Thin Solid Films*, 535:27, 2013.

[278] H. Katagiri, K. Jimbo, S. Yamada, T. Kamimura, W. S. Maw, T. Fukano, T. Ito, and T. Motohiro. *Appl. Phys. Express*, 1:041201, 2008.

[279] S. Marchionna, P. Garattini, A. Le Donne, M. Acciarri, S. Tombolato, and S. Binetti. *Thin Solid Films*, 542:114, 2013.

[280] Narayana Thota, Y. P. Venkata Subbaiah, P. Prathap, Y. B .K. Reddy, and G. Hema Chandra. *Physica B Condens Matter.*, 449:255, 2014.

[281] M. G. Sousa, A. F. da Cunha, P. A. Fernandes, J. P. Teixeira, R. A. Sousa, and J. P. Leitão. *Sol. Energy Mater. Sol. Cells*, 126:101, 2014.

[282] H. Araki, A. Mikaduki, Y. Kubo, T. Sato, K. Jimbo, W. S. Maw, H. Katagiri, M. Yamazaki, K. Oishi, and A. Takeuchi. *Thin Solid Films*, 517:1457, 2008.

[283] C. Platzer-Björkman, J. Scragg, H. Flammersberger, T. Kubart, and M. Edoff. *Sol. Energy Mater. Sol. Cells*, 98:110, 2012.

[284] J. H. Werner, J. Mattheis, and U. Rau. *Thin Solid Films*, 480-481:399, 2005.

[285] P. Jackson, D. Hariskos, E. Lotter, S. Paetel, R. Wuerz, R. Menner, W. Wischmann, and M. Powalla. *Prog. Photovoltaics*, 19:894, 2011.

[286] H. Katagiri, K. Jimbo, M. Tahara, H. Araki, and K. Oishi. volume 1165 of *MRS Proceedings*, 2009.

[287] A. Nagoya, R. Asahi, R. Wahl, and G. Kresse. *Phys. Rev. B*, 81:113202, 2010.

[288] Dong Han, Y. Y. Sun, Junhyeok Bang, Y. Y. Zhang, Hong-Bo Sun, Xian-Bin Li, and S. B. Zhang. *Phys. Rev. B*, 87:155206, 2013.

[289] I. Repins et al. In *2016 IEEE 43rd Photovoltaic Specialists Conference (PVSC)*, page 0309, 2016.

[290] D. Abou-Ras, N. Schäfer, C. J. Hages, S. Levcenko, J. M'arquez, and T. Unold. *Solar RRL*, 2:1700199, 2018.

[291] G. Rey, G. Larramona, S. Bourdais, C. Choné, B. Delatouche, A. Jacob, G. Dennler, and S. Siebentritt. *Sol. Energy Mater Sol. Cells*, 179:142, 2018.

[292] C. Kittel. *Introduction to Solid State Physics*. John Wiley & Sons, Inc, New York, 8 edition, 2005.

[293] B. P. Falcão, J. P. Leitão, M. R. Correia, M. F. Leitão, M. R. Soares, M. V. B. Moreira, A. G. de Oliveira, F. M. Matinaga, and J. C. Gonzaléz. *J. Mater. Chem. C*, 2:7104, 2014.

[294] P. Van Mieghem. *Rev. Mod. Phys.*, 64:755, 1992.

[295] S. K. Wallace, D. B. Mitzi, and A. Walsh. *ACS Energy Lett.*, 2:776, 2017.

[296] J. I. Pankove. *Optical Processes in Semiconductors*. Dover Publications, New York, 1975.

[297] B. I. Shklovskii and A. L. Efros. *Electronic Properties of Doped Semiconductors*. Springer-Verlag, Berlin, 1991.

[298] T. Gokmen, O. Gunawan, T. K. Todorov, and D. B. Mitzi. *Appl. Phys. Lett.*, 103:103506, 2013.

[299] S. Schorr. *Sol. Energy Mater Sol. Cells*, 95:1482, 2011.

[300] J. J. S. Scragg, J. K. Larsen, M. Kumar, C. Persson, J. Sendler, S. Siebentritt, and C. Platzer Björkman. *Phys. Status Solidi B*, 253:247, 2016.

[301] I. Dirnstorfer, M. Wagner, D. M. Hofmann, M. D. Lampert, F. Karg, and B. K. Meyer. *Phys. Status Solidi (a)*, 168:163, 1998.

[302] J. P. Leitao, N. M. Santos, P. A. Fernandes, P. M. P. Salomé, A. F. da Cunha, J. C. González, G. M. Ribeiro, and F. M. Matinaga. *Phys. Rev. B*, 84:024120, 2011.

[303] T. Unold, S. Kretzschmar, J. Just, O. Zander, B. Schubert, B. Marsen, and H. Schock. In *Photovoltaic Specialists Conference (PVSC), 2011 37th IEEE*, page 002820, 2011.

[304] O. Gunawan, T. Gokmen, C. W. Warren, J. D. Cohen, T. K. Todorov, D. A. R. Barkhouse, S. Bag, J. Tang, B. Shin, and David B. Mitzi. *Appl. Phys. Lett.*, 100:253905, 2012.

[305] V. Kosyak, N. B. Mortazavi Amiri, A. V. Postnikov, and M. A. Scarpulla. *J. Appl. Phys.*, 114:124501, 2013.

[306] D. P. Halliday, R. Claridge, M. C. J. Goodman, B. G. Mendis, K. Durose, and J. D. Major. *J. Appl. Phys.*, 113:1, 2013.

[307] B. I. Shklovskii and A. L. Efros. *Sov. Phys. JETP*, 34:435, 1972.

[308] J. P. Teixeira, R. A. Sousa, M. G. Sousa, A. F. da Cunha, P. A. Fernandes, P. M. P. Salomé, and J. P. Leitão. *Phys. Rev. B*, 90:235202, 2014.

[309] P. W. Yu. *J. Appl. Phys.*, 48:5043, 1977.

[310] P. M. P. Salomé, P. A. Fernandes, A. F. da Cunha, J. P. Leitão, J. Malaquias, A. Weber, J. C. González, and M. I .N. da Silva. *Sol. Energy Mater Sol. Cells*, 94:2176, 2010.

[311] J. Tauc. *Materials Research Bulletin*, 5:721, 1970.

[312] Evan O. Kane. *Phys. Rev.*, 131:79–88, 1963.

[313] B. I. Halperin and M. Lax. *Phys. Rev.*, 148:722–740, 1966.

[314] A. L. Efros. *Phys. Usp.*, 16:789, 1974.

[315] J. K. Katahara and H. W. Hillhouse. *J. Appl. Phys.*, 116:173504, 2014.

[316] J. K. Katahara and H. W. Hillhouse. *J. Appl. Phys.*, 119:239901, 2016.

[317] F. Urbach. *Phys. Rev.*, 92:1324, 1953.

[318] M. H. Cohen, M. Y. Chou, E. N. Economou, S. John, and C. M. Soukoulis. *IBM J. Res. Dev.*, 32:82, 1988.

[319] W. Sritrakool, V. Sa-yakanit, and H. R. Glyde. *Phys. Rev. B*, 33:1199, 1986.

[320] L. J. Lewis and B. Movaghar. *Solid State Commun.*, 75:885, 1990.

[321] M. Kemp and M. Silver. *Appl. Phys. Lett.*, 62:1487, 1993.

[322] E. O. Kane. *Solid-State Electronics*, 28:3, 1985.

[323] J. K. Katahara and H. W. Hillhouse. In *2014 IEEE 40th Photovoltaic Specialist Conference (PVSC)*, page 0866, 2014.

[324] C. Malerba, M. Valentini, and A. Mittiga. *Solar RRL*, 1:1700101, 2017.

[325] A. Meeder, D. Fuertes Marrón, A. Rumberg, M. Ch. Lux-Steiner, V. Chu, and J. P. Conde. *J. Appl. Phys.*, 92:3016, 2002.

[326] J. T. Heath, J. D. Cohen, W. N. Shafarman, D. X. Liao, and A. A. Rockett. *Appl. Phys. Lett.*, 80:4540, 2002.

[327] P. T. Erslev, J. W. Lee, W. N. Shafarman, and J. D. Cohen. *Thin Solid Films*, 517:2277, 2009.

[328] M. Troviano and K. Taretto. *Sol. Energy Mater Sol. Cells*, 95:3081, 2011.

[329] D. W. Miller, C. W. Warren, O. Gunawan, T. Gokmen, D. B. Mitzi, and J. D. Cohen. *Appl. Phys. Lett.*, 101:142106, 2012.

[330] M. A. Majeed Khan, S. Kumar, M. Alhoshan, and A .S. Al Dwayyan. *Optics Laser Technology*, 49:196–201, 2013.

[331] C. Malerba, F. Biccari, C. L. A. Ricardo, M. Valentini, R. Chierchia, M. Muller, A. Santoni, E. Esposito, P. Mangiapane, P. Scardi, and A. Mittiga. *Journal of Alloys and Compounds*, 582:528, 2014.

[332] G. Teeter, S. P. Harvey, and S. Johnston. *J. Appl. Phys.*, 121:043102, 2017.

[333] L. Q. Phuong, M. Okano, G. Yamashita, M. Nagai, M. Ashida, A. Nagaoka, K. Yoshino, and Y. Kanemitsu. *Phys. Rev. B*, 92:115204, 2015.

[334] B. G. Mendis, A. A. Taylor, M. Guennou, D. M. Berg, M. Arasimowicz, S. Ahmed, H. Deligianni, and P. J. Dale. *Sol. Energy Mater Sol. Cells*, 174:65, 2018.

[335] T. Shioda, S. Chichibu, T. Irie, H. Nakanishi, and T. Kariya. *J. Appl. Phys.*, 80:1106, 1996.

[336] S. M. Wasim, C. Rincón, G. Marín, P. Bocaranda, E. Hernández, I. Bonalde, and E. Medina. *Phys. Rev. B*, 64:195101, 2001.

[337] H. Nakanishi, T. Sawaya, S. Endo, and T. Irie. *Jpn. J. Appl. Phys.*, 32:200, 1993.

[338] C. J. Hages, N. J. Carter, and R. Agrawal. *J. Appl. Phys.*, 119:014505, 2016.

[339] P. J. Dean. *Progress in Solid State Chemistry*, 8:1, 1973.

[340] J. Krustok, T. Raadik, M. Grossberg, M. Kauk-Kuusik, V. Trifiletti, and S. Binetti. *Mater. Sci. Semicond. Process.*, 80:52, 2018.

[341] T. Schmidt, K. Lischka, and W. Zulehner. *Phys. Rev. B*, 45:8989, 1992.

[342] V. V. Osipov, T. I. Soboleva, and M. G. Foigel. *Sov. Phys. Semicond.*, 11:752, 1977.

[343] S. Siebentritt, N. Papathanasiou, and M.Ch. Lux-Steiner. *Physica B: Condensed Matter*, 376-377:831, 2006.

[344] J. P. Teixeira, R. A. Sousa, M. G. Sousa, A. F. da Cunha, P. A. Fernandes, P. M. P. Salomé, J. C. González, and J. P. Leitão. *Appl. Phys. Lett.*, 105:163901, 2014.

[345] J. P. Teixeira, R. A. Sousa, M. G. Sousa, A. F. da Cunha, P. A. Fernandes, P. M. P. Salomé, J. C. González, and J. P. Leitão. Erratum: Appl. Phys. Lett. 105, 163901 (2014). *Appl. Phys. Lett.*, 107:049903, 2015.

[346] M. Lang, C. Zimmermann, C. Krämmer, T. Renz, C. Huber, H. Kalt, and M. Hetterich. *Phys. Rev. B*, 95:155202, 2017.

[347] S. A. Schumacher, J. R. Botha, and V. Alberts. *J. Appl. Phys.*, 99:063508, 2006.

[348] P. W. Yu and Y. S. Park. *J. Appl. Phys.*, 48:2434, 1977.

[349] S. Oueslati, G. Brammertz, M. Buffiare, C. Koble, T. Oualid, M.Meuris, and J. Poortmans. *Sol. Energy Mater Sol. Cells*, 134:340, 2015.

[350] S. H. Park and B. D. Choe. *J. Appl. Phys.*, 68:5916, 1990.

[351] A. Jagomägi, J. Krustok, J. Raudoja, M. Grossberg, M. Danilson, and M. Yakushev. *Physica B: Condensed Matter*, 337:369, 2003.

[352] A. Yamada, P. Fons, S. Niki, H. Shibata, A. Obara, Y. Makita, and H. Oyanagi. *J. Appl. Phys.*, 81:2794, 1997.

[353] S. Shirakata, K. Ohkubo, Y. Ishii, and T. Nakada. *Sol. Energy Mater Sol. Cells*, 93:988, 2009.

[354] M. J. Romero, H. Du, G. Teeter, Y. Yan, and M. Al-Jassim. *Phys. Rev. B*, 84:165324, 2011.

[355] S. Shirakata, S. Chichibu, H. Miyake, and K. Sugiyama. *J. Appl. Phys.*, 87:7294, 2000.

[356] J. Krustok, H. Collan, M. Yakushev, and K. Hjelt. *Physica Scripta*, 1999:179, 1999.

[357] R. Kondrotas, M. Colina, M. Guc, M. Neuschitzer, S. Giraldo, X. Alcobé, F. Oliva, Y. Sánchez, P. Pistor, V. Izquierdo-Roca, A. Pérez-Rodriguez, and E. Saucedo. *Sol. Energy Mater Sol. Cells*, 160:26, 2017.

[358] J. Krustok, J. Raudoja, M. Yakushev, R. D. Pilkington, and H. Collan. *Phys. Status Solidi (a)*, 173:483, 1999.

[359] J. K. Larsen, K. Burger, L. Gütay, and S. Siebentritt. In *2011 37th IEEE Photovoltaic Specialists Conference*, page 000396, 2011.

[360] A. P. Levanyuk and V. V. Osipov. *Soviet Physics Semiconductors*, 7:727, 1973.

[361] A. Le Donne, S. Marchionna, P. Garattini, R. A. Mereu, M. Acciarri, and S. Binetti. *Int. J. of Photoenergy*, 2015:1, 2015.

[362] T. Gershon, B. Shin, N. Bojarczuk, T. Gokmen, S. Lu, and S. Guha. *J. Appl. Phys.*, 114:154905, 2013.

[363] L. Van Puyvelde, J. Lauwaert, P.F. Smet, S. Khelifi, T. Ericson, J.J. Scragg, D. Poelman, R. Van Deun, and C. Platzer-Björkman. *Thin Solid Films*, 582:146, 2015.

[364] S. Sahayaraj, G. Brammertz, B. Vermang, T. Schnabel, E. Ahlswede, Z. Huang, S. Ranjbar, M. Meuris, J. Vleugels, and J. Poortmans. *Sol. Energy Mater Sol. Cells*, 171:136, 2017.

[365] S. Niki, H. Shibata, P. J. Fons, A. Yamada, A. Obara, Y. Makita, T. Kurafuji, S. Chichibu, and H. Nakanishi. *Appl. Phys. Lett.*, 67:1289–1291, 1995.

[366] K. Yoshino, M. Sugiyama, D. Maruoka, S. F. Chichibu, H. Komaki, K. Umeda, and T. Ikari. *Physica B: Condensed Matter*, 302-303:357, 2001.

[367] F. Luckert, M. V. Yakushev, C. Faugeras, A. V. Karotki, A. V. Mudryi, and R. W. Martin. *J. Appl. Phys.*, 111:093507, 2012.

[368] I. Dirnstorfer, D. M. Hofmann, D. Meister, B. K. Meyer, W. Riedl, and F. Karg. *J. Appl. Phys.*, 85:1423, 1999.

[369] N. Rega, S. Siebentritt, I.E. Beckers, J. Beckmann, J. Albert, and M. Lux-Steiner. *Thin Solid Films*, 431-432:186, 2003.

[370] P. W. Yu. *Solid State Communications*, 18:395, 1976.

[371] F. Luckert, D. I. Hamilton, M. V. Yakushev, N. S. Beattie, G. Zoppi, M. Moynihan, I. Forbes, A. V. Karotki, A. V. Mudryi, M. Grossberg, J. Krustok, and R. W. Martin. *Appl. Phys. Lett.*, 99:062104, 2011.

[372] M. V. Yakushev, I. Forbes, A. V. Mudryi, M. Grossberg, J. Krustok, N. S. Beattie, M. Moynihan, A. Rockett, and R.W. Martin. *Thin Solid Films*, 582:154, 2015.

[373] H. Tassoult, A. Bouloufa, M. Pawlowski, and M. Igalson. *Mater. Sci. Semicond. Process.*, 88:167, 2018.

[374] L. Q. Phuong, M. Okano, Y. Yamada, A. Nagaoka, K. Yoshino, and Y. Kanemitsu. *Appl. Phys. Lett.*, 104:081907, 2014.

[375] M. Grossberg, J. Krustok, T. Raadik, M. Kauk-Kuusik, and J. Raudoja. *Curr. Appl. Phys.*, 14:1424, 2014.

[376] S. Zott, K. Leo, M. Ruckh, and H.-W. Schock. *Appl. Phys. Lett.*, 68:1144, 1996.

[377] V. P. Dobrego and I. S. Shlimak. *Phys. Status Solidi (b)*, 33:805, 1969.

[378] A. P. Levanyuk and V. V. Osipov. *Soviet Physics Semiconductors*, 7:721, 1973.

[379] K. Tanaka, T. Shinji, and H. Uchiki. *Sol. Energy Mater. Sol. Cells*, 126:143, 2014.

[380] M.V. Yakushev, A. Jack, I. Pettigrew, Y. Feofanov, A.V. Mudryi, and J. Krustok. *Thin Solid Films*, 511:135, 2006.

[381] M. Grossberg, T. Raadik, J. Raudoja, and J. Krustok. *Curr. Appl. Phys.*, 14:447, 2014.

[382] L. Yin, G. Cheng, Y. Feng, Z. Li, C. Yang, and X. Xiao. *RSC Adv.*, 5:40369, 2015.

[383] Kunihiko Tanaka, Yoshiharu Takamatsu, and Shinya Miura. *Phys. Status Solidi c*, 14:1600138, 2017.

[384] J. Márquez-Prieto, M. V. Yakushev, I. Forbes, J. Krustok, P. R. Edwards, V. D. Zhivulko, O. M. Borodavchenko, A. V. Mudryi, M. Dimitrievska, V. Izquerdo-Roca, N. M. Pearsall, and R. W. Martin. *Sol. Energy Mater. Sol. Cells*, 152:42, 2016.

[385] M. V. Yakushev, M. A. Sulimov, J. Márquez-Prieto, I. Forbes, J. Krustok, P. R. Edwards, V. D. Zhivulko, O. M. Borodavchenko, A. V. Mudryi, and R. W. Martin. *Sol. Energy Mater Sol. Cells*, 168:69, 2017.

[386] J. Sendler, M. Thevenin, F. Werner, A. Redinger, S. Li, C. Hägglund, C. Platzer-Björkman, and S. Siebentritt. *J. Appl. Phys.*, 120:125701, 2016.

[387] D. Tiwari, E. Skidchenko, J. Bowers, M. V. Yakushev, R. Martin, and D. J. Fermin. *J. Mater. Chem. C*, 5:12720, 2017.

[388] M. Grossberg, J. Krustok, J. Raudoja, K. Timmo, M. Altosaar, and T. Raadik. *Thin Solid Films*, 519:7403, 2011.

[389] Pedro Salomé. *Chalcogenide Thin Films for Solar Cells: Growth and Properties.* PhD thesis, Aveiro University, 2011.

[390] Filipe Martinho. Development of cztsse thin film solar cells with inclusion of selenium in the precursor stack. Master's thesis, Aveiro University, 2017.

[391] Samaneh Ranjbarrizi. *Development of Kesterite Solar Cell: Improvement of Absorber layer and Cell Architecture.* PhD thesis, Aveiro University, 2018.

[392] P. M. P. Salomé, J. Malaquias, P. A. Fernandes, and A. F. da Cunha. *J. Phys. D: Appl. Phys.*, 43:345501, 2010.

[393] B. Vermang, J. T. Wätjen, C. Frisk, V. Fjällström, F. Rostvall, M. Edoff, P. Salomé, J. Borme, N. Nicoara, and S. Sadewasser. *IEEE J. Photovoltaics*, 4:1644, 2014.

[394] P. M. P. Salomé, A. Hultqvist, V. Fjällström, M. Edoff, B. Aitken, K. Vaidyanathan, K. Zhang, K. Fuller, and C. K. Williams. *IEEE J. Photovoltaics*, 3:852–858, 2013.

[395] M. J. Romero D. Abou-Ras, M. Nichterwitz and S. S. Schmidt. Electron microscopy on thin films for solar cells. In D. Abou-Ras, T. Kirchartz, and U. Rau, editors, *Advanced Characterization Techniques for Thin Film Solar Cells.* Willey, Berlin, 2011.

[396] S. Schorr, C. Stephan, T. Törndahl, and R. Mainz. X-ray and neutron diffraction on materials for thin-film solar cells. In D. Abou-Ras, T. Kirchartz, and U. Rau, editors, *Advanced Characterization Techniques for Thin Film Solar Cells.* Willey, Berlin, 2011.

[397] V. Izquierdo-Roca J. Alvarez-Garcia and A. Perez-Rodriguez. Raman spectroscopy on thin films for solar cells. In D. Abou-Ras, T. Kirchartz, and U. Rau, editors, *Advanced Characterization Techniques for Thin Film Solar Cells*. Willey, Berlin, 2011.

[398] D. E. Goldstein, J.and Newbury, D. C. Joy, C. E. Lyman, P. Echlin, E. Lifshin, L. Sawyer, and J. R Michael. *Scanning Electron Microscopy and X-Ray Microanalysis*. Springer US, 3 edition, 2003.

[399] K. Durose, S. E. Asher, W. Jaegermann, D. Levi, B. E. McCandless, W. Metzger, H. Moutinho, P. D. Paulson, C. L. Perkins, J. R. Sites, G. Teeter, and M. Terheggen. *Prog. Photovoltaics*, 12:177, 2004.

[400] J. Leitão, A. Carvalho, J. Coutinho, R. Pereira, N. Santos, A. Ankiewicz, N. Sobolev, M. Barroso, J. Lundsgaard Hansen, A. Nylandsted Larsen, and P. Briddon. *Phys. Rev. B*, 84:165211, 2011.

[401] Wolfgang W. Gärtner. *Phys. Rev.*, 116:84, 1959.

[402] J. J. Scragg, P. J. Dale, L. M. Peter, G. Zoppi, and I. Forbes. *Phys. Status Solidi B*, 245:1772, 2008.

[403] J. Tauc, R. Grigorovici, and A. Vancu. *Phys. Status Solidi (b)*, 15:627, 1966.

[404] P.A. Fernandes, P.M.P. Salomé, A.F. da Cunha, and B.-A. Schubert. *Thin Solid Films*, 519:7382, 2011.

[405] M. Richter, M. S. Hammer, T. Sonnet, and J. Parisi. *Thin Solid Films*, 633:213, 2017.

[406] H. Liang, W. Liu, S. Lee, J. van Duren, T. Franklin, M. Patten, and S. Nijhawan. In *2012 38th IEEE Photovoltaic Specialists Conference*, page 003102, June 2012.

[407] I. Khatri, H. Fukai, H. Yamaguchi, M. Sugiyama, and T. Nakada. *Sol. Energy Mater. Sol. Cells*, 155:280, 2016.

[408] C. Frisk, T. Ericson, S.-Y. Li, P. Szaniawski, J. Olsson, and C. Platzer-Björkman. *Sol. Energy Mater. Sol. Cells*, 144:364, 2016.

[409] J. C. González, G. M. Ribeiro, E. R. Viana, P. A. Fernandes, P. M. P. Salomé, K. Gutiérrez, A. Abelenda, F. M. Matinaga, J. P. Leitao, and A. F. da Cunha. *J. Phys. D Appl. Phys.*, 46:155107, 2013.

[410] A. Abelenda, M. Sánchez, G. M. Ribeiro, P. A. Fernandes, P. M .P. Salomé, A.F. da Cunha, J. P. Leitao, M .I. N. da Silva, and J. C. González. *Sol. Energy Mater Sol. Cells*, 137:164, 2015.

[411] K. Tanaka, Y. Miyamoto, H. Uchiki, K. Nakazawa, and H. Araki. *Phys. Status Solidi (a)*, 203:2891, 2006.

[412] B. G. Mendis, M. D Shannon, M. C. J. Goodman, J. D. Major, R. Claridge, D. P. Halliday, and K. Durose. *Prog. Photovoltaics*, 22:24, 2014.

[413] Yusuke Miyamoto, Kunihiko Tanaka, Masatoshi Oonuki, Noriko Moritake, and Hisao Uchiki. *Japanese J. Appl. Phys.*, 47:596, 2008.

[414] L. Quang Phuong, M. Okano, Y. Yamada, A. Nagaoka, K. Yoshino, and Y. Kanemitsu. *Appl. Phys. Lett.*, 103:191902, 2013.

[415] S. Levcenko, V. E. Tezlevan, E. Arushanov, S. Schorr, and T. Unold. *Phys. Rev. B*, 86:045206, 2012.

[416] Eliam Zacks and A. Halperin. *Phys. Rev. B*, 6:3072, 1972.

[417] P. W. Yu. *J. Appl. Phys.*, 47:677, 1976.

[418] Prashant K. Sarswat and Michael L. Free. *Physica B: Condensed Matter*, 407:108, 2012.

[419] W. Li, K. Jiang, J. Zhang, X. Chen, Z. Hu, S. Chen, L. Sun, and J. Chu. *Phys. Chem. Chem. Phys.*, 14:9936, 2012.

[420] K. Moriya, J. Watabe, K. Tanaka, and H. Uchiki. *Phys. Status Solidi C*, 3:2848, 2006.

[421] J. J. Scragg, P. J. Dale, and L. M. Peter. *Electrochem. Commun.*, 10:639, 2008.

[422] R. Sauer and J. Weber. *Physica B+C*, 116:195, 1983.

[423] T. Tiedje. *Appl. Phys. Lett.*, 40:627, 1982.

[424] R. B. V. Chalapathy, G. S. Jung, and B. T. Ahn. *Sol. Energy Mater Sol. Cells*, 95:3216, 2011.

[425] H. Zhou, W.-C. Hsu, H.-S. Duan, B. Bob, W. Yang, T.-B. Song, C.-J. Hsu, and Y. Yang. *Energy Environ. Sci.*, 6:2822, 2013.

[426] S.M. Pawar, A.I. Inamdar, B.S. Pawar, K.V. Gurav, S.W. Shin, Xiao Yanjun, S.S. Kolekar, Jung-Ho Lee, Jin Hyeok Kim, and Hyunsik Im. *Mater. Lett.*, 118:76, 2014.

[427] Myeng G. Gang, Kishor V. Gurav, Seung W. Shin, Chang W. Hong, Jung H. Min, Mahesh P. Suryawanshi, Sharad A. Vanalakar, Dong S. Lee, and Jin H. Kim. *Phys. Status Solidi C*, 12:713, 2015.

[428] J. B. Li, V. Chawla, and B. M. Clemens. *Adv. Mater.*, 24, 2012.

[429] A. R. Jeong, W. Jo, S. Jung, J. Gwak, and J. H. Yun. *Appl. Phys. Lett.*, 99:082103, 2011.

[430] J. Li, D. B. Mitzi, and V. B. Shenoy. *ACS Nano*, 5:8613, 2011.

[431] W.-J. Yin, Y. Wu, S.-H. Wei, R. Noufi, M. M. Al-Jassim, and Y. Yan. *Adv. Energy Mater.*, 4:1300712, 2014.

[432] G. Y. Kim, A. R. Jeong, J. R. Kim, W. Jo, D-H. Son, D-H. Kim, and J-K. Kang. *Sol. Energy Mater. Sol. Cells*, 127:129, 2014.

[433] T. M. Friedlmeier, P. Jackson, A. Bauer, D. Hariskos, O. Kiowski, R. Wuerz, and M. Powalla. In *Photovoltaic Specialist Conference (PVSC), 2015 IEEE 42nd*, page 1, June 2015.

[434] G. Rey, F. Babbe, T.P. Weiss, H. Elanzeery, M. Melchiorre, N. Valle, B. El Adib, and S. Siebentritt. *Thin Solid Films*, 633:162, 2017.

[435] T. Maeda, S. Nakamura, and T. Wada. *Japanese J. Appl. Phys.*, 51:10NC11, 2011.

[436] G. Sai Gautam, T. P. Senftle, and E. A. Carter. *Chem. Mater.*, 30:4543, 2018.

[437] A. S. Ibraheam, , Y. Al-Douri, , U. Hashim, D. Prakash, K. D. Verma, and M. Ameri. *J. Mater. Sci.*, 51:6876, 2016.

[438] M. Courel, A. Martinez-Ayala, T.G. Sanchez, E. Regalado-Perez, I. Montoya De Los Santos, N.R. Mathews, and X. Mathew. *Superlattices Microstruct.*, 122:324, 2018.

[439] F. Liu, C. Yan, J. Huang, K. Sun, F. Zhou, J. A. Stride, M. A. Green, and X. Hao. *Adv. Energy Mater.*, page 1600706, 2016.

[440] H. Sun, K. Sun, J. Huang, C. Yan, F. Liu, J. Park, A. Pu, J. A. Stride, M. A. Green, and X. Hao. *ACS Appl. Energy Mater.*, 1:154, 2018.

[441] Jekyung Kim, Sanghyun Park, Sangwoo Ryu, Jihun Oh, and Byungha Shin. *Prog. Photovoltaics*, 25:308, 2018.

[442] J. Jean, T. S. Mahony, D. Bozyigit, M. Sponseller, J. Holovský, M. G. Bawendi, and V. Bulović. *ACS Energy Lett.*, 2:2616, 2017.

[443] T. Kirchartz and U. Rau. *Adv. Energy Mater.*, 8:1703385, 2018.

[444] T. Kirchartz, K. Taretto, and U. Rau. *J. Phys. Chem. C*, 113:17958, 2009.

[445] D. Rudmann, A. F. da Cunha, M. Kaelin, F. Kurdesau, A. N. Zogg, H.and Tiwari, and G. Bilger. *Appl. Phys. Lett.*, 84:1129, 2004.

[446] D-H. Cho, K-S. Lee, Y-D. Chung, J-H. Kim, S-J. Park, and J Kim. *Appl. Phys. Lett.*, 101:023901, 2012.

[447] S. Ishizuka, A. Yamada, M. M. Islam, H. Shibata, P. Fons, T. Sakurai, K. Akimoto, and S. Niki. *J. Appl. Phys.*, 106:034908, 2009.

[448] P. Jackson, R. Wuerz, D. Hariskos, E. Lotter, W. Witte, and M. Powalla. *Phys. Stat. Sol. (RRL)*, 10:583, 2016.

[449] P. Jackson, D. Hariskos, R. Wuerz, O. Kiowski, A. Bauer, T. M. Friedlmeier, and M. Powalla. *Phys. Stat. Sol. (RRL)*, 9:28, 2015.

[450] O. Lundberg, M. Edoff, and L. Stolt. *Thin Solid Films*, 480-481:520, 2005.

[451] D. Shin, J. Kim, T. Gershon, R. Mankad, M. Hopstaken, S. Guha, B. T. Ahn, and B. Shin. *Sol. Energy Mater. Sol. Cells*, 157:695, 2016.

[452] M. H. Wolter, B. Bissig, E. Avancini, R. Carron, S. Buecheler, P. Jackson, and S. Siebentritt. *IEEE J. Photovoltaics*, 8:1320, 2018.

[453] Y. Ando, S. Ishizuka, S. Wang, J. Chen, M. M. Islam, H. Shibata, K. Akimoto, and T. Sakurai. *Jpn. J. Appl. Phys*, 57:08RC08, 2018.

[454] O. Ka, H. Alves, I. Dirnstorfer, T. Christmann, and B. K. Meyer. *Thin Solid Films*, 361:263, 2000.

[455] I. Repins, M. A. Contreras, B. Egaas, C. De Hart, J. Scharf, C. L. Perkins, B. To, and R. Noufi. *Prog. Photovoltaics*, 16:235, 2008.

[456] J-C. Chang, J-W. Guo, T-P. Hsieh, M-R. Yang, D-W. Chiou, H-T. Cheng, C-L. Yeh, C-C. Li, and S-Y Chu. *Surf. Coat. Technol.*, 231:573, 2013.

[457] I. Dirnstorfer, W. Burkhardt, W. Kriegseis, I. Österreicher, H. Alves, D. M. Hofmann, O. Ka, A. Polity, B. K. Meyer, and D. Braunger. *Thin Solid Films*, 361-362:400, 2000.

[458] M .V. Yakushev, A. Jack, I. Pettigrew, Y. Feofanov, A.V. Mudryi, and J. Krustok. *Thin Solid Films*, 511-512:135, 2006.

[459] M. N. Ruberto and A. Rothwarf. *J. Appl. Phys.*, 61:4662, 1987.

[460] F. Engelhardt, M. Schmidt, Th. Meyer, O. Seifert, J. Parisi, and U. Rau. *Phys. Lett. A*, 245:489, 1998.

[461] M. Igalson, P. Zabierowski, D. Prządo, A. Urbaniak, M. Edoff, and W. N. Shafarman. *Sol. Energy Mater. Sol. Cells*, 93:1290, 2009.

[462] T. M. Friedlmeier, P. Jackson, A. Bauer, D. Hariskos, O. Kiowski, R. Wuerz, and M. Powalla. *IEEE J. Photovoltaics*, 5:1487, 2015.

[463] N. Naghavi, D. Abou-Ras, N. Allsop, N. Barreau, S. Bücheler, A. Ennaoui, C.-H. Fischer, C. Guillen, D. Hariskos, J. Herrero, R. Klenk, K. Kushiya, D. Lincot, R. Menner, T. Nakada, C. Platzer-Björkman, S. Spiering, A.N. Tiwari, and T. Törndahl. *Prog. Photovoltaics*, 18:411, 2010.

[464] M. N. Mullings, C. Hägglund, and S. F. Bent. *J. Vac. Sci. Technol., A*, 31:061503, 2013.

[465] Z. I. Alferov, V. M. Andreev, D. Z. Garbuzov, and M. K. Trukan. *Soviet Physics Semiconductors*, 6:1718, 1973.

[466] P. W. Yu, W. J. Anderson, and Y. S. Park. *Solid State Communications*, 13:1883, 1973.

[467] S. Chichibu, T. Mizutani, K. Murakami, T. Shioda, T. Kurafuji, H. Nakanishi, S. Niki, P. J. Fons, and A. Yamada. *J. Appl. Phys.*, 83:3678, 1998.

[468] R. Passler. *Phys. Status Solidi (b)*, 216:975, 1999.

[469] M. Cardona, R. K. Kremer, R. Lauck, A. H. Romero, A. Muñoz, and A. Burger. *AIP Conference Proceedings*, 1506:40, 2012.

[470] D. S. Albin, J. J. Carapella, J. R. Tuttle, and R. Noufi. volume 228 of *MRS Online Proceedings Library Archive*, pages 267–272, 1991.

[471] C. Lei, M. Duch, I. M. Robertson, and A. Rockett. *J. Appl. Phys.*, 108:114908, 2010.

[472] K. Ramanathan, H. Wiesner, S. Asher, D. Niles, R. N. Bhattacharya, J.Keane, M. A. Contreras, and R. Noufi. In *Proc. 2nd World Conference on Photovoltaic Solar Energy Conversion, Vienna 6-10 July 1998, Austria*, volume 228, page 47, 1998.

[473] A. Hultqvist, J. V. Li, D. Kuciauskas, P. Dippo, M. A. Contreras, D. H. Levi, and S. F. Bent. *Appl. Phys. Lett.*, 107:033906, 2015.

[474] D. Liao and A. Rockett. *J. Appl. Phys*, 93:9380, 2003.

[475] K. Ramanathan, S. Wiesner, H.and Asher, D. Niles, J. Webb, J. Keane, and R. Noufi. volume 485 of *MRS Online Proceedings Library Archive*, page 121, 1997.

[476] U. Rau and Schmidt M. *Thin Solid Films*, 387:141, 2001.

[477] D. J. Schroeder and A. A. Rockett. *J. Appl. Phys.*, 82:4982, 1997.

[478] Janssen R. A. J. and Nelson J. *Adv. Mater.*, 25:1847, 2012.

[479] U. Rau, B. Blank, T. C. M. Müller, and T. Kirchartz. *Phys. Rev. Applied*, 7:044016, 2017.

[480] P. Szaniawski, P. Salomé, V. Fjällström, T. Törndahl, U. Zimmermann, and M. Edoff. *IEEE J. Photovoltaics*, 5:1775, 2015.

[481] S. Siebentritt, M. Igalson, C. Persson, and S. Lany. *Progress in Photovoltaics: Research and Applications*, 18:390, 2010.